



# UNIVERSITY OF BIRMINGHAM

UNIVERSITY OF BIRMINGHAM

SCHOOL OF PHYSICS & ASTRONOMY

---

## Enhancement of the UK Primary Standard for Absorbed Dose for Proton Radiotherapy

---

*Author:*

Samuel Flynn

*Primary Supervisor:*

Prof. Philip Allport

*Co-Supervisors:*

Prof. Stuart Green

Dr. Tony Price

Mr. Russell Thomas

A thesis submitted for the degree of

*PhD Medical Physics*

14th November 2021

UNIVERSITY OF  
BIRMINGHAM

**University of Birmingham Research Archive**

**e-theses repository**

This unpublished thesis/dissertation is copyright of the author and/or third parties. The intellectual property rights of the author or third parties in respect of this work are as defined by The Copyright Designs and Patents Act 1988 or as modified by any successor legislation.

Any use made of information contained in this thesis/dissertation must be in accordance with that legislation and must be properly acknowledged. Further distribution or reproduction in any format is prohibited without the permission of the copyright holder.

## Abstract

With the implementation of proton beam therapy; modern radiotherapy treatments have better outcomes than ever before. Likewise, the development of spatially fractionated radiotherapy treatments have shown tremendous potential in pre-clinical studies for improving patient outcomes. Both of these implementation come at the cost of increasing complexity, providing a greater challenge for both routine quality assurance and primary standard dosimetry. Simultaneously, recent advances in the field of silicon radiation detectors offer a possible solution for high resolution real-time monitoring would increase confidence in the dosimetry.

This thesis describes the application of Silicon Strip Detectors (SSD) and Complementary Metal-Oxide Semiconductor (CMOS) devices to X-ray and Proton beam therapies with the intention to develop new methods of quality assurance and a combined system using the NPL Graphite Calorimeter for proton radiotherapy. A combined system using a large-format CMOS is tested in 6 MV X-ray beams at the NPL, verifying the concept and providing a proof of principle.

These measurements produced some unexpected results, which required the development of a model of the Calorimeter in COMSOL, a finite-element simulation software package, to study and better understand the internal heat flow. The developed model can use parameterised beam data acquired by an independent silicon detector (whether CMOS or SSD detectors) as a heat source for coupled simulations of delivered beams. After validating against experimental results, the model was subjected to fields of radiation representative of Pencil beam scanning (PBS), providing confidence in the effectiveness of the NPL Graphite Calorimeter in these radiation beams.

**Key words:** Medical Physics, Proton Beam Therapy, Pencil beam scanning, Radiation Dosimetry, Graphite Calorimetry, CMOS, Microbeam Radiotherapy, X-ray Therapy

**Email:** sam.flynn@npl.co.uk

## Acknowledgements

I have been very fortunate throughout this PhD to be supported by an incredible team of supervisors; and I would like to express my gratitude to my academic team. They have been a very supportive group, going above and beyond to provide both academic and pastoral support. Thank you, Phil, Stuart, Russ, and Tony. I thank Nigel Lee for his relentless support, providing wisdom and expertise regarding all things calorimetry.

I take this opportunity to thank those who have helped me in my career to date. I wouldn't be where I am today without any of the following people: Neil Cafferky for enthusing me with a love for tinkering; Adrian Coventry, and all the team from Straininstall, for responding to my letter all those years ago and encouraging me; Ileana Silvestre Patallo, for her unwavering support and mentoring; and Sebastian Galer, for being an excellent friend and encouraging me to begin this PhD journey.

I would also like to express my gratitude to my family for supporting me through the years. There are too many people to list by name, to whom I am very grateful, special recognition must be given to my grandparents Gordon and Sylvia, and my mum Glynis.

Lastly, thank you to Alana Spence for being there for me through this entire journey. I don't think I could have done this PhD without your understanding and encouragement through the highs and lows.

This work was supported by the Science and Technology Facilities Council (grant ST/ P002552/1) and by the UK government's Department for Business, Energy and Industrial Strategy.

# Contents

<b>Abstract</b>	<b>1</b>
<b>Acknowledgements</b>	<b>1</b>
<b>List of Figures</b>	<b>5</b>
<b>List of Tables</b>	<b>11</b>
<b>Glossary</b>	<b>13</b>
<b>Acronyms</b>	<b>14</b>
<b>List of Symbols</b>	<b>17</b>
<b>1 Introduction</b>	<b>18</b>
1.1 Introduction to Metrology . . . . .	18
1.2 Metrology and National Measurement Institutions . . . . .	18
1.3 Thesis Outline . . . . .	20
<b>2 Detection and Measurement of Radiation in External Beam Radiotherapy</b>	<b>22</b>
2.1 Cancer . . . . .	22
2.1.1 What is Cancer . . . . .	22
2.1.2 Cancer Therapy . . . . .	23
2.2 Use of Radiation in Cancer Therapy . . . . .	25
2.2.1 Theory of Cancer Therapy . . . . .	25
2.2.2 History of Radiotherapy . . . . .	26
2.2.3 DNA damage mechanisms . . . . .	27
2.2.4 Dosimetry . . . . .	28
2.2.5 X-Ray Radiotherapy . . . . .	29
2.2.6 Proton Radiotherapy . . . . .	34
2.2.7 Quality Assurance in Proton Radiotherapy . . . . .	40

2.3	Silicon Detectors . . . . .	41
2.3.1	Silicon . . . . .	41
2.3.2	Depletion . . . . .	43
2.3.3	Interaction with Radiation . . . . .	45
2.3.4	Silicon Strip Detectors . . . . .	46
2.3.5	Complementary Metal-Oxide-Semiconductor Devices . . . . .	48
2.3.6	Radiation Damage in Silicon . . . . .	49
2.4	Calorimetry . . . . .	50
2.4.1	Calorimetry Theory . . . . .	52
2.4.2	Water Calorimetry . . . . .	53
2.4.3	Graphite Calorimetry . . . . .	54
2.4.4	NPL Graphite Calorimeter for Absorbed Dose for Proton Radiotherapy . . . . .	55
2.5	Project Justification . . . . .	62
<b>3</b>	<b>Characterisation, Reconstruction, and Evaluation of the PRAVDA Tracker for Proton Beam Monitoring</b>	<b>64</b>
3.1	Introduction . . . . .	64
3.2	Proton computed tomography . . . . .	65
3.3	PRAVDA tracker design . . . . .	65
3.3.1	pCT mode . . . . .	67
3.3.2	Therapeutic mode . . . . .	68
3.4	Image reconstruction . . . . .	70
3.4.1	Algorithms . . . . .	70
3.4.2	Beam centre evaluation . . . . .	71
3.5	X-ray beam investigation . . . . .	73
3.5.1	Motivation . . . . .	73
3.5.2	Expectation . . . . .	74
3.5.3	Methodology . . . . .	74
3.5.4	Profiles . . . . .	75
3.5.5	Pulse detection . . . . .	76
3.5.6	X-ray Linearity . . . . .	77
3.5.7	Static position reconstruction . . . . .	77
3.5.8	Dynamic position reconstruction . . . . .	81
3.6	MC40 Proton beam results . . . . .	83
3.6.1	Motivation . . . . .	83
3.6.2	Methodology . . . . .	83

---

3.6.3	Proton reconstruction . . . . .	86
3.7	Discussion . . . . .	88
3.8	Conclusion . . . . .	89
<b>4</b>	<b>Characterisation and Evaluation of CMOS detectors</b>	<b>90</b>
4.1	Introduction . . . . .	90
4.2	vM1212 Detector Studies . . . . .	90
4.2.1	Detector Characteristics . . . . .	90
4.2.2	Microbeam Dosimetry Investigations . . . . .	93
4.3	vM2428 Detector Studies . . . . .	96
4.3.1	Detector Characteristics . . . . .	96
4.3.2	Preliminary Evaluation in a Linear Accelerator . . . . .	98
4.3.3	Scanned Pencil Beam Measurements . . . . .	105
4.4	Conclusion . . . . .	111
<b>5</b>	<b>Calorimeter Studies</b>	<b>113</b>
5.1	Introduction . . . . .	113
5.2	Investigation with the NPL Proton Calorimeter . . . . .	113
5.2.1	Motivation . . . . .	113
5.2.2	Methodology . . . . .	113
5.2.3	Stationary Beams . . . . .	116
5.2.4	Moving Beams . . . . .	118
5.2.5	SRS Probe Investigation . . . . .	121
5.2.6	Film Study . . . . .	125
5.3	COMSOL Multiphysics simulations . . . . .	128
5.3.1	Introduction to COMSOL . . . . .	128
5.3.2	Prior work . . . . .	128
5.3.3	Proton calorimeter modelling . . . . .	129
5.3.4	Thermal Conductivity Studies . . . . .	130
5.4	Conclusion . . . . .	139
<b>6</b>	<b>Conclusion</b>	<b>141</b>
	<b>Bibliography</b>	<b>144</b>
	<b>References</b>	<b>145</b>
	<b>Appendices</b>	<b>166</b>

<b>A PRAVDA tracker reconstruction algorithms</b>	<b>167</b>
A.1 Reconstruction algorithms . . . . .	167
A.1.1 Fast reconstruction algorithm . . . . .	167
A.1.2 Slow reconstruction algorithm . . . . .	173
<b>B Presentations and Publications</b>	<b>176</b>
B.1 Poster presentations . . . . .	176
B.2 First-author publications . . . . .	176

# List of Figures

1.1	Location of National Measurement Institutes within Europe. . . . .	19
1.2	Example of a calibration chain in the UK for the kilogram. . . . .	20
2.1	Cancer therapy modality distributions, measured in England 2013-2016[43] . . . .	24
2.2	Annotated diagram of DNA damage via radiation. . . . .	27
2.3	Simplified diagram demonstrating interaction mechanism of an uncharged particles.	30
2.4	X-Ray PDDs obtained at NPL for various energies, data provided by Ileana Silvestre Patallo. . . . .	31
2.5	An annotated diagram of a Clinical Linear Accelerator (Linac). . . . .	32
2.6	Example of prostate TCP and rectum NTCP when treating prostate cancer[91]. . .	33
2.7	Simulated Bragg peaks for various energies, generated using Python[105]. . . . .	36
2.8	Approximate proton range in water for various energies, using data from NIST[106].	36
2.9	Simplified diagram demonstrating interaction mechanism of charged particles. . . .	37
2.10	Annotated diagram of a Spread-Out Bragg Peak. . . . .	38
2.11	An annotated diagram of a passive scattered pencil beam. . . . .	38
2.12	An annotated diagram of Pencil-Beam Scanning (PBS). . . . .	39
2.13	Intrinsic Silicon with no impurities. . . . .	42
2.14	<i>n</i> -type Silicon with phosphorus "donor". . . . .	43
2.15	<i>p</i> -type Silicon with boron "acceptor". . . . .	43
2.16	Diagram of depletion in a <i>pn</i> junction. . . . .	44
2.17	Annotated diagram showing voltage current response of a <i>pn</i> junction, not to scale.	44
2.18	Diagram showing hole-electron pairs created in silicon from a charged particle. . .	46
2.19	Photograph showing the separation of the silicon strips and readout board in a SSD that is part of a PRaVDA tracker unit. . . . .	47
2.20	Evidence of radiation damage from several investigations with the vM1212 detector manifesting as change in dark current. . . . .	50
2.21	Photon calibration chain in the UK. . . . .	51

LIST OF FIGURES

---

2.22	Simulation of Radiation Induced Temperature Rise in Adiabatic mode. . . . .	53
2.23	Schematic of three body Domen type graphite calorimeter, from 1972 patent application[152]. . . . .	54
2.24	The NPL Graphite Calorimeter for absorbed dose in Proton Radiotherapy. . . . .	56
2.25	Annotated engineering diagram of the cross-section of the NPL Graphite Calorimeter for absorbed dose for proton radiotherapy. . . . .	56
2.26	Annotated radiographic image of the NPL proton calorimeter, image provided by Nigel Lee. . . . .	58
2.27	The thermistor ( $R_4$ ) configured in a Wheatstone Bridge in the NPL Proton Calorimeter. . . . .	58
2.28	The configuration of the heating thermistors ( $R_2$ and $R_3$ ) in the NPL Proton Calorimeter. . . . .	59
2.29	Temperature measurement of the NPL Proton Calorimeter to a scanned pencil beam in QA mode. . . . .	60
2.30	Electrical power measurement of the NPL Proton Calorimeter to a scanned pencil beam in ISO mode. . . . .	61
3.1	Example of "ghosting" artefacts in with "XY" position tracking. . . . .	66
3.2	Internals of PRaVDA tracker unit. . . . .	67
3.3	Simulated effect of compositing multiple PRaVDA tracker frames with a median rank filter of 20. . . . .	69
3.4	Simulated effect of multiple PRaVDA tracker frames on Gamma Passing Rate with various median rank filters. . . . .	70
3.5	Gamma passing rate of simulated multiple PRaVDA for various median rank filter values. . . . .	70
3.6	Comparison of the two PRaVDA tracker reconstruction methods. . . . .	71
3.7	Simulated beam centre error of the PRaVDA tracker unit against number of frames in composite. . . . .	72
3.8	Investigation of threshold value on beam centre for increasing number of frames. . . . .	72
3.9	Effect of varying the threshold on reconstructed beam centre for 50% and 80% for a simulated $20 \times 20 \text{ mm}^2$ beam. . . . .	73
3.10	Energy Spectra of a typical 6 MV Linac compared to the Silicon Mass Energy-Absorption Coefficient. . . . .	74
3.11	Setup of the Proton Radiotherapy Verification and Dosimetry Applications (PRaVDA) tracker in an Elekta Synergy linear accelerator. . . . .	75
3.12	PRaVDA tracker positioned at isocentre with 5 cm of water equivalent build-up. . . . .	75

3.13	Raw profiles acquired from a 6 MV $15 \times 15 \text{ mm}^2$ 6 X-ray field. The $U$ -plane is orthogonal to the square of radiation, whilst the $X$ and $V$ planes are aligned at an angle. . . . .	75
3.14	Smoothed profiles acquired from a 6 MV $15 \times 15 \text{ mm}^2$ X-ray field. . . . .	76
3.15	Pulses from the linear accelerator, as recorded with the PRaVDA tracker for a 6 MV 400 Hz PRF beam and a 10 MV 200 Hz PRF beam. . . . .	77
3.16	Linearity of PRaVDA Tracking Unit in a 6 MV X-ray beam. . . . .	78
3.17	<i>Projection</i> reconstruction of $15 \times 15 \text{ mm}^2$ 6 MV X-ray field for increasing number of frames. . . . .	79
3.18	Beam profiles as measured by the PRaVDA tracker unit for various X-ray beam sizes. . . . .	80
3.19	Reconstruction of $10 \times 10 \text{ mm}^2$ 6 MV X-ray field. . . . .	80
3.20	Reconstruction of $30 \times 30 \text{ mm}^2$ 6 MV X-ray field. . . . .	80
3.21	Reconstruction of $15 \times 15 \text{ mm}^2$ 6 MV X-ray field positioned at (0 mm, -20 mm). . . . .	81
3.22	Reconstruction of $15 \times 15 \text{ mm}^2$ 6 MV X-ray field positioned at (-20 mm, 0 mm). . . . .	81
3.23	Analysis of moving X-ray fields for various prescribed Monitor Units. . . . .	82
3.24	Calculation of dwell time calculated for a sliding X-ray beam for different prescribed Monitor Units. . . . .	82
3.25	Calculated beam centres of a rotating 6 MV $15 \times 15 \text{ mm}^2$ field for various offset positions. . . . .	84
3.26	Setup of the PRaVDA tracker at the MC40 Cyclotron Facility. . . . .	85
3.27	Photograph of PRaVDA tracker with moveable collimator. . . . .	85
3.28	Linearity response of the PRaVDA tracker unit in a 36 MeV proton beam. . . . .	86
3.29	Beam profiles as measured by the PRaVDA tracker unit for a 0.10 nA 36 MeV proton beam. . . . .	86
3.30	Reconstructed images of a 36 MeV proton beam with nominal position of (0 mm, 0 mm). . . . .	87
3.31	Calculated positions of a moving proton beam using the PRaVDA tracker unit. . . . .	87
3.32	Calculation of the speed of a moving collimator using the PRaVDA tracker, compared to video. . . . .	88
3.33	Broken Internals of PRaVDA tracker unit. . . . .	89
4.1	Photograph of the vM1212 Detector. . . . .	91
4.2	Photograph of the beam window of the vM1212 Detector. . . . .	92
4.3	Maximum acquisition time of the vM1212 Detector as a function of integration time. . . . .	93
4.4	Photograph of the vM1212 Detector during the X-ray microbeam investigation. . . . .	93
4.5	Microbeam Profiles acquired for $100 \mu\text{m}$ nominal slit width. . . . .	94

---

4.6	Two Dimension Microbeam Profile acquired using the vM1212 detector. . . . .	95
4.7	Photograph of the vM2428 Detector. . . . .	96
4.8	Flat Field response of the vM2428 Detector. . . . .	98
4.9	vM2428 detector setup on treatment couch in Elekta Versa HD Linac for X-ray studies.	99
4.10	Investigation of $v_{pixel}$ response of vM2428 detector in a 6 MV FFF beam. . . . .	100
4.11	vM2428 Detector setup in Elekta Versa HD Linac for Horizontal Beam Tests. . . .	100
4.12	Comparison of vM2428 detector response with and without 5 cm of water equivalent buildup in a $10 \times 10 \text{ cm}^2$ 6 MV FFF field. . . . .	101
4.13	Average Detector Response to various 6 MV fields with 5 cm of water equivalent build-up. . . . .	102
4.14	Comparison of vM2428 Detector and EBT3 film measuring a $1 \times 1 \text{ cm}^2$ 6 FFF field.	102
4.15	Comparison of different X-ray profiles acquired using the vM2428 detector with 5 cm of build-up. . . . .	103
4.16	Comparison of rolling shutter artefacts for different integration times. . . . .	103
4.17	Determined positions for a rotating Linac collimator using the vM2428 detector using various offset X-ray fields. . . . .	104
4.18	vM2428 Detector being setup at the UCLH Proton Beam Facility. . . . .	105
4.19	Uncalibrated Image of vM2428 Detector measuring a 20 nA 220 MeV proton beam.	106
4.20	Linearity Response of vM2428 Detector in a 220 MeV proton beam. The range of values due to the cyclotron variation are shown as the Digital Value error bars. . .	107
4.21	Comparison of EBT3 Film Profile and vM2428 Detector for a Proton Beam Spot. .	108
4.22	Moving Pencil Beams measured using the vM2428 Detector . . . . .	109
4.23	Determined Positions for a moving scanned pencil beam. . . . .	110
4.24	Histogram of positions for a scanned pencil beam. . . . .	110
4.25	Moving Pencil Beams measured using the vM2428 Detector . . . . .	111
5.1	Photograph of the vM2428 Detector with the <i>NPL proton calorimeter</i> . . . . .	114
5.2	Photograph of the rear of the vM2428 detector with the <i>NPL proton calorimeter</i> . .	114
5.3	Photograph of the vM2428 Detector with <i>NPL proton calorimeter</i> with light shroud.	115
5.4	Radiation Profiles acquired for different field sizes using the vM2428 detector show- ing the relative position of the <i>NPL proton calorimeter</i> core. . . . .	116
5.5	Temperature increase in the <i>NPL proton calorimeter</i> core as a result of a $5 \times 5 \text{ cm}^2$ beam delivering multiple 500 MU exposures. . . . .	117
5.6	Temperature increase in the <i>NPL proton calorimeter</i> core as a result of a $5 \times 5 \text{ cm}^2$ beam delivering a single 500 MU exposure. . . . .	117

5.7	Comparison of measured Output Factor when using Dose (Gy) and Dose Area Product (MUmm <sup>2</sup> ). . . . .	118
5.8	Images acquired using the vM2428 detector for the moving X-ray beam, showing the relative position of the <i>NPL proton calorimeter</i> core . . . . .	119
5.9	Comparison of instantaneous dose rate and cumulative dose measured in the <i>NPL proton calorimeter</i> , and beam parameters acquired by the vM2428 detector, for multiple passes with a moving X-ray beam. . . . .	120
5.10	Comparison of instantaneous dose rate and cumulative dose measured in the <i>NPL proton calorimeter</i> , and beam parameters acquired by the vM2428 detector, for a single pass with a moving X-ray beam. . . . .	121
5.11	Photograph of the Stereotactic Radiosurgery collimator attached to the Elekta Versa HD Linac. . . . .	122
5.12	Dose measured as a function of position when exposing the <i>NPL proton calorimeter</i> core with a 4 mm FWHM SRS 6 MV FFF beam. . . . .	123
5.13	Dose profiles in the $x$ and $y$ axes when exposing the <i>NPL proton calorimeter</i> core with a 4 mm FWHM SRS 6 MV FFF beam. . . . .	123
5.14	Instantaneous dose rate measured by the <i>NPL proton calorimeter</i> for an off-centre beam showing the difference in response between the two sensing thermistors. . . .	124
5.15	Rise time difference as a function of position for the <i>NPL proton calorimeter</i> . . . .	125
5.16	Rise time difference profiles of the <i>NPL proton calorimeter</i> in the $x$ and $y$ axes. . . .	125
5.17	Annotated Photograph of the vM2428 Detector with film. . . . .	126
5.18	Comparison of EBT3 and vM2428 detector dose profiles. . . . .	127
5.19	Spatial reconstruction of X-Ray dose deposition using EBT3 Film dose profiles. . . .	127
5.20	Cross section of model of <i>NPL proton calorimeter</i> in COMSOL Multiphysics. . . .	130
5.21	Comparison of instantaneous dose rate for various thermal conductivity values. . . .	132
5.22	Simulation Rise Time comparison for various thermal conductivity values. . . . .	132
5.23	Simulated Rise Time Propagation Velocity against Thermal Conductivity. . . . .	133
5.24	Comparison of experimentally measured moving X-ray beam and COMSOL Multiphysics simulated. . . . .	133
5.25	Comparison of moving X-ray simulations in COMSOL Multiphysics for various thermal conductivity values. . . . .	134
5.26	Ratio of peaks for moving X-ray simulations in COMSOL Multiphysics for various thermal conductivity values. . . . .	135
5.27	Simulated Temperature response of the Calorimeter to small beam positioned at the centre of the <i>core</i> . . . . .	135

5.28	Raster scan positions for simulated PBS in COMSOL Multiphysics model. . . . .	136
5.29	Instantaneous dose rate and cumulative dose for simulated PBS study. . . . .	137
5.30	Relative surface temperature of <i>NPL proton calorimeter</i> core for simulated PBS. .	138
5.31	Instantaneous dose rate and cumulative dose for simulated PBS study with reversed <i>x</i> and <i>y</i> axes beam positions. . . . .	139
A.1	Diagram of PRaVDA reconstruction algorithm. . . . .	168
A.2	Simulated Gaussian profiles on the PRaVDA tracker layers with a 20 mm FWHM, centred at $X = 18.5$ mm, $U = 35.7$ mm and $V = -17.2$ mm. . . . .	169
A.3	Layer by layer reconstruction of the simulated Gaussian profiles for the PRaVDA tracker shown in Figure A.2. . . . .	169
A.4	Demonstration of the validation algorithm for a 2D Gaussian with 20 mm FWHM.	170
A.5	Demonstration of validation algorithm for a $20 \times 20$ mm <sup>2</sup> square. . . . .	170
A.6	Determining the beam centre of the reconstructed beam projection. . . . .	171
A.7	Position error of the reconstructed beam centre for different threshold values. . . .	172
A.8	Gamma evaluation of the "Fast" reconstruction algorithm with 3%/3mm parameters and a 20% dose cutoff. . . . .	173
A.9	"Slow" Reconstruction Algorithm step 1: Identifying the 1D positions of the threshold.	174
A.10	"Slow" Reconstruction Algorithm Step 2: Defining 2D threshold contours . . . . .	175
A.11	Gamma evaluation of the "Slow" reconstruction algorithm with 3%/3mm paramet- ers and a 20% dose cutoff. . . . .	175

# List of Tables

2.1	Overview of different treatment modalities available within radiotherapy. . . . .	25
2.2	Parameters in Bethe formula for Equation 2.11. . . . .	35
2.3	Labelled Graphite Calorimeter components in Figure 2.23 . . . . .	54
3.1	Specifications of the PRAVDA tracker silicon strip detector . . . . .	67
4.1	Specifications of the vM1212 Detector. . . . .	91
4.2	Specifications of the vM2428 detector. . . . .	97
5.1	Configuration of the <i>NPL proton calorimeter</i> operating in Quasi-Adiabatic mode. .	115
5.2	Parameters of the moving X-ray beam. . . . .	118

# Glossary

**Absorbed Dose** "The absorbed dose,  $D$ , is the quotient of  $d\bar{\epsilon}$  by  $dm$ , where  $d\bar{\epsilon}$  is the mean energy imparted by ionising radiation to matter of mass  $dm$ [1]. 7, 20, 21, 28, 29, 51, 53, 55, 56, 62, 117, 131, 144

**Charged-Particle Equilibrium** Charged-Particle Equilibrium is achieved when a volume has an equal number of charged particles entering as it does leaving[2].. 36

**COMSOL Multiphysics** COMSOL Multiphysics is a finite element simulation software developed by COMSOL Inc., which is capable of modelling heat flow[3]. 10, 11, 21, 128, 129, 130, 131, 133, 134, 135, 136, 137, 139, 140, 143, 144

**in-vitro** The study of tumour cells attached to plastic or glass tissue culture dishes or flasks[4]. 28

**LabVIEW** A graphical programming language, developed by National Instruments[5]. 167, 170

**Monte Carlo** A simulation technique in which random sampling of large quantities of numbers and statistical inference are used to determine quantities of interest[6] . 55, 61, 74, 126, 143, 144

# Acronyms

**ADC** Analog-to-Digital Converters. 48, 49, 98, 105

**BIPM** International Bureau of Weights and Measures. 20

**BNCT** Boron Neutron Capture Therapy. 25

**CCD** Charge-coupled device. 48

**CMOS** Complementary Metal–Oxide–Semiconductor. 21, 45, 48, 49, 50, 63, 90, 94, 96, 99, 101, 102, 111, 112, 139, 141, 142, 143

**CTV** Clinical Target Volume. 34

**DAP** Dose-Area-Product. 117, 120

**DaRT** Diffusing alpha-emitters radiation therapy. 25

**DNA** Deoxyribonucleic Acid. 6, 22, 23, 27, 28, 29, 36

**DU** Digital Units. 48

**ESRF** The European Synchrotron Radiation Facility. 57

**EURAMET** European Association of National Metrology Institutes. 19

**FFF** Flattening Filter Free. 9, 10, 31, 98, 99, 100, 101, 102, 103, 104, 113, 115, 116, 118, 122, 123, 126

**FWHM** Full width at half maximum. 10, 11, 39, 68, 73, 75, 86, 88, 95, 96, 97, 107, 120, 123, 126, 133, 135, 139, 169, 170

**GTV** Gross Tumour Volume. 34

**HEP** High Energy Physics. 46

- IAEA** International Atomic Energy Agency. 51, 75
- ICRU** The International Commission on Radiation Units and Measurements. 28
- IMRT** Intensity-modulated radiation therapy. 34, 55, 172
- IPEM** Institute of Physics and Engineering in Medicine. 51
- IQ** Intelligence Quotient. 37, 141
- ISO** Isothermal. 7, 61, 115, 129, 130, 143
- LET** Linear Energy Transfer. 29, 36, 50
- Linac** Linear Accelerator. 6, 7, 9, 10, 25, 30, 31, 32, 34, 51, 74, 75, 76, 77, 79, 81, 82, 83, 86, 88, 98, 99, 100, 101, 103, 104, 108, 113, 114, 115, 118, 120, 121, 122, 141
- MLC** Multileaf Collimator. 32, 77, 78, 79, 81, 98, 101, 113, 116, 118, 120, 134
- MOS** Metal–Oxide–Semiconductor. 41
- MRI** Magnetic resonance imaging. 65
- MRT** Microbeam Radiation Therapy. 93, 96
- MU** Monitor Units. 8, 9, 75, 76, 78, 82, 102, 107, 108, 110, 116, 117, 118, 122, 126
- NHS** National Health Service. 20, 30, 51, 141
- NMI** National Measurement Institute. 18, 19, 20, 50, 51, 55
- NPL** National Physical Laboratory. 6, 7, 9, 10, 11, 12, 18, 19, 30, 31, 51, 55, 56, 57, 58, 59, 60, 61, 62, 63, 64, 65, 73, 88, 89, 91, 92, 94, 97, 98, 99, 101, 105, 111, 113, 114, 115, 116, 117, 118, 119, 120, 121, 122, 123, 124, 125, 126, 128, 129, 130, 131, 134, 137, 138, 139, 140, 141, 143, 144
- NTCP** Normal Tissue Complication Probability. 6, 32, 33, 34, 52
- PBS** Pencil-Beam Scanning. 6, 11, 39, 40, 62, 63, 68, 73, 77, 79, 82, 88, 89, 90, 98, 104, 105, 111, 112, 114, 120, 121, 128, 129, 135, 136, 137, 138, 139, 140, 143
- PBT** Proton Beam Therapy. 34, 40, 76, 113, 141, 143
- PCB** Printed Circuit Board. 57, 59, 60, 91, 96, 97, 98, 99, 110, 114, 115, 125, 129, 143
- pCT** Proton Computed Tomography. 64, 65, 66, 67, 83, 89, 141, 167

- PDD** Percentage Depth Dose. 6, 30, 31, 101, 128, 140
- PID** Proportional–Integral–Derivative controller. 59, 62, 129, 130
- PRaVDA** Proton Radiotherapy Verification and Dosimetry Applications. 6, 7, 8, 11, 12, 47, 64, 65, 66, 67, 68, 69, 70, 71, 72, 73, 74, 75, 76, 77, 78, 79, 80, 81, 82, 83, 85, 86, 88, 89, 90, 92, 100, 101, 104, 141, 142, 169
- PRF** Pulse Repetition Frequency. 8, 76, 77, 88, 103, 115, 118
- PSI** Paul Scherrer Institute. 39, 41
- PTV** Planning Target Volume. 34
- PVDR** Peak-to-Valley Dose Ratio. 95
- QA** Quasi-Adiabatic. 7, 12, 60, 115, 129, 130, 143
- RAL** Rutherford Appleton Laboratory. 90, 91
- RAM** Random-Access Memory. 104
- RBE** Relative biological effectiveness. 37
- RIM** Radiation-Induced Malignancies. 27
- ROI** Region Of Interest. 97, 106, 110, 111, 112, 115
- SABR** Stereotactic ablative radiotherapy. 34
- SDR** Sigmoidal Dose Response. 32
- SI** Système International (d’unités). 18, 19, 28
- SNR** Signal to Noise Ratio. 55
- SOBP** Spread-Out Bragg Peak. 6, 37, 38
- SRS** Stereotactic Radiosurgery. 10, 34, 121, 122, 123
- SSD** Silicon Strip Detector. 6, 20, 21, 45, 46, 47, 48, 49, 63, 64, 66, 72, 75, 88, 89, 90, 99, 141, 142, 174
- TCP** Tumour Control Probability. 6, 32, 33, 34, 52
- UCLH** University College Hospitals London NHS Foundation Trust. 9, 105

**UHB** University Hospitals Birmingham. 68

**VMAT** Volumetric Modulated Arc Therapy. 34

**VSL** Van Swinden Laboratory. 53

**xCT** X-ray computed tomography. 33, 65, 66, 142

# Chapter 1

## Introduction

### 1.1 Introduction to Metrology

The term "Metrology" is defined by the Oxford Reference dictionary as the *"scientific study of measurement, especially the definition and standardisation of the units of measurement used in science"*[7]. Whilst not necessarily glamorous, the importance of metrology cannot be overstated for modern society. Comparability of traceable measurements underpin both international and domestic trade, modern science[8][9], and enable global improvements in areas of health, environment and quality of life[10].

At the most basic level, the definition for a physical unit is the multiplication of a numerical value by a defined unit (Equation 1.1)[11].

$$\text{physical quantity} = \text{numerical value} \times \text{unit} \quad (1.1)$$

There is an important distinction between metrology and measurement. The latter being concerned with obtaining a numerical value from an experiment, whilst metrology is responsible for both the definition of the defined unit, and the measurement of the numerical quantity. In order to communicate a physical quantity to another person or organisation, it is essential that both parties are in agreement for the value of the units used. As stated by Richard Brown of the National Physical Laboratory (NPL) states, "If philosophy is 'thinking about thinking', then metrology is 'measuring the measurement'"[12].

### 1.2 Metrology and National Measurement Institutions

The dissemination of the Syst me International (d'unit s) (SI) standards to end users is usually delegated to the National Measurement Institutes (NMIs) of the various countries. Most countries

globally and within Europe have established their own NMIs, with the exception of smaller countries such as the Vatican City State or the Republic of San Marino[13]. The location of all NMIs that are members of the European Association of National Metrology Institutes (EURAMET)[14] are shown in Figure 1.1. Within the United Kingdom of Great Britain and Northern Ireland, the NMI is the National Physical Laboratory (NPL).

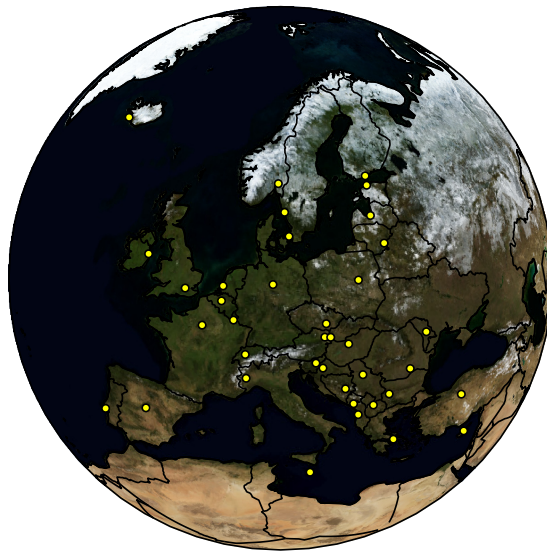


Figure 1.1: Location of National Measurement Institutes within Europe.

The equipment used to measure these Base and Derived SI units at the NMI level is referred to as a primary standard. These primary standards are not calibrated relative to other devices, as by definition they are what other devices calibrate against. Examples of primary standard instruments held at the NPL are the Kibble balance[15] and the Josephson primary standard for voltage[16]. It is worth noting that not every NMI holds every possible primary standard. These instruments are often prohibitively expensive to purchase, manufacture, and maintain; whilst requiring a non-trivial amount of specialist knowledge that is often not of interest to the vast majority of users. In many cases it is not economically justifiable. For when this is the case, there exists a network of Secondary Standards Laboratories whose role it is to provide traceable measurements for users within a country.

Whilst primary standard devices are designed with the lowest uncertainty possible, they are often impractical to use on a regular basis for simple measurements. The calibration chain exists to ensure the dissemination of the SI unit to all users that would need it. An example of this is shown in Figure 1.2, based on Stock *et al.* [17]. The primary standard instrument (held at a NMI) is used to calibrate secondary standard instruments, which are in turn used to calibrate tertiary instruments.

The appreciation of the limitations this imposes is captured by the philosopher Arthur David

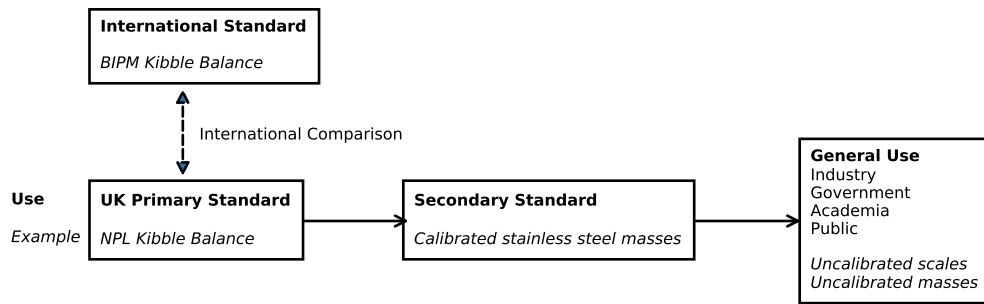


Figure 1.2: Example of a calibration chain in the UK for the kilogram.

Ritchie (1891 - 1967) when he stated "It is really just as bad technique to make a measurement more accurately than is necessary as it is to make it not accurately enough." [18]

All NMIs that are part of BIPM undergo regular intercomparison of primary standard instruments. When possible this is done directly with the primary standard devices themselves, otherwise secondary standard instruments are used as intermediaries.

Performing a single measurement of a quantity is not enough to accurately determine the true value. For every measurement there exists a probability distribution of possible values that could be recorded. These sources of uncertainty can be divided into two sections: "Type A", where the uncertainty can be quantified with repeated measurements and "Type B", where the uncertainty has to be determined via other methods [19].

### 1.3 Thesis Outline

The research presented in this thesis was motivated by the development of two National Health Service (NHS) Proton Beam facilities [20], complemented by private health facilities being constructed [21]. Recognising the challenges that this will pose to the primary standard for absorbed dose for proton radiotherapy, the objective of this thesis is primarily to reduce the uncertainty of the instrument.

This chapter provided the context and background for the role of primary standard instruments at NMIs. The concept of a calibration chain is explained, within the context of metrology.

Chapter 2 provides a background for modern detection techniques for modern external beam radiation therapy; introducing cancer, and radiotherapy techniques for treatment. A background to silicon detectors for monitoring radiation beams is provided. Finally, the primary standard device for absorbed dose in proton radiotherapy is introduced, and a technical description of how it operates is provided. The motivation behind reducing the measurement uncertainty of this device is discussed, and possibilities for doing so are presented.

Chapter 3 describes efforts using a Silicon Strip Detector (SSD) to monitor external beams of

radiation. A novel algorithm to reconstruct incident beams is presented, and the suitability of the technology for use with the primary standard device for absorbed dose in proton radiotherapy is discussed. This chapter expands upon research presented in a publication in JINST[22], describing measurements with multiple types of radiation.

In Chapter 4, a Complementary Metal–Oxide–Semiconductor (CMOS) device is evaluated and characterised and the results compared to the SSD. New applications in microbeam radiotherapy dosimetry using pixelated devices are presented, with the results of two publications summarised. An investigation using a CMOS detector at a clinical proton beam facility is described, demonstrating the viability of the technology for modern radiotherapy dosimetry applications.

Chapter 5 describes a series of measurements performed with the primary standard device for absorbed dose in proton radiotherapy with the discussed CMOS sensor. Due to the impact of COVID-19[23], it was not possible to conduct the required studies in a proton therapy beam however a conventional X-ray beam is used as a surrogate enabling conclusions to be inferred. The theorised need for position sensitive detectors is proven, and results from simulation study in the finite element software COMSOL Multiphysics are presented.

Finally, Chapter 6 is the concluding chapter to this thesis. Research achievements highlighted throughout this thesis are summarised, and emerging avenues of research are proposed.

## Chapter 2

# Detection and Measurement of Radiation in External Beam Radiotherapy

## 2.1 Cancer

### 2.1.1 What is Cancer

Cancer is the name for a collection of more than 200 diseases in which normal cell division is disrupted in otherwise healthy tissue. The human body is made up of approximately  $10^{13}$  individual cells[24], carrying out many complex processes such as homeostasis or respiration[25]. The processes that each cell carries out are determined by Deoxyribonucleic Acid (DNA), the complex molecule that contains our personal genetic information[26]. During cellular reproduction, random changes in DNA can cause cells in the body to no longer carry out the same complex processes as before. Whilst DNA changes can occur naturally, they are often impacted and influenced by external factors within the environment[27]. Up to  $7 \times 10^5$  DNA lesions may be created per cell per day resulting from environmental factors[28]. One of the most damaging aspects of the environment is the ultraviolet component of sunlight, which can create up to  $1 \times 10^5$  DNA lesions per cell per hour exposed[29][30]. Whilst most DNA lesions can be repaired by the cell's internal mechanisms, those that are not have the potential to become DNA mutations[31] in which the corrupted DNA is passed on to the next cellular generation. The rate at which DNA lesions become DNA mutations is very low, and is a very complex area of biology with many variables beyond the scope of this thesis[32].

In some cases, the damage to the DNA makes the cell non-viable ending the cell line[33]. Where

the cell is viable, but unregulated, the cell is instructed to perform apoptosis, or cell-death[34]. If the DNA cannot be repaired, is left uncorrected, and is viable: the cell can transform in to a rapidly proliferating, cancer-type cell [33]. Cancerous cells can grow and multiply faster than healthy cells[35] developing into tumours that compete with local tissue for access to blood, oxygen, and nutrients. It is in this manner that damage is inflicted to the local healthy tissue. Depending on the location within the body some tumours can cause damage to healthy tissue via compression, such as the case of intracranial tumours increasing the pressure of brain tissue against the skull[36].

A collection of cancerous cells is referred to as a tumour, and can be formed anywhere in the body where normal cell division takes place. Within a solid tumour, the cellular density is approximately  $10^8/\text{cm}^3$ [37]. The original tumour, originating where the DNA mutation resulting in the first cancerous cells appeared, is referred to as the primary tumour. Breakaway tumour cells that have spread from the primary tumour location, typically via the blood or lymphatic system, are referred to as metastatic or secondary tumours. Tumours are categorised into either benign tumours, which typically grow slowly; vs malignant tumours, which rapidly grow and can metastasise to other parts of the body[38]. The lethality of a cancer depends on the rate at which the cancer grows, the location within the body, the type of cells, and their resistance to treatment[39].

It is estimated that 50% of males and 45% of females born after 1960 in the UK will be diagnosed with some form of cancer at some point in their lives[40]. In the UK there are an estimated 2.5 million people living with cancer, a figure expected to rise to 4 million by 2030[41]. Globally, cancer is the second greatest cause of death after heart disease, with the World Health Organisation estimating that 9.6 million people died from the disease in 2018[42].

### 2.1.2 Cancer Therapy

There are many types of cancer therapy that are available, depending on both the size of the tumour and the location within the body. Across all tumours, the preferential treatment in the UK is surgical resection when available, involved with approximately 45% of all primary cancer therapy[43]. Chemotherapy is involved with 28% of primary cancer therapies, while Radiotherapy, or radiation therapy, ranks third at 27%. Radiotherapy is defined by the National Health Service as a treatment where “radiation is used to kill cancer cells”[44]. These proportions are shown in Figure 2.1(a), as well as "Other care" (at 33%) which among others represents hormonal replacement therapy, gene therapies, and management of symptoms. It is important to note that these methods of treatment are frequently used in combination, as shown in Figure 2.1(b) where those treatment combinations involving radiotherapy are highlighted.

A similar utilisation of radiotherapy for cancer therapy is observed in other developed na-

tions[45]. This is not consistent globally, with many low and middle income countries not having access to many of the more expensive or complex treatments. Radiotherapy, as discussed later in Section 2.2.1 is relatively cheap but still not readily available globally[46]. This is in part due to a combination of poor infrastructure and availability of skilled staff.

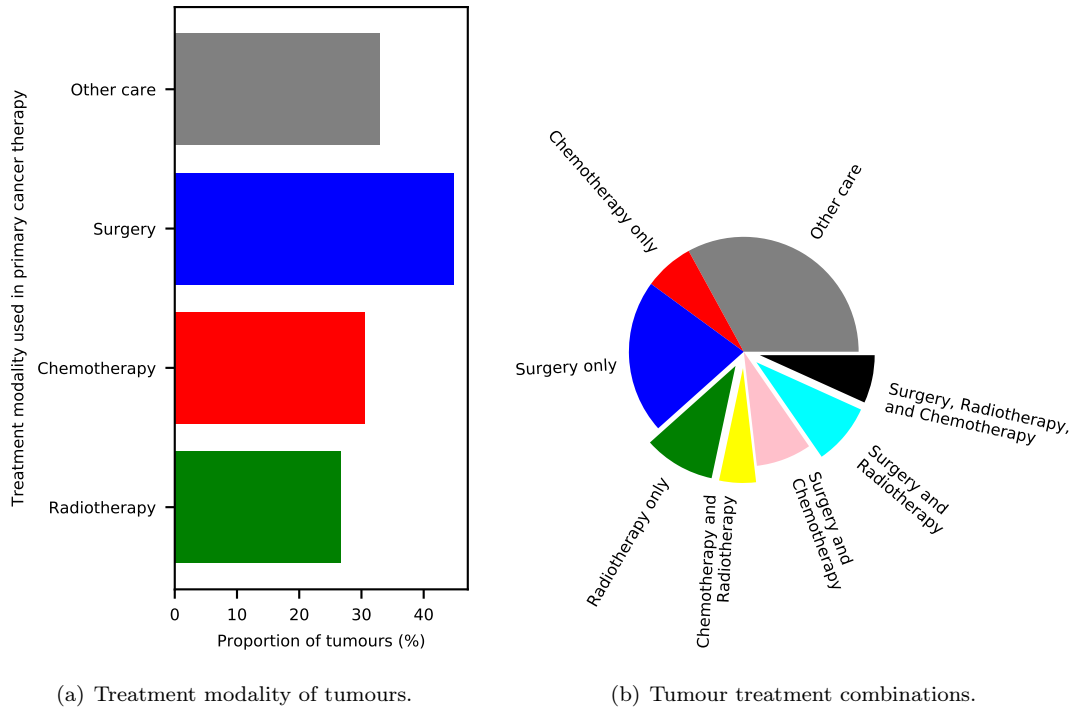


Figure 2.1: Cancer therapy modality distributions, measured in England 2013-2016[43]

The suitability of many of the treatments depends on the form and location of the tumour. A tumour may become too large for surgical resection, where the risk of further complications developing outweighs the benefit of removing the tumour. Situations like this can be improved by causing the tumour to shrink in size via radiation, drugs or other therapies enabling surgery. Radiotherapy is most suited towards the treatment of "solid mass" tumours which are defined as those without internal cysts or liquid areas[47].

As discussed, a primary tumour has the potential to have metastasised resulting in numerous secondary tumours throughout the body. In this situation, surgery is again unlikely to be the most appropriate course of action due to the prevalence of the tumours but other therapies may still be tried, whilst chemotherapy or radiotherapy may be more suitable.

Whilst the other therapy modalities for cancer treatment are given for context, the focus of this thesis is radiotherapy. By improving the quality of radiotherapy delivered to cancer patients, it is hoped that their survival probabilities and quality of life post therapy is increased accordingly.

## 2.2 Use of Radiation in Cancer Therapy

### 2.2.1 Theory of Cancer Therapy

The most commonly used form of radiotherapy in the UK is External Beam radiotherapy, where high-energy photons or particles are directed towards a patient from a controlled source (man-made or natural). This is in contrast to Brachytherapy, in which physical sources are inserted into a patient in the form of small pellets; or Molecular radiotherapy, in which targeted radionuclides are injected into a patient. A non-exhaustive summary of the most common modalities of radiotherapy available in the UK is shown in Table 2.1). More exotic forms of radiation therapy do exist, such as Boron Neutron Capture Therapy (BNCT), Carbon-ion therapy or Diffusing alpha-emitters radiation therapy (DaRT) but are not available in the UK and are very limited in patient numbers globally, and as such are beyond the scope of this document.

Treatment Modality	Location	Energy	Use case
High Energy X-rays	External	6-15 MV photons	Solid mass tumours
Superficial X-rays	External	10-400 kV photons	Superficial tumours
High Energy electron	External	6-20 MeV	Superficial tumours (with rapid drop off in dose)
Protons	External	60-250 MeV	Solid mass tumours close to critical structures
Brachytherapy	Internal	20.8 kV - 1.25 MV, site depending	Small tumourous volume close to sensitive structures
Molecular Radiotherapy	Internal	<i>Variable</i>	Targeted tumour sites with specific indications

Table 2.1: Overview of different treatment modalities available within radiotherapy.

By damaging cancer cells through ionisation (Section 2.2.3) the tumour may be killed or shrunk, having the effect of curing the patient or relieving symptoms, as is the case in palliative therapy. Radiotherapy does have high infrastructure costs, associated with shielding and accelerator equipment (if applicable). Costs associated with an X-ray Linac, the most common type of external beam radiotherapy, are typically £1.4-1.8 million per linear accelerator with an additional cost of over £500,000 per bunker for radiation shielding [48]. Despite this however, the average linear accelerator can be expected to treat over 5,000 patients in a 10-year life span providing a very modest cost of £3-4k per patient, inclusive of staff time[49]. Of the total expenditure for cancer treatments, radiotherapy composes 5% of the cost relative to surgery's 22% and chemotherapy's 18% [50].

### 2.2.2 History of Radiotherapy

Although the discovery of electromagnetic radiation other than visible was first published in 1800 by William Herschel[51], it was not until 1895 that Wilhelm Röntgen discovered a new type of radiation that we now refer to as X-rays[52]. Unlike previously discovered forms of radiation, these new X-rays were capable of passing through opaque objects. In the course of these experiments, it was quickly discovered that this new form of radiation would induce skin reactions in the hands of operators. A month after Röntgen's discovery, physicians Léopold Freund and Eduard Schiff suggested that it could be performed intentionally for a therapeutic effect, creating the field of *radiotherapy*. The first book on radiation therapy was published in 1901 by Schill[53]

Within a year of this proposal, the first radiation therapy was attempted by Victor Despeignes in 1896 on a patient diagnosed with stomach cancer. In combination with other treatments, radiation therapy was given to the patient. The tumour was observed to shrink, having an additional effect of reducing pain experienced by the patient, but was ultimately unsuccessful with the patient ultimately dying some time later. This is not a surprising result as over one hundred years later, the one-year survival probability between 2013-2017 for patients in the UK with stomach cancer is still only 50%.

The failure of the therapy did not deter others from attempting similar treatments. Independently, Léopold Freund treated his first patient in Vienna in late 1896 with a naevus pigmentosis piliferus. This patient was able to be followed up 70 years after this treatment, where she was observed to be in good health[54][53].

The maximum energy of X-rays that could be produced at the time, limited available treatments towards surface or shallow tumours (such as those on the skin) rather than those that are deep seated. Monitoring of these early radiotherapy was achieved by monitoring the electrical current and voltage inside the X-ray source, where a tolerance of 1% was used[55].

Technological advances in the generation of X-rays would enable higher energy photons to be created, which in turn increased the number of tumours that could be treated with radiotherapy. By 1930, radiotherapy was being used as the exclusive mode of therapy for lung cancer [56], and some cervical cancers[57].

In 1946, the idea of using protons (section 2.2.6) and heavier ions for radiotherapy was proposed by Robert R. Wilson[58], where the therapeutic possibility of the Bragg peak was suggested. It was not until 1958 when the first patients were treated at the Lawrence-Berkeley National Laboratory in the United State of America. This first trial focused on treating the pituitary gland of patients suffering from a variety of diseases and used a 340 MeV mono-energetic proton beam for this purpose. Despite not using the Bragg peak for this therapy clinical improvements were observed in many of the patients, encouraging further research in the field.

### 2.2.3 DNA damage mechanisms

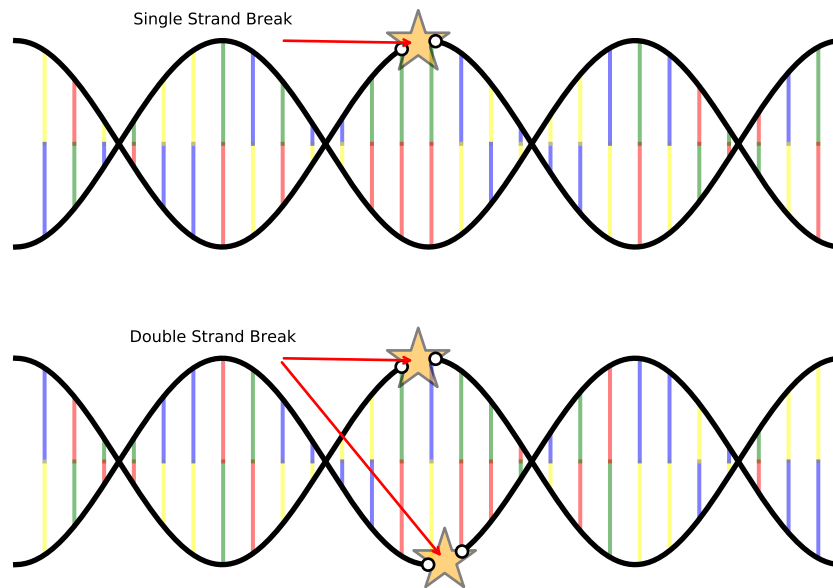


Figure 2.2: Annotated diagram of DNA damage via radiation.

There are two mechanisms of causing damage to DNA through radiation: direct and indirect. Direct damage occurs when the incident particle interacts with the DNA and disrupts the molecular structure[59]. Indirect damage occurs when the incident radiation ionises oxygen within the cell, creating free radicals as electrons are stripped away from their neutral atom or molecule. These ionised molecules proceed to interact within the cell, damaging DNA.

These two modalities occur in combination however the ratio between them is dependent on the modality of the radiation and the biology of the tumour. Indirect damage is dependent on the presence of oxygen molecules within the cell for the creation of the free radicals. As a result of this, tumours with poor oxygen penetration (defined as being "*hypoxic*") are often more radiation resistant than their healthy counterparts.

DNA damage to both healthy and cancerous cells can cause the cell to die through either radiation-induced apoptosis (where the cell undergoes a programmed cell death in response to radiation) or mitotic catastrophe (where the cell undergoes a premature death as a result of sufficient DNA damage)[60], [61].

It is possible to induce the creation of more DNA lesions via radiation damage if the cell is not killed[62]. Such lesions have the potential to develop into DNA mutations and become secondary cancers years to decades after the therapy for the primary cancer[63]. These late-stage complications are referred to as Radiation-Induced Malignancies (RIM)[64]. RIM are particularly a concern for paediatric patients, as their longer lifetimes post radiation therapy pose a greater risk of developing complications at some point[65]. To account for this, there is a great deal of research

performed globally to minimise this probability[66]. Advanced targeted therapies such as proton radiotherapy (Section 2.2.6) which reduce the total dose delivered to patient are highly desirable as they reduce the amount of tissue that can become cancerous.

### 2.2.4 Dosimetry

High quality metrology in cancer therapy is essential in ensuring the best quality of care for patients. It allows parameters involved in the treatment to become repeatable, and enable predictions on future patients using historical data of past patients. Whilst the ideal measurement would be a quantification of the amount of DNA damage, as an intracellular property this currently remains impossible to do quantitative analysis in all but in-vitro measurements. Instead the quantity of absorbed dose is used, as this is a physically quantifiable measurement that does not rely on biology. The field of dosimetry is the measurement of the quantity of absorbed dose, which has SI units of [J/kg]. The name of the unit named after "Gray" (symbol  $Gy$ ) after Louis Harold Gray for his work pioneering dosimetry[67].

The definition of the absorbed dose used in this thesis will be that as defined in the 2011 report by The International Commission on Radiation Units and Measurements (ICRU)[1]:

"The absorbed dose,  $D$ , is the quotient of  $d\bar{\epsilon}$  by  $dm$ , where  $d\bar{\epsilon}$  is the mean energy imparted by ionising radiation to matter of mass  $dm$ .

This can be expressed as Equation 2.1.

$$D = \frac{d\bar{\epsilon}}{dm} \tag{2.1}$$

The mean energy ( $d\bar{\epsilon}$ ) deposited within a certain volume in the material by ionising radiation can be expressed in terms of the kinetic energy of particles entering the volume ( $T_{in}$ ), the kinetic energy of those leaving the volume ( $T_{out}$ ), and the sum of all changes in the rest-mass of nuclei ( $Q$ ). This relationship is expressed in Equation 2.2[68], and is applicable for all types of radiation[69].

$$\epsilon = \sum T_{in} - \sum T_{out} + \sum Q \tag{2.2}$$

As stated, the concept of absorbed dose as a surrogate for DNA damage does not take into account the mechanisms for which radiation damage does occur. Using Equation 2.1 alone, the biological effects of different types of radiation might be overlooked. For an example, increasing the average temperature of a cell (of mass approximately 1 ng[70]) by 1°C with external heating is considered safe and would not result in cell death. Using the standard equation (Equation 2.3) connecting energy ( $E$ ), the mass of an object ( $m$ ), the specific heat capacity ( $c$ ), and an increase

in temperature ( $\Delta T$ ); it can be determined that approximately 4.2 nJ of energy is deposited. This corresponds to an excess of 4 kGy of radiation dose.

$$E = mc\Delta T \tag{2.3}$$

Studies have shown that the amount of damage to tissue (healthy or otherwise) can be influenced by dose rate[71], particle type[72], temporal fractionation[73], and cellular temperature among others[74]. Of particular interest for dosimetry is the concept of Linear Energy Transfer (LET), which is determined by the spatial and temporal structure of local energy deposition. The concept of absorbed dose is defined based on numerous individual interactions and statistical averages. Information about the behaviour of individual interactions is not accounted for[75]. "High LET" particles such as heavy ions, or protons at the end of of range, generate more double strand events than those with low LET value. Measurement of the dose deposited by individual particles on the sub-cellular microscopic level remains a difficult experimental challenge.

### 2.2.5 X-Ray Radiotherapy

#### 2.2.5.1 X-Ray interactions

Interactions between X-rays can take many different forms depending on the energy of the incident photon. In the range of X-ray energies used for therapy, the dominating interaction in matter is Compton Scattering. When undergoing this inelastic scattering, the incident photons interact with atoms to liberate a bound electron and emit a lower energy photon. A typical interaction of this type is shown in Figure 2.3, where a primary photon travelling from the left transfers enough energy to a bound electron to overcome its binding energy, imparting it with momentum and ionising the atom[76]. The range of the liberated electron is a few cm in water for typical energies in radiotherapy, due to numerous interactions with other still-bound electrons[77]. There is the potential for this electron to ionise further atoms, resulting in diminished kinetic energy.

There are many different pathways of energy transformation for a photon interaction with matter. The relevant end points for radiation cancer therapy are chemical changes (for DNA damage as discussed in Section 2.2.3), and heating of the medium (for calorimetry, discussed in Section 2.4).

Due to the probabilistic nature of X-ray interactions with matter, the change in intensity of an X-ray beam at a depth in material (whether that's water, silicon or tissue within a cancer patient) can be modelled as Equation 2.4 where the loss of intensity  $dI$  at a depth  $x$  is defined relative to the current intensity  $I$ ; the linear attenuation coefficient ( $\mu$ ); and mass density ( $\rho$ )[78]. Integrating this with respect to distance travelled through the medium results in Equation 2.5. With the

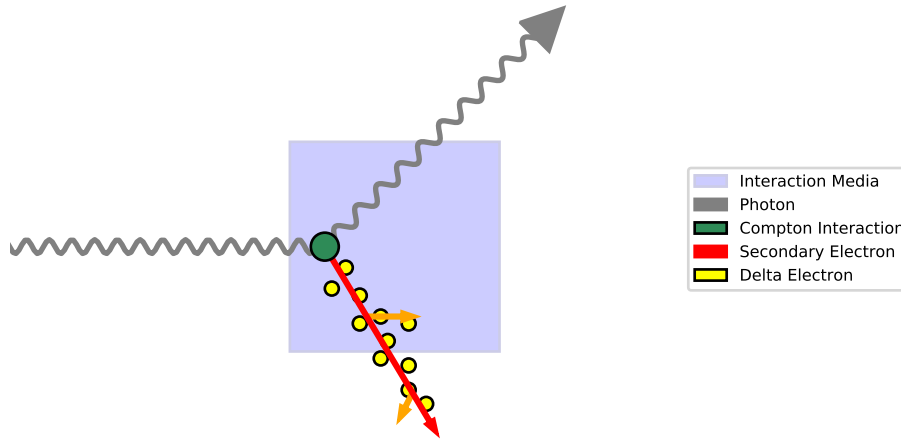


Figure 2.3: Simplified diagram demonstrating interaction mechanism of an uncharged particles.

assumption of a homogeneous material, this simplifies further to (Equation 2.6),

$$\frac{-dI}{I} = \frac{\mu(x)}{\rho(x)} dx \quad (2.4)$$

$$I = I_0 \exp \left[ - \int_0^x \frac{\mu(x')}{\rho(x')} dx' \right] \quad (2.5)$$

$$I = I_0 \exp \left[ - \left( \frac{\mu}{\rho} \right) x \right] \quad (2.6)$$

It is of note that the secondary electrons liberated by the incident photons do not necessarily deposit their kinetic energy at the spatial point at which they were generated, as was previously shown in Figure 2.3 with the secondary and delta electron leaving the interaction media volume. These electrons may travel several centimetres before all their energy has been transferred to the surrounding media. This results in a point of maximum dose ( $D_{max}$ ) that is not at the surface, which is followed by an exponential-like decay. A comparison of Percentage Depth Dose (PDD) measurements of various energy X-Ray beams obtained using an Elekta Linac at NPL can be shown in Figure 2.4. It can be noted in this, that the position of  $D_{max}$  increases as a function of the X-ray beam energy, due to the increase in kinetic energy transferred to the secondary electrons[79]. Due to the very sharp dose gradient before  $D_{max}$ , the International Code of Practice for Dosimetry IAEA TRS-398 does not recommend performing reference measurements prior to this point[80].

### 2.2.5.2 X-Ray generation

In 2016 NHS England treated 134,000 with radiotherapy from radiotherapy machines[81]. There are approximately 6.1 Linacs per million people in the UK, placing the country slightly below the

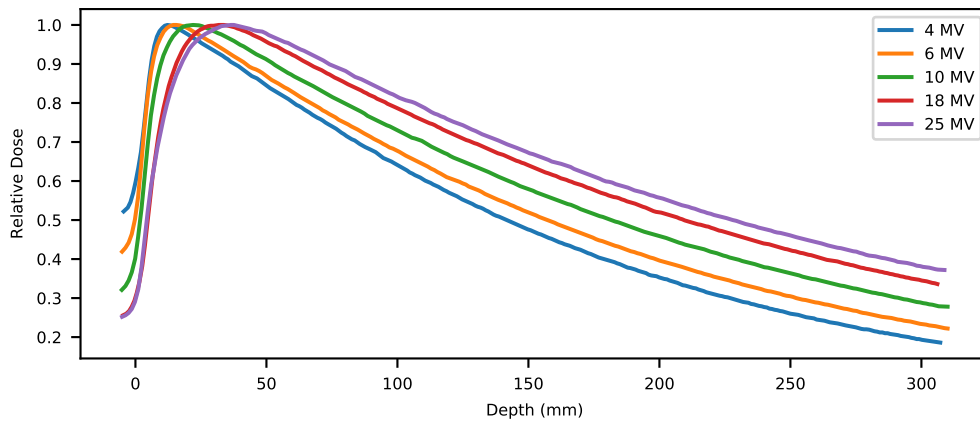


Figure 2.4: X-Ray PDDs obtained at NPL for various energies, data provided by Ileana Silvestre Patallo.

average for Europe[82]. At the time of writing there are over 12,000 Linacs available worldwide[83]. The distribution of these Linacs is not even throughout the world however. The World Health Organisation recommends 4-8 Linacs per 1 million people[84], a figure not achieved in many low and middle income countries[85].

In most clinical Linacs, the X-rays are generated by first liberating electrons in an "*electron gun*" from a heated filament cathode via *thermionic emission*. The electrons are then accelerated towards a perforated ground anode[86], before they are then accelerated to a desired energy using a radiofrequency waveguide[87]. Using electromagnets, the electron beam is then steered to  $270^\circ$  to now align with the "Beam Axis", with internal ionisation chambers used to monitor the beam asymmetry and provide feedback to the magnets to correct for errors in steering. If the desired treatment modality is X-rays, the electron beam will then collide with a Tungsten target.

Interaction within the Tungsten converts the electron beam to a photon beam, via "*Bremsstrahlung*" X-rays. This generated beam is typically divergent, requiring a collimator to be applied to filter out only specified angles to produce a collimated X-ray beam. The generated X-rays are still not uniform with the centre of the beam typically  $3\times$  the intensity of the periphery, and are passed through a conical shaped Tungsten "*flattening filter*" in order to create a flat uniform beam[87]. Removal of the "*flattening filter*" is possible to create higher dose rate Flattening Filter Free (FFF) beams, which are used in Chapters 4 and 5. A diagram of this process is shown in Figure 2.5.

This entire process of generating the final beam is quite inefficient, with losses converting from electrons to photons[88], and further losses with the flattening filter. In addition, as a result of this generation method of therapeutic X-ray radiation, the radiation beam has a broad energy spectrum which would change the linear attenuation coefficient ( $\mu$ ) in Equation 2.6.

When treating a patient with radiotherapy, it is essential to minimise the radiation dose that is delivered to healthy tissue. For a solid mass tumour at depth, treatment with photons results

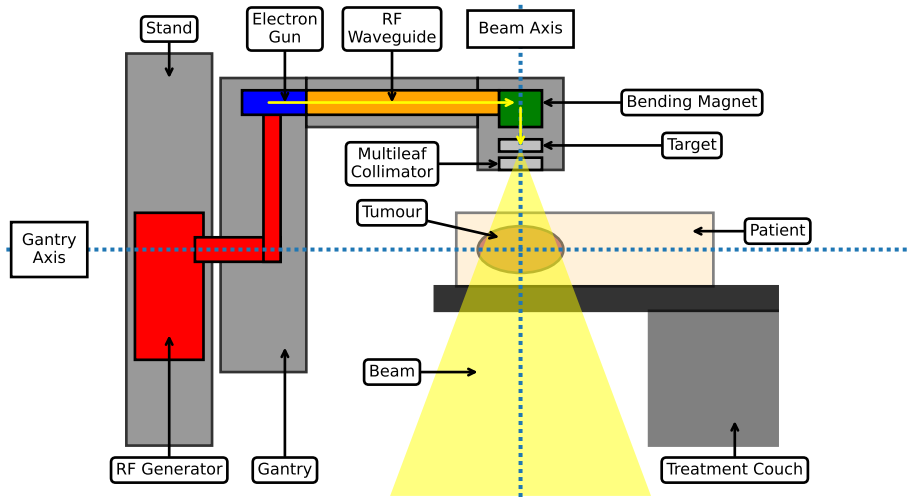


Figure 2.5: An annotated diagram of a Clinical Linac.

in an unavoidable entry and exit dose.

The generated beam of photons can be further shaped with the implementation of a Multileaf Collimator (MLC). These are tungsten leaves attached to electrical motors which are embedded within the treatment head of the Linac, capable of dynamically changing the radiation field for tumour conformation.

### 2.2.5.3 Dose Response Models

When delivering modern external beam radiotherapy non-palliatively, the objective is to deliver sufficient dose to a tumour to kill all cancerous cells. The probability of achieving this, is described by the Tumour Control Probability (TCP). The TCP is typically described by a Sigmoidal Dose Response (SDR), and can be seen in Equation 2.8. It is a function of the equivalent uniform dose to the organ or tumour ( $EUD$ ); which is described in Equation 2.7 in terms of the dose delivered ( $D_i$ ) to fractional organ volume ( $v_i$ ); and a tissue specific parameter ( $a$ ).

$$EUD = \left( \sum_i v_i D_i^a \right)^{1/a} \quad (2.7)$$

Equation 2.8 and Equation 2.9 describe the TCP and Normal Tissue Complication Probability (NTCP) using the equivalent uniform dose; a tumour control dose for 50% of the tumour ( $TCD_{50}$ ); a tolerance dose for a 50% complication probability ( $TD_{50}$ ); and a normalised dose response gradient ( $\gamma$ )[89][90].

$$TCP = \frac{1}{1 + \left( \frac{TCD_{50}}{EUD} \right)^{4\gamma}} \quad (2.8)$$

$$NTCP = \frac{1}{1 + \left(\frac{TD_{50}}{EUD}\right)^{4\gamma}} \quad (2.9)$$

The therapeutic window is described as the probability of successfully treating the tumour, without causing normal tissue complications. It is described in Equation 2.10.

$$TW = TCP \times [1 - NTCP] \quad (2.10)$$

An example of these three parameters can be shown in Figure 2.6, comparing the TCP of a prostate cancer and NTCP of the rectum when treating with X-rays in 2 Gy fractions[91]. The therapeutic window is used to determine the dose at which the probability of maximum tumour control without normal tissue complication can be achieved. The impact of accurate calorimetry (Section 2.4) can be seen here as any uncertainty in the dose delivered impacts the probability of the TCP, the NTCP, and the therapeutic window.

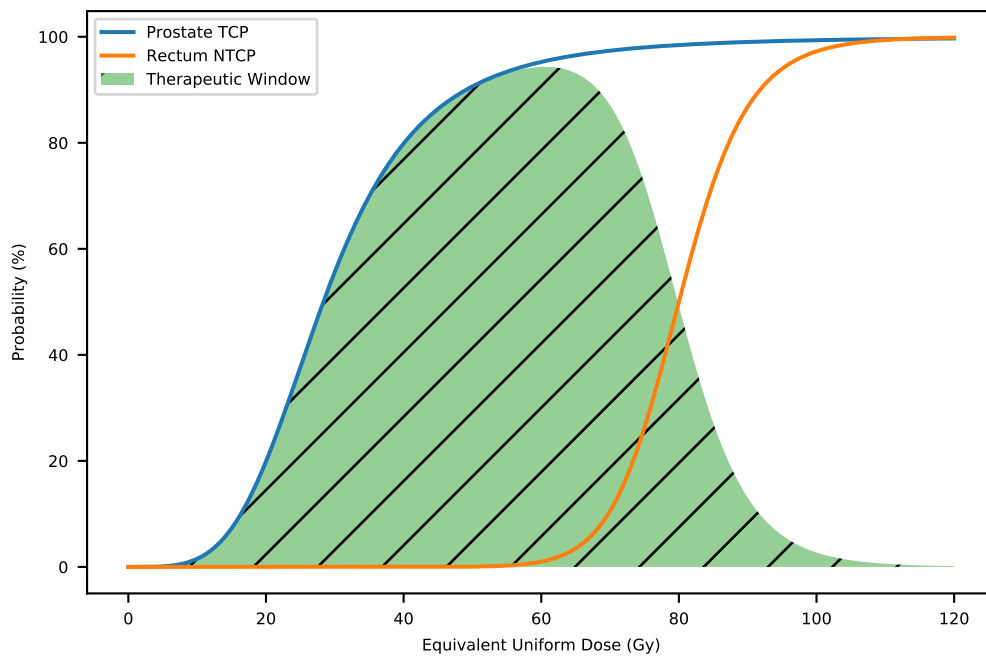


Figure 2.6: Example of prostate TCP and rectum NTCP when treating prostate cancer[91].

#### 2.2.5.4 Modern X-Ray Radiotherapy

Modern X-ray radiotherapy relies on X-ray computed tomography (xCT) imaging techniques. Diagnostic X-rays (of < 150 kV energy) are used to scan the patient and treatment volume. Doing so they are able to identify the location of the tumour and local organs, whilst determining the mass attenuation coefficient of the tumour and surrounding volume. This allows clinicians to predict the

dose deposition in a heterogeneous material of the X-rays using Equation 2.5. A technique known as "Inverse Planning" is used with this information to develop complex yet conformal treatment plans for Volumetric Modulated Arc Therapy (VMAT), Intensity-modulated radiation therapy (IMRT), and Stereotactic Radiosurgery (SRS)[92]. The term Gross Tumour Volume (GTV) refers to the volume defined as being part of the tumour. This volume is encompassed by a larger CTV, which is designed to cover microscopic tumour cells that cannot be imaged. Finally, the CTV is encompassed by an even larger Planning Target Volume (PTV), which accounts for uncertainties in the planning or delivery of the therapy[93].

Whilst in the past, radiotherapy treatments would involve static fields delivered to the patient, VMAT treatments involve the Linac rotating around the patient whilst delivering radiation. The key difference between VMAT and IMRT is that IMRT has the Linac deliver radiation at discrete steps (typically less than 10 fixed-field beam angles), whilst VMAT continually rotates[94]. In both cases, rotating the Linac in this manner allows the redistribution of the dose that is deposited before and after the tumour in three dimension[95]. The delivered dose creates a "*dose bath*", in which more healthy tissue is expected to receive a low amount of radiation (with low NTCP), but allows for dose escalation within the tumour volume (for high TCP). Despite the dose bath, it still is possible to minimise the dose delivered to organs that are particularly radiation-sensitive (such as the bowel or reproductive organs).

Another modern technique is SRS, in which multiple convergent beams of radiation are used to deliver dose to a discrete, radio-graphically-defined treatment volume[96]. SRS is most suitable for patients suffering from brain tumours with a GTV diameter that is less than 3 cm[97]. When applied to areas that are outside head, the more general term Stereotactic ablative radiotherapy (SABR) is used.

Unlike conventional radiotherapy (VMAT or otherwise), in SRS the entire radiation dose necessary to kill the tumour is delivered to the patient in a single fraction. As a consequence of this, it is especially important to fully understand where the dose will be delivered within the patient. Different manufacturers have approached the challenge of delivering SRS in different methods. Accuray[98] have developed the "CyberKnife" system in which a small linear accelerator is attached to a robotic arm[99]. Elekta[100] offer the "Gamma Knife" device, in which an array of  $\text{Co}_{60}$  delivered dose to a targeted inter-cranial area[101]. In addition, SRS "Cones" (Small, circular collimators) are offered by many vendors for conventional Linacs.

### 2.2.6 Proton Radiotherapy

Proton Beam Therapy (PBT) is a type of radiation therapy in which high-energy protons are used therapeutically. Unlike photons, protons are charged particles with mass that directly interact

with matter and constantly undergo interactions as they propagate. This interaction with matter is probabilistic and is described by the Bethe equation, which describes the average energy loss per unit distance ( $\langle \frac{dE}{dx} \rangle$ )[102]. This quantity is also referred to as "Stopping Power" of the material. The full Bethe formula is given in Equation 2.11 with parameters listed in Table 2.2.

$$\langle -\frac{dE}{dx} \rangle = \rho 4\pi N_A r_e^2 m_e c^2 \frac{Z}{A} \frac{z^2}{\beta^2} \left[ \frac{1}{2} \ln \frac{2m_e c^2 \beta^2 \gamma^2}{I} - \beta^2 - \frac{\delta}{2} - \frac{C}{Z} + zL_1 + z^2 L_2 \right] \quad (2.11)$$

Term	Meaning
$E$	Energy of proton beam
$x$	Distance
$\rho$	Mass density of absorbing material
$N_A$	Avagadro's number
$r_e$	Classical electron radius
$m_e$	Electron rest mass
$c$	Speed of light
$Z$	Atomic number of absorbing material
$A$	Atomic weight of the absorbing material
$z$	Charge of the particle ( $z = 1$ for protons)
$\beta$	Particle velocity relative to the speed of light, $\beta = \frac{v}{c}$
$\delta$	Density correction arising from remote electrons being shielded
$\gamma$	Lorentz factor, $\gamma = \sqrt{1 - \beta^2}$
$I$	Mean excitation potential of absorbing material
$C$	"Bichsel's Shell correction" term
$L_1$	"Barkas correction" term
$L_2$	"Bethe correction" term

Table 2.2: Parameters in Bethe formula for Equation 2.11.

For non-relativistic particles, the rate of energy loss in Equation 2.11 is approximately proportional to the inverse of the energy ( $E$ ) of the particle. This is described in Equation 2.12.

$$\langle -\frac{dE}{dx} \rangle \propto \frac{1}{E} \text{ or } \frac{1}{v^2} \quad (2.12)$$

The rate at which high energy protons lose energy is broadly consistent across different media, however upon reaching a critical minimum ionisation energy the rate of energy loss rapidly increases to become several orders of magnitude higher. The effect of this is that protons travelling through matter sharply lose their energy towards the end of a finite range, where there is a significant increase in the number of ionisations, named the Bragg peak after its discoverer William Henry Bragg[103]. An example of three Bragg peaks in water for various energies is shown in Figure 2.7.

The maximum range of protons is determined by the initial energy they possess. This distal range is defined as the position where 10% of the maximum dose is recorded ( $D_{10}$ )[104]. The relationship between energy and maximum range can be shown in Figure 2.8, where the maximum range in water increases with the energy of the proton. To facilitate the delivery of Bragg peaks within the human body (which is modelled as water), proton beams with energy 80-250 MeV are

used as these have appropriate range for sufficient penetration.

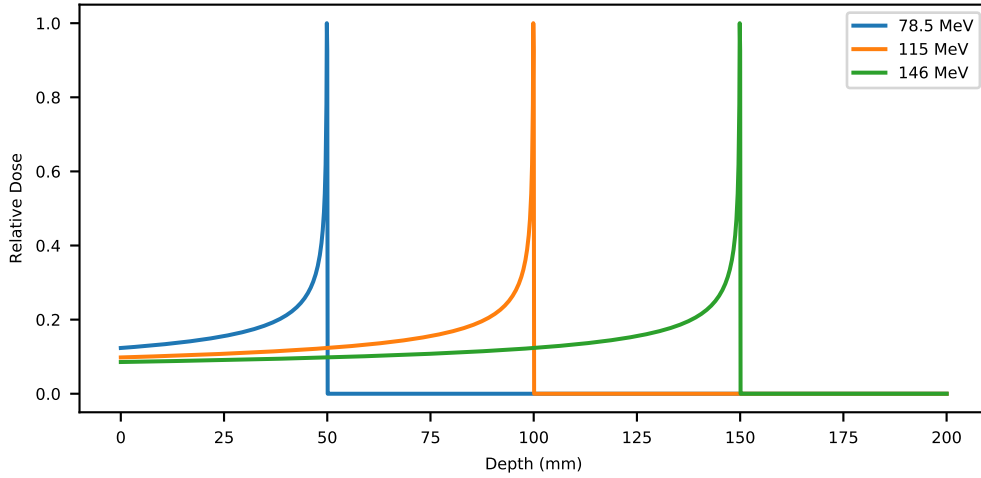


Figure 2.7: Simulated Bragg peaks for various energies, generated using Python[105].

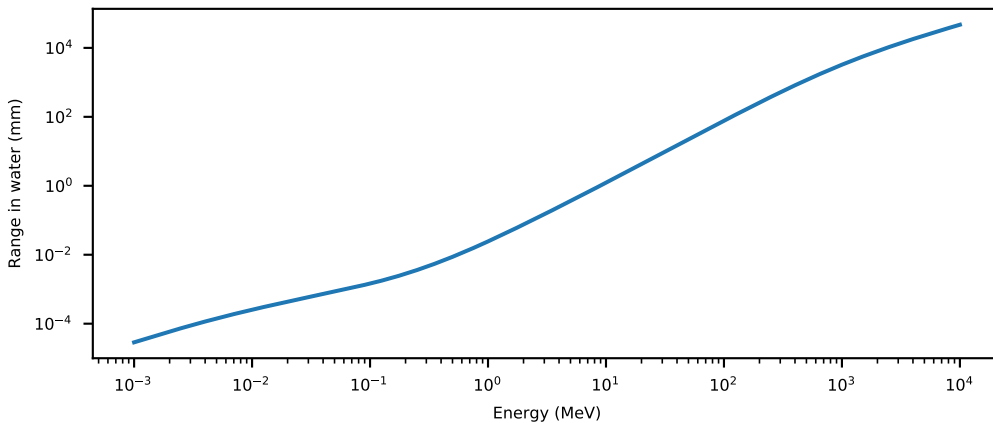


Figure 2.8: Approximate proton range in water for various energies, using data from NIST[106].

The microscopic energy deposition of proton radiotherapy is very different to X-ray radiotherapy discussed previously. An example of this is shown in Figure 2.9. As an incident proton propagates through a material, it will continually undergo interactions with the local media. Linear Energy Transfer (LET) describes the amount of energy that an incident particle will transfer to the local media per unit distance travelled. The proton interacts with the media via three main mechanisms[107]: Elastic Coulomb interaction with atomic electrons; Elastic Coulomb scattering with atomic nuclei; and non-elastic nuclear interaction with atomic nuclei. LET is very similar concept to "Stopping Power" discussed previously, however LET refers to the energy absorbed by the media whilst "Stopping Power" specifically refers to the energy lost by the incident particle. The two are only equal in the special case of Charged-Particle Equilibrium.

The Elastic Coulomb interactions with atomic electrons are primarily responsible for the damage to Deoxyribonucleic Acid (DNA) (Section 2.2.3) which potentially causes cellular damage, or

with silicon (Section 2.3) enabling detection by instrumentation. This interaction has the ability to ionise atoms along the path of the proton, liberating secondary electrons. If sufficient energy is transferred to the ionised electron, it has the potential to undergo further elastic Coulomb interactions and ionise additional "Delta Electrons" in clusters. The distinction between interactions between the primary and secondary particles is discussed in Section 2.2.3.

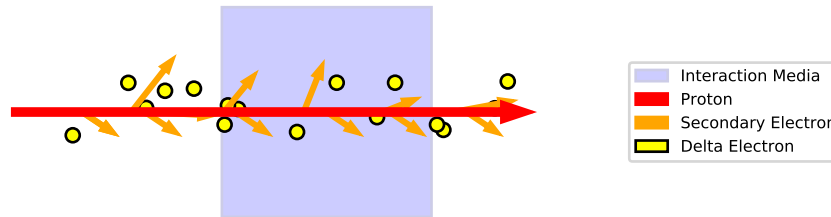


Figure 2.9: Simplified diagram demonstrating interaction mechanism of charged particles.

Due to the Bragg peak and lack of an exit dose, proton radiotherapy has been identified as a suitable treatment modality for many intra-cranial tumour types. Previous long-term studies following up paediatric patients suffering from brain tumours has indicated that in X-ray radiotherapy, the "dose bath" (the excess radiation dose to healthy tissue) causes a reduction of 1.1 Intelligence Quotient (IQ) points per year, relative to their peers. Comparable studies for proton radiotherapy indicate that this is absent, with no IQ loss[108].

Although beyond the scope of thesis, the Bethe equation is applicable to other types of heavy particle therapy (such as Helium, Carbon or Neon), or exotic hadron therapy (such as the historical pion therapy[109] or the proposed antiproton[110] and muon therapies[111]), which also possess Bragg peaks. The Bragg peaks of these heavy ion therapies are typically sharper relative to their "plateau" and are suitable for tumours with greater radiation resistance, due to their higher RBE[112], however due to nuclear fragmentation of the incident particle dose deposited after the Bragg peak becomes non-trivial[113]. Many of the dosimetry techniques discussed in this thesis would also be applicable to these treatment modalities.

The finite range of protons is utilised within the radiotherapy community to spare healthy tissue. By appropriately weighting Bragg peaks of varying energy, it is possible to deliver a uniform dose distribution to the tumour. The resulting dose profile is known as a Spread-Out Bragg Peak (SOBP), with an example shown in Figure 2.10.

### 2.2.6.1 Passive Scattered

The concept of passive scattering is that a small collimated proton beam is passed through a material with high atomic number to induce scattering with minimal energy loss. To ensure greater

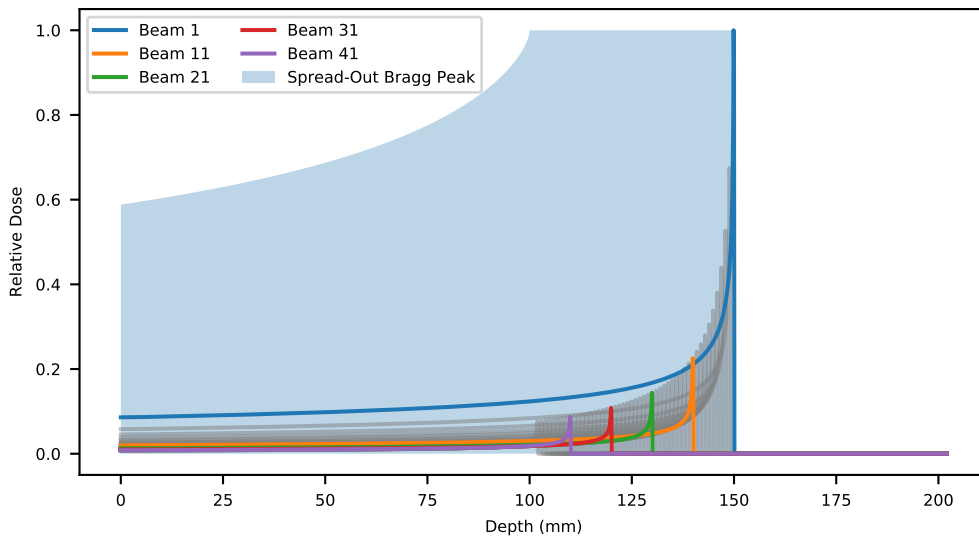


Figure 2.10: Annotated diagram of a Spread-Out Bragg Peak.

conformity of the resultant beam, it is common to have a second scattering layer spatially separated. To conform the lateral shape of the beam to that of the tumour, a patient specific collimator is manufactured (typically of brass) to stop unwanted protons. A SOBP is generated using a Range Modulation Wheel, which consists of a rotating disk of Perspex (with minimal scattering and higher energy loss) with various thicknesses. Conforming the distal edge of radiation field to the lateral shape in the tumour volume is achieved with the implementation of a brass compensator, which has to be manufactured per patient and if necessary per tumour[114]. Protons passing through the compensator undergo a reduction of energy, bringing the location of the Bragg peak closer to the surface. The entire method of double scattering, collimation and compensation is inefficient, with only approximately 5% of protons considered useful[115], and it also generates a non-trivial amount of secondary neutron radiation[116].

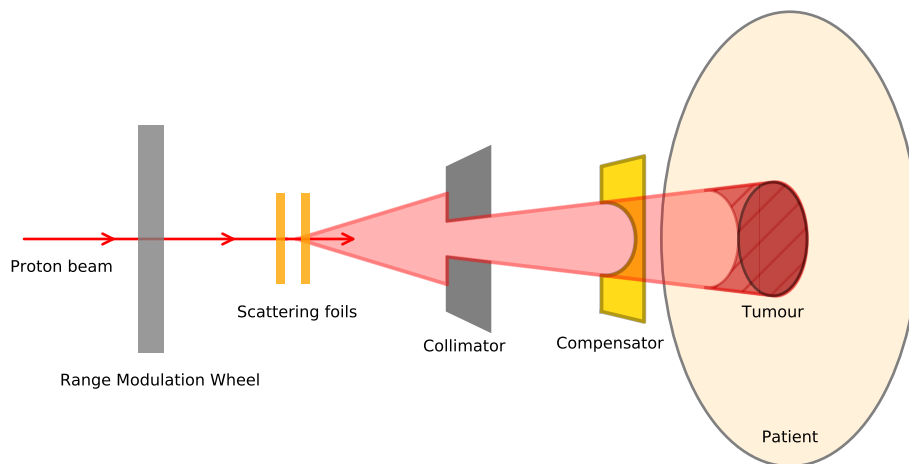


Figure 2.11: An annotated diagram of a passive scattered pencil beam.

As the compensator in passive scattering is matched to the distal edge of the tumour, the proximal side of the delivered radiation field is pulled forward accordingly. This can be shown in Figure 2.11 as the two horizontal "horns" within the patient, that are outside of the tumour volume. Unfortunately with passive scattering technology there is no method to remove this effect, although its magnitude can be minimised with the implementation of multiple beam angles. In addition, the collimators used to shape the radiation become radioactive after use, adding further complication to the process. The requirement for patient specific machined collimators reduces the adaptability for new radiation fields, whilst increasing costs associated with the treatment.

### 2.2.6.2 Scanned Pencil Beam

The first implementation of what is now known as Pencil-Beam Scanning (PBS) was in 1979 at the National Institute of Radiation Sciences in Japan by Kanai T *et al.*. This system consisted of using pairs of scanning magnets to change the trajectory of a 70 MeV proton beam, to deliver dose to a prescribed shape. By changing the current supplied to the bending magnets, they were able to move a single beam spot around to deliver a uniform dose (within  $\pm 2.5\%$ ) to an 18 cm square field.

The technique was incorporated in 1995 into a clinical facility at the Paul Scherrer Institute (PSI), Switzerland[117]. This system expanded on the previous one, increasing the energy range of protons that could be utilised to 85 - 270 MeV, enabling clinical applications. The technique known as PBS will be available at the majority of new proton facilities under construction at the time of writing[118]. By delivering thousands of individual Bragg peaks of differing energy, position and intensity, a prescribed 3D dose distribution could be created. Each of the incident proton beams typically have a FWHM of 7-12 mm[119], approximately the same dimensions of a pencil. A depiction of PBS system is shown in Figure 2.12.

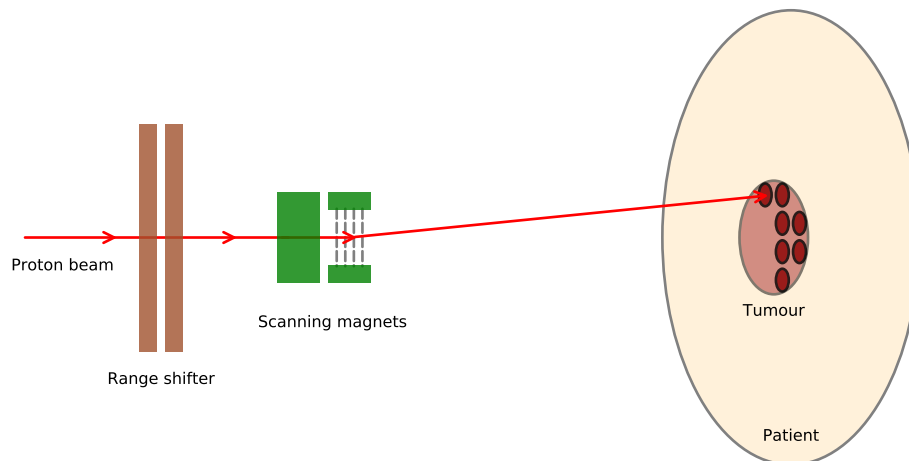


Figure 2.12: An annotated diagram of Pencil-Beam Scanning (PBS).

The lateral dose profile is not delivered instantaneously, but instead the 2D dose profile is "painted" layers at a time. When using a cyclotron based system, to change the energy of PBS and deliver Bragg peaks at different depths, a graphite wedge is electrically driven into the proton beam upstream before the bending dipoles. This differs to a synchrotron based system in which protons are accelerated only to their target, removing the requirement for energy degradation.

A key advantage that PBS has over other passively scattered PBT is sparing of even more healthy tissue. The proximal edge of the prescribed dose distribution does not have to match the distal, as was the case with passive scattering, sparing that tissue. In addition, the dose distribution within the target does not have to be uniform. By changing the weighting of different spots, it is possible to intentionally create regions of higher and lower dose, which may be of interest to clinicians wanting to obtain specific effects within the dose volume.

As no patient specific manufactured pieces are required for PBS, the clinical team is offered significantly more flexibility in the types of therapy that could be delivered. This has resulted in therapies with multiple treatment angles and variable intensities being used[120].

As of 2020, of the 227 clinical gantries delivering proton therapy globally almost 70% are capable of PBS with or without passive scattering[121].

There exist various techniques within PBS that are worth noting[122]:

- Spot Scanning: in which the dose is deposited with separate beams one spot at a time.
- Raster Scanning: in which the beam current is not stopped between adjacent spots in order to reduce the total beam time delivery. This introduces dose deposition in the transient regions, with the beam current stopping for spots separated about a specified distance threshold.
- Line Scanning: in which the dose is delivered along horizontal or vertical lines. Dose profiles are achieved by varying the scan speed of the beam spot and the beam current.

### 2.2.7 Quality Assurance in Proton Radiotherapy

It is essential to perform quality assurance of radiation therapy to a high level of accuracy, ensuring that the therapeutic dose delivered to patients during their treatment is to the highest possible standard. Although the focus of this thesis is proton therapy, there exists a significant overlap with quality assurance for conventional X-ray radiotherapy. The additional complexity of PBS requires the addition of extra beam monitoring devices to determine that the beam is being steered correctly.

When using PBS and assuming no setup error the possibility of misalignment still remains due to uncertainties in steering magnets and the beam delivery nozzle, an uncertainty estimated to be 1-2 mm[123]. Peterson, S. *et al.* (2009) determined that deliberate lateral displacements of only 0.5 mm produced a hot spot within the target region of 5%[124]. A spot position tolerance

of only  $\pm 1$  mm originating from momentum deviation would cause a range disparity of between 0.4 - 1.9%[125]. Additionally information regarding spot size as well as position could be used to further reduce margins around tumour sizes, sparing even more healthy tissue than current proton therapy procedures[126].

Ionisation chambers currently used routinely for daily quality assurance to measure beam profile and position have strip intervals of 2.22 mm[127]. Whilst this is smaller than the 4 mm strip pitch used in the initial implementation at PSI[117], it does not possess the necessary resolution to determine fluctuations at the smallest level. Radiochromic film can reduce this to 0.1 mm[128] if not lower[129], but the recommended development time of film of 24 – 48 hours would render any daily measurements out of date by the time they have developed.

## 2.3 Silicon Detectors

In the last century, Silicon has proven itself to be an extremely valuable material for industrial, scientific, and consumer applications alike. Since the first transistor was developed in 1947 by John Bardeen, Walter Brattain and William Shockley at the then Bell Telephone Laboratories, over  $13 \times 10^{21}$  Metal–Oxide–Semiconductor (MOS) transistors have been built globally[130].

### 2.3.1 Silicon

Silicon is an element in the periodic table with atomic number 14, and a standard atomic weight of 28.084 g/mol. Its position in the period table, with a total of 14 electrons, results in silicon being able to form 4 covalent bonds per atom in order to fill the outer  $3p$  electron shell. This enables silicon to form "face-centred diamond-cubic" lattices where each silicon atom is bonded to four other silicon atoms as shown in Figure 2.13, in a similar structure to diamond.

The use of electrons as charge carriers in solids relies on unoccupied electronic states. For conductive metals such as copper or gold, there is no energy gap between the "conductance" and "valence" energy bands enabling electrical current to flow. This is not the case for "insulators" such as glass or diamond, where the large energy gap prevents electrons between bands, thus preventing electrical current. "Semi-conductors" such as silicon or germanium exist partway between these two extremes where there is a small energy difference, hindering most free electron movement whilst still allowing a small amount. In silicon, this band gap between the valence and conductance bands is approximately 1.12 eV at room temperature[131]. Semiconductors in this category are referred to as being "Intrinsic".

Due to random fluctuations in thermal energy, a fraction of the bound electrons will often have sufficient energy to thermally ionise, and transition between the two energy bands. When

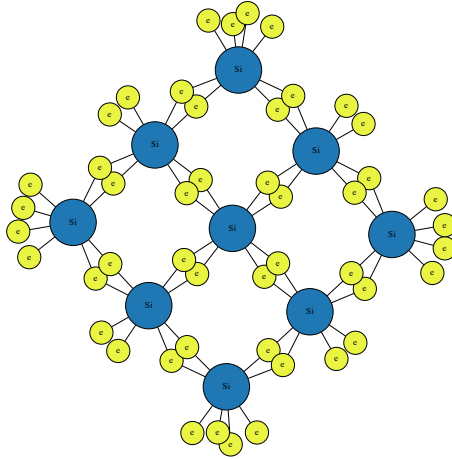


Figure 2.13: Intrinsic Silicon with no impurities.

doing so they leave behind a positive "electron hole", which can act as a positive charge carrier by taking bound electrons from neighbouring atoms, moving the "electron hole". The intrinsic number of unbound electrons in the conductance band that can act as charge carriers is governed by Equation 2.13; where the negative charge density per cubic metre ( $n_0$ ) depends on the effective mass ( $m^*$ ), temperature ( $T$ ), the energy of the conductance band ( $E_C$ ), the Fermi energy ( $E_f$ ), the Boltzmann constant ( $k_B$ ), and the reduced Planck's constant ( $\hbar$ )[131].

$$n_0 = 2 \left( \frac{m^* k_B T}{2\pi \hbar^2} \right)^{3/2} e^{-\frac{(E_C - E_f)}{k_B T}} \quad (2.13)$$

For room temperature silicon, this equates to  $9.65 \times 10^9$  electrons per  $\text{cm}^3$ . Electrical charge is conserved in this process, and an equal number of electron holes would be created.

### 2.3.1.1 Doping, $p/n$ type silicon

"Doping" is achieved by replacing atoms of silicon within the lattice with atoms of another element. The added elements are referred to as dopants, and are categorised as either electron donors or acceptors depending on their position in the periodic table and the number of electrons they have in their outermost shell. Doped semiconductors are referred to as "Extrinsic".

When an electron donor such as phosphorus (with 5 electrons in its outer  $3p$  electron shell) is inserted into the lattice, the additional valence electron is not tightly bound to the original element creating an opportunity for an excess negative charge carrier. The additional unbound electron is shown in Figure 2.14.

For comparison, when the electron acceptor boron (with only 3 electrons in its outer  $3p$  electron

shell) is inserted into the lattice, the loss of an electron (relative to silicon) can induce an "electron hole" positive charge carrier. The position of the boron within the lattice cannot change, however the position of the positive charge (caused by the absence of the full electron shell of the acceptor) is able to move as electrons from full shell silicon atoms donate their electrons.

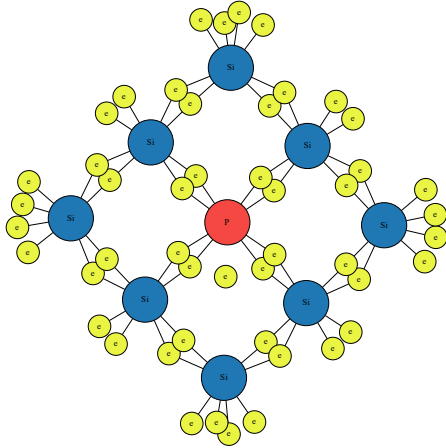


Figure 2.14: *n*-type Silicon with phosphorus "donor".

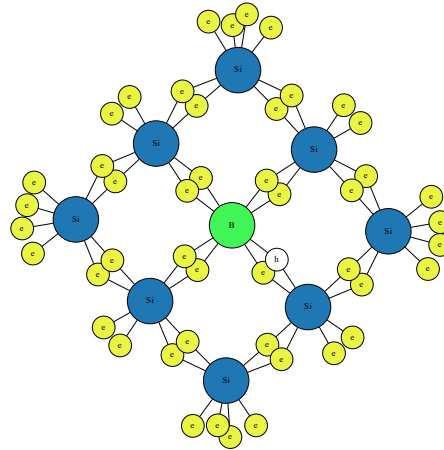


Figure 2.15: *p*-type Silicon with boron "acceptor".

### 2.3.2 Depletion

Depletion occurs when there is a lack of charge carriers locally available. A *pn* junction is formed when doped *n*-type and *p*-type silicon are physically connected, and is the basic component of a diode. In this case, the excess electrons from the *n*-type will combine with the electron holes of the *p*-type to remove both types of charge carrier creating a zone of depletion. The width of this region of depletion is dependent upon the carrier concentration (and thus degree of doping) in both regions.

Applying a potential difference across a *pn* junction can cause a number of effects, highlighted in Figure 2.17. A positive applied voltage across the junction beyond what is called "knee voltage" results in the potential difference barrier between the doped regions reducing, and large amounts of current flowing across the junction as the electrons and "electron holes" are attracted to the anode and cathode respectively. For silicon diodes, the "knee voltage" is typically of the order 0.7 V.

Applying a negative potential difference across the junction causes the zone of depletion to physically extend, as the mobile charge carriers are pulled away in opposite directions. The depletion region can keep growing, until the entire junction becomes fully depleted and there are

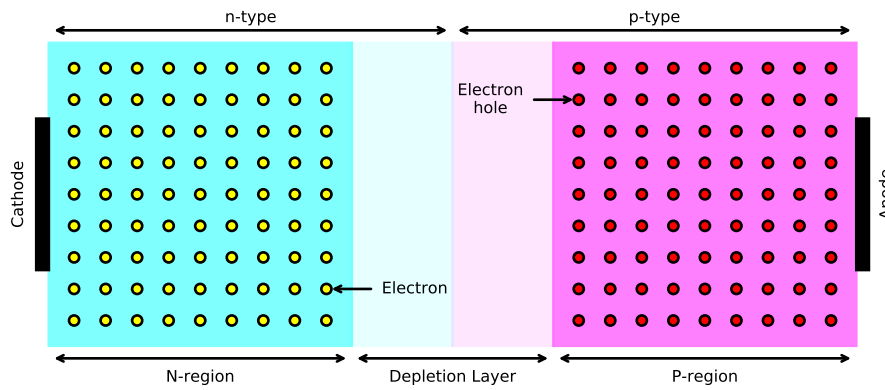


Figure 2.16: Diagram of depletion in a  $pn$  junction.

no majority charge carriers available left. Increasing the magnitude of the negative potential difference even further causes the silicon to undergo "breakdown", as the electrostatic force pulling the electrons to the terminals is greater than that binding them to their original atoms. This can result in a significant current flow, as newly liberated electrons may collide with electrons that are still bound liberating them as well, resulting in an avalanche cascades of electrons[132]. Electrical breakdown occurs when the average electron energy gain from the applied electrical field exceeds the average energy loss of the electron to phonons[133]. For silicon, this occurs with field strengths in excess of  $1 \times 10^7$  V/m.

The common use of  $pn$  junctions as diodes relies on these properties, as while operating in reverse bias almost no current passes for low potential differences.

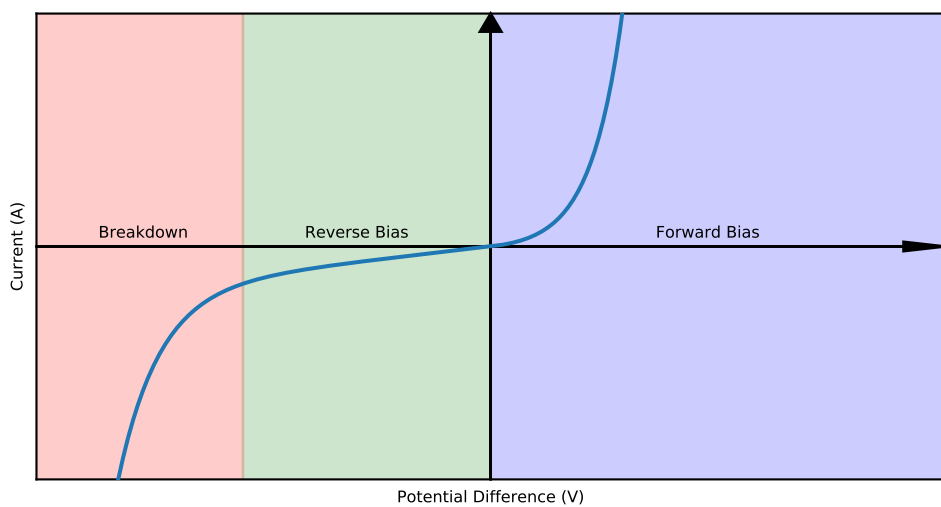


Figure 2.17: Annotated diagram showing voltage current response of a  $pn$  junction, not to scale.

### 2.3.3 Interaction with Radiation

When incoming radiation interacts with the depleted region of silicon, energy is locally deposited. This applies regardless of the modality of radiation. If sufficient energy is supplied, electrons formerly bound to the silicon are liberated creating electron - electron hole pairs of charge carriers. The average energy for electron-hole creation in silicon at room temperature is 3.62 eV[134]. This is greater than the band gap with the excess energy being transferred into lattice vibrations. The number of charge carrier pairs ( $N$ ) created is approximately determined by Equation 2.14 , where  $E_{rad}$  is the energy deposited by the radiation and  $\epsilon$  is energy required to create an electron - electron hole pair. These induced charge carriers are referred to as *minority charge carriers*, and are electrons in the  $p$ -type silicon and electron holes in the  $n$ -type silicon.

$$N = \frac{E_{rad}}{\epsilon} \quad (2.14)$$

As previously discussed in section 2.2.5 and section 2.2.6, the different radiation modalities deposit their energy locally via different methods. Crucially, both modalities produce electron and hole pairs.

A charged particle interacting may produce in excess of  $10^6$  charged carrier pairs, however at room temperature silicon has an intrinsic carrier density of  $9.65 \times 10^9$  pairs per  $\text{cm}^3$ , orders of magnitude greater than that induced by the radiation.

By depleting the silicon with a negative potential difference the intrinsic charge carriers become suppressed, enabling the silicon to operate as a highly sensitive radiation detector. The number of electron hole pairs ( $N_{pairs}$ ) generated for a prescribed dose ( $D$ ) in silicon can be determined using the pair generation constant ( $g$ ) of  $4.2 \times 10^{13} \text{ cGy}^{-1} \text{ cm}^{-3}$  in Equation 2.15[135],

$$N_{pairs} = g \times D \quad (2.15)$$

Figure 2.18 demonstrates the electron - holes pairs being generated in a thin layer of silicon substrate along the path of a charged particle. Modern designs for silicon detectors typically consist of a lightly doped  $n$ -type silicon substrate sandwiched between a heavily doped  $n$ -type and  $p$ -type region, connected to a cathode and anode respectively. This design expands on that shown in Figure 2.17, to include multiple anodes, separated by the insulator silicon dioxide. Silicon manufactured in this manner is capable of being used in position sensitive devices, such as SSDs (section 2.3.4) or CMOS devices (section 2.3.5).

There exists two mechanisms for charge collection of the induced minority charge carriers: drift and diffusion. Diffusion current can occur without an external bias applied to the semiconductor, and is the movement of charge carriers away from high concentrations of charge to low concentra-

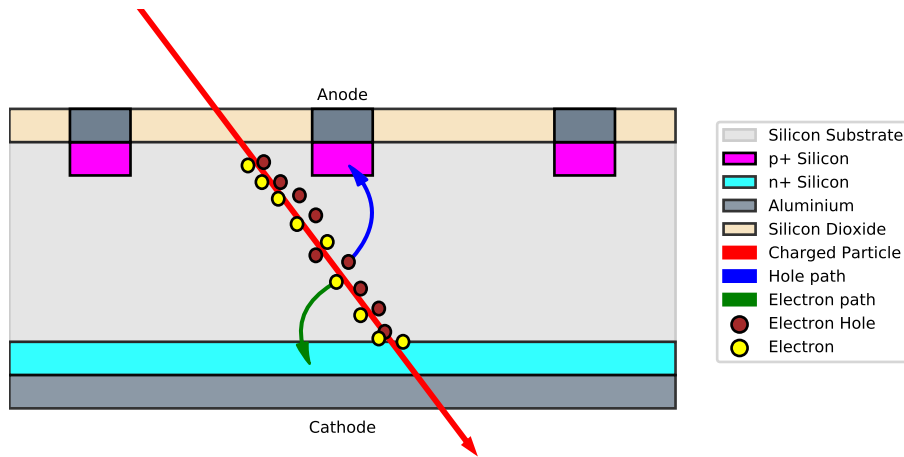


Figure 2.18: Diagram showing hole-electron pairs created in silicon from a charged particle.

tions via a "random walk" of the charge carriers. It is possible that not all excess minority carriers generated by the radiation are able to be recorded as signal, as charge carriers will undergo recombination. Typically, the excess charge carriers must be generated within a "diffusion length" ( $L_n$ ) before collection. This parameter is determined by Equation 2.16, with the diffusion coefficient of minority carriers ( $D_n$ ); and the mean lifetime of minority carriers ( $\tau_n$ )[136].

$$L_n = \sqrt{D_n \tau_n} \quad (2.16)$$

For detectors, this could result in non-spatially-uniform responses to radiation where an identical radiation dose deposited at two different points could be measured as different signal intensities. It is therefore of importance to designers of silicon detectors to minimise the effect of this.

The drift current can only occur when a potential difference is applied to the semiconductor, generating an electric field which in turn induces movement of the charge carriers (and thus an electric current). This happens in conjunction with the diffusion current, At the microscopic scale, the motion is highly non-directional with the mobile charge carriers frequently colliding with the lattice, dopants or other carriers. Due to the attraction of the electric field however, there is a net movement of charge carriers towards the anode and cathode.

### 2.3.4 Silicon Strip Detectors

Within HEP, devices used to measure the positions of the particle fragments are known as "trackers" and have the requirements of having good spatial and temporal resolution, in order to reconstruct the trajectory and momentum of the particle with minimum uncertainty. Devices that come under the category SSD consist of large portions of lightly doped  $n$ -type silicon which are preferentially extended into one axis. An important feature of a SSD is that each elongated piece

of silicon is one of many identical channels, electrically separated by a thin region of high resistance insulator. Strip pitch, defined as the distance between the centre of two adjacent channels, is typically of the order  $100\ \mu\text{m}$ . As a result of this design, SSDs are only able to sample or measure incident radiation in a single axis. In order to record the position of a particle, combinations of SSDs are required at different angles to overcome this limitation. SSDs with only one strip channel are uncommon[137], but are typically reserved for specialist applications.

SSDs come under the category of "Hybrid" detectors, as they consist of two separate components that are mechanically and electrically bonded together. The silicon channels are made of *n*-type silicon, which is depleted by applying a negative potential difference to ensure depletion. Electrical bonding to separate readout boards is achieved using a low resistance material such as gold, copper, or aluminium. Conversion of the electrical signal to digital values is performed on this separate readout board. Separation of the two devices in this manner has the advantage of sparing the sensitive electronics from many of the hazards of radiation, with appropriate shielding it is possible to only expose the silicon strips to radiation, prolonging the lifetime of the device. In addition separation of the two devices allows for one component to be replaced should it become damaged, without needing to replace both components. This is highlighted in Figure 2.19, where the silicon strip is irreparably damaged, however the readout electronics remained undamaged, allowing the system to be repaired with a replacement piece of silicon.

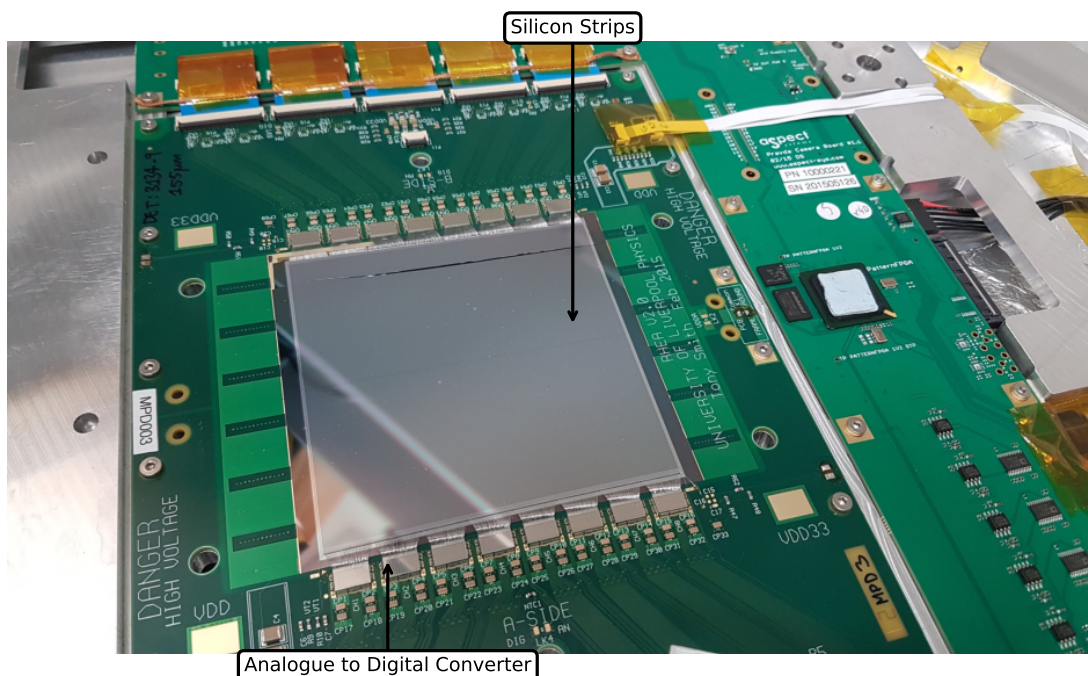


Figure 2.19: Photograph showing the separation of the silicon strips and readout board in a SSD that is part of a PRAVDA tracker unit.

Conversion of the acquired electrical charge on each strip to a digital signal is achieved using a

Analog-to-Digital Converters. The ADC converts the signal into a digital fractional number ( $D$ ), using a number of bits ( $N$ ), as with the most common method shown in Equation 2.17 [138]. When used without the fractional component, this is often referred to as Digital Units (DU).

$$D = \sum_{i=1}^N b_i 2^{-i} \quad (2.17)$$

A key advantage of SSDs over pixel technologies, is the increased readout rate. If all the SSD channels were to be read out at the same time, the amount of time required to do this would be of the order  $O(N)$ , where  $N$  is the number of channels in the detector and limited by the rate of the ADC. To read out all pixels of a pixelated sensor with one ADC, the time required would be of the order  $O(N^2)$ , potentially thousands of times longer than SSDs. Designers of both types of silicon devices are often able to increase the refresh rate, with the introduction of triggering systems. To reconstruct the position a particle, often only knowledge of which strip channels or individual pixels measured signal is required. By only reading strips or pixels that are known to have information it is possible to obtain triggering rates that are magnitudes higher than that of full frame rates, for SSDs this limit becomes the internal clock speed; whilst for pixelated detectors (depending on the architecture) this can be reduced to  $O(N)$ , where  $N$  is the number of pixels in a column.

### 2.3.5 Complementary Metal-Oxide-Semiconductor Devices

The invention of the Complementary Metal–Oxide–Semiconductor (CMOS) component was published in 1963[139]. This device combined both  $n$  and  $p$  type transistors and was able to collect and store charge in a method that was of tremendous interest to computing[140].

The technology was developed into an imaging device by Chamberlain in 1969[141] with the incorporation of a photodiode to acquire charge. In this configuration, a  $10 \times 10$  array of pixels using CMOS technology could independently collect charge and be addressed for conversion into a digital signal. The major imaging technology at the time, Charge-coupled device (CCD), required that the charge needed to be transferred between neighbouring pixels before it could be converted into a digital signal. This resulted in a low readout speed and frame rate that did not scale well for sensors with large amounts of pixels. In addition, the transfer of electrical charge offered opportunities for acquired charge to be lost as a result of inefficiencies in the charge transfer, resulting in additional corrections needed in the acquired digital signal. As pixels in CMOS sensors can be individually addressed, the loss of signal via charge transfer inefficiency is not an issue for the technology.

The first application of a commercial CMOS sensor for radiation detection can be traced back to Servoli *et. al* [142]. When detecting radiation, there is option of using an additional scintillator

material to increase the amount of signal that is collected by the CMOS sensor. In this case, the incident radiation will interact with the scintillator to produce additional photons, which increases the signal acquired in photodiode. This is of interest when using the sensor for diagnostic or industrial imaging, as it increases the efficiency of the detector and reduces the amount of radiation that the patient or sample needs to be exposed to. This has the disadvantage of reducing the spatial resolution, and increasing the material thickness. Using a CMOS sensor without a scintillator is possible, with the direct interaction mechanism for silicon shown in Figure 2.18.

Readout of the CMOS sensor is performed by individually addressing each pixel, transferring the collected charge to column storage capacitors. From here, the charge is converted into a digital signal with a ADC using the same method as an SSD discussed previously.

Most CMOS sensors are designed with the "3T" pixel design in which rows have to be read sequentially, with a small delay between consecutive rows. For a typical consumer CMOS sensor with millions of pixels (and thus thousands of rows), this results in a non-trivial delay of the order 10 ms between the first and last row. CMOS pixels are fundamentally more radiation sensitive than SSDs, as the electronics for CMOS pixels is directly embedded within each pixel.

### 2.3.6 Radiation Damage in Silicon

The effects of radiation interacting with silicon (doped or otherwise) are not limited to creating electron-electron hole pairs of charge carriers. Incident radiation has the ability to cause damage to silicon detectors, and is broadly categorised into two components: "Surface Damage" and "Bulk Damage". This is of relevance to this project as any device made of silicon that is used to monitor radiation for radiotherapy would be exposed to harmful conditions where damage is likely. This damage will manifest as a reduction in performance of the detector, as well as a change in characteristics.

"Surface Damage" occurs when the thin layer of oxide ( $\text{SiO}_2$ ) interacts with radiation and causes electron holes to become permanently trapped at the  $\text{SiO}_2$ -Si boundary.[143] For SSDs, this manifests as changing the interstrip resistance and capacitance[144].

"*Bulk Damage*" occurs when incident radiation dislodges an atom of silicon from within the lattice structure. Whilst some displaced atoms (referred to as interstitials) will combine with the induced lattice vacancy[131], others can form stable defects by interacting either with other interstitials, or naturally occurring defects in the silicon. These defects can effect the response of the semiconductor by increasing the reverse-bias current; changing the motion of the charge carriers inducing the signal; or requiring that a greater reverse-bias be applied to the semiconductor before depletion. In addition, the presence of defects causes a reduction in signal acquired. The scale of the damage strongly depends on both the amount of the energy and the mass of the incident

particle, in a manner similar to LET.

Figure 2.20 shows the effect of multiple X-ray studies on the vM1212 large-format CMOS detector. As shown the position of the radiation damage is very localised to where the radiation was deposited, revealing the damage from X-ray microbeam studies discussed in Chapter 4. The increase in the "dark current" of the detector has the effect of reducing the overall dynamic range of the detector, limiting its total lifespan.

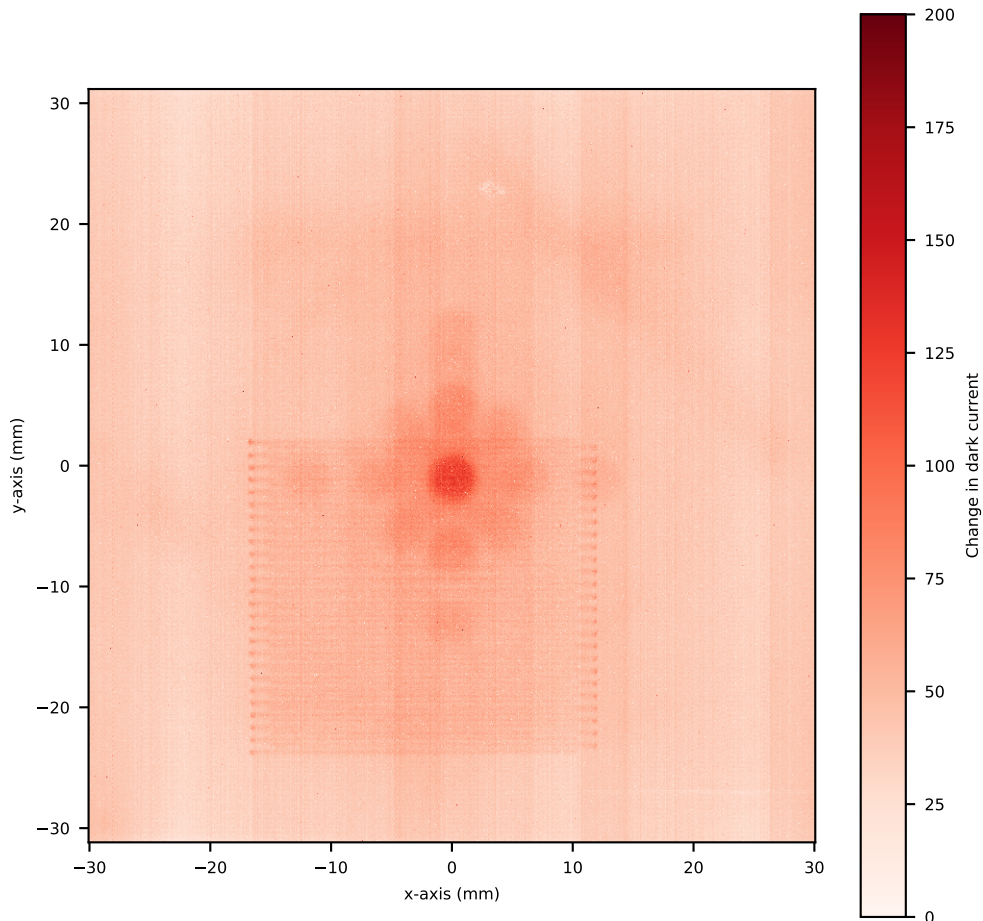


Figure 2.20: Evidence of radiation damage from several investigations with the vM1212 detector manifesting as change in dark current.

## 2.4 Calorimetry

The motivation of calorimetry is to accurately measure the thermal energy deposited within a region or object, in order to perform dosimetry and determine the radiation dose that has been delivered by a reference field. By quantifying and calibrating a radiation source, a known radiation dose can thus be delivered to a patient.

Within the framework of metrology, radiation calorimetry is typically at the primary standard level held at NMIs, with other devices (such as ionisation chamber) calibrated relative. The 1990,

the Institute of Physical Sciences in Medicine issued a Code of Practice[145] defining calibrations for photon radiotherapy in the UK (later updated by Institute of Physics and Engineering in Medicine (IPEM) in 2020[146]) to ensure traceability in radiation dose delivered to patients. Under this framework, individual hospitals or National Health Service (NHS) trusts own both secondary standard ionisation chambers and tertiary standard ionisation chambers. Working through the calibration chain, secondary standard ionisation chambers are directly calibrated against the NPL photon calorimeter using the Linacs at the NPL. Using the Linacs at the hospitals, these secondary standards are used to calibrate tertiary standard ionisation chambers which can be used daily for quality assurance and verification of delivered therapies. The uncertainty (95% confidence level) on the absorbed dose in water of the secondary standard in reference conditions is typically of the order 1.5%[80]. A simplified depiction of the calibration chain for photon radiotherapy is shown in Figure 2.21. The impact of uncertainty in the calibration chain is discussed by Bolt *et al.*[147], where an overall uncertainty in delivered dose of 2.1% can be divided into a 0.7% uncertainty due to initial calibration; 0.8% due to a calibration drift; 0.1% due to a drift during treatment; and 0.2% from daily variations (all uncertainties quoted at a 95% confidence interval).

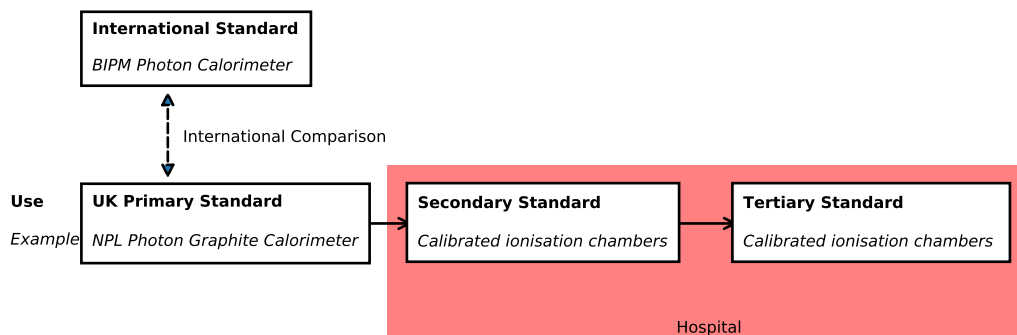


Figure 2.21: Photon calibration chain in the UK.

As many NMIs do not have their own proton beams necessary for calibration of secondary standards against primary standard calorimeters, the same procedure cannot be replicated for proton radiotherapy. In 2000, International Atomic Energy Agency (IAEA) published TRS-398[80], a code of practice for dosimetry in external beam radiotherapy. In addition to dosimetry for electron and X-ray modalities, this document prescribed calibrating ionisation chambers for proton beams in  $\text{Co}_{60}$  beams, and performing corrections based on the beam quality of the proton beam. As this process requires the additional step in the user's proton beam before a calibration of the chamber can be performed - the uncertainty on the absorbed dose to water measurement of a secondary standard to be 2-2.3% (95% confidence level), depending on the type of chamber. As a result of the calibration chain, the uncertainty on dose delivered to patients (including other sources of uncertainty such as patient positioning) is on average 5% (95% confidence level)[148].

Using TCP models of tumour response, delivering less dose to a tumour by as little as 5% can reduce the Tumour Control Probability by a clinically significant 7.5%. Likewise, the NTCP response suggests that a dose uncertainty of less than 3-5% (depending on the tumour) is required in order to reduce the probability of radiation induced toxicity[90]. However due to fractionation, in which the total dose to the tumour is delivered in smaller doses separated in time, the impact of dose uncertainty is reduced. A standard deviation of 10% of the dose delivered per fraction leads to radiobiological effects of less than 1%[149]. This however only applies to random causes of uncertainty, as systematic uncertainty in dose calculation would not be reduced with fractionation.

### 2.4.1 Calorimetry Theory

The purpose of calorimetry is to measure the dose deposited by radiation by detecting a change in temperature as a result of dose deposited. In order to accurately determine the amount of thermal energy absorbed by the material, the properties and interactions of the material need to be fully understood.

The "Heat Capacity" of a material ( $C$ ) is described using Equation 2.18, and is defined by the amount of thermal energy ( $\Delta Q$ ) necessary to cause a material (of mass  $M$ ) to cause an increase in temperature ( $\Delta T$ ).

$$C(T) = \lim_{\Delta T \rightarrow 0} \frac{\Delta Q}{\Delta T} \quad (2.18)$$

The "Specific Heat Capacity" (or "Reduced Heat Capacity") of a material ( $c$ ) is defined by Equation 2.19 as the "Heat Capacity" ( $C$ ) per unit mass ( $M$ ).

$$c(T) = \frac{C(T)}{M} = \lim_{\Delta T \rightarrow 0} \frac{1}{M} \frac{\Delta Q}{\Delta T} \quad (2.19)$$

Equating Equations 2.1 and 2.20 results in Equation 2.21, which provides a relationship between the absorbed radiation dose of a material and the predicted temperature increase.

$$D = \int_T^{T+\Delta T} c(T') dT' \quad (2.20)$$

For a typical radiation dose of 2 Gy, the temperature increase of water is less than 0.5 mK. Due to the very small increase in temperature, the specific heat capacity of water ( $c$ ) would change before and after irradiation by less than 0.00001%[150]. The effect of this change can be largely ignored within an irradiation, resulting in Equation 2.21.

$$D = c(T)\Delta T \quad (2.21)$$

### 2.4.2 Water Calorimetry

The concept of water calorimetry is perhaps the simpler of the two calorimeter types that will be discussed within this body of work. The core premise of this device is that a volume of deionised water is cooled to 6°C, with radiation induced temperature changes recorded by embedded thermistors. Performing measurements at this temperature reduces the number of corrections that would otherwise have to be applied, reducing the number of sources of uncertainty. These devices are often referred to as "Sealed Water Calorimeters", as they are sealed from the air to maintain the temperature and purity of the water.

The most recent water calorimeter was developed in 2013 by the Van Swinden Laboratory (VSL), the Netherlands, for X-ray radiotherapy dosimetry in the presence of a magnetic field, and proton radiotherapy. The uncertainty in temperature measurements in this device is 1  $\mu\text{K}$ [151]

As stated previously, due to the different attenuations and stopping powers of various media, the same incident beam of radiation will produce differing dose deposition profiles. To simplify this clinicians in radiotherapy prescribe the dose in terms of dose to water,  $D_{water}$ . Water calorimeters have an innate advantage in that the dose measured is already in water.

Water calorimeters typically operate in what is referred to as "Adiabatic mode". In this mode, the entire system is kept at a constant thermal temperature before the incident radiation irradiates the system causing an increase in temperature, which is used to calculate the absorbed dose deposited in water. The system is then required to cool back to the baseline temperature, only after which further irradiations can take place. This process is shown in Figure 2.22 for a simulated model, in which 25 seconds of irradiation (shown in red) causes an excess of 200 seconds of cooling.

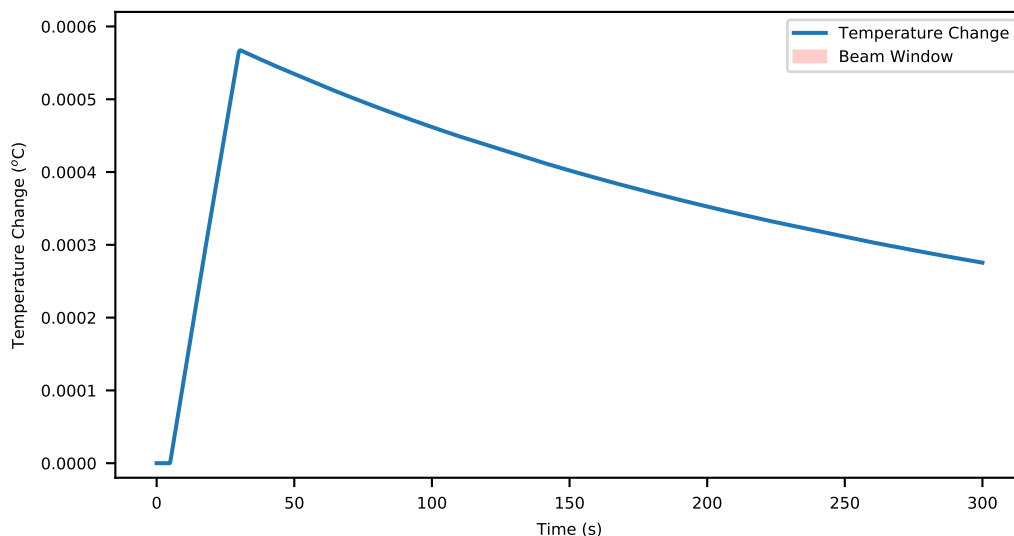


Figure 2.22: Simulation of Radiation Induced Temperature Rise in Adiabatic mode.

### 2.4.3 Graphite Calorimetry

The original Graphite calorimeters was described in a 1972 patent by Steve Domen of the National Bureau of Standards, Washington, [152] and consisted of a central graphite core, enclosed within a graphite jacket which is within a graphite shield. This can be seen in Figure 2.23(a), with Figure 2.23(b) showing how the components are nested together.

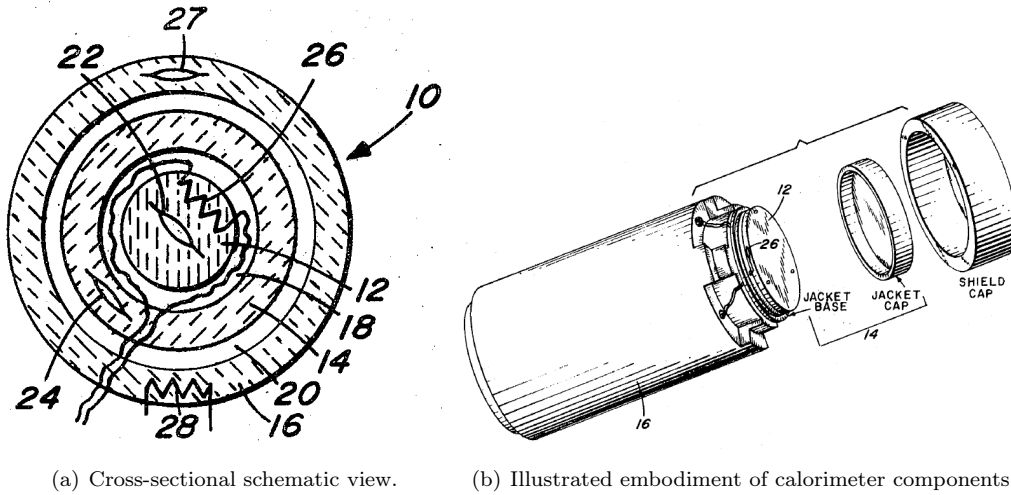


Figure 2.23: Schematic of three body Domen type graphite calorimeter, from 1972 patent application[152].

Label	Component
10	Calorimeter
12	Graphite Core
14	Graphite Jacket
16	Graphite Shield
18	Vacuum Gap
20	Vacuum Gap
22	Core Sensing Thermistor
24	Jacket Sensing Thermistor
26	Core Heating Resistor
27	Shield Sensing Thermistor
28	Jacket Heating Resistor

Table 2.3: Labelled Graphite Calorimeter components in Figure 2.23

Graphite has a low atomic number of 6 which is similar to water, which has an effective atomic number of 7.42[153]. As a result of this the radiation interactions that occur in the materials are broadly similar, enabling comparison.

Compared to water calorimeters, those made of graphite have several key advantages. It is easily machinable and relatively inexpensive, this allows for calorimeters to be designed for specific applications (such as the portable Aarrow graphite calorimeter[154]). Another key motivation behind a solid graphite calorimeter was based on the lower specific heat capacity of graphite (Equation 2.19), which is approximately  $1/6^{th}$  that of water[150]. As the induced temperature

in a material is indirectly proportional to specific heat capacity (Equation 2.3), this results in a temperature rise of the order 6 times greater temperature rise.

If a similar amplitude of noise ( $A_{noise}$ ) is achieved in both instruments, a 6 fold increase in the acquired signal ( $A_{signal}$ ) would result in the Signal to Noise Ratio (SNR) increasing by a factor of 36 (Equation 2.22).

$$\text{SNR} = \left( \frac{A_{signal}}{A_{noise}} \right)^2 \quad (2.22)$$

Such a large increase in SNR is of considerable interest to NMIs. A higher SNR reduces uncertainty on individual measurements and reduces the number of measurements required to achieve statistical significance.

Unfortunately Graphite calorimeters are not perfect instruments and do have some disadvantages that water calorimeters do not. Correction factors derived obtained from Monte Carlo are required for converting the determined absorbed dose in graphite ( $D_{graphite}$ ) to absorbed dose in water  $D_{water}$ [155]. This task is not trivial, and needs to be conducted per energy and fluence.

In addition, within graphite calorimeters there are several different types of heat flow: Conductive, Radiative and Convective. As a result of this, the internal heat flow is not as simple as in the water calorimeter and needs to be modelled accordingly. It is possible to minimise these effects however. The impact of convective heat flow can be minimised by sealing the graphite calorimeter and removing the gas inside with a vacuum pump. Conductive heat flow, along the internal wires connecting the sensing thermistors to external electronics, can be minimised by minimising diameter of the wire and introducing long heat paths.

#### 2.4.4 NPL Graphite Calorimeter for Absorbed Dose for Proton Radiotherapy

The National Physical Laboratory (NPL) has developed numerous calorimeters for specific applications in radiotherapy for many years. Calorimeters have been developed for electron radiotherapy, X-ray radiotherapy, and IMRT to name a few.

##### 2.4.4.1 Construction

The NPL Graphite Calorimeter for Absorbed Dose for Proton Radiotherapy, referred to thenceforth as the "*NPL proton calorimeter*" is constructed based on the Domen design, but with many subtle differences. A photograph of the *NPL proton calorimeter* can be seen in Figure 2.24.

The central core of the calorimeter, labelled in Figure 2.25, is a 16 mm diameter disc of thickness 2 mm graphite. The dimensions of the core were chosen to match the collection volume of a Roos plane-parallel ionisation Chamber[156]. The core is thermally isolated from the other components

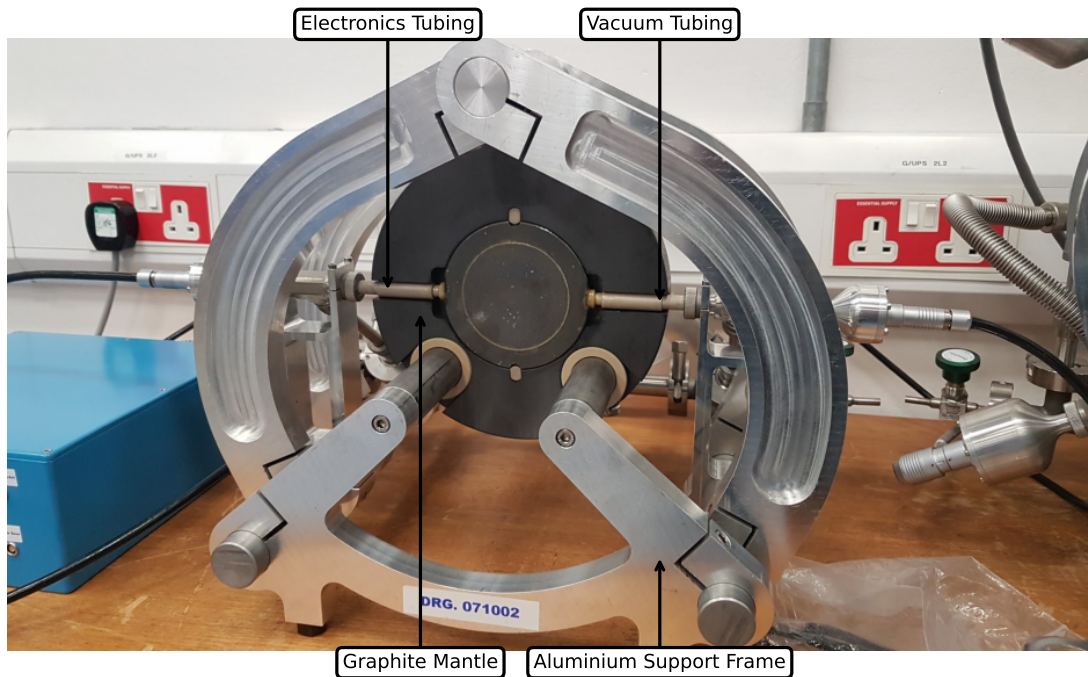


Figure 2.24: The NPL Graphite Calorimeter for absorbed dose in Proton Radiotherapy.

and held in a vacuum.

It is surrounded on all sides by a graphite jacket which is composed of two halves, an "upper" and "lower" section, labelled on Figure 2.25. When assembled, this component is simply referred to as the "*inner jacket*". The *inner jacket* is again thermally isolated, held in vacuum. It is surrounded by a final jacket composed of two sections, an "upper" and "lower" section, which together are referred to as the "*outer jacket*". Finally, the *outer jacket* is placed in a solid graphite "*mantle*", which acts to provide mechanical support as well as radiation scatter for large radiation fields.

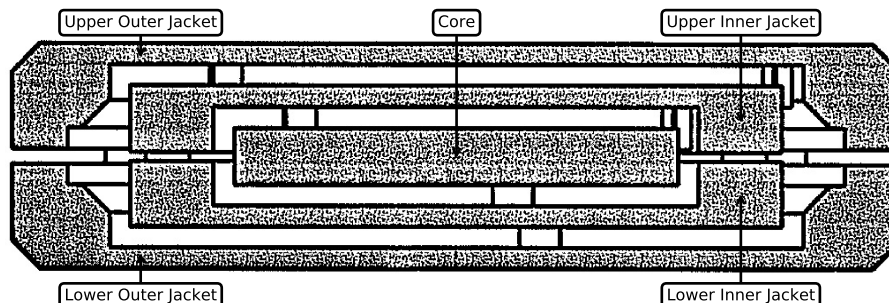


Figure 2.25: Annotated engineering diagram of the cross-section of the NPL Graphite Calorimeter for absorbed dose for proton radiotherapy.

Temperature monitoring and control of the *NPL proton calorimeter* is performed with numerous thermistors that are embedded within the device in the different internal components.

These thermistors are hermetically sealed and glass-encapsulated. Primary heat measurements are performed with two sensing thermistors placed within the core, referred to as "Core 1" and "Core 2". These thermistors are placed  $\pm 6$  mm in the Y direction whilst a pair of heating thermistors, are placed at  $\pm 6$  mm in the X direction. The positions of these thermistors can be seen in Figure 2.26, a radiographic image of the *NPL proton calorimeter* obtained at The European Synchrotron Radiation Facility (ESRF). All of the thermistors within the core are placed in a plane that passes through the centre of the core.

Within each half of the inner jacket are embedded 16 individual thermistors. These are divided equally between the two sections and with an angular separation between them of  $45^\circ$ , which is offset by  $22.5^\circ$  relative to the thermistors in the core. Within each section, all of the thermistors are wired in parallel and as such there is no direct electrical connection between the "upper" and "lower" sections.

There are also 16 thermistors embedded within the outer jacket, similar to those within the inner jacket. These are again separated by  $45^\circ$ , and offset by  $22.5^\circ$  relative to those in the inner jacket such that they are now in line with the core.

Embedded within the inner jacket and the outer jacket is a 0.4 mm thick PCB shaped as an annulus, with an inner radius of 12.5 mm and outer radius of 23 mm. The thermistors within the calorimeter are electrically connected to this PCB, which connects to external equipment for measurement and control. Before embedding within the calorimeter, each thermistor (both heating and sensing) undergo extensive calibration to understand both the temperature response and repeatability of the component.

#### 2.4.4.2 Electronic Circuitry

Each sensing thermistor is configured within its own Wheatstone Bridge circuit (Figure 2.27) to enable a more sensitive measurement of the thermistor's resistance. Each Wheatstone Bridge circuit consists of three  $25\text{ k}\Omega$  hermetically sealed, metal foil resistors which are selected for the circuit to balance at approximately  $22^\circ\text{C}$ . The out-of-balance voltages, are measured with Keithley K2182A nanovoltmeters[157].

When balanced the potential difference between the two arms of the bridge,  $V_{BA}(T)$ , is equal to zero. However, when unbalanced the potential difference between the two arms is given by Equation 2.23, where  $R_4(T) = R + \Delta r(T)$  and equating the three fixed resistors  $R_1, R_2, R_3$  to  $R$ . This equation holds for small values of  $\Delta r(T)$ , which is true for the thermistors used in the calorimeter. If  $R \gg \Delta r(T)$ , the relationship is approximately linear.

$$V_{BA}(T) = V_S \frac{\Delta r(T)}{4R + 2\Delta r(T)} \quad (2.23)$$

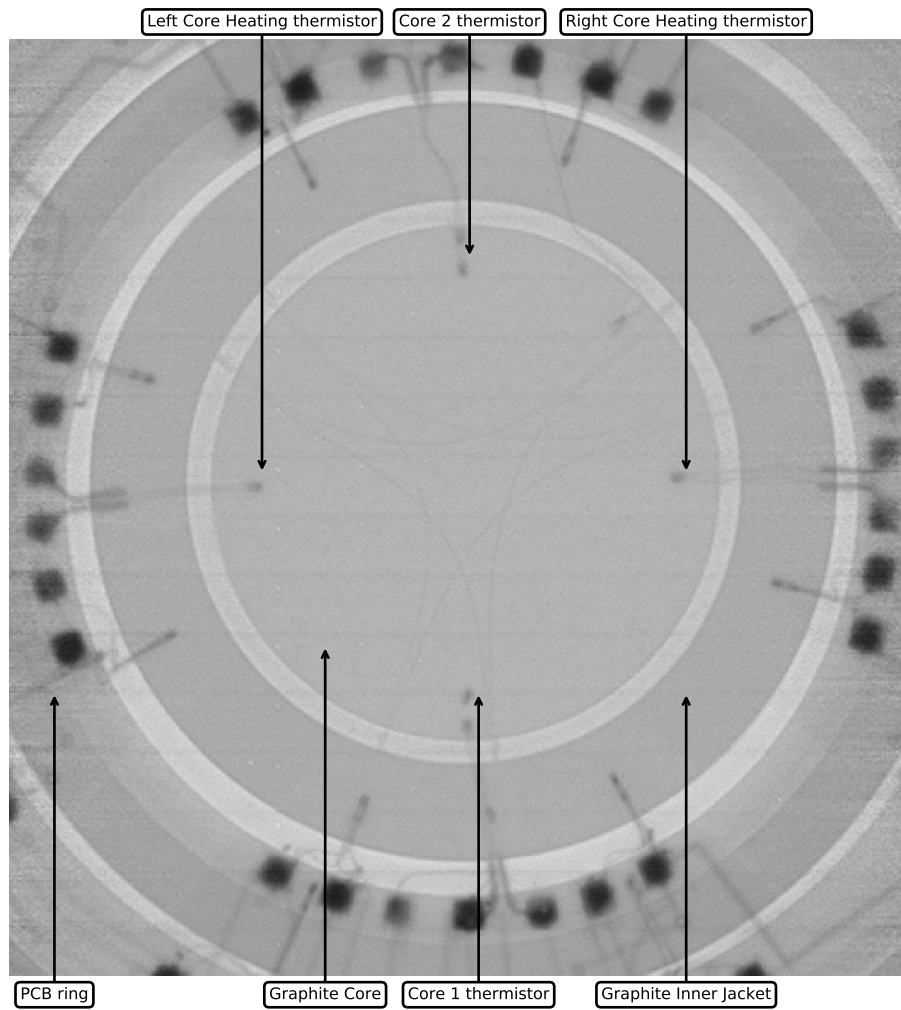


Figure 2.26: Annotated radiographic image of the NPL proton calorimeter, image provided by Nigel Lee.

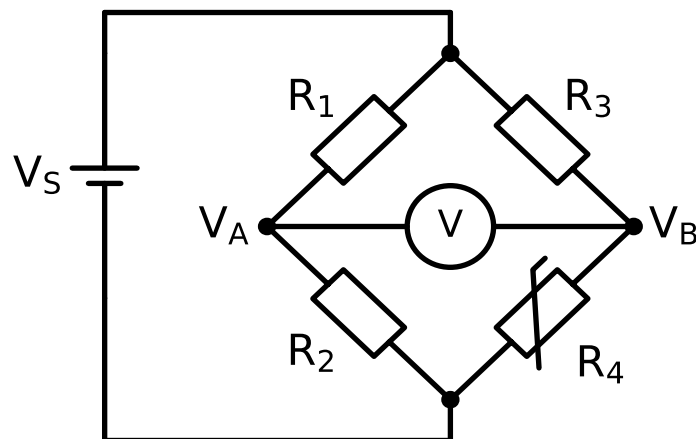


Figure 2.27: The thermistor ( $R_4$ ) configured in a Wheatstone Bridge in the NPL Proton Calorimeter.

The heating thermistors within the calorimeter are not separately connected, and are instead connected in parallel to form local networks for each graphite component. Each network is attached in series to a  $100\ \Omega$  shunt resistor, over which a digital multimeter is positioned in parallel to measure the potential difference and thus power supplied to each network ( $P = \frac{V_{shunt}^2}{R_{shunt}}$ ). The circuit diagram for the heating thermistors embedded in the core is shown in Figure 2.28. To protect each network from an excess of power supplied, a 50 mA fuse is attached to each network (not shown for simplicity) in addition to software limits on maximum power supply.

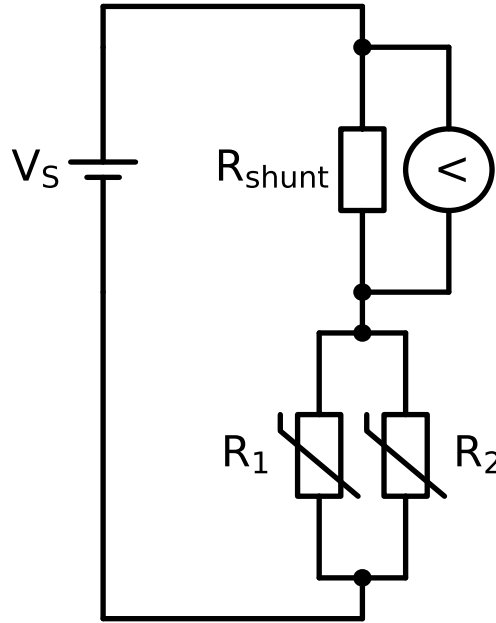


Figure 2.28: The configuration of the heating thermistors ( $R_2$  and  $R_3$ ) in the NPL Proton Calorimeter.

The temperature feedback controller that ensures that each graphite component is held at the prescribed temperature uses the Proportional–Integral–Derivative controller (PID) formalism[158], shown in Equation 2.24.

$$u(t) = K_p \left( e(t) + \frac{1}{T_i} \int_0^t e(t') dt' + K_d \frac{de(t)}{dt} \right) \quad (2.24)$$

Using the definition for the temperature error correction term ( $e(t)$ ) in 2.25.

$$e(t) = T_{target} - T(t) \quad (2.25)$$

The electrical signals and power that connect the embedded thermistors and external equipment are connected via the intermediary PCB, described previously. Thin platinum wires of diameter

0.1 mm connect the thermistors to the PCB, travelling radially inwards with minimal path length. To enable the wires to reach the *core* and other internal components, thin grooves are etched into the two halves of the graphite where necessary.

### 2.4.4.3 Dose to Graphite Determination

In Quasi-Adiabatic (QA) mode, the radiation induced temperature rise in the core needs to be calculated. Whilst the beam delivery system may be able to determine when the beam is turned on and off, the calorimetry system needs to be independent from this. To do this, the beam on/off points are determined by observing the temperature gradient over a nominal window. The beam on/off positions are identified by a large change in the absolute gradient.

These temporal positions are then fine tuned using an internal algorithm which minimises residual errors. A second order polynomial fit is then applied to the temperature drift before and after these calculated beam on/off positions. Using these two polynomials, an extrapolation is then performed towards the midpoint between the beam on/off positions, at which point the temperature difference can be calculated. This process is demonstrated in Figure 2.29, where the *NPL proton calorimeter* was exposed in a scanned pencil beam delivering three layers of dose to the calorimeter core.

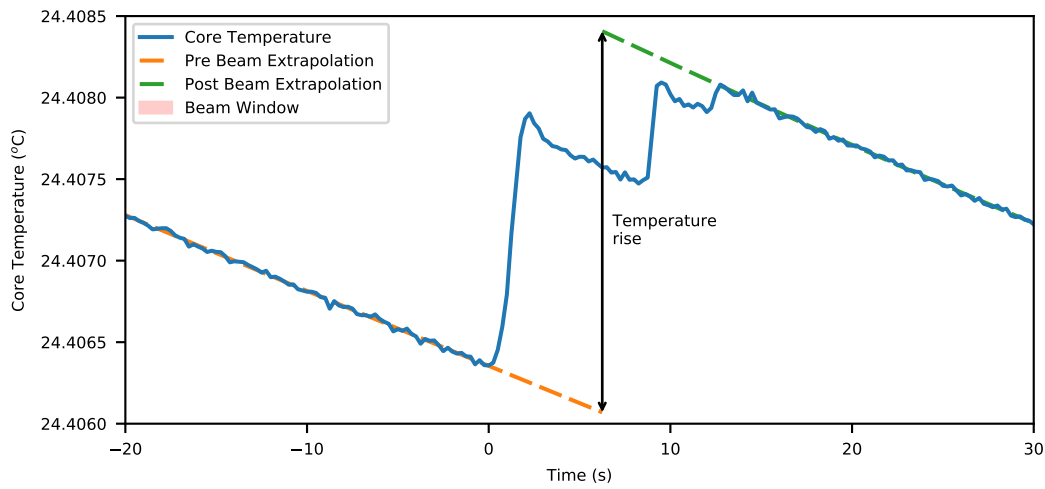


Figure 2.29: Temperature measurement of the NPL Proton Calorimeter to a scanned pencil beam in QA mode.

To calculate dose to graphite, Equation 2.26 is used, expanding on Equation 2.21 with the inclusion of correction factors ( $k_i$ ) such as those for impurities in the graphite ( $k_{imp}$ ) or the physical gap between components within the calorimeter ( $k_{gap}$ ).

$$Dose_{Graphite} = c(T)\Delta T \cdot \prod k_i \quad (2.26)$$

The uncertainty in the dose to graphite measurement ( $\sigma_{Dose}$ ) is calculated using Equation 2.27, and is a combination of uncertainty of the calorimeter ( $\sigma_{Calorimeter}$ ), which includes the uncertainties on the calorimeter mass; Monte Carlo based uncertainties ( $\sigma_{MonteCarlo}$ ); uncertainties in the electrical calibration of the measuring equipment ( $\sigma_{Electrical}$ ); uncertainties in the determination of the specific heat capacity ( $\sigma_{SpecificHeatCapacity}$ ); and uncertainties directly resulting from within the measurement and analysis process ( $\sigma_{Measurement}$ ).

$$\sigma_{Dose(QA)}^2 = \sigma_{Calorimeter}^2 + \sigma_{MonteCarlo}^2 + \sigma_{Electrical}^2 + \sigma_{SpecificHeatCapacity}^2 + \sigma_{Measurement}^2 \quad (2.27)$$

The introduction of the heating system to the calorimeter system, enables the operation of "Isothermal (ISO) mode". In this mode, the core of the calorimeter is kept at a constant temperature using the feedback mechanism and embedded heating thermistors described. When incident radiation causes a heating effect, the temperature control algorithm reacts and this is observed as a drop in electrical power required to maintain the temperature. This is demonstrated in Figure 2.30, where the calorimeter again receives three layers of dose in a pencil beam delivery. It can be observed that the feedback mechanism briefly overcompensates in power supplied to the core after the incident beam stops, however this is balanced by the accompanying decrease in power immediately after.

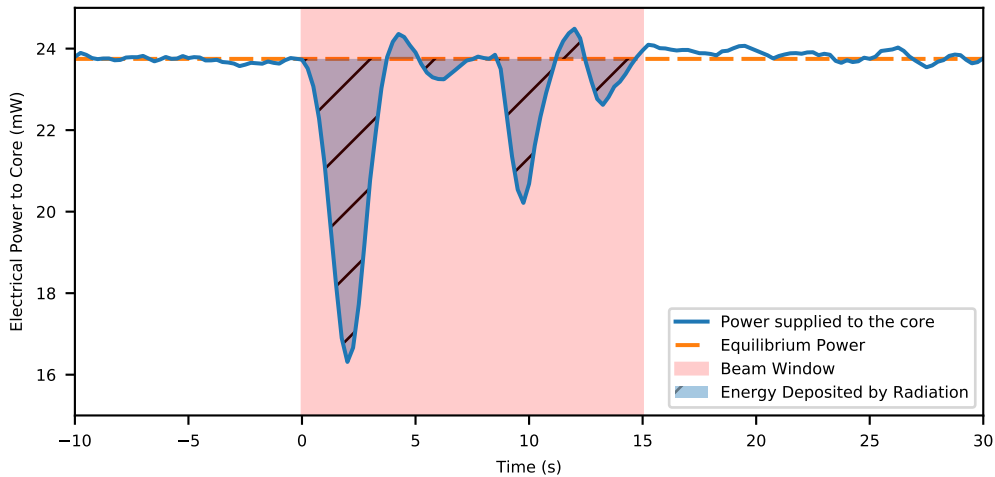


Figure 2.30: Electrical power measurement of the NPL Proton Calorimeter to a scanned pencil beam in ISO mode.

In isothermal mode, the dose deposited in the core by the radiation is calculated using equation 2.28, where  $\Delta P_{Elec}$  corresponds with the change in electrical power. As in Equation 1.1, a number of correction factors need to be applied to the result. Of note is that this equation does

not require information about the specific heat capacity of graphite.

$$Dose_{Graphite} = \frac{\int_0^t \Delta P_{Elec}(t') dt'}{m_{core}} \cdot \prod k_i \quad (2.28)$$

Removal of the specific heat capacity does change the uncertainty in the dose determined (Equation 2.29), however it is not necessarily lower due to the inclusion of uncertainties associated with the PID mechanism ( $\sigma_{PID}^2$ ).

$$\sigma_{Dose(ISO)}^2 = \sigma_{Calorimeter}^2 + \sigma_{MonteCarlo}^2 + \sigma_{Electrical}^2 + \sigma_{Measurement}^2 + \sigma_{PID}^2 \quad (2.29)$$

This mode of operation has several advantages: The primary reason being that it allows a semi-independent measurement to determine absorbed dose to graphite using a different technique. The second reason that is perhaps not obvious is it becomes possible to reduce the time between measurements as there is no longer a requirement to establish a temperature trend in quasi-adiabatic mode between measurements.

## 2.5 Project Justification

The first justification for this project is that the *NPL proton calorimeter* needs to be aligned relative to the proton beam delivery system. The uncertainty in this position alignment is contained within the parameter  $\sigma_{Measurement}$  in Equation 2.27 and Equation 2.29. As a primary standard instrument, it is not sufficient to trust the treatment delivery system implicitly, whether that be the alignment lasers or the internal log files. Measurement of this should therefore be independent. Radiochromic film is a valid option for measuring the beam with high resolution, but it is a slow process requiring 24-48 hours of self-development time for accurate dosimetry[159]. Compliance with a future Code of Practice for absolute dosimetry in proton beam therapy would most likely require uniform delivery to a volume, and this would need to be independently measured and verified in-situ.

A second justification for this project is that the *NPL proton calorimeter* was originally designed for dosimetry of passively scattered proton beams of diameter entering the device, centred at the core. Prior to irradiation thermal equilibrium is achieved between the internal components of the calorimeter, with no net flow of heat. With this mode of irradiation, the *core*, *inner jacket*, and *outer jacket* are uniformly exposed, with the assumption that this would cause disruption of the thermal equilibrium.

The introduction of PBS presents an issue for this assumption, as the temporal energy depos-

ition is no longer uniform. Depending on the dose rate, the number of spots in a layer, and the time between spots, the time dependent local temperature response may respond in different manners. A more thorough understanding of heat flow within the *NPL proton calorimeter* is required, requiring experimental and computational studies.

Characterisation of the calorimeter in moving pencil beams was performed by Petrie *et. al* in 2016[160], however it was limited in scope to "slow" moving Gaussian beams (speed 1 mm/s ) in single axes at a time. This is not the case in therapeutic PBS, where the beam spot is magnetically deflected in two dimensions at variable speeds. Understanding the internal heat transfer in these situations requires more sophisticated thermal modelling and high resolution information on the pencil beam's position, size and uniformity. This thermal modelling of these complicated dose delivery systems could be carried out using the treatment delivery log files, but as discussed as a primary standard device it needs to be as independent from manufacturer influence as possible.

It is with this challenge in mind, that the prospect of using radiation-tolerance silicon devices arises. These devices must not only be able to withstand the harsh radiation environment of medical physics, where dose rates vary between 0.1-50 Gy/s, but also survive sufficient accumulated dose such that studies can be performed before damage renders the device unusable. To monitor the incident radiation in such a way that it does not perturb or influence the measurement by the *NPL proton calorimeter*, the monitoring devices must be sufficiently thin. Further to this, any silicon device must have high spatial resolution in order to determine the radiation that has been delivered to the small components within the calorimeter. As discussed, SSD and CMOS devices have been used with success in particle physics, an environment that demands many similar characteristics as radiotherapy and have been selected for evaluation.

The objective of this thesis is therefore to apply a selection of silicon detectors to better understand the radiation delivered to the *NPL proton calorimeter*, facilitating further computation study, in order to improve measurements of dosimetry.

## Chapter 3

# Characterisation, Reconstruction, and Evaluation of the PRaVDA Tracker for Proton Beam Monitoring

### 3.1 Introduction

As described in Chapter 2 the use of a SSD to monitor radiation is not a new concept. SSDs are well established in the realm of radiation monitoring, with applications ranging from particle accelerators[161] to dosimetry of microbeams in a synchrotron.[162]. After reviewing the SSD devices that the University of Birmingham had available that could be promising devices for beam monitoring for the *NPL proton calorimeter*, the tracking unit developed for the Proton Radiotherapy Verification and Dosimetry Applications (PRaVDA)[163] project was selected as a promising candidate. Prior to this investigation the PRaVDA tracker unit had only operated in a low beam current mode as part of research into Proton Computed Tomography (pCT). This is several orders of magnitude lower than therapeutic particle rates where a particle rate of  $10^{10}$  per second is not uncommon[164]. While technically capable of monitoring radiation beams with higher particle rates, the tracker unit needed to be evaluated and understood before use with the *NPL proton calorimeter*. In addition, the three projections per plane read-out of the tracker unit meant that specialised reconstruction algorithms are needed to be developed. This had already been established for pCT mode[165], however a new algorithm would need to be built and evaluated for therapeutic mode.

The large active area of the PRaVDA tracker unit, defined as the region in which all three planes overlap, is approximately a 5 cm radius. This is sufficiently large to cover the central core

of the *NPL proton calorimeter* and many of the internal components but is not large enough for a  $10 \times 10 \text{ cm}^2$  reference field[166].

More details on the results presented in this chapter can be found in [22], which is also reproduced in Appendix B.

## 3.2 Proton computed tomography

Clinically, the Bragg peak is exploited in proton radiotherapy to deliver a precise dose at a defined depth within the patient. Human beings are not composed solely of water, but a non-uniform mixture of bone, adipose, and muscle, amongst other things. Even within the same bone, the density can dramatically change depending on the location[167].

This presents a significant issue of proton radiotherapy as the stopping power of the medium ( $\langle \frac{dE}{dx} \rangle$ ) is influenced by the density, as previously described in Equation 2.11. Having a higher density than expected would result in the proton Bragg peak being a shallower depth, whilst for a lower density than expected the reverse is true. The latter is particularly problematic for proton radiotherapy of lung tumours, where the lung's lower density than a tumour could result in dose delivered to a patient's heart if the beam is misplaced[168].

For treatment planning, traditionally X-ray computed tomography (xCT) is used to identify the tumour and determine the density distributions within the patient however this method is not without inaccuracies.

It as been shown that Magnetic resonance imaging (MRI) could be used within the treatment workflow for proton radiotherapy[169] By itself, MRI cannot determine electron density of tissue which is necessary to perform treatment planning, and a conversion must be done to matched xCT images to determine this[170].

In pCT the target is imaged with high energy protons such that the Bragg peak is not within the patient or phantom. The particles are tracked before and after the target, with the path the particle has taken reconstructed using statistical analysis tools (such as Bayesian formalism [171]). Using a range telescope or other method, the residual energy of the particle can be measured, which in turns enables energy loss along the path (and thus stopping power) to be determined.

To tackle this problem and develop new instrumentation for pCT, the PRaVDA consortium was established[172].

## 3.3 PRaVDA tracker design

The instrumentation developed for the PRaVDA project needed to track the position of individual protons before and after passing through a phantom (or patient) and the residual energy after

exiting the patient phantom. To compute the stopping power of the tissue, a minimum of  $10^9 - 10^{10}$  particles are required, with greater numbers required to reduce the uncertainties further.

With current research systems, the time required to acquire data is significantly larger than xCT. In pCT, there is a non-trivial amount of scatter that the particles undergo as they propagate through the phantom or tissue. In order to reconstruct the path that is taken, the incident and exiting particle tracks for each particle must be recorded separately for each particle. The measuring equipment for pCT must thus be able to record at a fairly rapid rate, else the duration required to image a patient becomes unreasonable.

It was determined that to measure particles in this manner, the most appropriate technique would be to use Silicon Strip Detector (SSD) technology. Unlike a full 2D sensor, the single dimension acquired by a SSD would significantly reduce the amount of data acquired, increasing the obtainable frames/second. By having two separate SSD layers orthogonal to each other, the X and Y of a particle can be determined and thus reconstructed. This does introduce a limitation on the number of particles/frame that is not present for a fully 2D pixel sensor, as demonstrated in Figure 3.1. As the SSD would be unable to distinguish different particles, a phenomenon known as "Ghosting" occurs, where it is impossible to determine which of the particles are real and which are "ghosts". The ratio of true particles:"Ghost" particles gets significantly worse as the number of particles/frame increases, following a  $n : (n - 1)!$  relationship, where  $n$  is the number of particles.

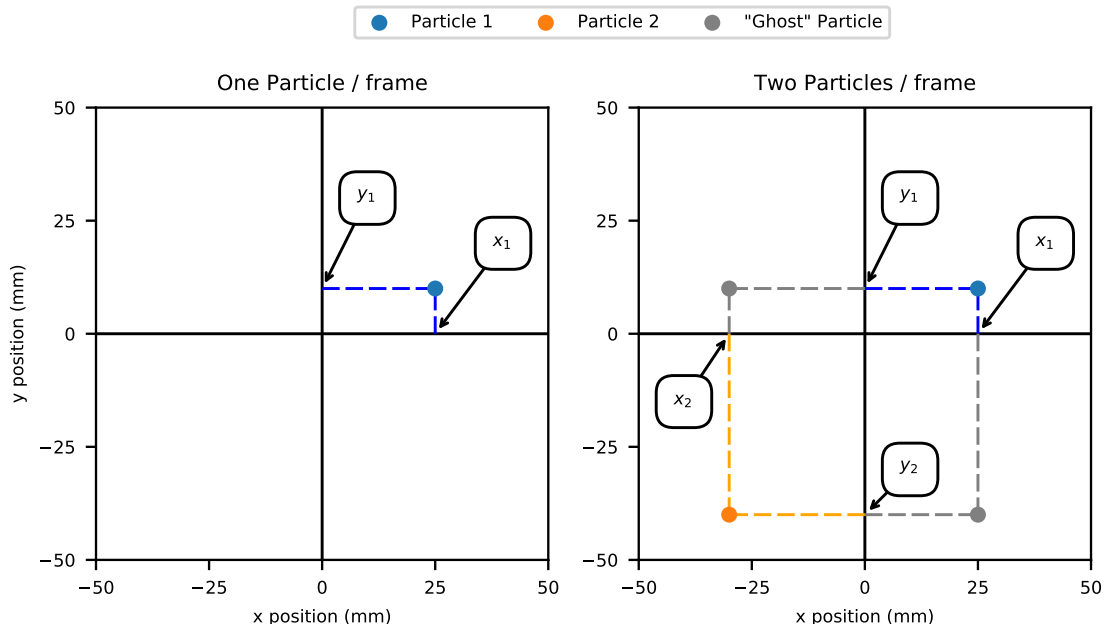


Figure 3.1: Example of "ghosting" artefacts in with "XY" position tracking.

Clearly the effect of ghosting could be suppressed with the inclusion of a third SSD layer, as documented in by Spieler[173]. The three layers of the PRAVDA tracker were oriented at

non-orthogonal 60° intervals in an "XUV" orientation. A photograph of the partially assembled PRaVDA tracker can be seen in Figure 3.2.

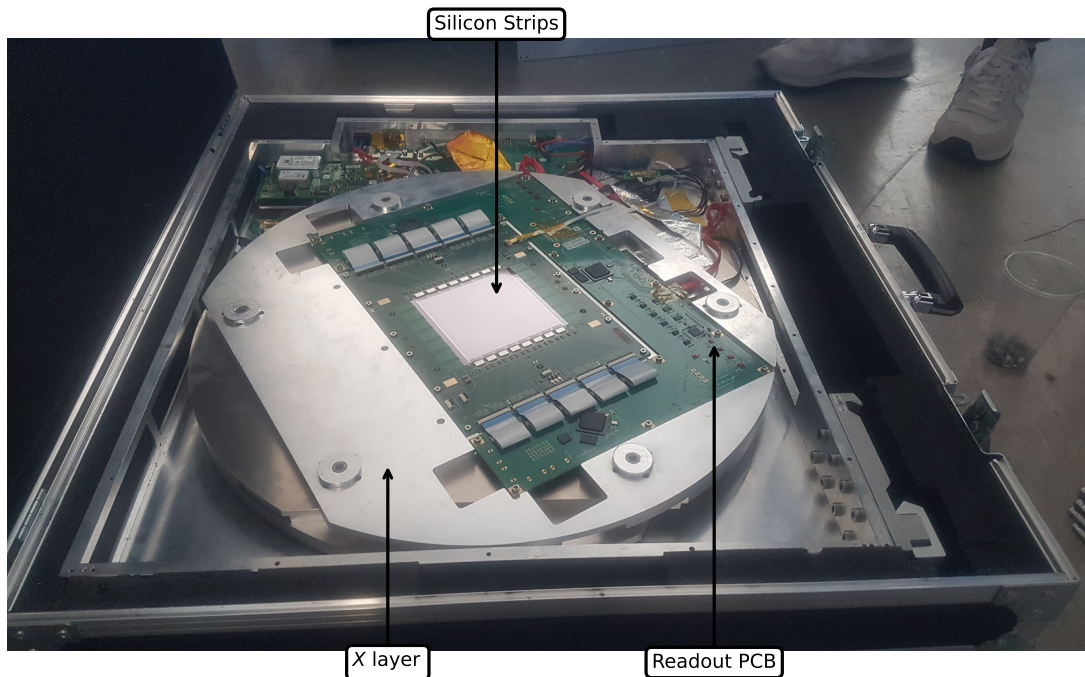


Figure 3.2: Internals of PRaVDA tracker unit.

The specifications of the PRaVDA tracker unit are shown in Table 3.1, whilst a detailed description of the electronics and circuitry is described by Esposito *et al.*[163].

Name	Quantity	Units
strip pitch	90.8	$\mu\text{m}$
strip thickness	150	$\mu\text{m}$
strip count	1024	
refresh rate (pCT)	26	MHz
refresh rate (treatment mode)	6000	Hz
active area (strip half)	93 x 48	$\text{mm}^2$
active area (combined)	93 x 96	$\text{mm}^2$

Table 3.1: Specifications of the PRaVDA tracker silicon strip detector

### 3.3.1 pCT mode

In pCT mode, and at low particle rates, the PRaVDA tracker unit is capable of recording the position and time stamp (to an accuracy of 38.5 ns) of individual particles as they pass through the silicon. The clock speed of the PRaVDA tracker unit is 26 MHz, matched to the frequency of the cyclotron at the iThemba Labs proton facility, and as such the detector is capable of measuring pulses from the accelerator. For low numbers of particles in each bunch passing through the tracker per frame, the tracker unit is able to distinguish individual events and, via an algorithm, reconstruct

the path of the individual particles. Incoming signal generated by the tracker units are converted into outgoing coordinates and their associated vectors. If multiple angles of the phantom are imaged, a backprojection-then-filtering algorithm is used to reconstruct the 3D image [174].

### 3.3.2 Therapeutic mode

At therapeutic dose rates the PRaVDA tracker unit is unable to differentiate between individual particles, due to the very high number of particles per frame. Data acquired by the detector in treatment mode is semi-digital; it is possible to count the number of interactions in each frame by assessing whether two charge thresholds have been reached. The first charge threshold could be set between 200-10,000 electrons per frame, whilst the second could be set between 20,000-160,000 per frame. These can be adjusted using the provided software to an arbitrary value however due to the design of the tracker unit it was not possible to perform calibrations of these threshold levels via external charge injection.

For each frame of acquired data, information was available for each strip channel telling whether the charge was above each of the set thresholds. The first threshold was expressed as raw bits for each strip channel, whilst the data of the second threshold was compressed into binary numbers. Multiple frames need to be combined to reconstruct a beam profile but clearly the plot of hits vs position will still saturate for any strips where there is often more than 2 hits per frame. Several consecutive frames are composited to reconstruct a profile.

Assuming that the probability of a threshold being exceeded is proportional to the intensity of the incident radiation; the effect of superimposing numerous frames can be seen in Figure 3.3. With the prior knowledge that the majority of incident radiation beams in PBS will be Gaussian-like, a median rank filter of variable size can be introduced to minimise the impact of random fluctuations. Note that the numerical simulations presented do not include masked channels, which would never report a signal over threshold.

This purely numeric simulation explored the gamma index passing rate of the resultant profile up to 600 frames (representing approximately 0.1 seconds of recorded data). The gamma index compares dose difference (DD) and distance to agreement (DTA) between two dose distributions, and is described mathematically in appendix A.1.1.4. An incident Gaussian was centred on strip channel 512 and with a FWHM of 200 strips. To evaluate the accuracy of the acquired strip profile, the gamma conditions were set at 3%/3 mm, and with a dose cutoff of 20%; matching clinically used conditions at University Hospitals Birmingham (UHB).

As expected, it can be shown that the gamma passing rate increases with the number of frames in the composite however after 600 frames the passing rate is still less than 70% and would be considered a failure in a clinical environment. This is due to local fluctuations caused by the

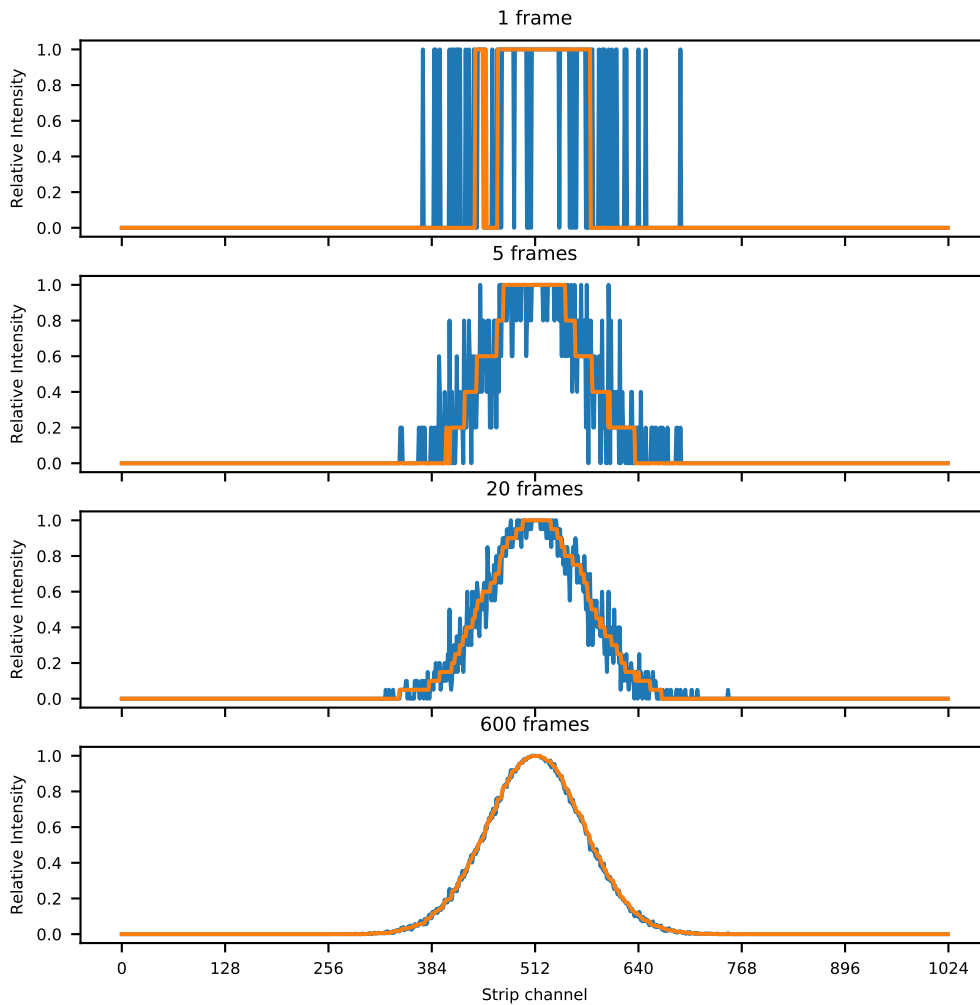


Figure 3.3: Simulated effect of compositing multiple PRaVDA tracker frames with a median rank filter of 20.

random nature of the signal deposition. It is possible to mitigate this however by applying a median rank filter to the generated profiles, with the effect of a rank of 5, 10, and 15, shown in Figure 3.4. When applying a median rank of 15, an excess of 70% gamma passing rate is achievable after approximately 100 frames (0.016 seconds), with greater than 90% achievable after 600 frames.

The effect of changing the median rank filter on the raw therapeutic mode data acquired over 600 frames can be shown in Figure 3.5. For a modest median rank of 15, the gamma passing rate greatly increases. A median rank in excess of 60 begins to lower the gamma passing rate, likely due to details being smoothed out. There is a notable oscillation on every odd/even rank value, this is due to the filter mechanism interpolating between adjacent pixels for even values[175]. The recommendation based on this small investigation is to have the median rank filter should be odd and as low as possible whilst removing the effect of masked frames or noise fluctuations. A median rank value of 15 is used for the rest of this section, unless explicitly stated.

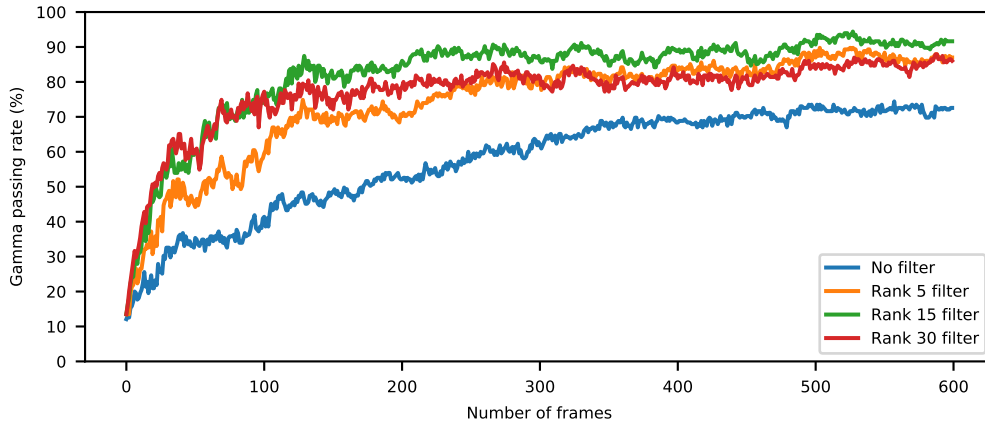


Figure 3.4: Simulated effect of multiple PRAVDA tracker frames on Gamma Passing Rate with various median rank filters.

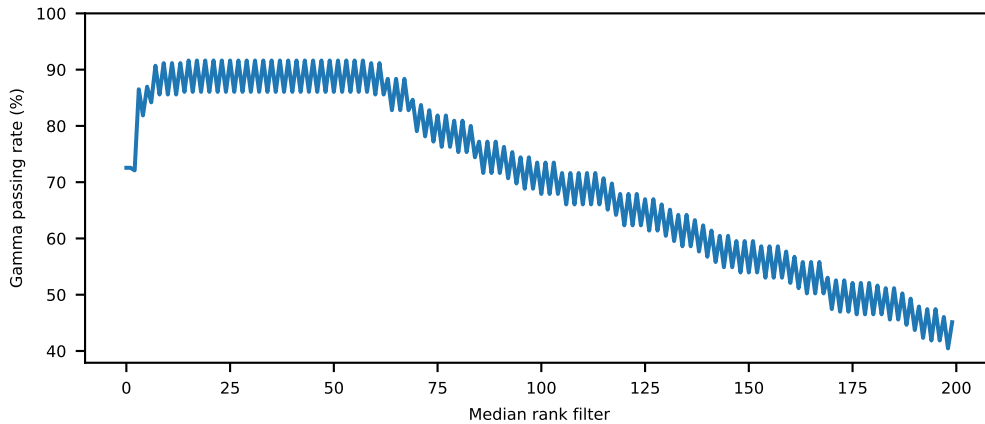


Figure 3.5: Gamma passing rate of simulated multiple PRAVDA for various median rank filter values.

## 3.4 Image reconstruction

### 3.4.1 Algorithms

Two algorithms were developed to reconstruct the signal as part of the investigation into the PRAVDA tracker unit, which will be referred to as the *projection* and *interpolation* methods. A comparison of the two methods reconstructing an arbitrary  $25 \times 15 \text{ mm}^2$  ellipsoid that is rotated  $23^\circ$  can be shown in Figure 3.6. The centre of the reconstruction is the same for both methods, however the peripheral and other information is different.

The *projection* method is characterised by its hexagonal shape, originating from the smearing of signal received by each of the three non-orthogonal planes. This method imposes minimum bias on the incident signal and is capable of reconstructing noisy signal in the presence of masked strips. Gamma passing rates of the *projection* method are typically less than 5%, making it clinically unacceptable.

By comparison, the *interpolation* method is defined by its lack of hexagonal streaking. This method uses the beam centre, calculated via the *interpolation method*, and attempts to use the 1D beam profile acquired by a strip to infer the 2D beam profile. A significant amount of pre-processing is required with this method; requiring normalisation and increased computational time, and being unable to cope with noisy strip data necessitating additional smoothing. Despite this, the gamma passing rate of this method is significantly higher, with passing rates of 60% being achieved, although it is still not high enough to be clinically acceptable.

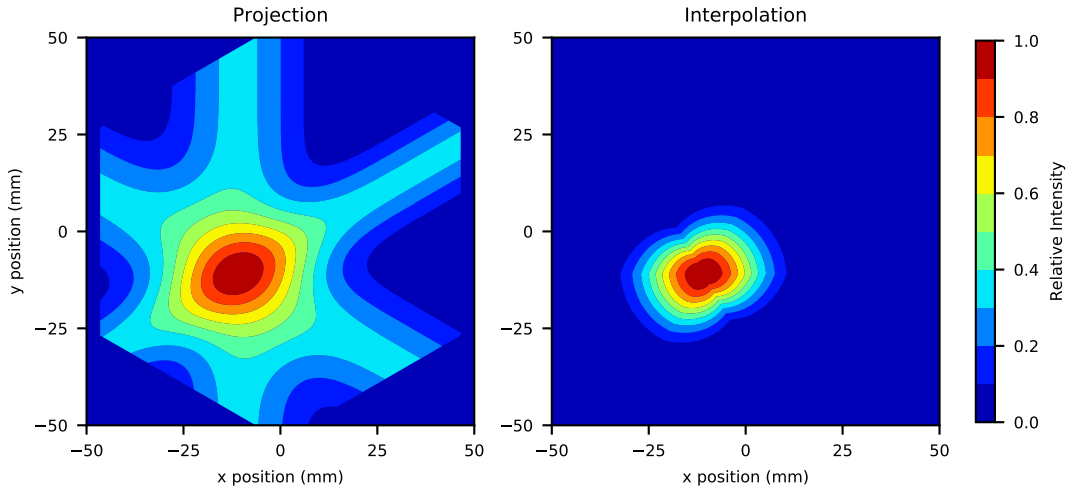


Figure 3.6: Comparison of the two PRAVDA tracker reconstruction methods.

The *projection* reconstruction algorithm was designed with rapid validation of the incident beam in mind, prioritising the speed of reconstruction. The aim of this, was that if the project were taken further clinically then real-time validation of proton beam spot-scanning could be achieved. The *interpolation* reconstruction algorithm was designed for off-line reconstruction of the incident beam, prioritising accuracy of the reconstruction.

A full description of the algorithms behind the two methods is described in Appendix A.1.

### 3.4.2 Beam centre evaluation

Both reconstruction methods generate a 2D array of pixels, capable of further analysis. The beam centre of the beam with the *projected* method was determined by calculating the centre of mass for all points (with equal weighting) above a determined pixel threshold. A technical report on this method with a threshold value of 50% was submitted to JINST[22].

To determine how appropriate this threshold value was for determining the centre of mass, a number of reconstructed beams were simulated for varying number of frames. A medium rank filter of 15 was again used, with each target number of frames simulated 20 times for the mean and standard deviation to be determined. The beam centres of these simulated beams is shown

in Figure 3.7. The unsuitability of the 25% threshold was predicted and confirmed, the *projection* reconstruction method generating streaked artefacts that are 33% of the maximum signal. Comparing the 50% and 75% thresholds, there is no obvious advantage in one over the other from this figure alone.

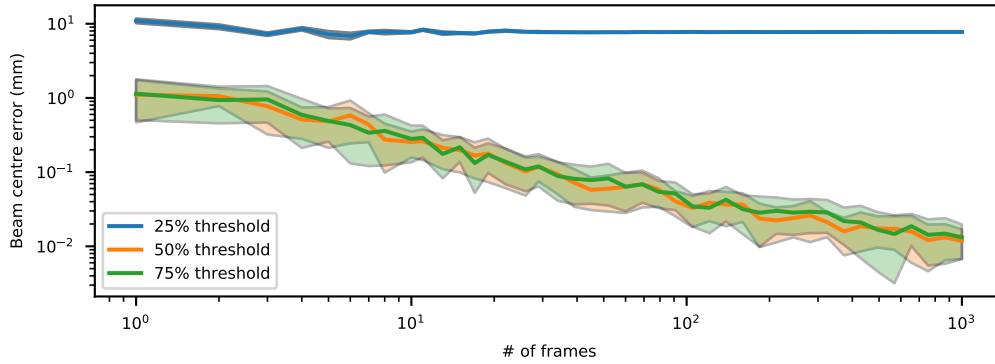


Figure 3.7: Simulated beam centre error of the PRaVDA tracker unit against number of frames in composite.

Evaluating more thresholds results in Figure 3.8, where the sharp reduction in reconstructed beam centre error can be observed at 33% threshold. As shown in Figure 3.7, increasing the number of frames available for the reconstruction does appear to reduce the beam centre error across all threshold values. Between approximately 40% and 80% there is no significant difference in the beam centre error, as it is observed to plateau, however there appears to be a trend, especially in the region with frames in excess of 900, where increasing the threshold value increases the beam centre error.

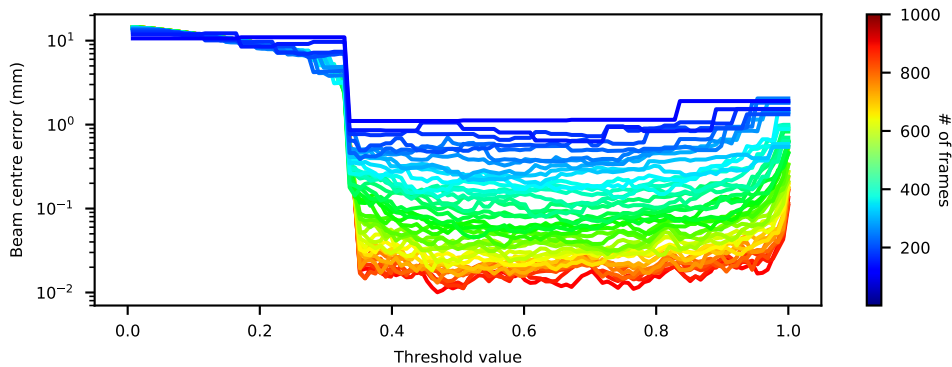


Figure 3.8: Investigation of threshold value on beam centre for increasing number of frames.

There is motivation for the threshold value to be as high as possible, without increasing the beam centre error. A low threshold requires that more of the beam profile must be captured on each SSD, effectively reducing the available area for beam capture. For comparison, a higher threshold can tolerate more of the beam not being captured by the profiles, increasing the available area

for beam capture. This is demonstrated in Figure 3.9, where the beam centre error for differing threshold values is calculated for an array of  $20 \times 20 \text{ mm}^2$  beams centred at different points on the detector.

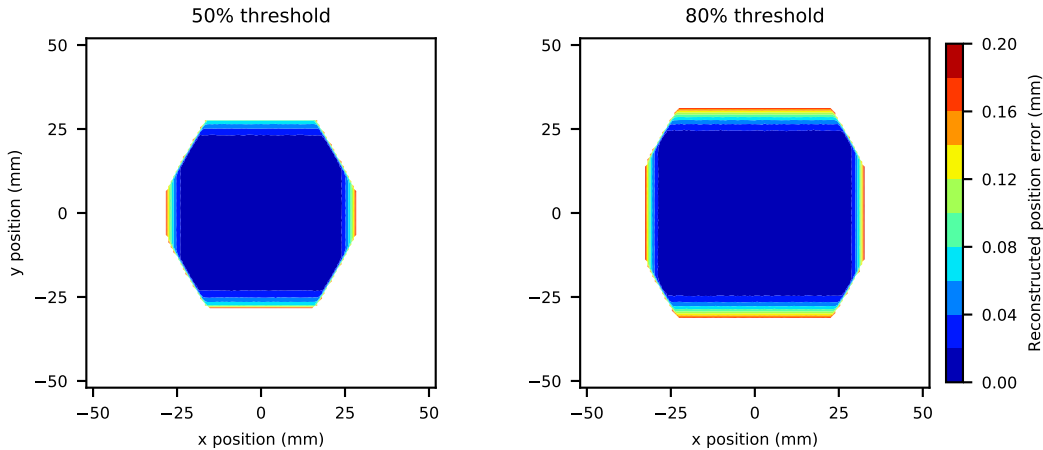


Figure 3.9: Effect of varying the threshold on reconstructed beam centre for 50% and 80% for a simulated  $20 \times 20 \text{ mm}^2$  beam.

For the 50% threshold simulation, the viable area for reconstructing the beam centre within an acceptable tolerance of 2 mm was found to be  $2660 \text{ mm}^2$ . At a simulated 80 % threshold, this viable area is  $3780 \text{ mm}^2$ , a 40% increase. The "viable areas" of the thresholds are thus inferred to depend on the FWHM of the incident beam, with narrower beam possessing a larger "viable area". Likewise, a wider beam would possess a greater difference between the 50% and 80% threshold values.

It is important to note however, that exposing this additional area where the beam centre can be reconstructed to radiation would also irradiate the sensitive electronics supporting each strip layer, the radiation tolerance of which will be lower than the silicon strips. A compromise between the two thresholds is thus advisable where the viable region from the 50% threshold simulation is used as a target, but the 80% signal threshold is used in the reconstruction.

## 3.5 X-ray beam investigation

### 3.5.1 Motivation

Evaluation of the PRaVDA tracker unit in therapeutic mode was first performed at the NPL, using an Elekta Synergy linear accelerator. Despite being a different radiation modality to PBS, due to difficulties securing proton beam access future evaluation of the PRaVDA tracker unit with the *NPL proton calorimeter* is easier to perform at NPL.

### 3.5.2 Expectation

Due to the low mass-energy absorption coefficient of silicon at therapeutic energies it was expected that the PRAVDA tracker unit would have a very low detection efficiency. It was theorised that despite this there could be sufficient X-rays of low enough energy that it is should be possible to detect something from the beam, although a full Monte Carlo simulation would be required to validate this. A comparison of the energy spectrum of a 6 MV Linac generated using PRIMO[176], and reference Silicon Mass-Energy Absorption Coefficient values[78] can be seen in Figure 3.10.

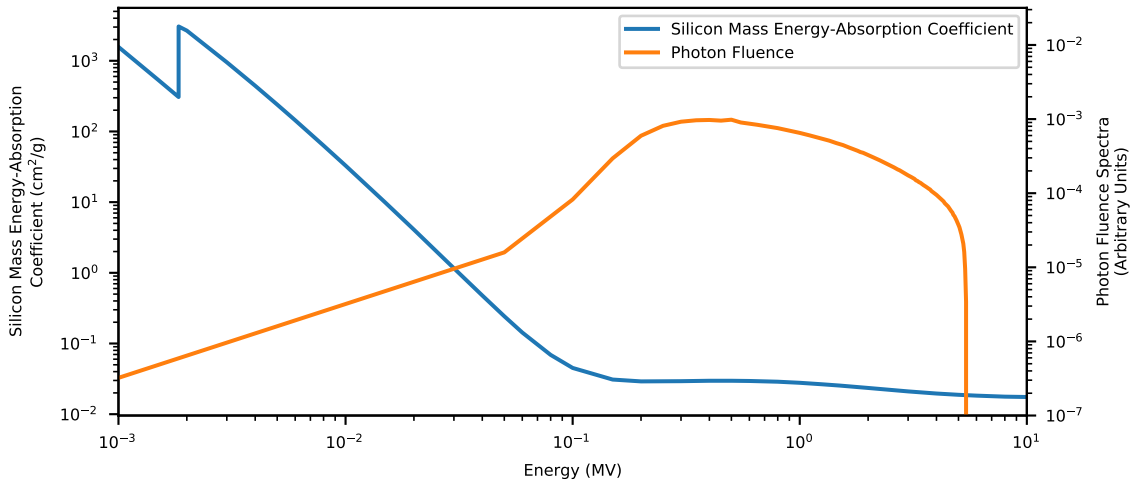


Figure 3.10: Energy Spectra of a typical 6 MV Linac compared to the Silicon Mass Energy-Absorption Coefficient.

In addition, there is expected to be a non-trivial amount of contamination of the X-ray beam by secondary electrons[177]. Such electrons would certainly interact with the PRAVDA tracker unit, but predicting the signal response would again require a dedicated Monte Carlo study.

We can thus estimate that the average photon will have 1.5 MV energy and have a Mass Energy-Absorption of  $3.5 \times 10^{-2} \text{ cm}^2/\text{g}$ . From literature, the fluence rate in comparable Linacs at 6 MV is  $6.6 \times 10^7 / \text{cm}^2/\text{pulse}$ [178]. Together we can estimate that each Linac pulse could result in 80000 photons/ $\text{cm}^2$ , which would liberate approximately  $3 \times 10^{10}$  electrons/ $\text{cm}^2$ . This is comparable to the second electron threshold, and as such likely to generate measurable signal, although saturation is likely to be an issue for large field sizes.

### 3.5.3 Methodology

The PRAVDA tracker unit was positioned at isocentre in the Linac, with the middle tracker layer aligned to the positioning laser. Due to the physical separation of the three layers within the tracker, there was concern that angular misalignment would cause systematic errors. Angular positioning was thus achieved by use of a reflective mirror placed on the front of the PRAVDA

tracker unit. 5 cm of WT1[179] water equivalent build up placed directly in front of the tracker, as per IAEA recommendations[80]. The Linac was tuned and fully warmed up before the investigation, delivering 530 Monitor Units (MU) per minute at 6 MV and 450 MU per minute at 10 MV.

The value of the second electron signal threshold was varied until the resultant profiles in the three planes no longer saturated.

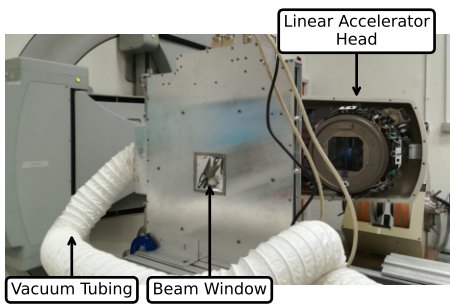


Figure 3.11: Setup of the PRaVDA tracker in an Elekta Synergy linear accelerator.

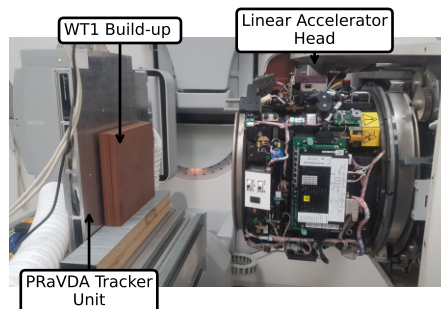


Figure 3.12: PRaVDA tracker positioned at iso-centre with 5 cm of water equivalent build-up.

### 3.5.4 Profiles

The raw profile result for a  $15 \times 15 \text{ mm}^2$  X-ray beam positioned in the centre of the tracker can be seen in Figure 3.13. As with the simulations overlaying acquired frames, the profile has a degree of noise associated with it. The effect of masked strips can be seen in the figure as abrupt drops to half, or zero signal. This is due to the separate strip halves of each SSD responding independently.

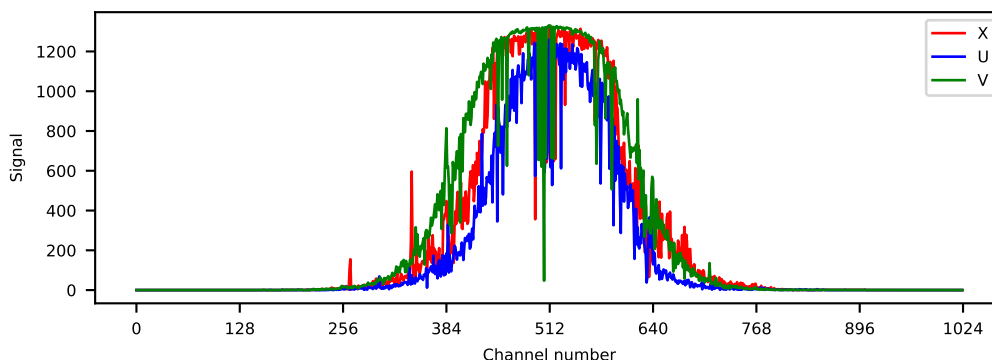


Figure 3.13: Raw profiles acquired from a 6 MV  $15 \times 15 \text{ mm}^2$  X-ray field. The  $U$ -plane is orthogonal to the square of radiation, whilst the  $X$  and  $V$  planes are aligned at an angle.

The FWHM of this beam is approximately 160 strip channels on each plane, 14.5 mm, as expected. Applying a medium rank filter of 15 to all of the planes produces Figure 3.14, where the effect of masked frames or noisy variations is removed.

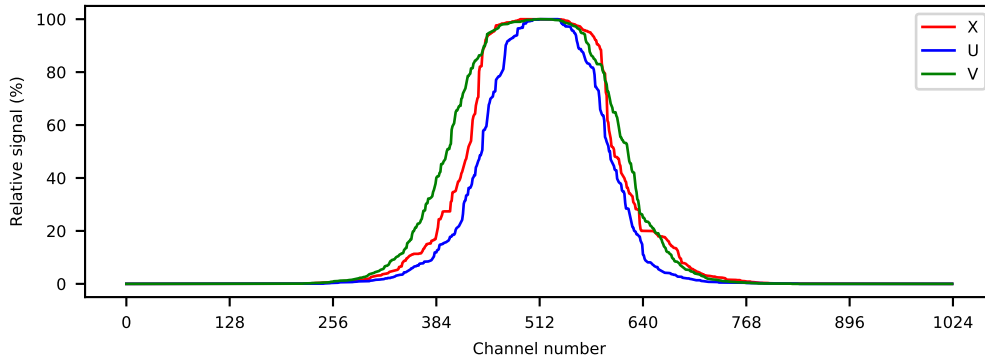


Figure 3.14: Smoothed profiles acquired from a 6 MV  $15 \times 15 \text{ mm}^2$  X-ray field.

### 3.5.5 Pulse detection

The expected temporal dose profile provided by the Linac is composed of short  $3 \mu\text{s}$  long pulses. The number of pulses delivered per second by the Linac, known as the Pulse Repetition Frequency (PRF), is variable and depends on the energy of the radiation being emitted and other treatment parameters. The photon spectra of the Linac was not measured, as this is not a trivial task, but comparisons can be made to prior results in literature[180] as long as the accelerators are dosimetrically matched[181].

The PRaVDA tracker unit was able to detect the 400 Hz pulses from the linear accelerator, as demonstrated in Figure 3.15. By comparing the pulse rate detected by the tracker against radiation pulses from the Linac, it was possible to confirm that the PRaVDA tracker unit was operating at  $6000 \pm 60$  frames per second.

This could be directly compared to a 10 MV beam, which has a PRF of 200 Hz, and can be also seen in Figure 3.15. The dose rate of this beam was a lower 450 MU/min, however each individual pulse deposits approximately 70% more dose. This is reflected in the y-axis of Figure 3.15, where the average number of hits/frame/layer is several times that seen in Figure 3.15 for 200 Hz PRF.

Temporal analysis of the pulses from the Linac reveal that due to the low duty cycle of the beam only approximately 1 in 30 frames had viable data in 6 MV mode that could be used for reconstruction. This decreases to 1 in 60 frames for the 10 MV beam with 200 Hz PRF. This presents a potential issue for a reliable reconstruction of the incident beam, requiring  $30\times$  the amount of frames in order to reconstruct a profile on each plane that is within the gamma passing rate limit of 95%. This issue would be unique to X-ray radiotherapy, and should not be an obstacle in PBT.

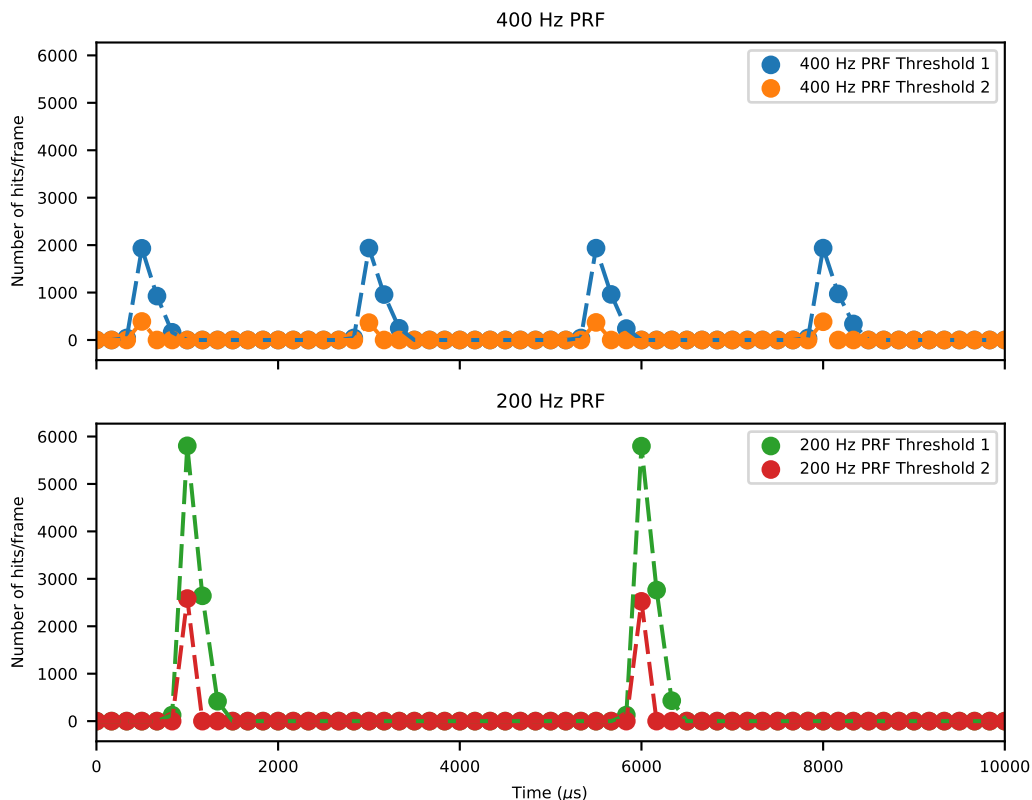


Figure 3.15: Pulses from the linear accelerator, as recorded with the PRaVDA tracker for a 6 MV 400 Hz PRF beam and a 10 MV 200 Hz PRF beam.

### 3.5.6 X-ray Linearity

The linearity of the PRaVDA tracker unit was investigated by changing the dose rate of the Linac. The gun current supplied to the filament was changed, thus reducing the number of electrons per pulse whilst maintaining the number of pulses generated per second. For a  $15 \times 15 \text{ mm}^2$  field the central strip in the  $x$ -plane was studied, using the threshold values determined previously. Dose rate was measured using the Linac’s internal ionisation chamber. The linearity response can be seen in Figure 3.16.

The response was not found to be very linear, showing a saturated response from approximately 70 MU/min. An unexpected feature is the lack of response before approximately 30 MU/min. This is likely due to charge accumulated in that strip in each frame not exceeding the first threshold.

### 3.5.7 Static position reconstruction

To validate the ability of the PRaVDA tracker unit to reconstruct static beam positions, a series of static beams at different beam centres were used.  $15 \times 15 \text{ mm}^2$  square fields were used for this as they are approximately the same size as beamlets in PBS. In the Elekta Synergy model of Linac, the beam is shaped by Tungsten MLC leaves that are 8 cm thick with 1 cm resolution, which is

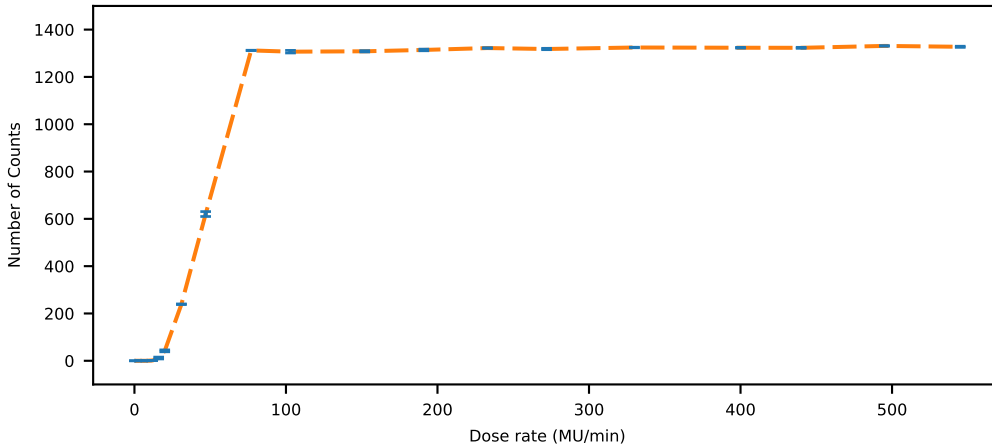


Figure 3.16: Linearity of PRaVDA Tracking Unit in a 6 MV X-ray beam.

supported with a backup diaphragm. To accommodate the desired 15 mm edges, the diaphragm was prescribed to partially shield a nominal  $20 \times 15 \text{ mm}^2$  field to create the desired square shape.

The reconstruction of a beam positioned at the centre of the PRaVDA tracker unit using the *projection* method for increasing number of frames can be seen in 3.17. The beam centre for this full data set was calculated to be (0.28 mm, 0.52 mm). Based on the simulations presented in Figure 3.7, the uncertainty on this can be estimated at less than 0.1 mm.

The ability of the PRaVDA tracker unit to reconstruct beams of smaller sizes was briefly investigated by reducing the size of the field generated by the MLC, maintaining setup and threshold settings. In these measurements, the PRaVDA tracker unit suffered from insufficient signal to varying degrees. Clinically, when delivering a fixed number of MU and changing the field size the measured dose is observed to change in an effect referred to as the "*Output factor*"[182]. The PRaVDA tracker unit is observing this phenomenon, however instead it is the dose rate that is changing.

With this lower dose rate, it was found that the gain tuning of the second signal threshold (previously optimised for the  $15 \times 15 \text{ mm}^2$  field) was no longer suitable. Beam profiles in the *x*-layer acquired by the PRaVDA tracker unit in 1.6 seconds for different beam sizes is shown in Figure 3.18. Beams smaller than the  $15 \times 15 \text{ mm}^2$  reference were found to under respond. Whilst the profile acquired of  $10 \times 10 \text{ mm}^2$  field is Gaussian-like, the number of counts is significantly reduced. Applying a calibration using the linearity measurements to correct for this could not be achieved due to the non-linearity as shown in Figure 3.16. A reconstruction using the  $10 \times 10 \text{ mm}^2$  can be shown in Figure 3.19. In the  $5 \times 5 \text{ mm}^2$ , no signal was acquired in threshold two whilst threshold one was again still found to saturate.

The opposite problem occurs for larger beams, as shown in Figure 3.20, as the overall dose rate in the beams is increased the second signal threshold begins to saturate. Saturation can be

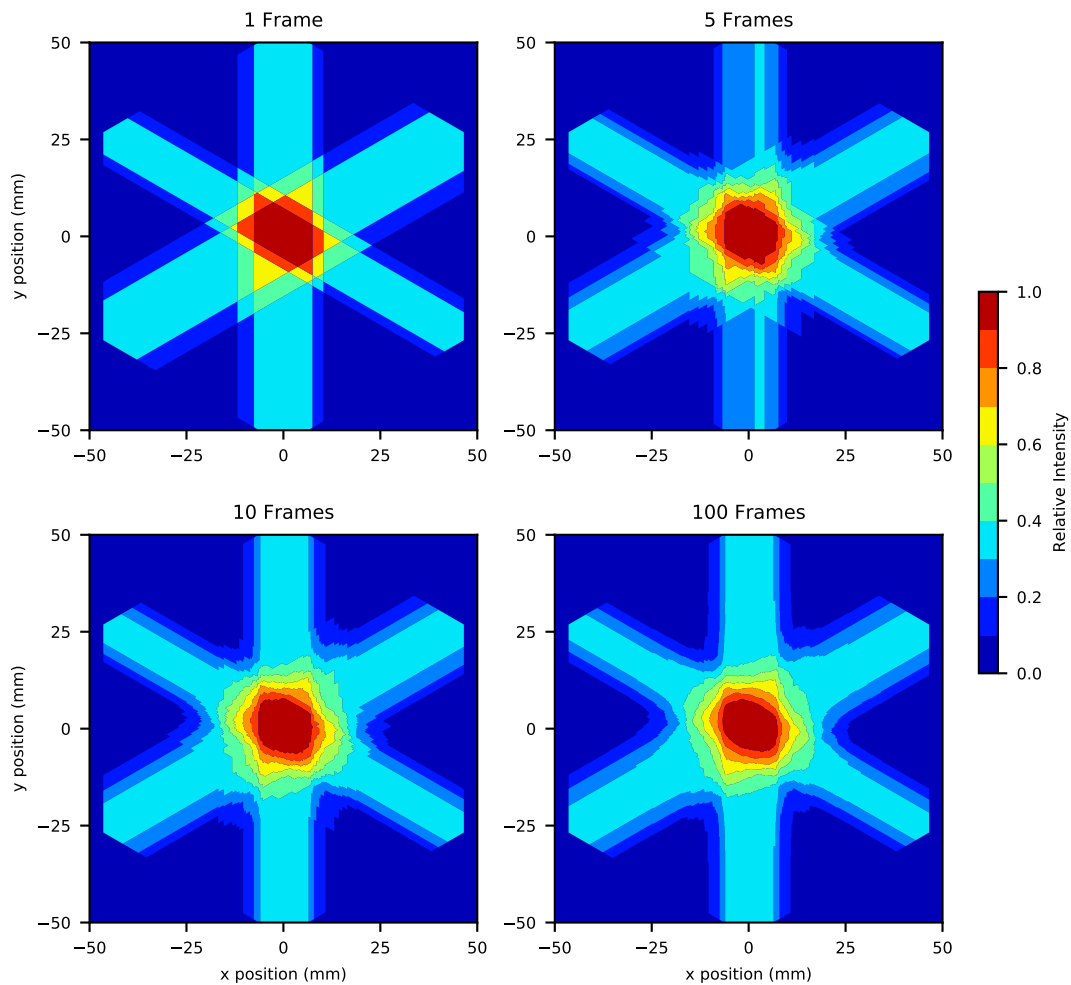


Figure 3.17: *Projection* reconstruction of  $15 \times 15 \text{ mm}^2$  6 MV X-ray field for increasing number of frames.

observed directly in the plane profile as the flat signal with a value corresponding to the number of Linac pulses $\times 2$ , as there are two strip halves per plane.

The significant decrease in signal for the smaller beams is much more prominent than would be expected from prior literature of the output factor. This would suggest that the PRaVDA tracker unit may not be suitable for beam monitoring of X-ray beams without being able to dynamically change the threshold values; however this is unlikely to be an issue for PBS, which do not significantly change size.

Returning to the  $15 \times 15 \text{ mm}^2$  beam, the PRaVDA tracker unit was then exposed with beams of radiation at different positions within the active area, again by changing the MLC configuration and rotating the Linac collimator head. These reconstructed beams at different positions can be seen Figures 3.21, and 3.22. Despite the observed shape of the beam distorting, all beam centres were within 0.1 mm of their prescribed location relative to the beam centred at (0 mm, 0 mm).

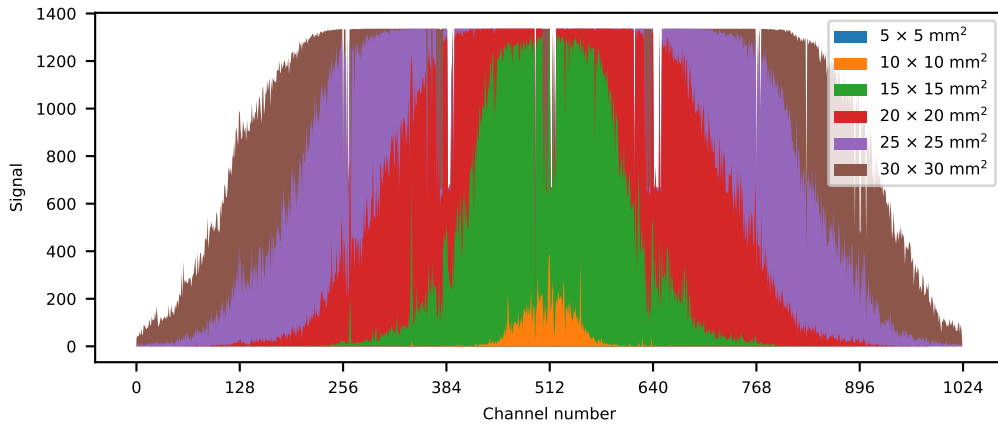


Figure 3.18: Beam profiles as measured by the PRAVDA tracker unit for various X-ray beam sizes.

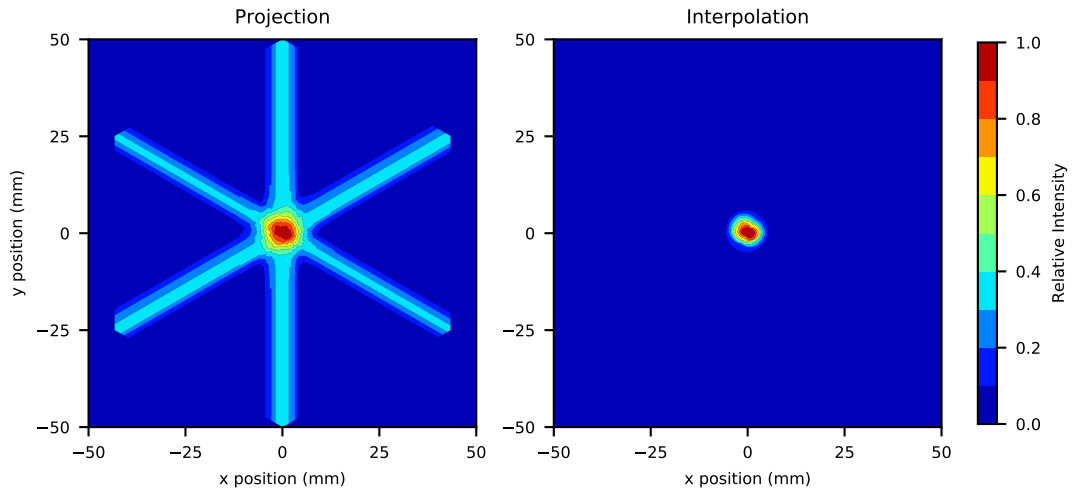


Figure 3.19: Reconstruction of  $10 \times 10 \text{ mm}^2$  6 MV X-ray field.

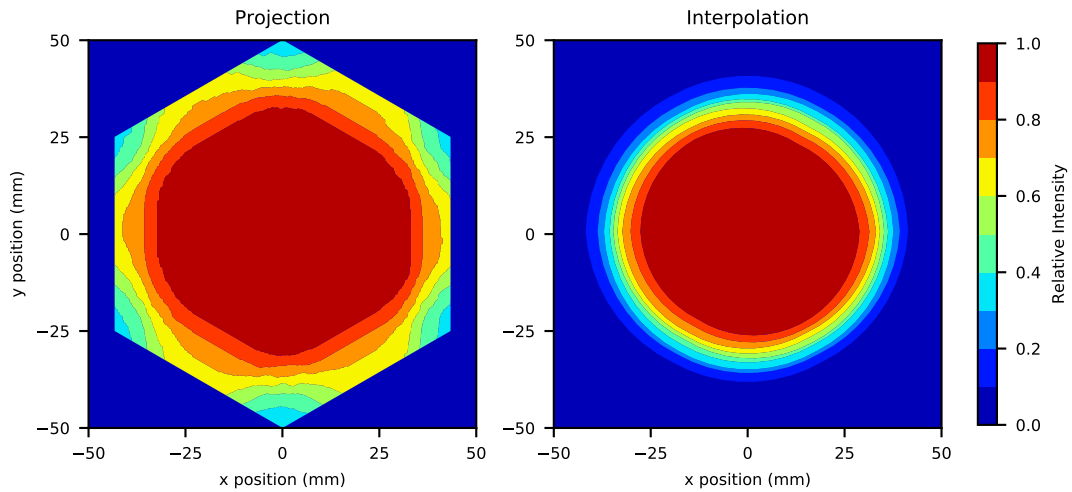


Figure 3.20: Reconstruction of  $30 \times 30 \text{ mm}^2$  6 MV X-ray field.

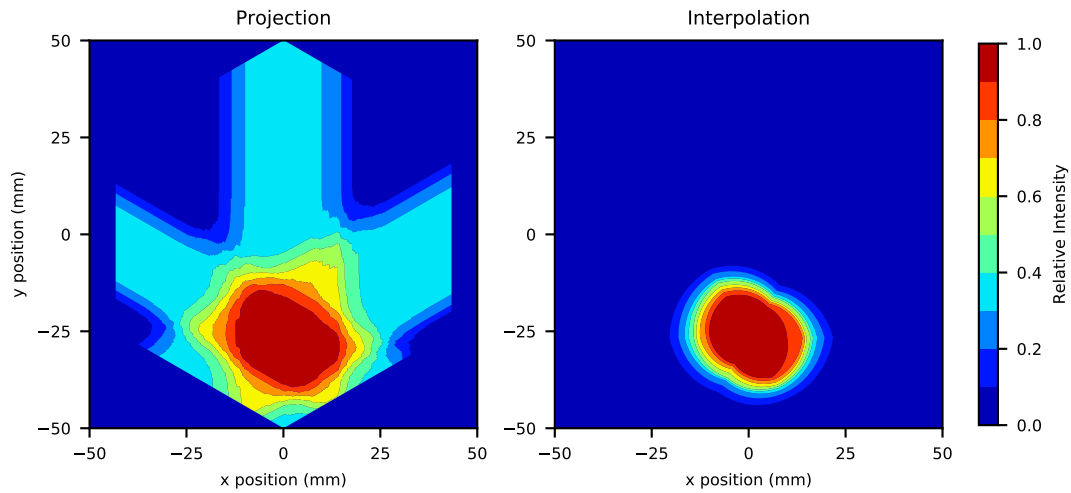


Figure 3.21: Reconstruction of  $15 \times 15 \text{ mm}^2$  6 MV X-ray field positioned at  $(0 \text{ mm}, -20 \text{ mm})$ .

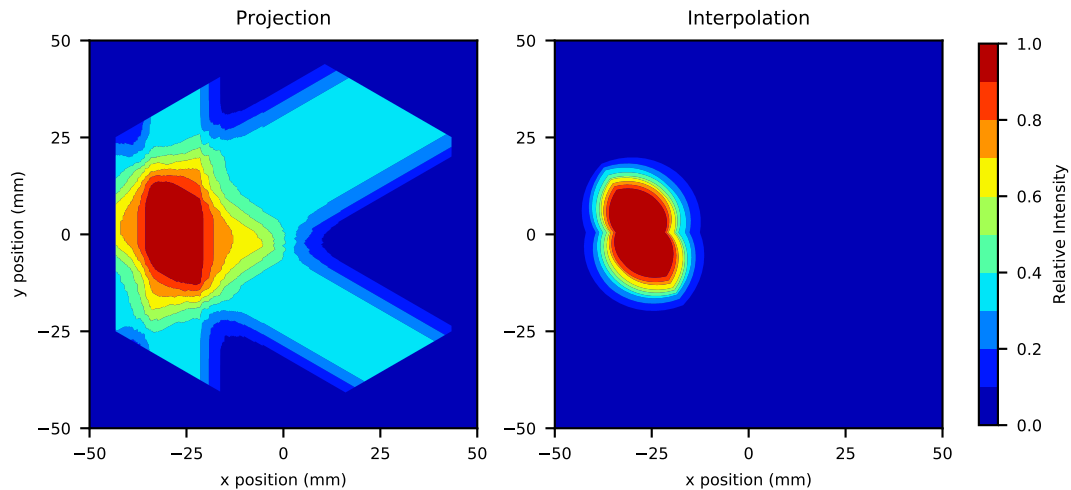


Figure 3.22: Reconstruction of  $15 \times 15 \text{ mm}^2$  6 MV X-ray field positioned at  $(-20 \text{ mm}, 0 \text{ mm})$ .

### 3.5.8 Dynamic position reconstruction

#### 3.5.8.1 Sliding X-ray beam

The first test of dynamic position reconstruction using the PRaVDA tracker unit was moving the MLC of the Linac during beam delivery. This was achieved by using the iCom Customer Acceptance Test (iComCAT) software version 14.0.0.0 (Elekta Ltd, Crawley, UK) to program the Linac to deliver a repeatable moving field. The central pair of leaves from each side of the MLC within the Linac head ( $Y_{120}, Y_{121}, Y_{220}$ , and  $Y_{221}$ ) were programmed to move between  $\pm 60 \text{ mm}$ , creating a  $20 \times 15 \text{ mm}^2$  beam. The diaphragms within the Linac were programmed to follow, making the beam size  $15 \times 15 \text{ mm}^2$  to match previous measurements.

The PRaVDA tracker unit was configured to obtain 10,000 frames as before, however the frames were divided into 25 composites for sequential beam reconstruction, each with 400 frames. In this

configuration each composite would be expected to have 13-14 frames with pulse data from the Linac and as such the estimated position reconstruction uncertainty is of the order  $\pm 0.2$  mm. The rate that the beam moved was controlled by changing the total number of MU was that to be delivered to the target volume, whilst the Linac was configured to deliver the maximum dose rate possible.

Figure 3.23 shows the displacement of the reconstructed beam from the first frame in each acquisition. The relationship between beam position and time is linear, implying that the Linac delivered a uniform dose rate for each measurement. For comparison, the displacement for subsequent frames was calculated for a stationary  $15 \times 15$  mm<sup>2</sup> beam positioned in the centre of the PRAVDA tracker unit.

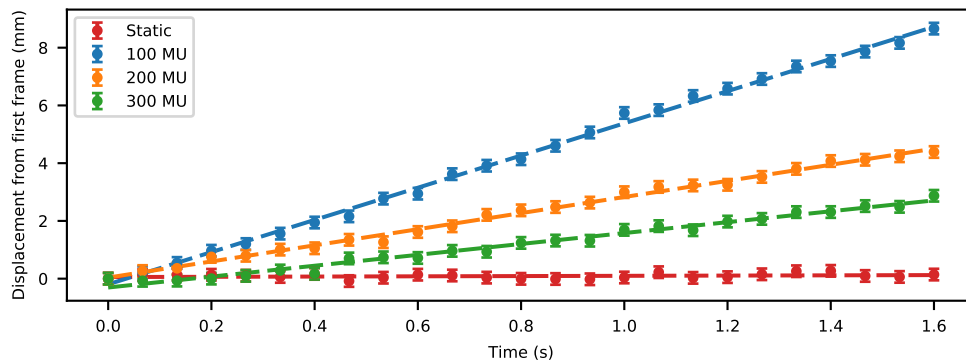


Figure 3.23: Analysis of moving X-ray fields for various prescribed Monitor Units.

It can be shown in Figure 3.24 that there is a linear relationship between the inverse of the calculated beam velocity, a quantity comparable to "Dwell time" in PBS, and the total MU delivered. There is a linear relationship between these points that when extended intersects with the origin. This result is expected, and confirms that the Linac was able to deliver the same dose rate for each measurement.

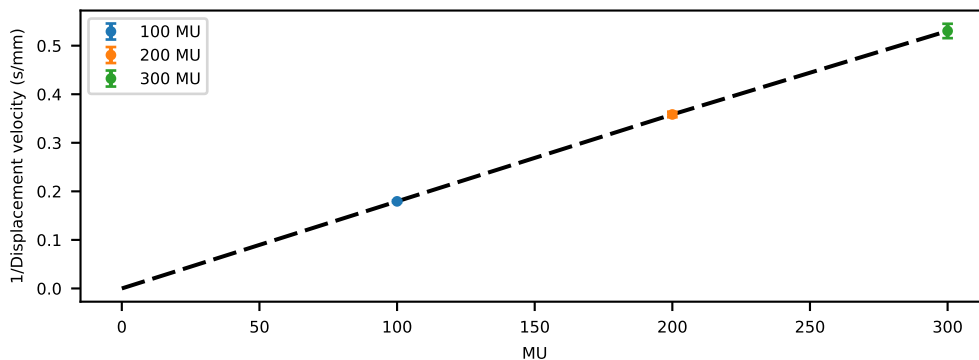


Figure 3.24: Calculation of dwell time calculated for a sliding X-ray beam for different prescribed Monitor Units.

### 3.5.8.2 Rotating X-ray beam

A moving beam of radiation was first achieved by delivering a  $15 \times 15 \text{ mm}^2$  square field offset from the isocentre by a variable distance in one axis. The PRaVDA tracker unit was set to record 10 consecutive samples of 10,000 frames each whilst the Linac head was manually rotated between  $\pm 180^\circ$  without interrupting the beam. The effects of a rotating a beam with offset of 20 and 40 mm can be seen in Figure 3.25, with 400 frames per reconstructed spot (approximately 12-13 frames with data per composite). For comparison, a stationary measurement of a  $15 \times 15 \text{ mm}^2$  beam irradiating (0 mm, 0 mm) was also analysed and used as a reference.

Relative to the stationary beam, the arc of the 20 mm offset beam was determined to be a radius of  $20.14 \pm 0.40 \text{ mm}$ . This relatively large uncertainty is as a result of insufficient frames per composite. For moving beams, this presents a potential issue as whilst more frames per composite could reduce the spatial uncertainty, it would increase the temporal uncertainty. Despite this large uncertainty, there is indeed agreement between the calculated and predicted radius.

The arc of the 40 mm offset beam was determined to be of a radius  $36.81 \pm 0.78 \text{ mm}$ . This is significantly lower than could be expected, and is attributed to the beam profile not being fully captured by the PRaVDA tracker unit layers, as previously predicted. The profile from the sensor becomes clipped at the edge, moving the centroid further inwards.

## 3.6 MC40 Proton beam results

### 3.6.1 Motivation

Further testing was to be performed at the MC40 cyclotron at the University of Birmingham, a particle accelerator capable of accelerating protons between 3-38 MeV. The facility is very suited for research, capable of delivering a large variety of beam currents. The lowest beam currents that can be delivered are typically of the order 1 fA, and correspond to a single proton or less per pulse of the cyclotron whilst the highest beam currents capable are of the order 0.1 mA, for isotopes production.

This facility is of particular advantage for evaluating the PRaVDA tracker unit, due to extensive prior experience in pCT mode for the PRaVDA project.

### 3.6.2 Methodology

The PRaVDA tracker unit was placed on the optical rails in front of the beam nozzle, as shown in Figure 3.26. This allowed the PRaVDA tracker unit to be moved perpendicularly away from the beam nozzle, while ensuring that the sensor is central to the beam. The sensor was positioned at

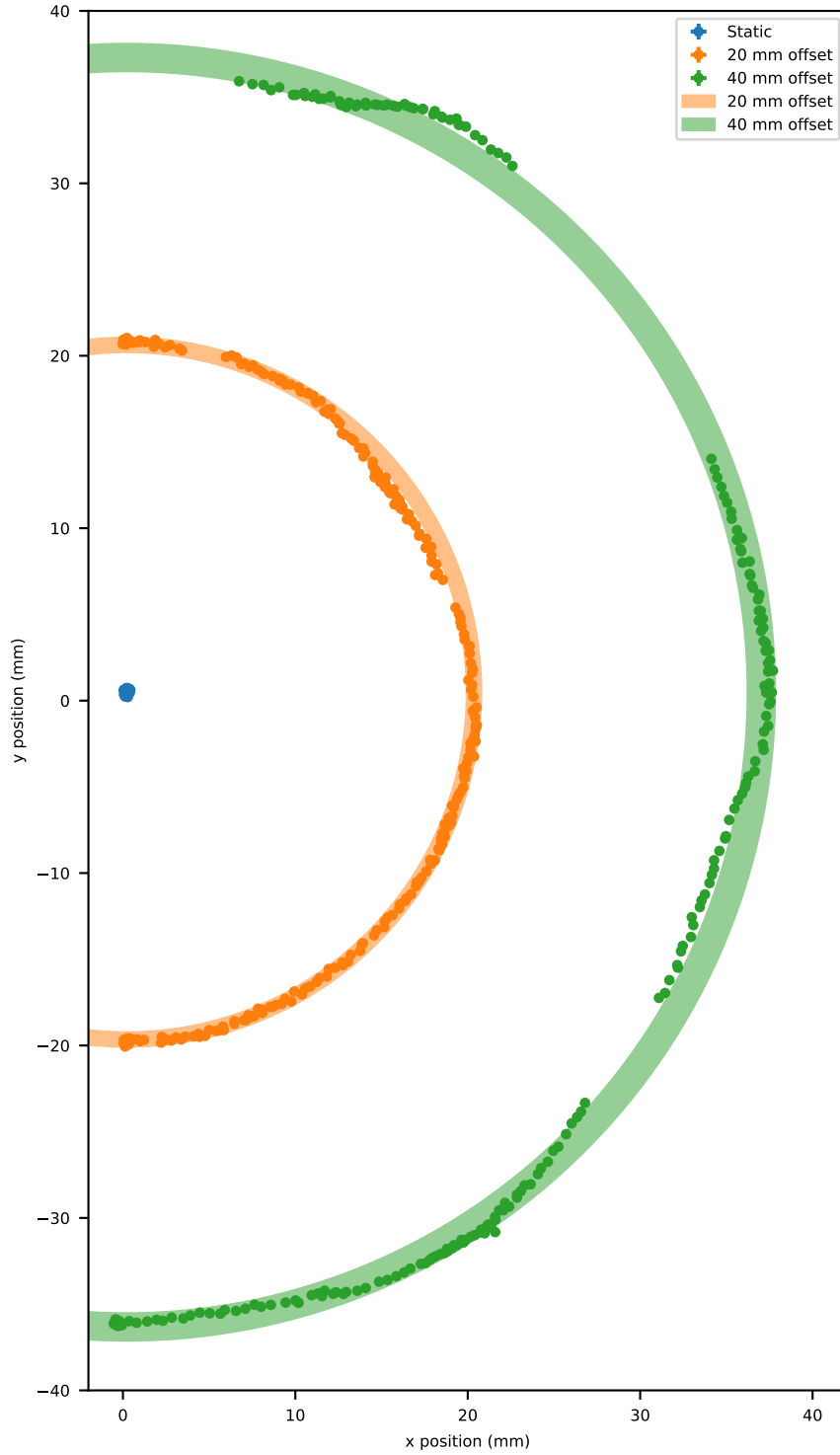


Figure 3.25: Calculated beam centres of a rotating 6 MV  $15 \times 15 \text{ mm}^2$  field for various offset positions.

a distance of 17 cm from the beam nozzle.

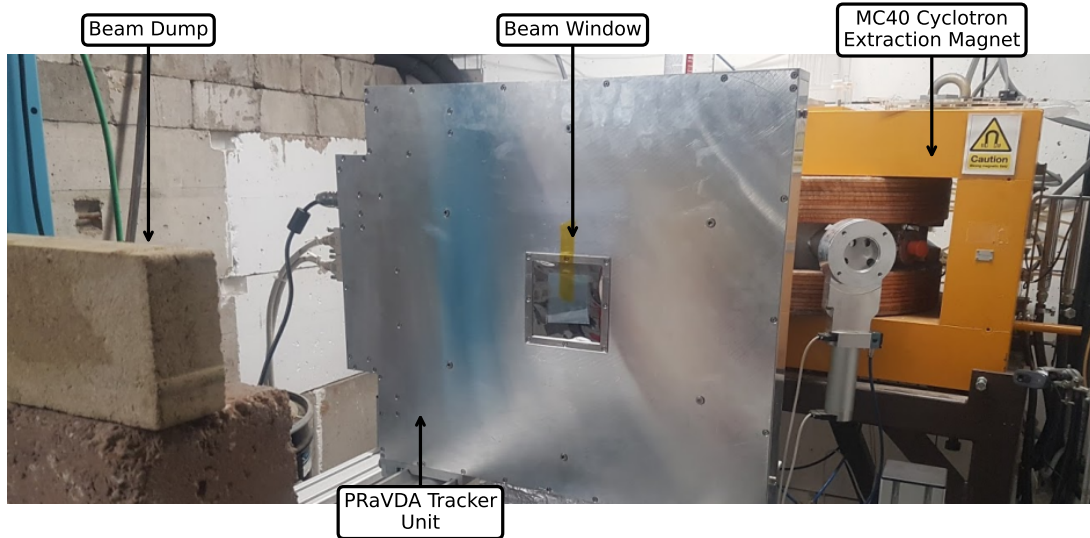


Figure 3.26: Setup of the PRAVDA tracker at the MC40 Cyclotron Facility.

In order to reduce the size of the proton beam, an aluminium collimator was placed on the beam nozzle with a 30 mm diameter. This was supported by a second aluminium collimator with 20 mm diameter aperture placed closer to the PRAVDA tracker unit. The second collimator was placed on a pneumatic piston, enabling the proton beam to move laterally in one direction. A photograph of the setup can be seen in Figure 3.27.

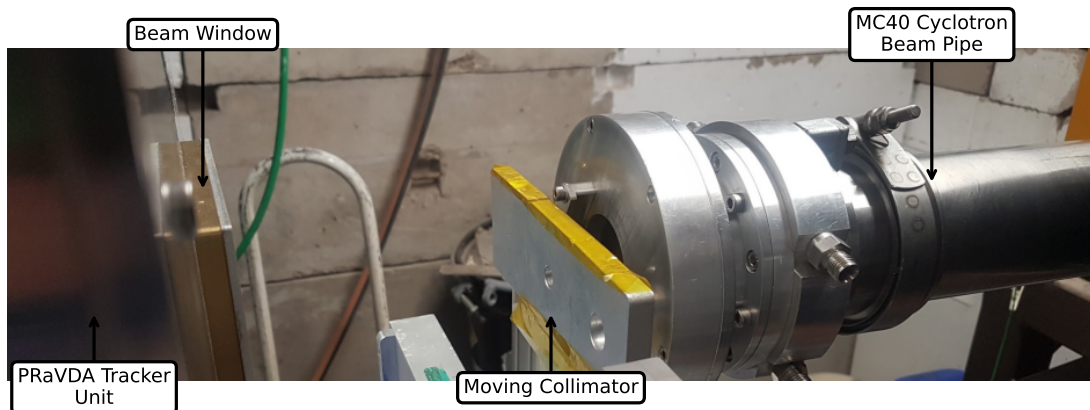


Figure 3.27: Photograph of PRAVDA tracker with moveable collimator.

For a stationary beam, the sensor was exposed to 36 MeV protons with a variety of beam currents evaluated between 0.02 and 0.1 nA in order to assess linearity and detector performance. For a constant beam current of 0.1 nA, the threshold values were again tuned to prevent saturation. Whilst this value is less than proton currents used in clinical environments, it enables the study of the detector without fear of inducing radiation damage.

The linearity of the PRaVDA tracker unit can be seen in Figure 3.28. The response of the detector was significantly more linear than in the previous Linac measurement, an effect attributed to the different interaction properties of protons.

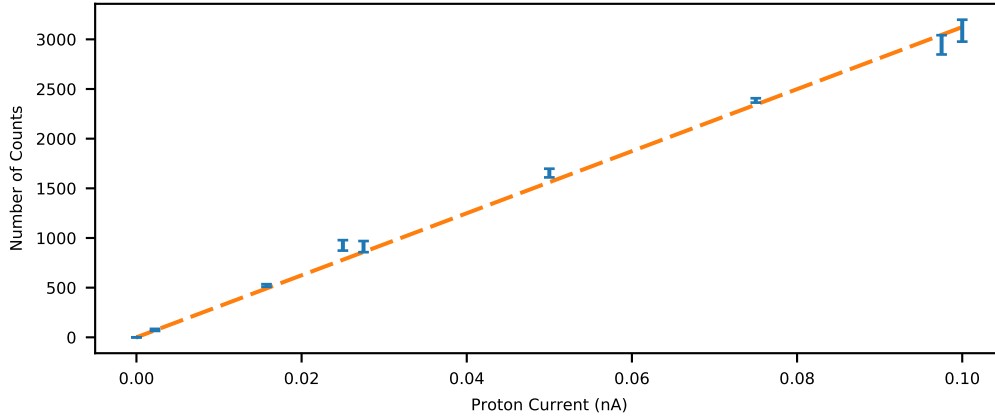


Figure 3.28: Linearity response of the PRaVDA tracker unit in a 36 MeV proton beam.

### 3.6.3 Proton reconstruction

The profiles acquired by the PRaVDA tracker unit for the stationary beam central to be detector can be shown in Figure 3.29. The FWHM of the resultant beam can be estimated at approximately 30 mm using the profiles. This is larger than the collimator, and would be as a result of the low energy protons scattering in the air and geometric divergence.

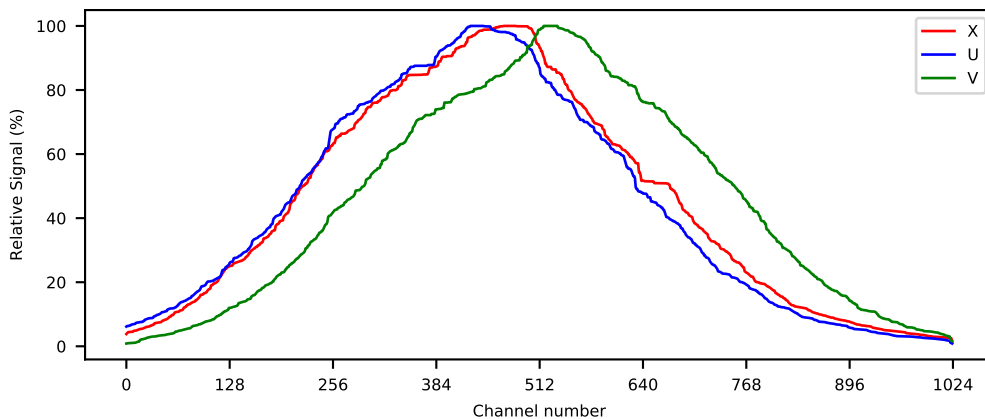


Figure 3.29: Beam profiles as measured by the PRaVDA tracker unit for a 0.10 nA 36 MeV proton beam.

The reconstruction of the proton beam with the 20 mm diameter collimator placed centrally to the PRaVDA tracker unit can be seen in Figure 3.30. The centre of this beam is estimated at  $(-6.30, -4.81 \text{ mm}) \pm 0.20 \text{ mm}$ .

The ability of the PRaVDA tracker unit to record and reconstruct moving proton beams was

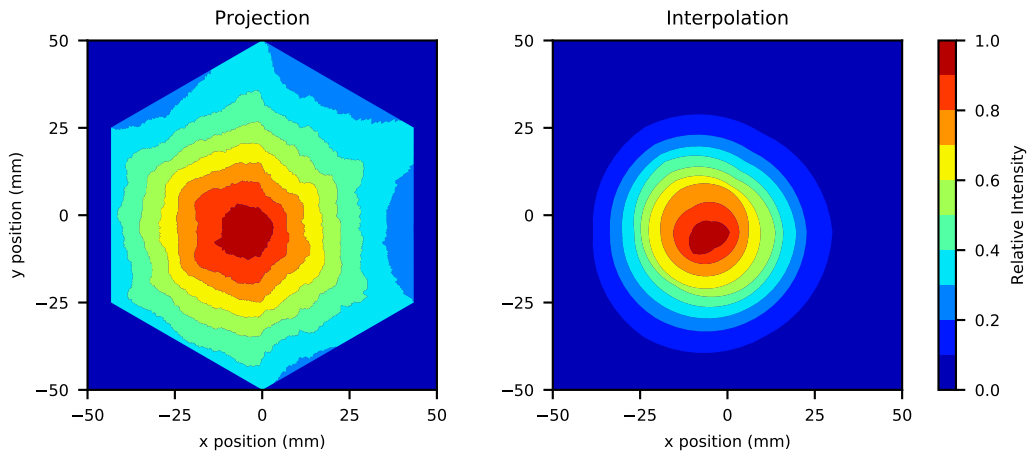


Figure 3.30: Reconstructed images of a 36 MeV proton beam with nominal position of (0 mm, 0 mm).

evaluated by moving the collimator back and forth whilst acquiring data. Building on experience gained for a moving X-ray beam, the number of frames per measurement acquired was increased to 100,000, equivalent to almost 17 seconds.

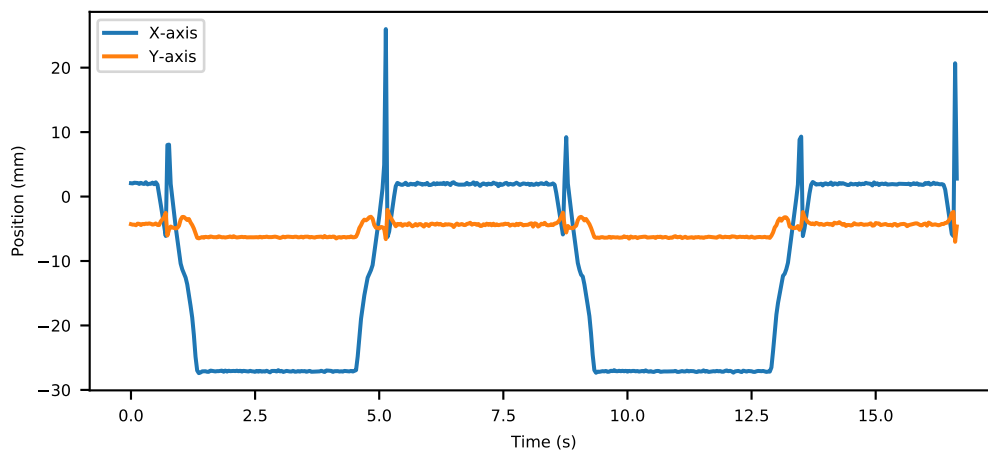


Figure 3.31: Calculated positions of a moving proton beam using the PRaVDA tracker unit.

Figure 3.31 shows the reconstructed  $x$  and  $y$  position. It can be observed that there are regular spikes in the calculated position as the collimator moves to each side. This is likely to be a result of protons scattering off of the edge of the second collimator.

It is possible to determine the speed that the collimator moves by calculating the x-axis gradient whilst the collimator is moving. The speed of the moving shutter could also be estimated by recording the shutter move with a mobile phone, allowing the transition time to be estimated by counting video frames. This method of measuring the speed makes the assumption that the collimator moves exactly 40 mm, with negligible acceleration. A comparison between the speed of the collimator acquired via these two methods can be seen in Figure 3.32. The average speed, as determined

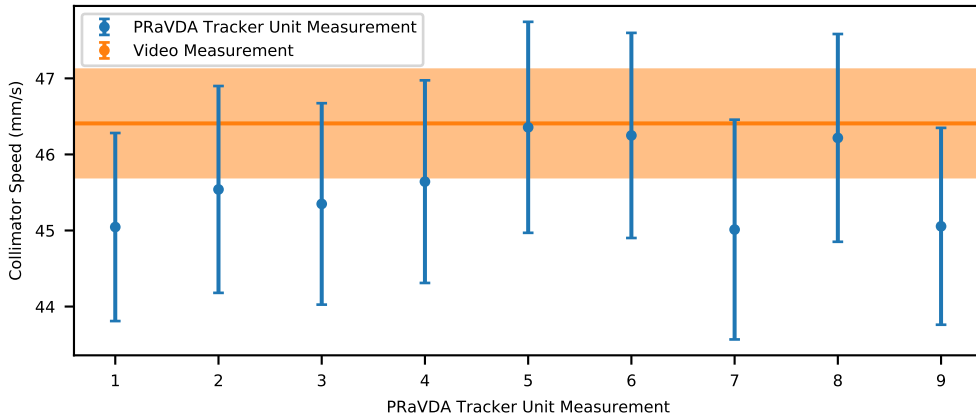


Figure 3.32: Calculation of the speed of a moving collimator using the PRaVDA tracker, compared to video.

by the PRaVDA tracker unit was determined to be  $45.60 \pm 0.45$  mm/s, consistent with that as determined by the video at  $46.51 \pm 0.71$  mm/s.

### 3.7 Discussion

The limitation of the PRaVDA tracker unit requiring an excess of 200 frames in order to reconstruct one dimensional to an acceptable gamma passing rate is not to be underestimated. When factoring in the low duty cycle factor for the Linac (with a PRF of 400 Hz), this indicates that the PRaVDA tracker unit would require approximately 1 second per image. As shown in sections 3.5.7 and 3.5.8, quantifiable data regarding the beam such as beam centre and FWHM can still be extracted on significantly smaller timescales. This highlights the importance of expectation regarding what information can be extracted with the PRaVDA tracker unit when used with the *NPL proton calorimeter*.

With the results obtained thus far, a decision was made to perform a measurement with both the *NPL proton calorimeter* and the PRaVDA tracker unit in a high energy PBS facility. This experiment would have exposed both devices; recording dose deposited on the calorimeter and beam position and intensity with the PRaVDA tracker unit. To prepare for this, the tracker unit was shipped from the University of Birmingham to the National Physical Laboratory. Unfortunately, during shipping damage occurred to 2/3 of the SSD layers, as shown in Figure 2.19, rendering the device inoperable.

Whilst there were remaining PRaVDA tracker unit devices that could still being used to progress this project, they were crucial for other experiments and could not be spared.

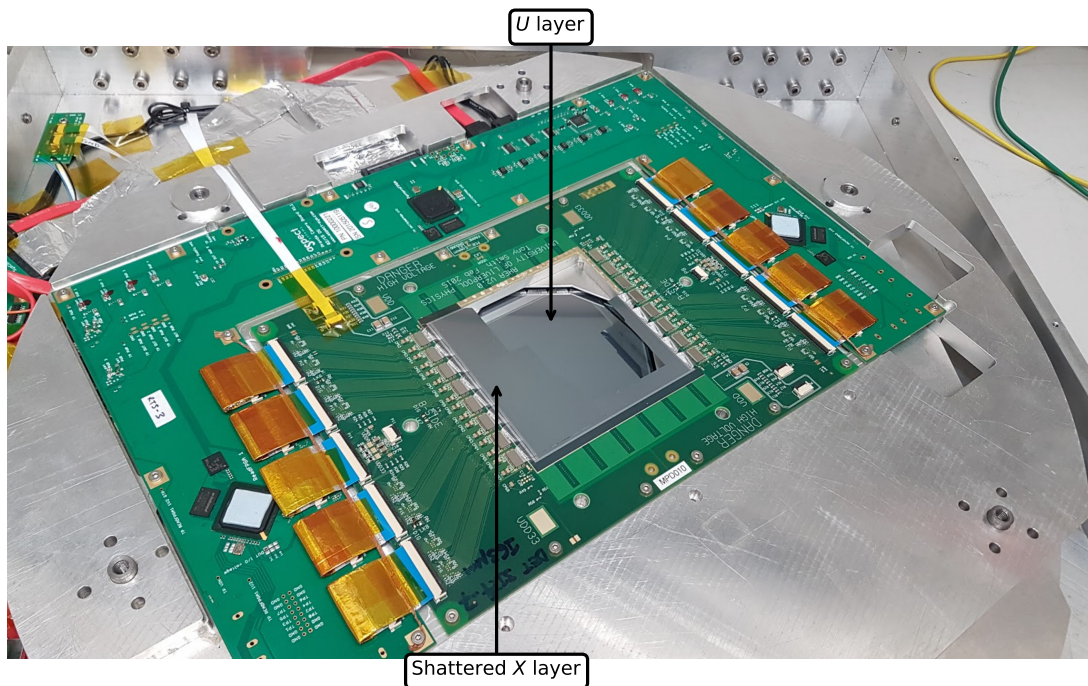


Figure 3.33: Broken Internals of PRaVDA tracker unit.

### 3.8 Conclusion

From prior pCT work, the PRaVDA tracker unit was known to work with protons as can be found in literature. However it has not been used in "treatment mode" before, and with the development of reconstruction algorithms is now capable of providing usable information on proton and X-ray beam locations. As a result, the PRaVDA tracker unit demonstrated itself as a viable candidate for PBS monitoring for use with the *NPL proton calorimeter* as required by this project.

The non-orthogonality of the PRaVDA tracker unit, as required for pCT is likely a hindrance for the therapeutic dose rate monitoring with the third layer becoming superfluous. In addition to increasing equipment costs, the third layer would cause additional energy loss and scattering of the beam. Beam monitoring with two layers of a detector is common in radiotherapy, with devices such as the IC128-25LC-2I device by Pyramid[183][184].

As discussed in this chapter, the PRaVDA tracker unit has many features designed for pCT that are not suited for clinical use. The use of SSD for beam monitoring in PBS is already in use at many facilities around the globe; and whilst they may benefit from the lower pitch of the PRaVDA tracker unit, the three layers would not provide any benefit in their current form.

## Chapter 4

# Characterisation and Evaluation of CMOS detectors

### 4.1 Introduction

To evaluate suitable technologies for monitoring radiation in PBS, it was determined that there should be a comparison of the beam tracking suitability of a technology other than SSD.

For comparison with the PRaVDA tracker unit, a large format CMOS detector was evaluated to determine its suitability for proton beam monitoring as part of this project. After consulting with the CMOS Sensor Design Group at the Rutherford Appleton Laboratory (RAL), who have extensive experience developing radiation hard CMOS sensors for a wide range of applications, a prototype for a newly developed CMOS for medical and scientific imaging was provided.

Unlike SSD technology, a significant advantage of using CMOS would be to be able to measure a 2D dose distribution with no reconstruction required. This would enable it to measure the dose distribution within a proton beam, determining whether it is symmetrical and homogeneous or has non-uniformities.

### 4.2 vM1212 Detector Studies

#### 4.2.1 Detector Characteristics

The supplied CMOS detector was a vM1212 pixelated detector, which was based on the "*LASSENA*" sensor which was developed by RAL[185], and then licensed and manufactured into a full detector assembly by vivaMOS Ltd[186], now incorporated into Nordson DAGE[187]. A photograph of the vM1212 detector sensor can be seen in Figure 4.1.

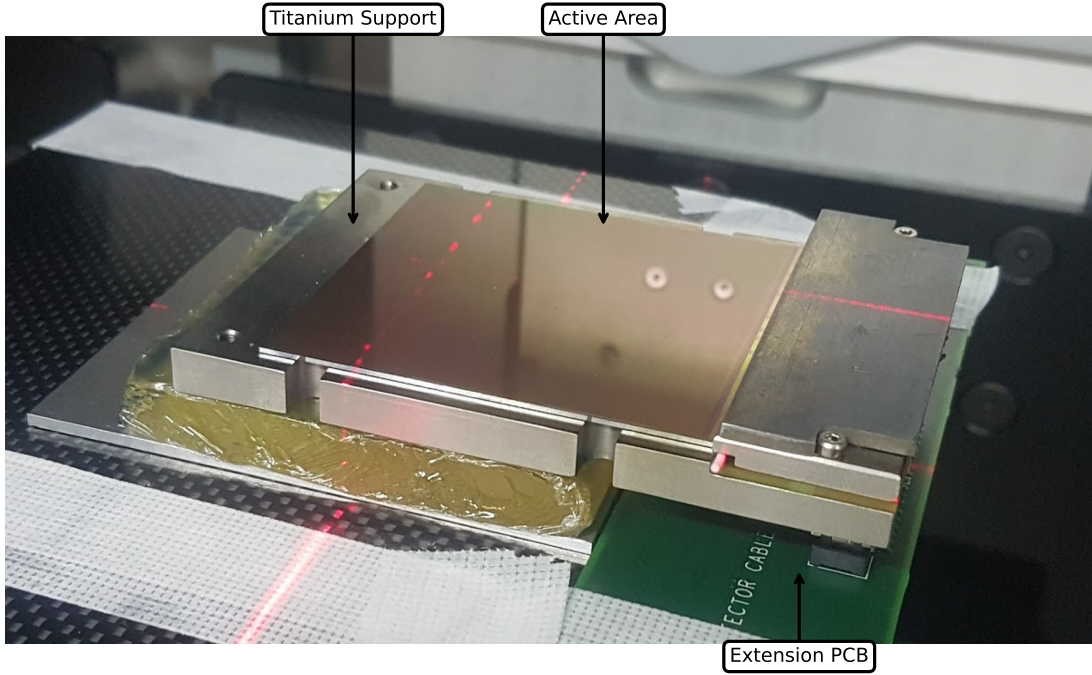


Figure 4.1: Photograph of the vM1212 Detector.

The vM1212 detector has a pixel pitch of  $50 \mu\text{m}$  and sensitive area of approximately  $6 \times 6 \text{ cm}^2$ . The pixels were designed to be tolerant against ionising dose, which was achieved by arranging the internal layout of the pixels as recommended by Snoeys *et al.*[188]. The pixel are of the "3T" design and as such lacks a global shutter. A list of the specifications of the detector can be seen in Table 4.1.

Name	Quantity	Units
pixel pitch	50	$\mu\text{m}$
resolution	$1204 \times 1248$	pixels
active area	$60.2 \times 62.4$	$\text{mm}^2$
minimum integration time	28.3	ms
maximum frames per second	35.3	Hz
water equivalent thickness	$\approx 1.5$	mm

Table 4.1: Specifications of the vM1212 Detector.

The detector was composed of a PCB and sensor, which connect together back to back. For low energy diagnostic imaging, a 2 mm thick lead plate can be placed between the two components to shield the PCB from radiation damage. This is not ideal for this project however, as the PCB would be exposed to damaging high-energy radiation capable of penetrating the shielding, so a pair of extension PCBs are used to separate the detector sensor and control PCB. These extension boards were provided by RAL, with an extension board visible in Figure 4.1.

The sensor was glued to a titanium support approximately 5 mm thick. This amount of material would severely impact incident proton beams to the *NPL proton calorimeter* with a non-trivial

amount of beam energy lost, whilst inducing a large amount of scatter. To overcome this, a small square of approximately  $4.5 \times 4.5 \text{ cm}^2$  was removed with the sensor only supported at the edges. As with the PRaVDA tracker unit, this is not large enough to cover a  $10 \times 10 \text{ cm}^2$  reference field for use with the *NPL proton calorimeter* but would fully capture beams irradiating the calorimeter core and facilitate preliminary testing. A photograph of the beam window can be seen in Figure 4.2.

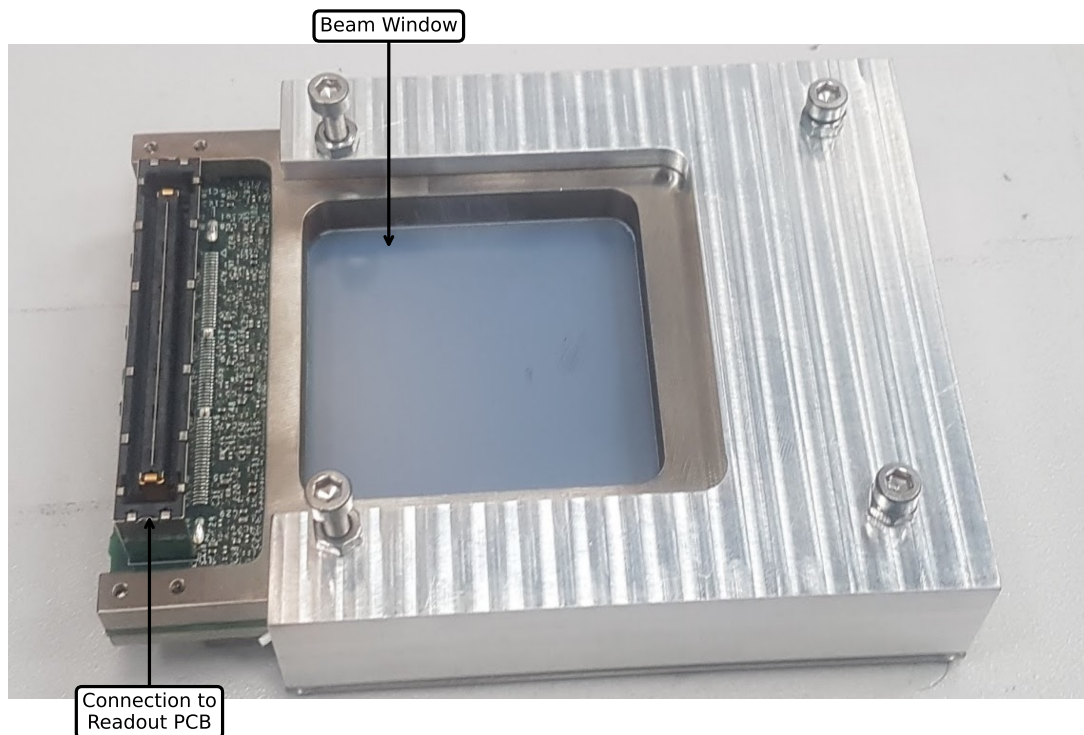


Figure 4.2: Photograph of the beam window of the vM1212 Detector.

The vM1212 detector obtains frames at a rate higher than it is able to transmit them to a controlling computer. When this occurs, the untransmitted data is stored in volatile memory on the detector while it waits to be transferred. This storage is however finite and it is possible to exceed it, causing the device to crash. The result of varying the integration time against maximum acquisition time (defined as  $N_{frames} \times t_{integration}$ ) is shown in Figure 4.3. As all the transferred files are the same size in memory, this relationship was found to be independent of the signal acquired by the detector. For the minimum acquisition time of 28.3 ms, the maximum continuous acquisition time was approximately 11 seconds, or approximately 370 frames before this memory was filled. Increasing the integration time per frame increased the maximum acquisition time, owing to the detector having longer to transmit each frame and there being less frames per second. The results of a small investigation demonstrating this can be seen in Figure 4.3, where a positive but non-linear relationship can be shown.

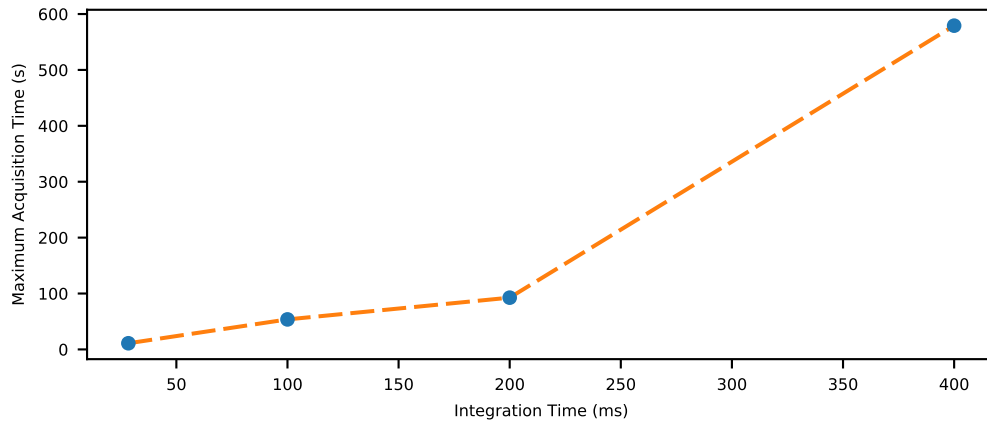


Figure 4.3: Maximum acquisition time of the vM1212 Detector as a function of integration time.

## 4.2.2 Microbeam Dosimetry Investigations

The combination of high spatial resolution, high dynamic range of the pixels, and predicted radiation tolerance of the device suggested that the vM1212 detector was a viable candidate for dosimetry in Microbeam Radiation Therapy (MRT). MRT is a novel type of radiation therapy in which narrow beams of radiation selectively irradiate portions of the target volume[189]. Preclinical studies have indicated that this modality has greater efficacy than conventional radiotherapy using a single uniform radiation field[190]. The reason for this is not currently fully understood, but mechanisms under investigation are the preferential damage to vascular tissue in tumours[191][192][190], radiation-induced bystander and abscopal effects[193][194], and chemical interactions[195].

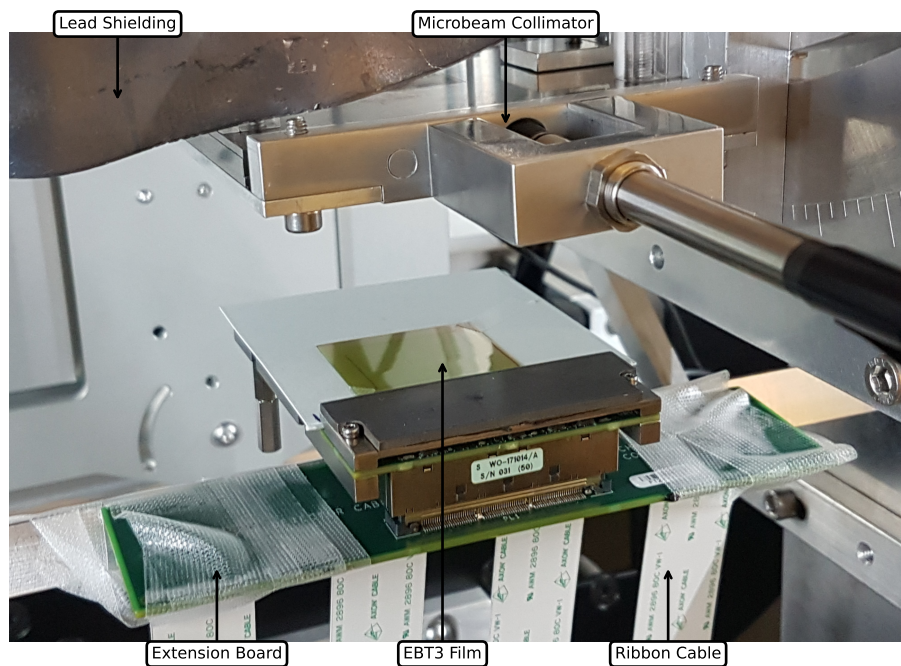


Figure 4.4: Photograph of the vM1212 Detector during the X-ray microbeam investigation.

An investigation was conducted to evaluate the vM1212 detector at the Technical University of Munich, Germany, in collaboration with colleagues from the NPL. This facility has developed a Tungsten microbeam collimator capable of generating 220 kV X-ray microbeams through nominal slit widths between 0 - 100  $\mu\text{m}$ . For comparison to radiochromic film, the current gold standard for microbeam dosimetry, a small piece of film was placed directly on top of the detector allowing simultaneous exposure to microbeam radiation. Figure 4.5 shows microbeam profiles at 100  $\mu\text{m}$  nominal slit with acquired with the vM1212 detector and Gafchromic film (scanned with two methods). The vM1212 detector was calibrated against a PTW 30012 ionisation chamber, quantifying the response of both instruments as a function of beam current and thus dose. It was found that for the minimum integration time, the maximum beam current of 5 mA did not fully saturate the pixels, although the non-linearity had to be accounted for. The quantity dose rate was used for consistency throughout this investigation as the EBT3 radiochromic film[196] required substantially longer to acquire a measurement than the CMOS sensor.

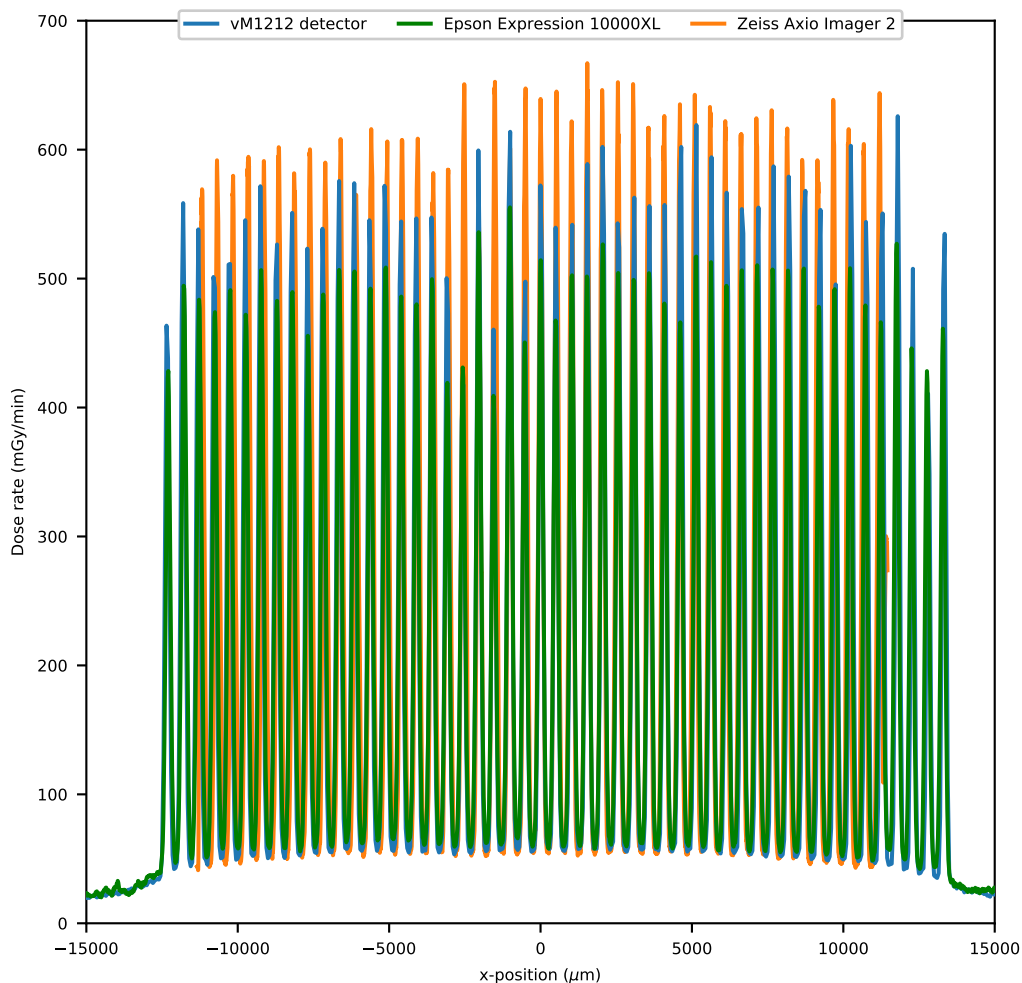


Figure 4.5: Microbeam Profiles acquired for 100  $\mu\text{m}$  nominal slit width.

In this experiment, it was found that the CMOS detector was capable of resolving microbeam

peaks and valleys at a level comparable with EBT3 Gafchromic film. An example of a 2D profile, again with 100  $\mu\text{m}$  nominal slit width, obtained with the vM1212 detector can be seen in Figure 4.6. Acquired microbeam parameters (FWHM, PVDR, peak to peak separation) were comparable to EBT3 film. This research was published in the journal "The International Journal of Medical Physics Research and Practice"[197], with a copy included in Appendix B.2.

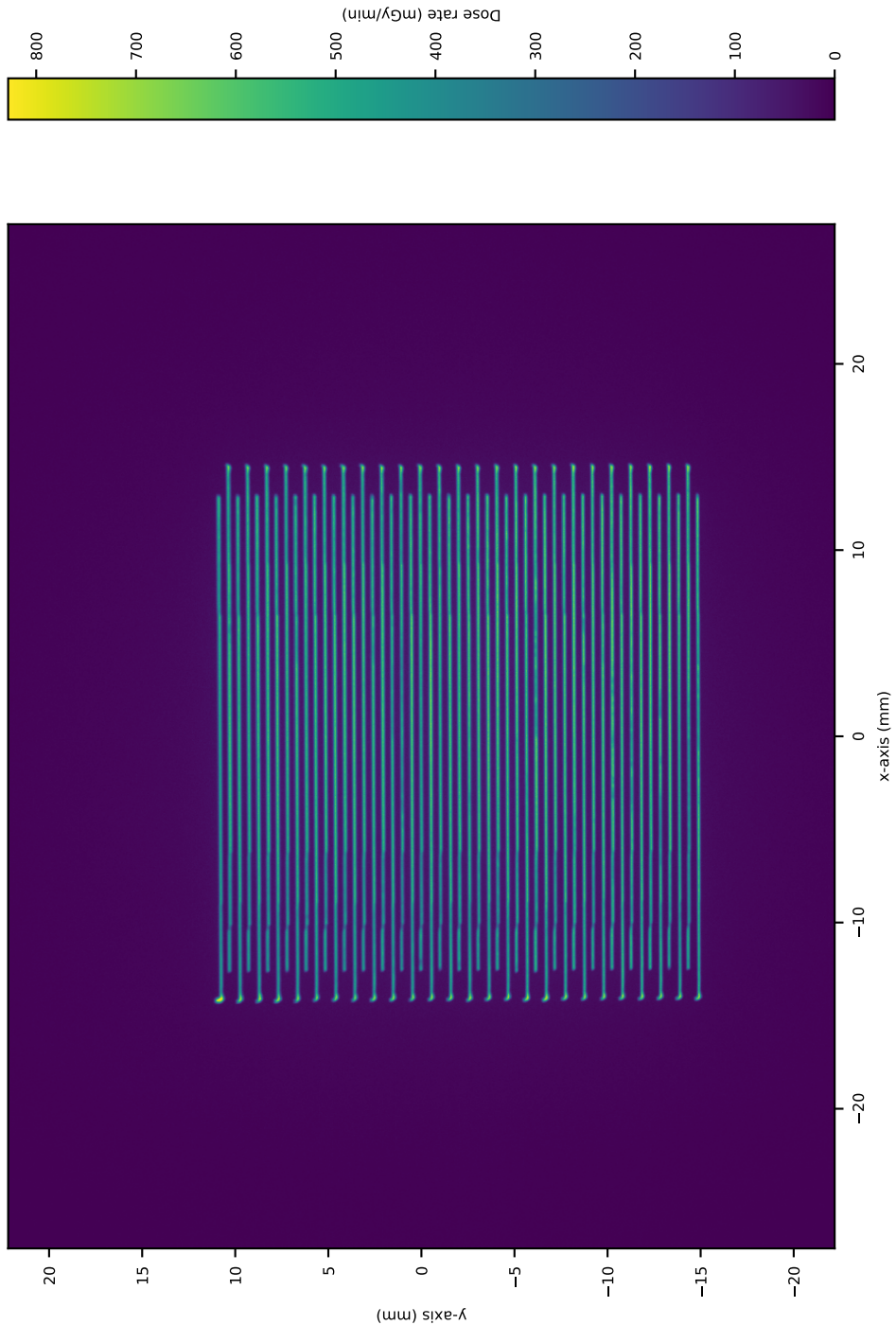


Figure 4.6: Two Dimension Microbeam Profile acquired using the vM1212 detector.

In addition to this, further analysis of the data acquired for dynamic frames, in which the

nominal slit width changed during a measurement, was possible. It was found that the vM1212 detector was capable of performing analysis on single frames, acquiring the microbeam specific parameters in a two dimensional space at a rate impossible with radiochromic film. Due to the limitations of the beam delivery system it was not possible to change the nominal slit width of the microbeam collimator other than in a single direction, however the linear change in FWHM indicated that the system was working as expected. Unfortunately, this analysis was performed with a low performance laptop and as a result the maximum acquisition time was limited to less than 4 seconds, limiting the amount of data that could be collected in a given run. It was concluded from this analysis, that it could be possible to use a CMOS detector for real-time dosimetry in MRT in the future. This research was published in the journal "Nuclear Instruments and Methods in Physics Research Section A"[198], with a copy included in Appendix B.2.

### 4.3 vM2428 Detector Studies

#### 4.3.1 Detector Characteristics

The vM2428 detector is the second generation of the LASSENA CMOS detector and developed by vivaMOS Ltd[186]. A photograph of this device can be seen in Figure 4.7.

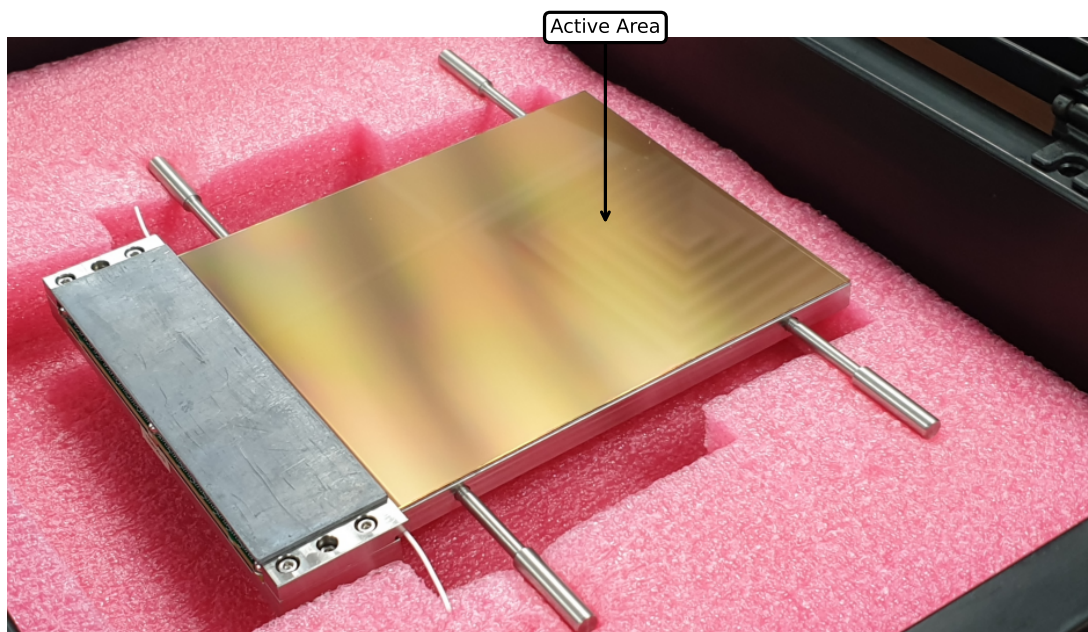


Figure 4.7: Photograph of the vM2428 Detector.

This device extends the capabilities offered by the vM1212 detector with a larger active area and dynamic range. Like the vM1212 detector, the vM2428 detector was also manufactured in two separate parts; the sensor and control PCB. Unlike the vM1212 detector, these could be separated

by an off-the-shelf cable purchased from Samtec[199], omitting the requirement for an extension PCB.

Using the linear Full Well capacity of  $112000\text{ e}^-$ [185], it becomes possible to estimate that in a 225 MeV proton beam with a flat (non-Gaussian) beam with a 8 mm FWHM the vM1212 detector will saturate at less than 1 nA of proton current. When taking into account that real proton beams will be Gaussian-like, the proton current required to cause saturation in the centre of the beam will be even lower. This is too low for clinical therapies which typically operate at 20-40 nA proton current for therapeutic beams, but is close enough that with sufficient accommodations it could be overcome.

The vM2428 detector introduced "high dynamic range" mode which reconfigured an internal capacitor in each pixel to increase the amount of signal that can be acquired by factor of approximately 10. In addition, the vM2428 detector implemented Region Of Interest (ROI) selection which when enabled could allow lower integration times to be used. In addition to increasing the frame rate of the detector, this can be used to reduce the amount of dose deposited in each pixel per frame to overcome saturation, getting closer to clinical proton beam currents.

A curated list of the specifications of the vM2428 detector can be seen in Table 4.2.

Name	Quantity	Units
pixel pitch	50	$\mu\text{m}$
resolution	$2400 \times 2800$	pixels
active area	$120 \times 140$	$\text{mm}^2$
minimum integration time (full frame)	28.3	ms
minimum integration time (region of interest)	$\approx 0.1$	ms/row
maximum frames per second (full frame)	35.3	Hz
water equivalent thickness	$\approx 1.5$	mm

Table 4.2: Specifications of the vM2428 detector.

Before measurements with radiation, the uniformity of the vM2428 detector needed to be evaluated<sup>1</sup>. This was performed using a large uniform lightbox, previously used at NPL for diagnostic studies of ionisation chambers prior to repair. This lightbox did not have variable light intensity, and was found to cause pixel saturation on even the lowest full-frame integration time. To reduce the signal acquired on the detector, layers of high quality printing paper were added. In addition to reducing the intensity of the light, this caused increased diffusion of the light and would further improve the uniformity of the light. The average relative response of the columns and rows in the vM2428 detector can be seen in Figure 4.8.

Several notable features could be observed in the flat-field response. The x-axis is not uniform, showing a distinct profile across the detector as a result of the stitching blocks. The y-axis is more uniform, only changing rapidly at the edges however there is a distinctive pattern between odd and

<sup>1</sup>This was measured for the vM1212 detector by James Kendrick of the University of Birmingham, but was not used in the microbeam investigation and is thus omitted from this thesis.

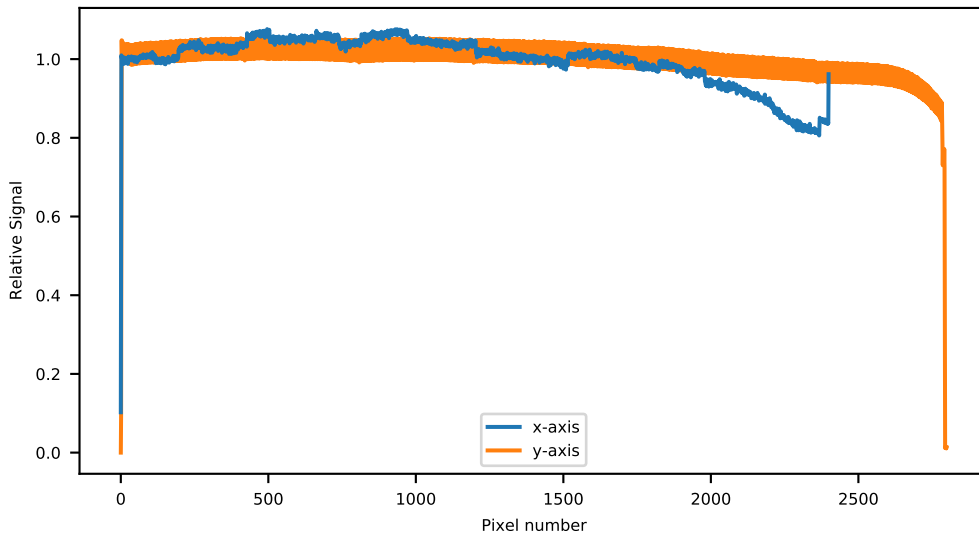


Figure 4.8: Flat Field response of the vM2428 Detector.

even rows. This is a result of the detector using two different ADCs to increase the readout rate of the detector. This results in slightly different responses (typically less than 5%) between odd and even rows. Both of these traits can be corrected by dividing a standard dark corrected frame by the relative response acquired from the lightbox using Equation 4.1. The corrected frame ( $C$ ) is a function of a raw frame ( $R$ ), a dark frame ( $D$ ), and the lightbox flat measurement ( $F$ ).

$$C = (R - D) \star \left( \frac{F - D}{\langle F - D \rangle} \right)^{-1} \quad (4.1)$$

### 4.3.2 Preliminary Evaluation in a Linear Accelerator

The vM2428 detector was placed in the Versa HD Elekta Linac at the NPL. This Linac has twice the number of leaves in the MLC as the Synergy used previously, with 5 mm leaf pitch, otherwise it has very comparable characteristics. Using this model of Linac enables the use of 6 MV FFF beams, in addition to conventional 6 MV, which provides the higher dose rates closer to those of PBS. This Linac would have a similar spectrum to that discussed previously in Section 3.5.2.

The detector was placed flat on the treatment couch at the isocentre, with the control PCB physically separated to prevent radiation damage. 4 cm of plastic was required to lift the detector from the treatment couch in order to facilitate the right-angled cables to the PCB. A thin plastic box was placed over the instrument, to provide physical protection, with blackout fabric[200] placed on top. This was necessary to minimise signal generation from visible light, which the vM2428 detector is especially sensitive to. A photograph of the device without the blackout fabric can be seen in Figure 4.9.

With this setup, the vM2428 detector's high dynamic range mode was enabled for investigation.

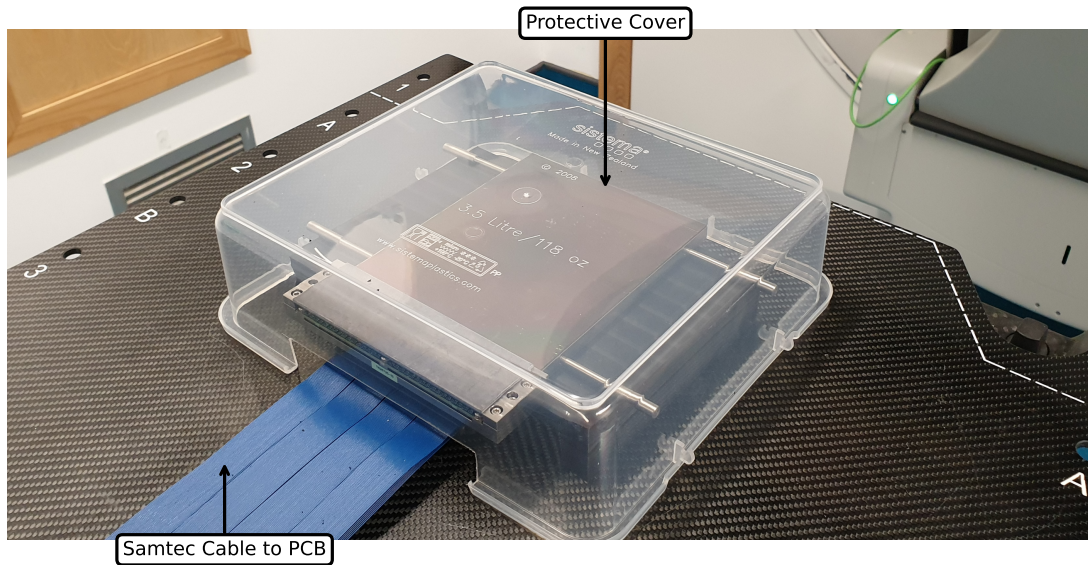


Figure 4.9: vM2428 detector setup on treatment couch in Elekta Versa HD Linac for X-ray studies.

This study was required, after it was determined that using the manufacturer’s recommended  $V_{pixel}$  settings there was dark current suppression. The sensor was irradiated with a  $10 \times 10 \text{ cm}^2$  6 MV FFF field, with a minimum integration time selected of 28 ms. Non-destructive read mode was enabled, in which groups of 14 consecutive frames could be acquired without destroying the charge of each pixel. In this mode, it is possible to rapidly evaluate the linearity of the CMOS pixels for various internal voltage configurations. This can be seen in Figure 4.10, where changing  $V_{pixel}$  appears to have minimal change on the shape of the pixel response but does appear to change the dark current offset of the device. Whilst the manufacturer’s recommended  $V_{pixel}$  value of 3.1 V was taken into consideration, it was found that in such a configuration the device would not acquire signal below a certain threshold. This would manifest as losing the penumbra or low intensity regions of exposed beams, as well as preventing a dark frame to be properly acquired. The internal pixel voltages of 2.8 V were selected for further investigation, as a compromise between minimising the charge threshold and maximising the overall range of the detector.

Following from this, a versatile mounting setup was created. The primary function of this is that it would enable predicable positioning with the *NPL proton calorimeter*, but in addition would enable the vM2428 detector to conduct horizontal beam tests. In this configuration, the vM2428 detector was suspended vertically with the PCB held above the active area, physically separating it from most of the radiation. The surface of the vM2428 detector was placed at the isocentre of the Linac, at 100 cm SSD. Mirrors were used on the front and back of the detector to align the plane of the detector such that it is orthogonal to be incident beam. Finally, to prevent light contamination black-out fabric[200] was placed over the detector and the room lights were

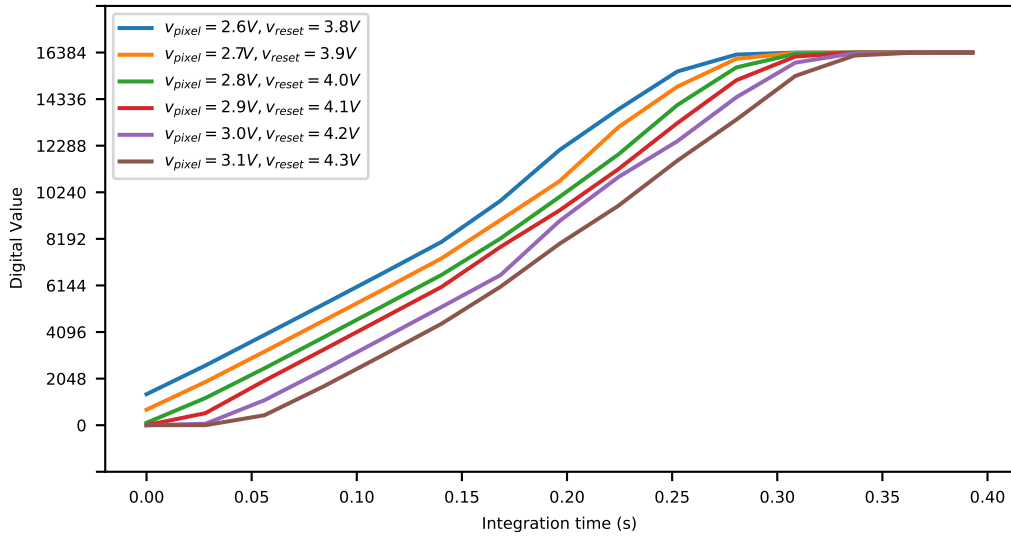


Figure 4.10: Investigation of  $v_{pixel}$  response of vM2428 detector in a 6 MV FFF beam.



Figure 4.11: vM2428 Detector setup in Elekta Versa HD Linac for Horizontal Beam Tests.

turned off. The full setup can be seen in Figure 4.11.

For the above selected determined pixel voltage configuration, the linearity at a fixed integration time of 28 ms was then investigated with and without WT1 water equivalent build-up material[179]. This was performed by changing the electrons per pulse generated by the Linac, in the same process as for the PRaVDA tracker unit in Chapter 3. As with the voltage study, the detector was irradiated with a  $10 \times 10 \text{ cm}^2$  6 MV FFF beam. 5 cm of WT1 material was placed in front of the detector to cause radiation build-up. The results of this can be seen in Figure 4.12.

The response of the detector with and without build-up was found to be very linear. Regardless, a third order polynomial function (Equation 4.2) was used to convert the dark corrected digital value ( $y$ ) to the calculated dose per frame of the detector ( $x$ ). The ratio between with build-up

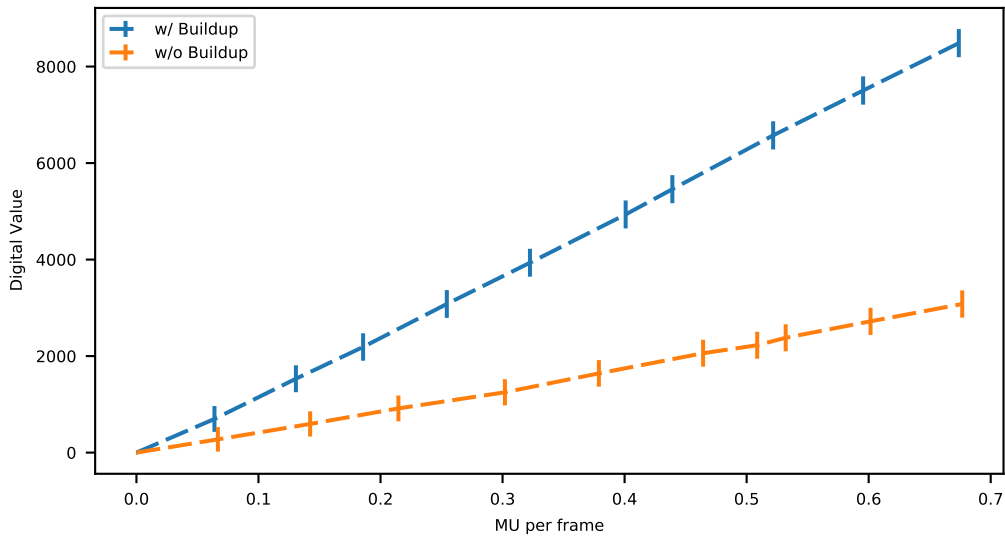


Figure 4.12: Comparison of vM2428 detector response with and without 5 cm of water equivalent buildup in a  $10 \times 10 \text{ cm}^2$  6 MV FFF field.

and without is approximately  $\frac{1}{3}$ , consistent with previous PDD measurements conducted on this Linac as shown previously in Figure 2.4.

$$x(y) = ay + by^2 + cy^3 \quad (4.2)$$

An example of instantaneous frames for various 6 MV field sizes with build-up can be seen in Figure 4.13. The presence of horizontal bands across the detector is a result of a rolling shutter artefact. As expected, the measured signal on the vM2428 detector increased with the area of the field. Unlike with the PRAVDA tracker unit described in Chapter 3, the corners of the field are clearly visible and are not blurred out.

The two dimensional ability of the vM2428 detector to measure dose was highlighted for the  $1 \times 1 \text{ cm}^2$  field measurement. Here it was found that the central MLC leaves were misaligned, likely a result of miscalibration. Due to the infrequency of these measurements at the NPL, it is unknown how long this error may have lasted, but again highlights the versatility of CMOS devices for in-vivo verification. A comparison of the vM2428 detector response and EBT3 film for a  $1 \times 1 \text{ cm}^2$  6 MV FFF field can be seen in Figure 4.14. In this measurement, the EBT3 film was placed in a groove in the supporting mount 0.5 cm from the surface of the detector. The fine detail as a result of radiation leakage between the MLC leaves would not be visible using the PRAVDA tracker unit with either reconstruction method.

This type of miscalibration would almost certainly have a clinical impact. If this Linac were to treat patients, the MLC error would have resulted in an incorrect radiation field being delivered with the potential for harmful or fatal consequences. This highlights the potential application of

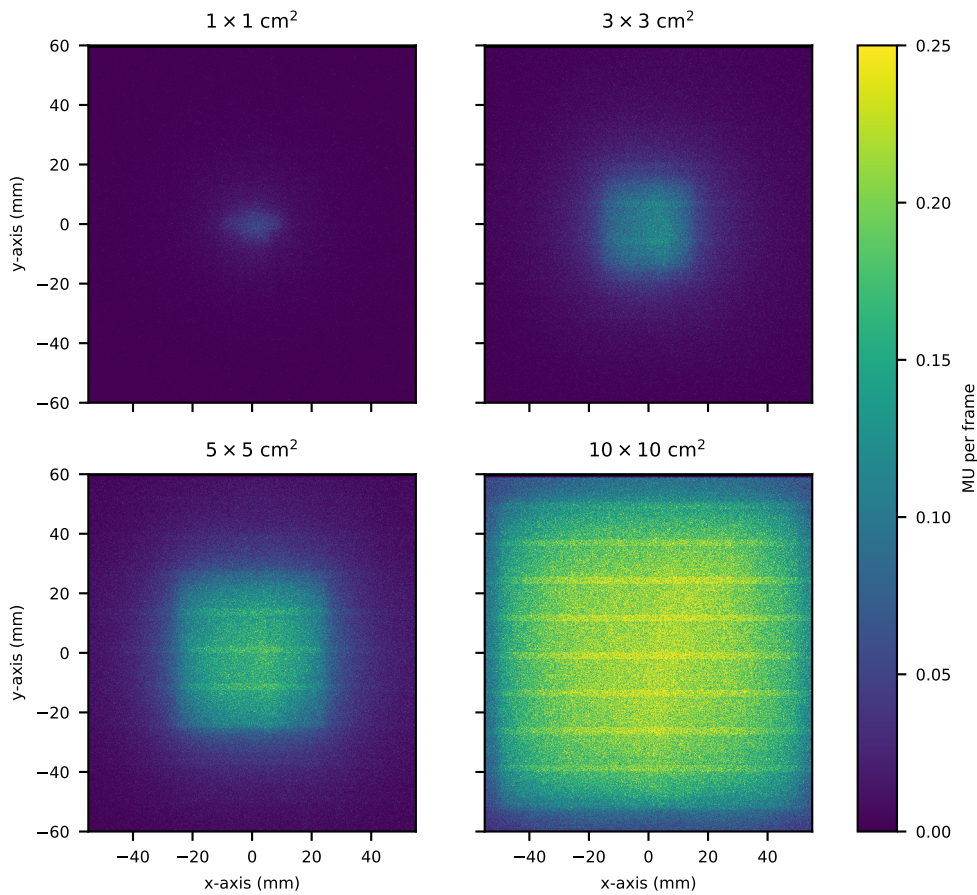


Figure 4.13: Average Detector Response to various 6 MV fields with 5 cm of water equivalent build-up.

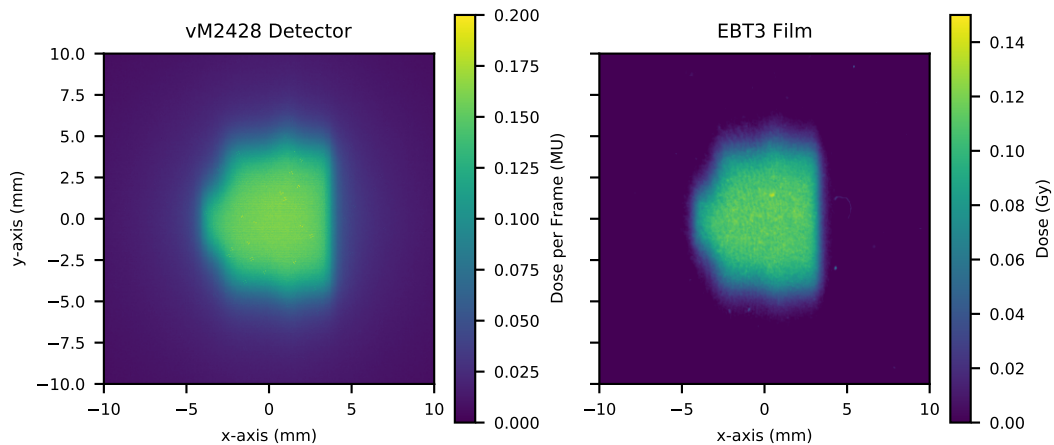


Figure 4.14: Comparison of vM2428 Detector and EBT3 film measuring a  $1 \times 1 \text{ cm}^2$  6 FFF field.

CMOS devices for upstream transmission verification of radiotherapy treatments, as described by Beck *et al.*[201].

Profiles acquired through the y-axis for various fields with build-up can be seen in Figure 4.15. It can be again shown that FFF beams increase the MU delivered per frame by a factor of ap-

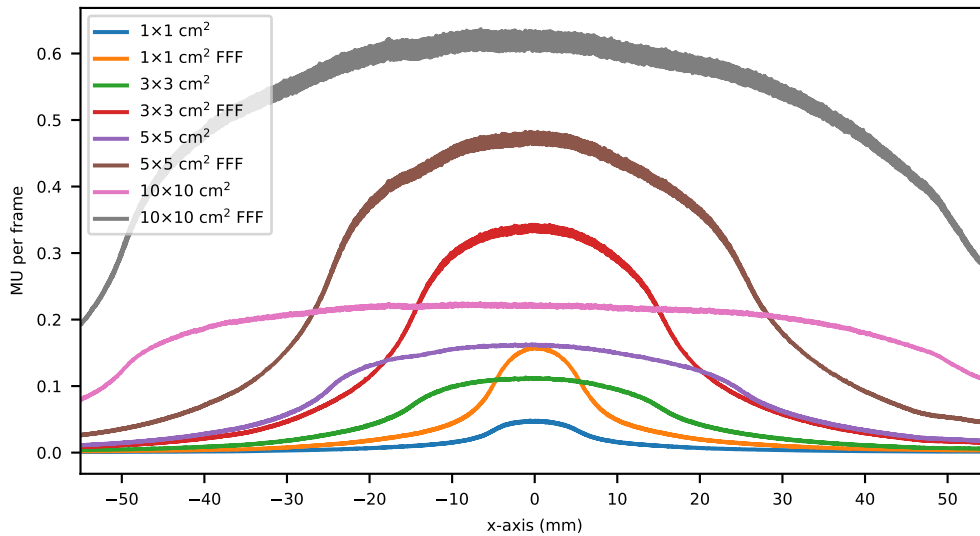


Figure 4.15: Comparison of different X-ray profiles acquired using the vM2428 detector with 5 cm of build-up.

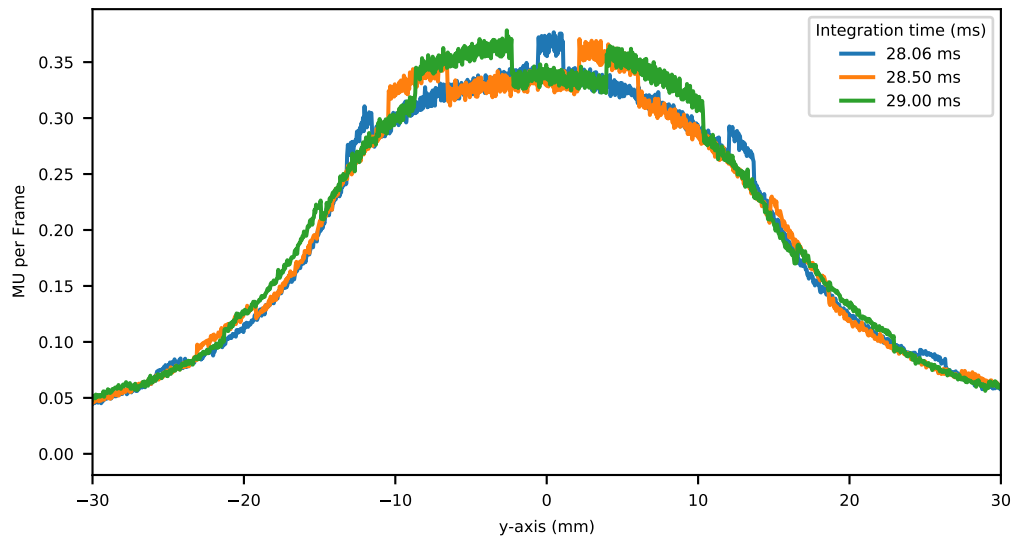


Figure 4.16: Comparison of rolling shutter artefacts for different integration times.

proximately  $3\times$ . The FFF beams being more peaked than the conventional X-ray beams is to be expected, and demonstrates why the flattening filter is required.

As the rolling shutter artefacts are a result of different numbers of Linac pulses being recorded on different sections of the detector, changes in the integration time of the detector will result in different artefact patterns. This is shown in Figure 4.16, where small increments of 0.5 ms change the ratio of the high:low regions. This behaviour is expected for the 400 Hz PRF Linac, as the average number of pulses per frame increases to 11.2, to 11.4, then 11.6 for 28, 28.5, and 29 ms integration times respectively.

To study the ability of the vM2428 detector to measure position across its surface, the rotational

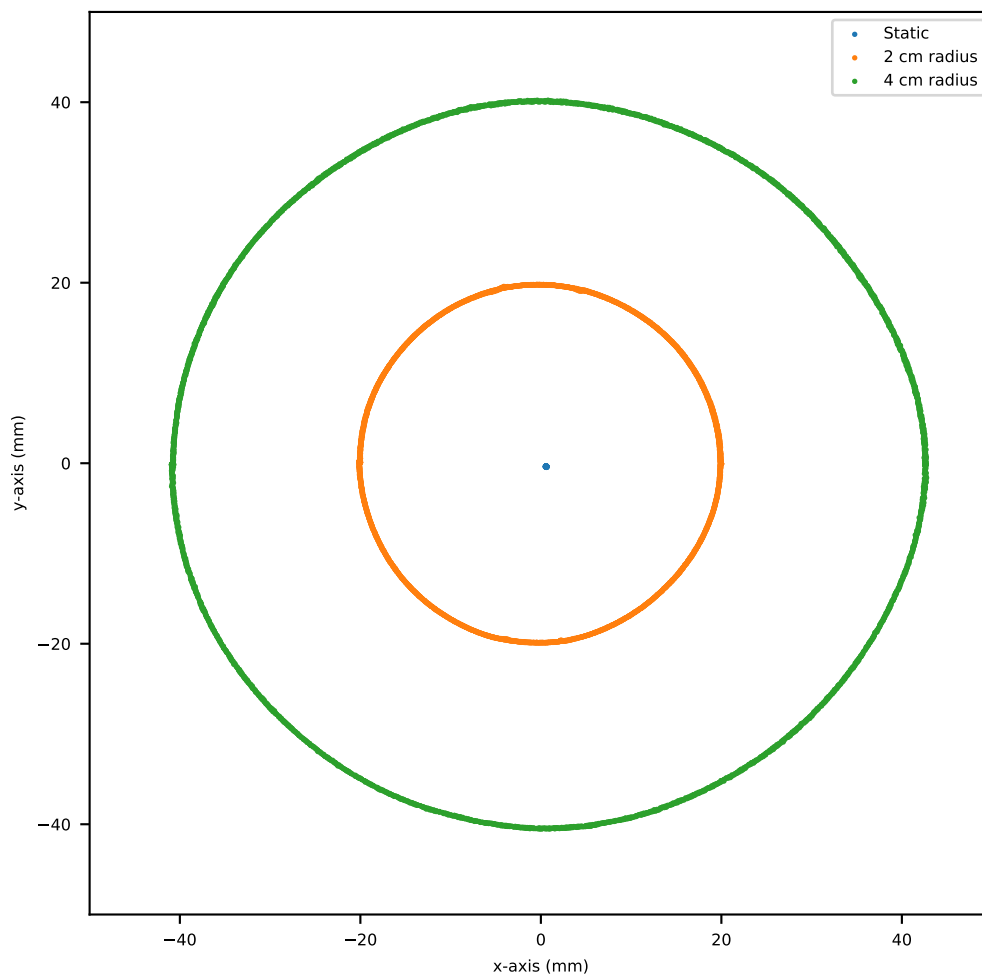


Figure 4.17: Determined positions for a rotating Linac collimator using the vM2428 detector using various offset X-ray fields.

test conducted using the PRaVDA tracker unit was repeated with a few modifications. Firstly 6 MV FFF was used, providing a higher dose rate slightly closer to that of PBS. Secondly the angles used were between  $\pm 180^\circ$ , resulting in a full circle of measurements. Two rotational measurements (at 2 cm and 4 cm radius) and one stationary were conducted using a  $20 \times 20 \text{ mm}^2$  field. A total of 4000 frames were acquired for each position, with beam centre calculated by taking an average of the rows and columns and fitting Gaussian functions appropriately. The results for this can be seen in Figure 4.17. The measured radii were  $19.86 \pm 0.15 \text{ mm}$  and  $40.73 \pm 0.72 \text{ mm}$  respectively for the 20 mm and 40 mm arc rotation. Unlike the PRaVDA tracker unit, there is no observed distortion on the 40 mm radius arc due to the larger active area of the vM2428 detector.

Unlike the vM1212 detector, the vM2428 detector has no issues with on-board memory filling up. Instead the amount of consecutive frames that can be obtained is determined by the amount of Random-Access Memory (RAM) on the computer, the rate at which they are acquired from the detector, and the processing power on the computer. Whilst the PRaVDA tracker unit was only capable of 10s of seconds of acquisition, the vM2428 detector was capable of over 3 minutes

of continuous reading at full frame maximum frame rate.

#### 4.3.3 Scanned Pencil Beam Measurements

Following the success of the X-ray tests, it was possible to acquire a small amount of beam time at University College Hospitals London NHS Foundation Trust (UCLH) in London, England, a PBS facility for measurements with the vM2428 detector. This facility uses a Varian ProBeam[202] cyclotron and was capable of delivering between 70-245 MeV protons at therapeutic energies and currents. Due to time restrictions and availability, it was not possible to perform this measurement with the *NPL proton calorimeter* however validation of the vM2428 detector was still valuable for predicting future behaviour.

As the radiation hardness properties of the vM2428 detector had not been studied yet, the decision was made to use a lower quality model with manufacturing defects. This detector had an issue with one of the ADCs, which resulted in odd rows not receiving any signal. The behaviour of the device was not expected to change, but would mean that the effective resolution was instead  $50 \times 100 \mu\text{m}^2$ . To evaluate the vM2428 detector, the instrument was placed horizontally on the treatment couch with the beam gantry angled at  $0^\circ$  at isocentre. In order to represent measurements with the *NPL proton calorimeter*, no build-up was placed on top of the detector. A photograph of the setup can be seen in Figure 4.18. High dynamic range mode is used throughout this investigation. It was found that the exposure room was able to get sufficiently dark such that the blackout fabric was not required.

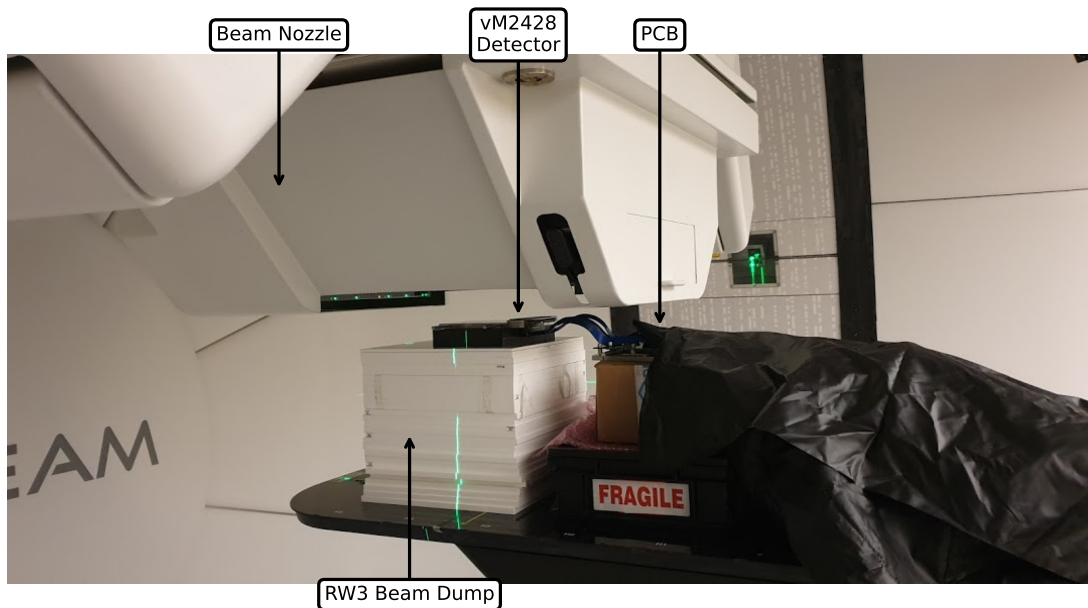


Figure 4.18: vM2428 Detector being setup at the UCLH Proton Beam Facility.

It was found that due to the high localised dose rate, the proton beam was observed to saturate the vM2428 detector, even at the lowest deliverable proton beam current of 12 nA and minimum full-frame integration time of 28 ms. The uncalibrated response of the vM2428 detector can be seen in Figure 4.19. The saturated response means details within the beam spot could not be acquired, but features such as beam position would still be possible to determine. A defective column can be seen to the left of the spot.

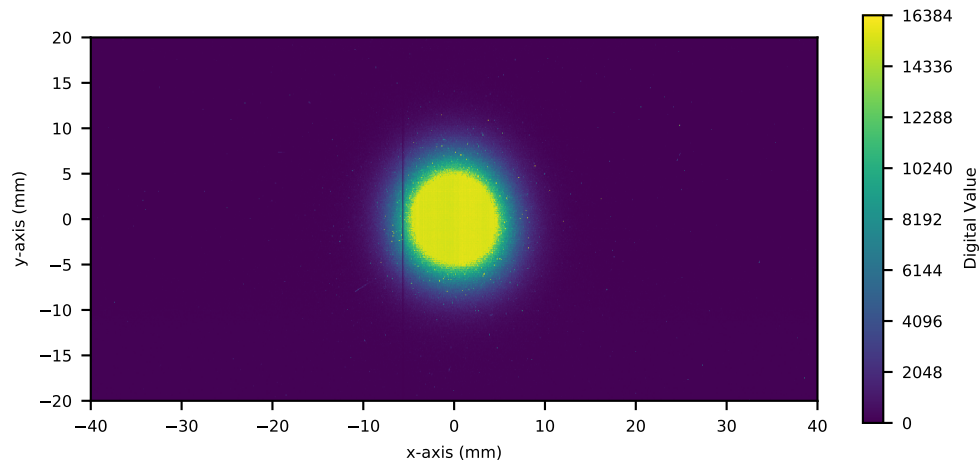


Figure 4.19: Uncalibrated Image of vM2428 Detector measuring a 20 nA 220 MeV proton beam.

Due to the small size of the beam and the ROI capability of the detector, it was possible to further reduce the integration time of the pixels by a substantial amount by reducing the number of rows acquired by the instrument. By reducing the ROI to only the central 400 rows, it was possible to reduce the integration time to 4.1 ms per frame where the detector was found not to saturate in the proton beam. With this lower integration time, the linearity of the device was investigated by changing the proton beam current delivered by the cyclotron operating in "Service" mode. Using the peak of the Gaussian deposited in the detector, this response curve was used to calibrate the pixel response. For a 220 MeV beam, the response of the vM2428 detector can be seen in Figure 4.20.

It was found that the cyclotron was unable to deliver a beam current below 12 nA without triggering an interlock error. Even for higher beam currents, it was found that the beam current was unstable and was not a reliable metric for calibration. This is shown in Figure 4.20 as the large spread in digital values recorded using the vM2428 detector for each calibration point, which was not observed at other facilities. The response of the detector becomes asymptotic after 35 nA as the detector becomes saturated. Despite this, it was found that the detector responded very linearly, with a line projected from 12, 15, and 25 nA intercepting the origin. The detector was

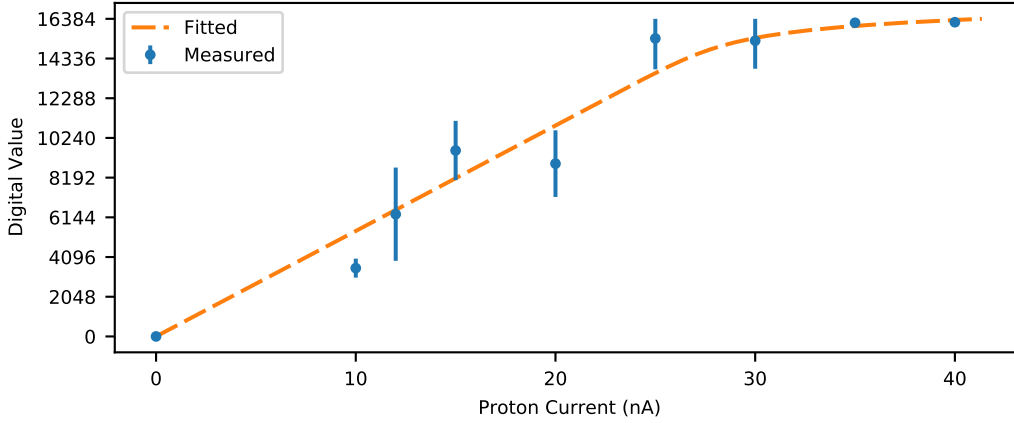


Figure 4.20: Linearity Response of vM2428 Detector in a 220 MeV proton beam. The range of values due to the cyclotron variation are shown as the Digital Value error bars.

calibrated using a hybrid linear-exponential function, as described in Equation 4.3.

$$x(y) = ay + be^{c(y-d)} - be^{-cd} \quad (4.3)$$

To validate the response of the vM2428 detector, a small piece of EBT3 film was placed on the detector for offline comparison. Due to time constraints it was not possible to perform either a calibration of the vM2428 detector in terms of dose, or an EBT3 film comparison. Instead a previous calibration in 28 MeV protons was used as a surrogate. 100 MU were delivered to both devices simultaneously, at a rate of 30 nA in order to avoid saturation of the vM2428 detector. To facilitate a comparison between the different units (which is assumed to be a linear relationship), both the profiles are self-normalised. A comparison of the profiles acquired via both methods can be seen in Figure 4.21.

The vM2428 detector was found to be in agreement with film regarding the shape of the beam profile, although without a full calibration it is difficult to a full comparison. The FWHM of the beam was determined to be  $7.06 \pm 0.01$  mm in the  $x$ -axis and  $8.05 \pm 0.02$  mm in the  $y$ -axis using the vM2428 detector, whilst measuring to be  $6.72 \pm 0.04$  in the  $x$ -axis and  $7.80 \pm 0.11$  mm in the  $y$ -axis for the EBT3 film. There is a consistent increase in the FWHM values as measured using the vM2428 detector, with one possibility suggested being the different energy response of the silicon; however this is beyond the scope of this thesis to investigate further.

Finally, it was possible to conduct a small study using a moving scanned pencil beam. To do this, the delivery system was put in "Clinical" operating mode, and a beam was programmed to deliver a total of 19 spots of 200 MU, with  $5.36 \pm 0.10$  mm separation. Operating in "Clinical" mode meant that all proton beam current settings were determined automatically, defaulting to 40 nA where possible. As shown previously in Figure 4.20, this resulted in saturation of the pixels.

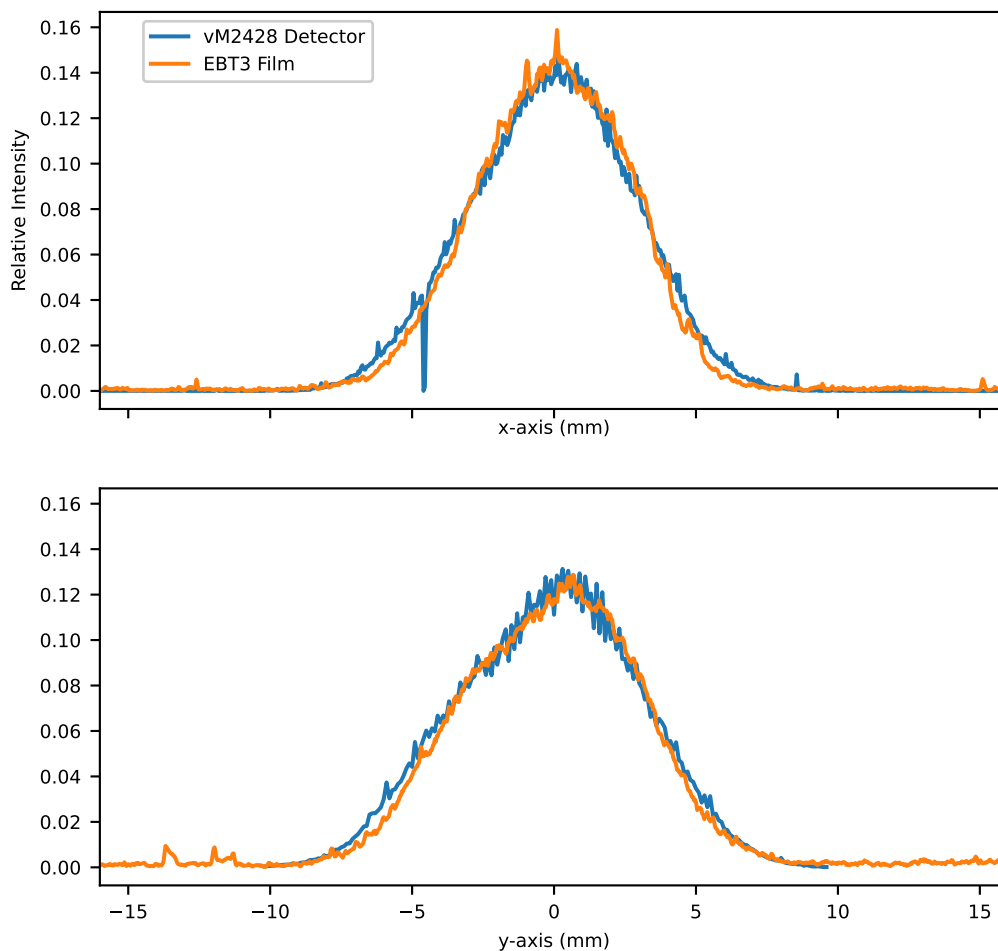


Figure 4.21: Comparison of EBT3 Film Profile and vM2428 Detector for a Proton Beam Spot.

Frames acquired using the vM2428 detector can be seen in Figure 4.22.

By observing the calculated beam position as a function of time, Figure 4.23, it becomes possible to observe the individual positions delivered by the treatment planning system. If the detector were not saturated, it is likely that features such as asymmetry and non-uniformity could also be determined, in addition to verifying the amount of MU delivered to each spot. It was found that the calculated y-axis of the beam spot was found to move between +1.3 mm and -1.0 mm, indicating that the detector was misaligned by approximately  $13^\circ$ . A histogram of the x-axis beam spot positions, Figure 4.24, allows further visibility of the distinct positions delivered.

In both Figure 4.23 and Figure 4.24, it is possible to see the occasional calculated beam position separated from the rest. This is due to rolling shutter artefacts, as previously discussed in Section 4.3.2. Unlike with the Linac this is not due to pulsing of the cyclotron as the machine has a pulse frequency of 72.8 MHz[203], which is fast enough to be considered uniform for the detector. Instead, it is due to the proton beam moving during a single frame exposure. This can be seen in Figure 4.25, where three consecutive frames are shown. During the centre frame, the top half of one spot and the bottom half of another are visible. Omitting these transient artefacts, it becomes

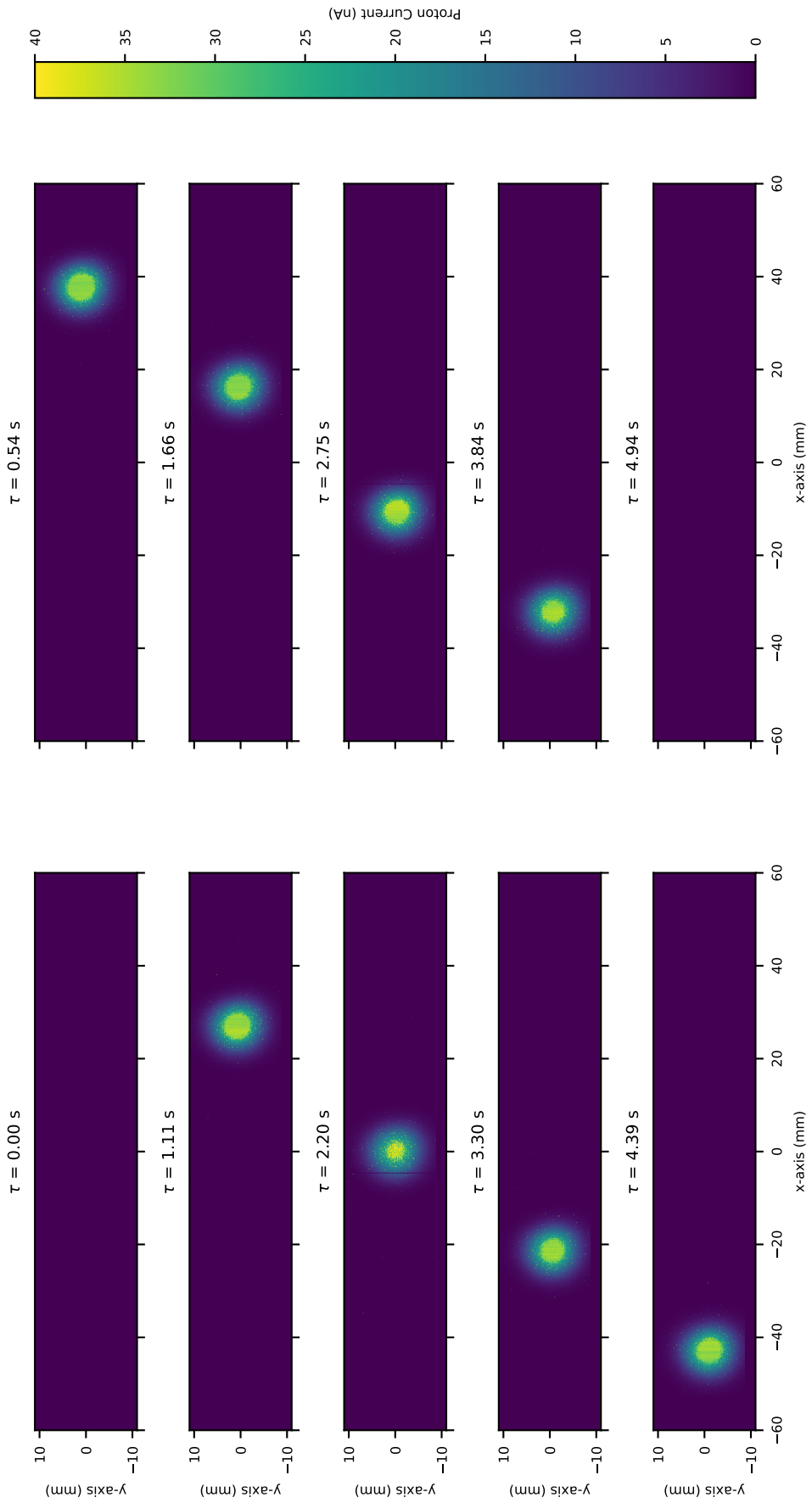


Figure 4.22: Moving Pencil Beams measured using the vM2428 Detector

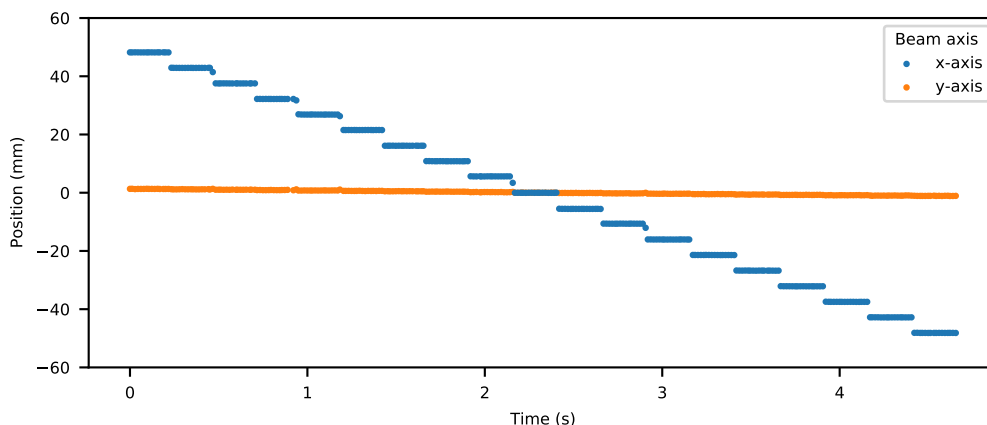


Figure 4.23: Determined Positions for a moving scanned pencil beam.

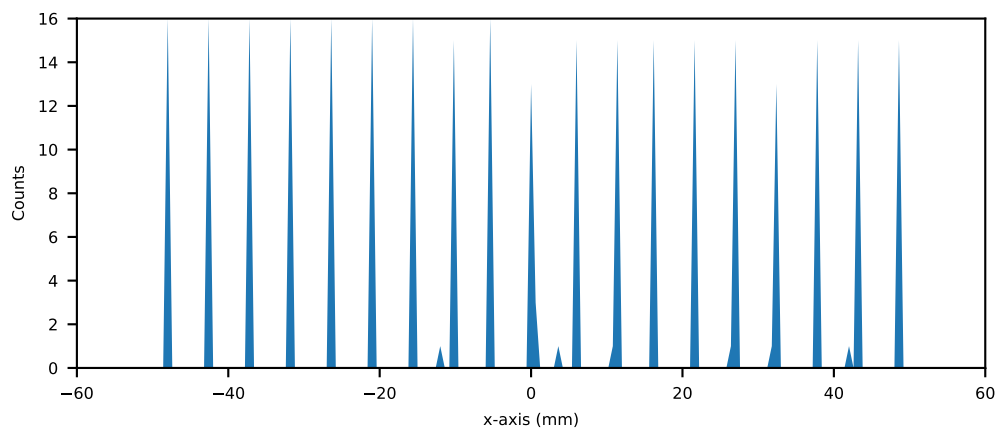


Figure 4.24: Histogram of positions for a scanned pencil beam.

possible to perform analysis on each spot. At each position it can be determined that the beam is on for  $0.23 \pm 0.01$  seconds. If the vM2428 detector was not saturated, it would be possible to combine this information with the 2D dose distribution to estimate total MU delivered at each spot.

By comparing each frame within a spot position the uncertainty in position was determined to be  $\pm 0.03$  mm, implying very little beam wobbling was occurring. The average spot to spot separation was determined to be  $5.35 \pm 0.03$  mm, this is in agreement with the treatment planning software. It was found that a significant number of frames were being lost at the lower ROI, with only 1/7 being recorded. It was not clear whether this was due to the PCB or the laptop, but as the vM2428 detector software recorded the timestamp of valid frames this was determined not to be a significant issue for this measurement. This is something to investigate in the future as deliveries with less than the 20 MU per spot may result in entire spot positions being lost.

Unfortunately due to the saturation of the detector it is not possible to perform profile measurements per frame. This capability has been demonstrated in "Service" mode at a lower proton

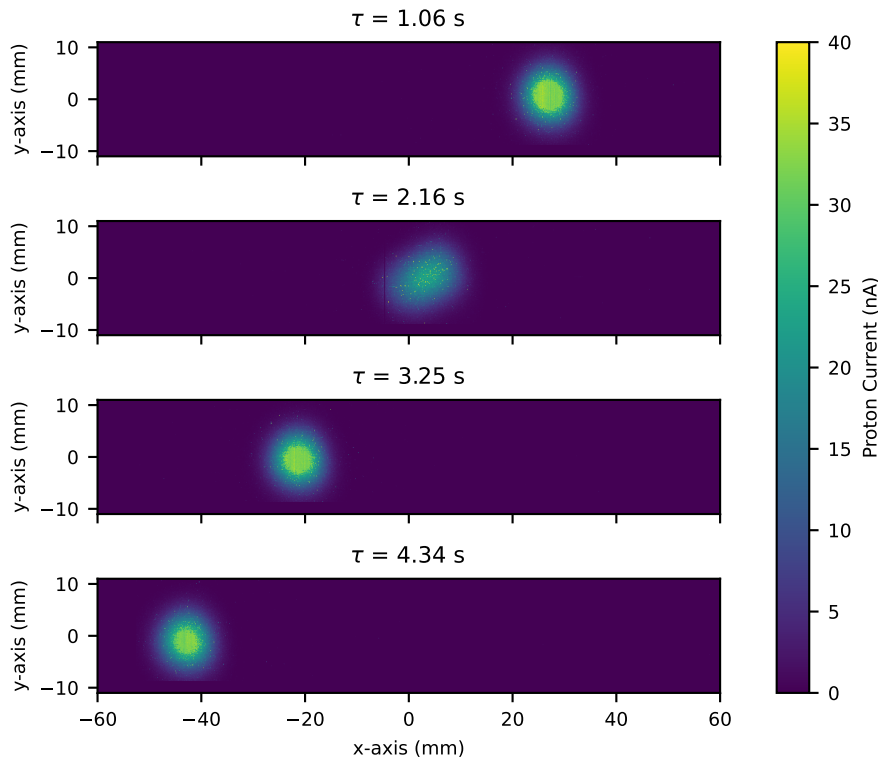


Figure 4.25: Moving Pencil Beams measured using the vM2428 Detector

beam current and would be possible with a smaller ROI in "Clinical" mode. Knowledge of beam shape, position, and asymmetry in a method that is non-destructive to the beam would be useful clinically as well as will the *NPL proton calorimeter*.

## 4.4 Conclusion

In this chapter we have evaluated large format CMOS sensors based on the "*LASSEN*A" pixel design. It has been shown that such devices are viable candidates for beam monitoring in PBS for the *NPL proton calorimeter*, capable of acquiring profiles and positions of incident beams in real-time. The use of the CMOS detectors for microbeam dosimetry invites many future research opportunities, where combined with the *NPL proton calorimeter* it could be used for accurate calorimeter of proton micro and minibeams.

Due to the current ROI implementation it is currently only possible to monitor moving pencil beams in one direction, however this is expected to be rectified in future firmware revision. Ideally a full-frame image would be acquired, however as shown due to saturation effects this was not possible. The long-term viability of either the vM1212 or vM2428 detector to radiation damage was not studied, however it has been shown in this Chapter that as a proof of principle they are suitable for use with the *NPL proton calorimeter*.

Although the "*LASSENA*" detectors were not designed for external beam radiotherapy, they have performed better than expected, highlighting the strength and versatility of CMOS devices. A pixel designed specific for the application of PBS would ideally share many of the properties of the "*LASSENA*" pixel design. If a more sophisticated data capture, such as global shutter, and larger full well could be introduced without sacrificing the tolerance to ionising radiation many of the limitations described in this chapter could be overcome.

To expand this work to be relevant to the clinical practice in the delivery of scanned pencil beams, additional measurements are required in high energy proton beams. The narrow ROI of the vM2428 detector limits its usefulness, however changes in the firmware could enable this to be programmatically changed, which would facilitate following a moving proton beam.

Longer term, the requirement of a ROI is a limiting factor, and future CMOS detectors for proton or X-ray dosimetry would need to be able to capture the entire frame without saturating. Further to this, as the vM2428 detector is only 3-sides buttable, the maximum tiling area of the vM2428 detector is  $(N * W \times 2 * H)$  cm<sup>2</sup>: where  $N$  is the number of detectors;  $W$  is the width of each detector (12 cm); and  $H$  is the height of each detector (14 cm). This is much less than a 40 × 40 cm<sup>2</sup> reference field, and as such each future CMOS detector would be required to have a much larger height (assuming a 3-sides buttable design).

## Chapter 5

# Calorimeter Studies

### 5.1 Introduction

In this chapter the importance of detailed modelling of the heat flow within the calorimeter is discussed along with a number of unexpected results which could be of importance for correct proton dosimetry in some proposed future delivery modalities.

### 5.2 Investigation with the NPL Proton Calorimeter

#### 5.2.1 Motivation

Radiation studies were carried out at NPL on the Elekta Versa HD Linac using high energy photons, to enable the study of internal heat flow with localised radiation sources and dynamic radiation beams. The decision to use the *NPL proton calorimeter* in an X-ray beam was due to difficulties in accessing PBT facilities at the time of this PhD programme due to the "*COVID-19*" Coronavirus Disease Pandemic[23].

This had several advantages: as a non-clinical facility more time for detailed study would be available; and the vM2428 detector was already characterised for this beam. The main disadvantage however is that the instantaneous dose rate from the X-rays is less than that of protons and as such the heat flow may be different. 6 MV FFF can be used to partially bridge this discrepancy. Whilst a moving beam can be generated using the MLC system, it is not physically possible to move the internal collimators as fast as a scanned pencil beam can move.

#### 5.2.2 Methodology

Using the mount discussed in Chapter 4, the vM2428 detector was physically connected to the *NPL proton calorimeter*. This mount, shown in Figure 5.1, suspends the vM2428 detector vertically and

aligns the centre of the two devices. The vM2428 detector hangs from the front of the *NPL proton calorimeter* frame, with the PCB suspended above it. This horizontal separation from the surface of the calorimeter to the edge of the rails is necessary to provide space for the graphite build-up plates used in high energy proton beam therapy, however these were not used in this experiment. The *NPL proton calorimeter* was positioned at the Linac isocentre using the alignment lasers.

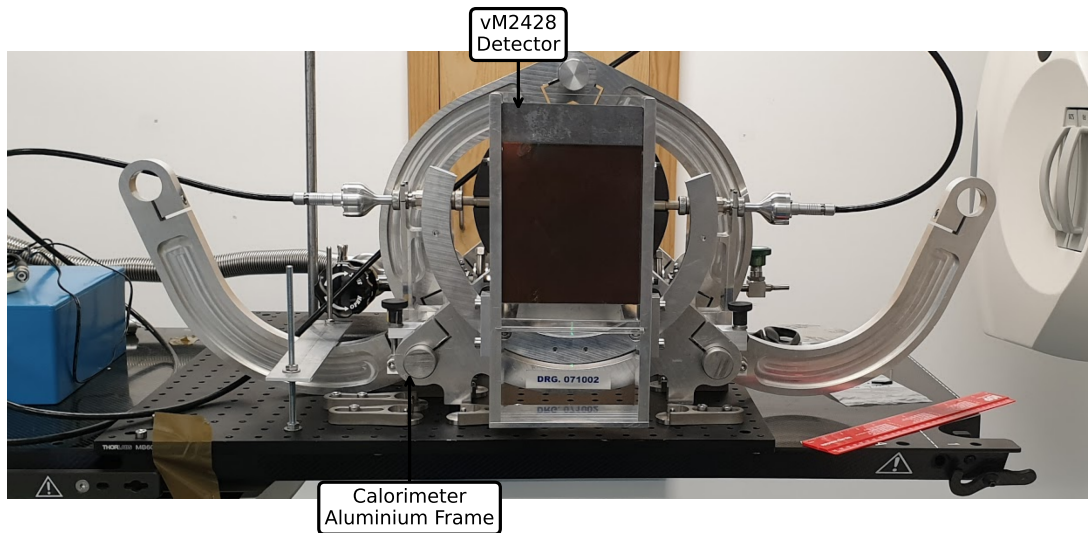


Figure 5.1: Photograph of the vM2428 Detector with the *NPL proton calorimeter*.

The mount is designed such that the vM2428 detector can rotate  $\pm 45^\circ$ , whilst keeping the centre of the two devices aligned. This is necessary as the *NPL proton calorimeter* is rotated for PBS measurements in order to capture the entire  $10 \times 10 \text{ cm}^2$  reference field without irradiating the calorimeter rails. For the purposes of this measurement, the *NPL proton calorimeter* was kept at  $0^\circ$ . A photograph of the rear of the setup can be seen in Figure 5.2.

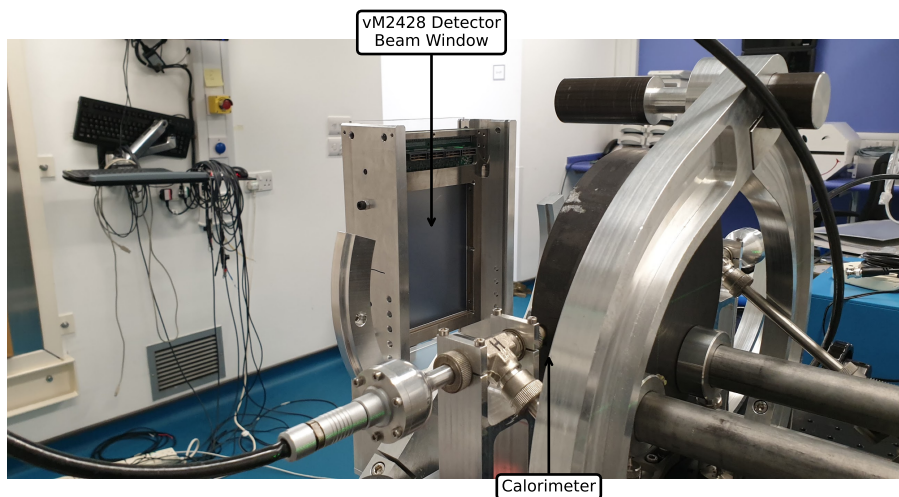


Figure 5.2: Photograph of the rear of the vM2428 detector with the *NPL proton calorimeter*.

## 5.2. Investigation with the NPL Proton Calorimeter

To shield the vM2428 detector from light contamination, two layers of blackout fabric[204] were again used. A photograph of the complete setup with the *NPL proton calorimeter* positioned with the core at isocentre, blackout fabric, and vM2428 PCB can be seen in Figure 5.3.

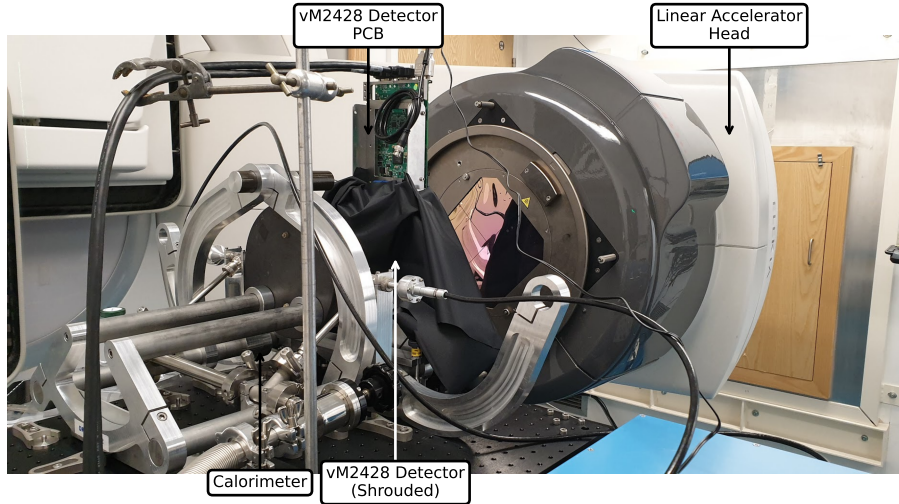


Figure 5.3: Photograph of the vM2428 Detector with *NPL proton calorimeter* with light shroud.

For the investigation, the integration time of the detector was chosen to be 50 ms with the full frame selected as the ROI. It was determined that for a  $10 \times 10 \text{ cm}^2$  6 MV FFF beam that this did not provide saturation in high dynamic range mode. This choice in integration time was evenly divisible by the PRF of the Linac and as such was predicted to minimise any rolling shutter artefacts. As the conditions of the vM2428 were different to those measured previously, it was appropriate to repeat the measurement of the linearity of the vM2428 detector. This was performed by changing the electrons per pulse in a 6 FFF beam and measuring the average digital value in the centre of the peak.

The *NPL proton calorimeter* was configured to operate in QA mode, with only the *Outer Jackets* of the calorimeter heated. A constant  $10 \mu\text{W}$  was delivered to the *core* and *Inner Jackets* in order to avoid transient effects when transitioning to ISO mode. The full configuration is described in Table 5.1.

Name	Quantity	Units
Core Power	10.0	$\mu\text{W}$
Front Inner Jacket Power	10.0	$\mu\text{W}$
Rear Inner Jacket Power	10.0	$\mu\text{W}$
Front Outer Jacket Temperature	25.070	$^{\circ}\text{C}$
Rear Outer Jacket Temperature	25.000	$^{\circ}\text{C}$

Table 5.1: Configuration of the *NPL proton calorimeter* operating in Quasi-Adiabatic mode.

### 5.2.3 Stationary Beams

With the calorimeter positioned at isocentre, both devices were irradiated with a series of stationary 6 MV FFF fields between  $0.5 \times 0.5 \text{ cm}^2$  and  $5 \times 5 \text{ cm}^2$ . To correct for any mechanical misalignment of the vM2428 detector relative to the *NPL proton calorimeter*, the centre of the  $3 \times 3 \text{ cm}^2$  was defined as the centre of the vM2428 detector. Frames acquired during each of the four stationary measurements can be seen in Figure 5.4. An outline of the graphite core is drawn in white to represent to provide scale. The miscalibration of the MLC, discussed previously in Section 4.3.2 can again be seen. It is possible to see that there are still rolling shutter artefacts, most likely due to additional dead time per frame.

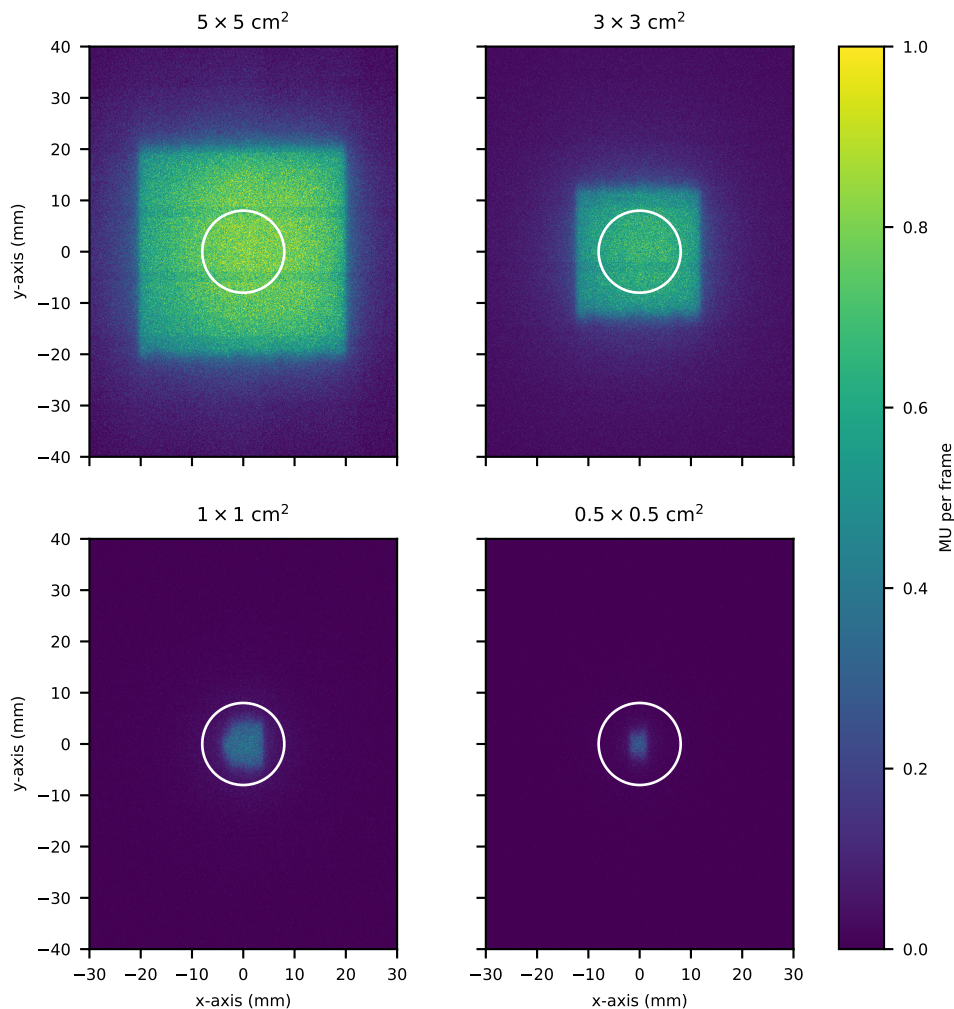


Figure 5.4: Radiation Profiles acquired for different field sizes using the vM2428 detector showing the relative position of the *NPL proton calorimeter* core.

Figure 5.5 shows the temperature response of the *NPL proton calorimeter* core, when irradiated with ten 6 MV FFF  $5 \times 5 \text{ cm}^2$  fields each delivering 500 MU. The temperature response of a single exposure can be seen in Figure 5.6. Using the NPL analysis software and the method previously discussed in Section 2.4.4.3, the dose deposited in the core from these measurements was found to

be  $4.056 \pm 0.003$  Gy.

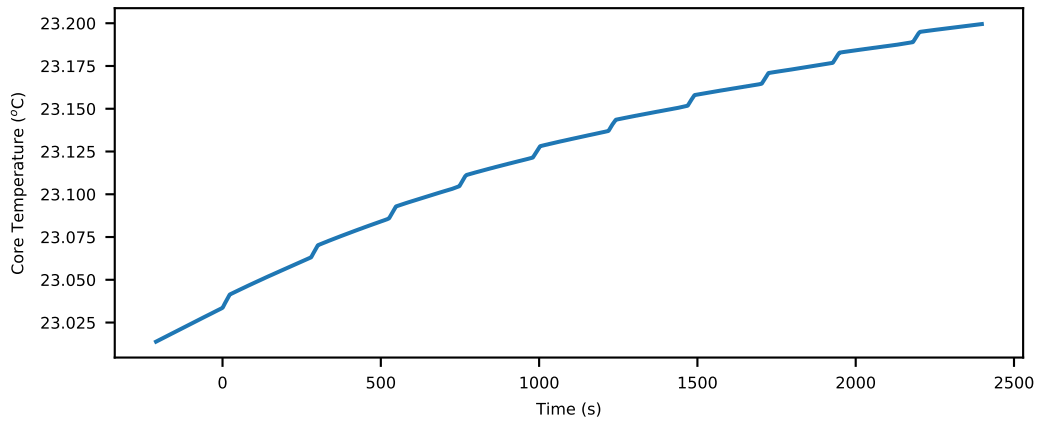


Figure 5.5: Temperature increase in the *NPL proton calorimeter* core as a result of a  $5 \times 5$  cm<sup>2</sup> beam delivering multiple 500 MU exposures.

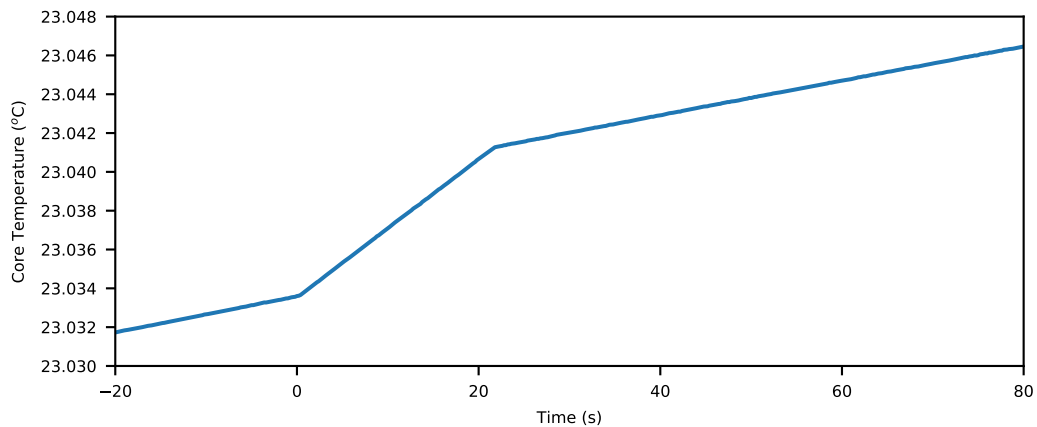


Figure 5.6: Temperature increase in the *NPL proton calorimeter* core as a result of a  $5 \times 5$  cm<sup>2</sup> beam delivering a single 500 MU exposure.

The effect of changing the field size on absorbed dose is shown in Figure 5.7. An attempt to predict absorbed dose using the vM2428 detector was conducted by summing the MU per frame within the area defined as the *NPL proton calorimeter* core, a unit typically referred to as Dose-Area-Product (DAP). The DAP was be calculated using Equation 5.1.

$$DAP = \iint D(x, y) dx dy \quad (5.1)$$

It was found that there is not a clear relationship between DAP and absorbed dose. This can be attributed to scatter, radiation directed outside of the core depositing energy within it; and the increase in electron contamination for larger fields.

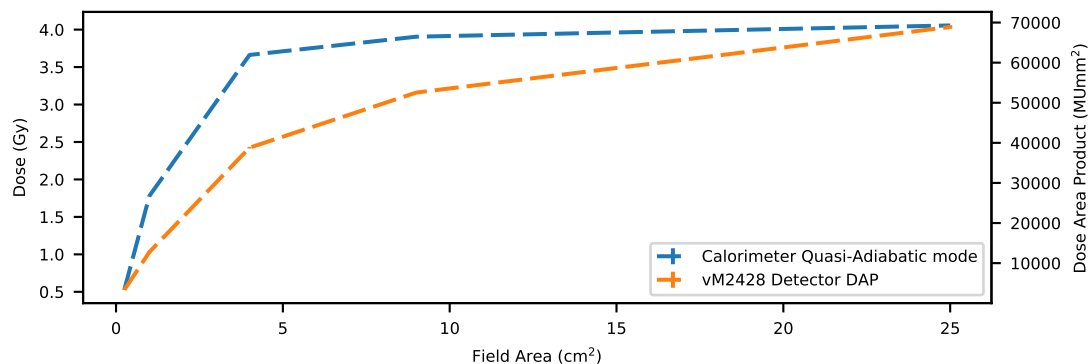


Figure 5.7: Comparison of measured Output Factor when using Dose (Gy) and Dose Area Product (MUmm<sup>2</sup>).

### 5.2.4 Moving Beams

To study heat flow within the *NPL proton calorimeter*, it and vM2428 detector were irradiated with moving beams of radiation. This was again achieved by using iCom Customer Acceptance Test (iComCAT) software version 14.0.0.0 (Elekta Ltd, Crawley, UK) to create exposures in which the parameters of the Linac could be varied.

For the first test, a moving  $1 \times 1$  cm<sup>2</sup> field was created by moving the central pairs of leaves on either side (Y1<sub>40</sub>, Y1<sub>41</sub> and Y2<sub>40</sub>, Y2<sub>41</sub>) between +4/+3 cm and -3/-4 cm respectively. All other leaves were set to 0 cm. This would create a square beam that would appear to move between  $\pm 3.5$  cm, which is was programmed to do a total of four times. 6 MV FFF was used for this to provide the maximum dose rate possible. A total of 3000 MU was prescribed to be delivered, with each pass delivering 750 MU. Between each pass of the moving beam, the Linac would momentarily turn off the radiation and reset the internal MU ionisation chamber. This was an automatic process with the Linac to ensure that each pass did not deliver more than 1000 MU per segment, which would have triggered the machine to interrupt beam delivery when operating in clinical mode. A table describing the Linac parameters can be seen in Table 5.2.

Pass	PRF (Hz)	Prescribed Dose (MU)	Cumulative Dose	Nominal Dose Rate (MU/min)
1	400	750	25%	1600
2	400	750	50%	1600
3	400	750	75%	1600
4	400	750	100%	1600

Table 5.2: Parameters of the moving X-ray beam.

Frames acquired by the vM2428 detector during this measurement can be seen in Figure 5.8. As discussed previously, the Y1<sub>39</sub> and Y2<sub>39</sub> pair of leaves in the MLC are misaligned causing radiation to leak through the gap created. This results in a constant amount of radiation being delivered to the *NPL proton calorimeter core* throughout the measurement.

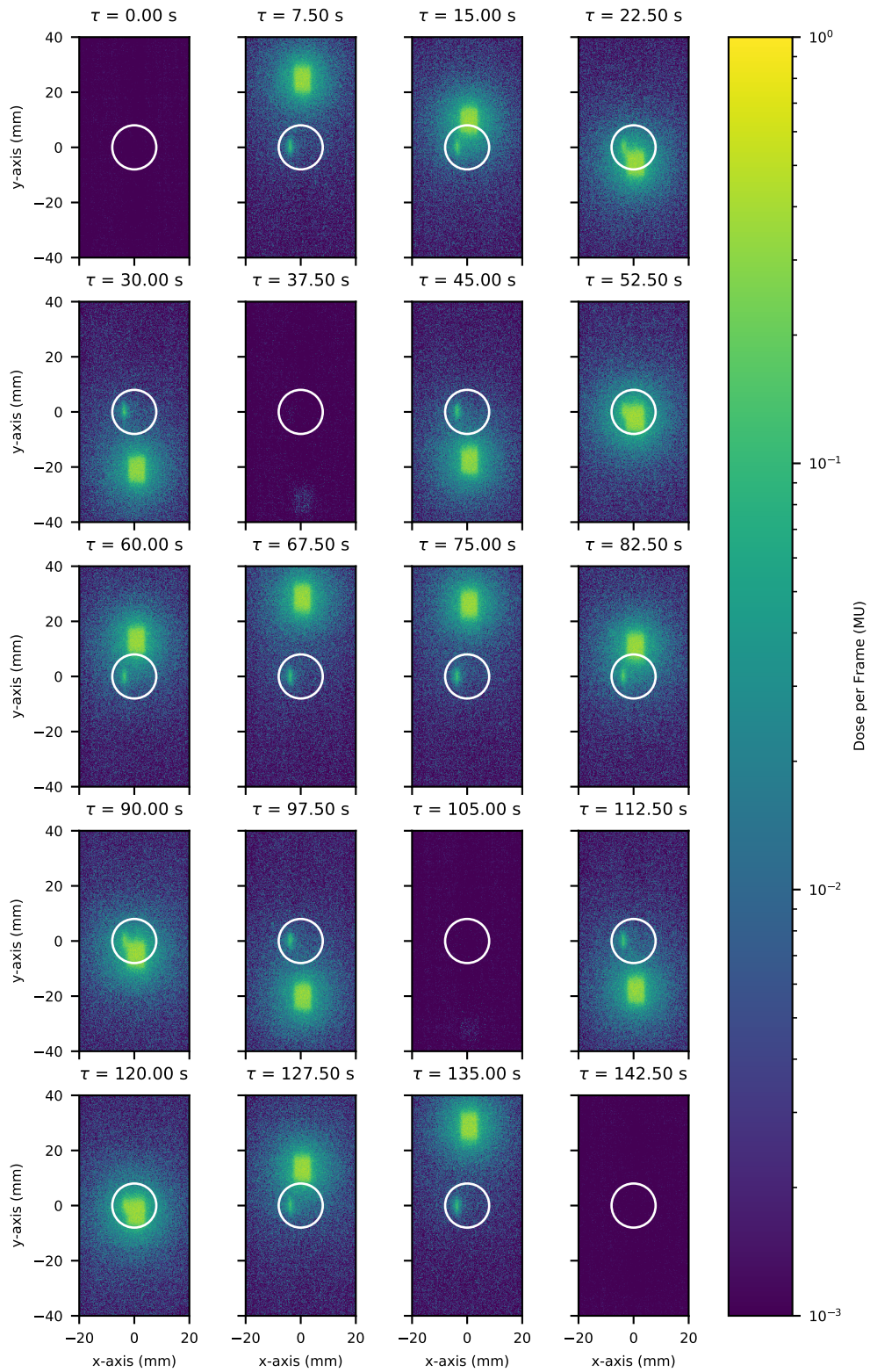


Figure 5.8: Images acquired using the vM2428 detector for the moving X-ray beam, showing the relative position of the *NPL proton calorimeter* core

The moving beam of radiation was observed to cause unpredicted heat effects within the *NPL proton calorimeter*. It was found that during each pass of the beam, the first thermistor to be exposed would increase in temperature gradually, whilst the second thermistor would show a much sharper peak. Analysis of the recorded beam by the vM2428 detector confirmed that the beam behaved as programmed, and so thus the odd behaviour of the thermistors was concluded to be related to internal heating effects. This is illustrated in Figure 5.9, showing the average instantaneous dose rate over 10 measurements as measured for each thermistor; the cumulative dose delivered; and the beam position as determined by the vM2428 detector, again averaged over the 10 measurements. Although the DAP has been demonstrated as an unreliable method of predicting dose in the *NPL proton calorimeter*, it is shown to demonstrate that the beam behaved consistently throughout. The FWHM of the beam, as measured by the vM2428 detector is shown around the  $y$ -axis position plot to help visualise the position and size of the beam relative to the *NPL proton calorimeter core*.

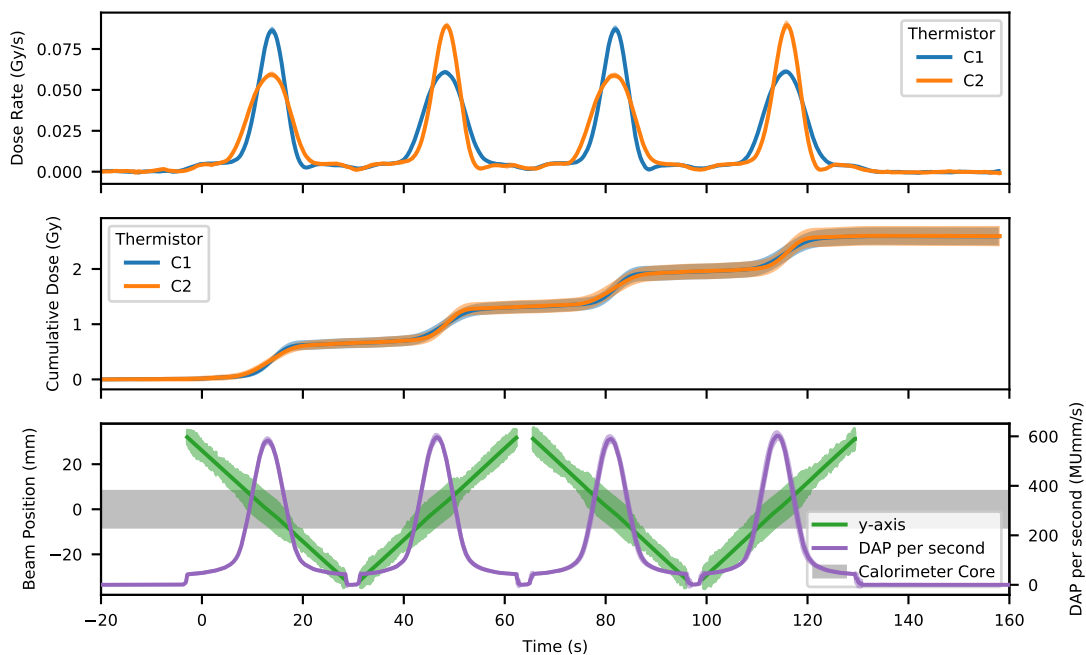


Figure 5.9: Comparison of instantaneous dose rate and cumulative dose measured in the *NPL proton calorimeter*, and beam parameters acquired by the vM2428 detector, for multiple passes with a moving X-ray beam.

The radiation leakage from the MLC can be seen in the instantaneous dose rate plot and the DAP plot as an offset from zero. The beam reset positions can clearly be seen in the DAP plot, however this appears blurred for the instantaneous dose rate figure. This was because the instantaneous dose rate is averaged over 16 measurement points (3.2 seconds), in order to reduce noise. Such a large averaging window would not be necessary in PBS, however it was necessary due to the low dose rate for photons in the Linac.

Figure 5.10 shows the same set of data, but instead focusing on the first pass of the radiation. Whilst it can be seen that the cumulative dose measured by both thermistors becomes the same, the second thermistor to be exposed measures a higher maximum instantaneous dose rate. Further to this, the standard deviation of the cumulative dose is higher for the first thermistor to be irradiated than the second although after four passes both the average and standard deviations of both thermistors agree. It can be inferred from this that delivering a moving beam of radiation from the same direction multiple times would result in a non-trivial asymmetry between the two thermistors. This may have implications in PBS delivery, something that has not yet been explored.

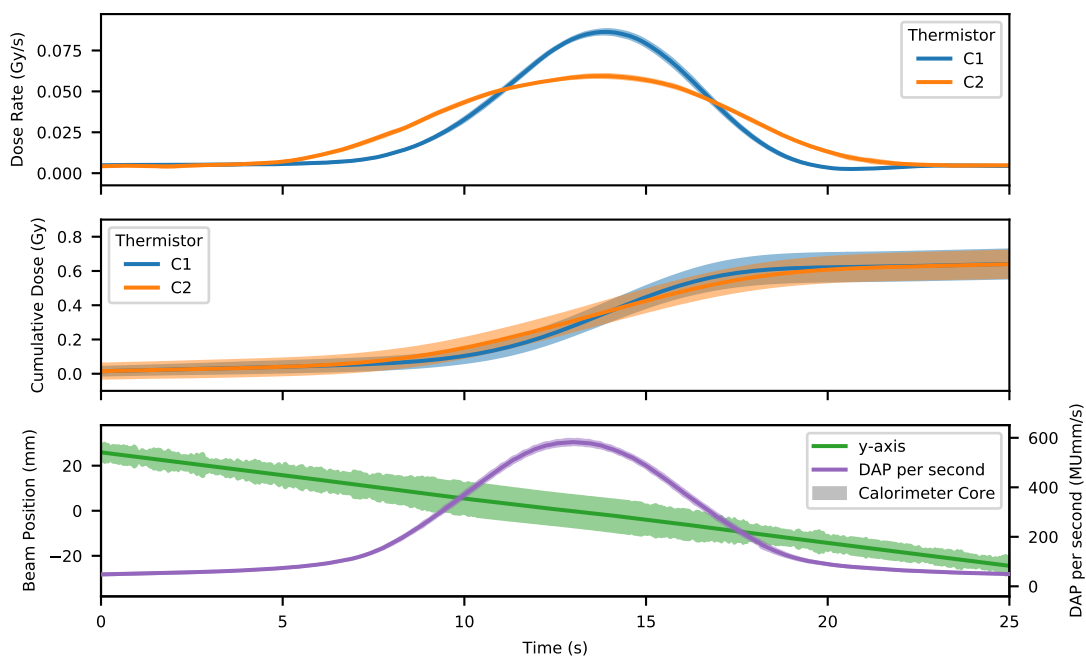


Figure 5.10: Comparison of instantaneous dose rate and cumulative dose measured in the *NPL proton calorimeter*, and beam parameters acquired by the vM2428 detector, for a single pass with a moving X-ray beam.

Using the data from the vM2428 detector, it is possible to determine that beam moved at a speed of  $2.00 \pm 0.01$  mm/s. This is significantly slower than PBS, which can have maximum scanning speeds of 2000-20000 mm/s[205].

### 5.2.5 SRS Probe Investigation

To further investigate heat flow within the calorimeter, the Linac was fitted with a Stereotactic Radiosurgery collimator, supplied by Elekta. This collimator was capable of further shaping the X-ray beam with the addition of 4 mm, 10 mm, and 50 mm circular "cones". To best create localised heating effects, only the 4 mm cone was used for study. A photograph of the collimator with the cone attached can be seen in Figure 5.11.

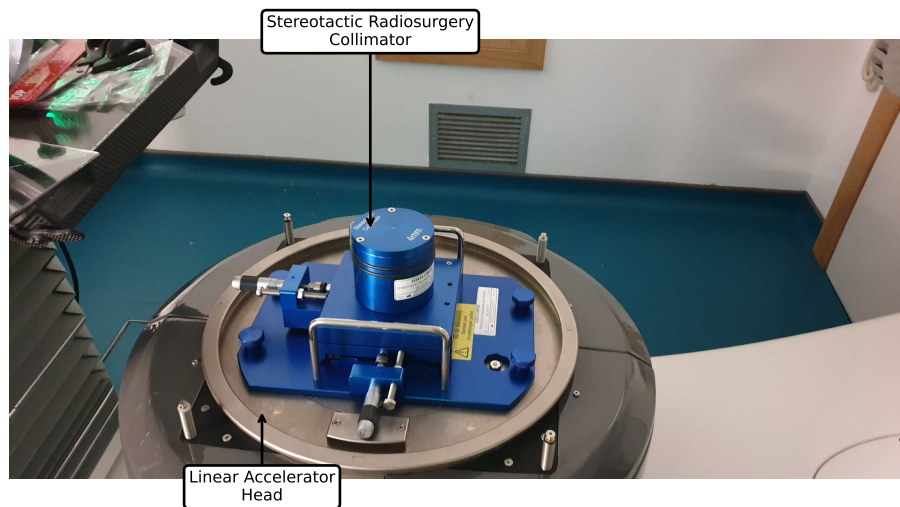


Figure 5.11: Photograph of the Stereotactic Radiosurgery collimator attached to the Elekta Versa HD Linac.

The *NPL proton calorimeter* was irradiated with the collimator fitted at various locations targeting the *core*, and internal thermistors. Each position was exposed a total of 10 times, again recording the radiation field with the vM2428 detector to enable the beam position and intensity to be recorded. Due to the low dose rate with the applicator fitted, it was necessary to use 6 MV FFF exclusively for exposing the *NPL proton calorimeter*. For the same reason, 1000 MU was used at each position.

Using the positions acquired by the vM2428 detector and the integral dose determined by the *NPL proton calorimeter*, the spatial sensitivity of both instruments can be seen in Figure 5.12. It can be immediately seen that the dose response is off-axis, suggesting that the *NPL proton calorimeter* is misaligned.

Taking profiles through the  $x$  and  $y$  axis measurements, it is possible to calculate the offset to be  $(1.5 \pm 0.4 \text{ mm}, 0.9 \pm 0.4 \text{ mm})$ . It was later confirmed with a standalone film measurement, that the laser alignment system of the Linac is offset from the beam isocentre by approximately  $(1.9 \pm 0.1 \text{ mm}, 0.7 \pm 0.1 \text{ mm})$ . This demonstrates an important role for the vM2428 detector in future measurements with the *NPL proton calorimeter* for confirming the true position of the beam.

The instantaneous dose rate of a beam directly over the "C1" thermistor can be seen in Figure 5.14. Not only does the C1 thermistor react first to the radiation, but it is also observed to temporarily over-shoot, peaking approximately 20% higher than the average dose rate in the pseudo-equilibrium state. This state lasts for approximately 40 seconds until the Linac beam is turned off, at which point the "C1" thermistor once again over-shoot. It is during this beam off state that the instantaneous dose rate recorded on the "C1" thermistor is observed to become negative, a result of the temperature in the thermistor decreasing as heat is lost to the surround-

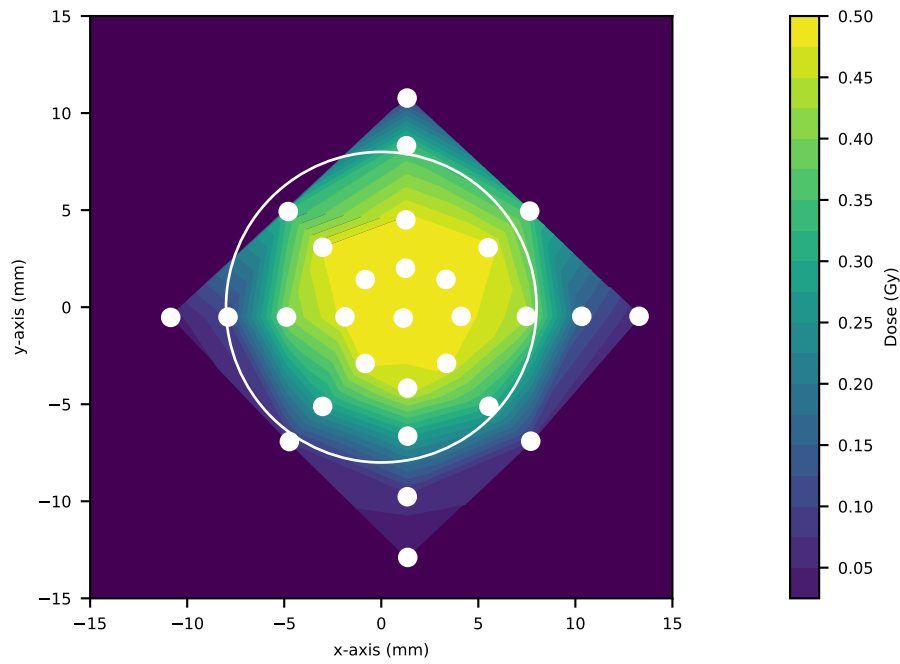


Figure 5.12: Dose measured as a function of position when exposing the *NPL proton calorimeter* core with a 4 mm FWHM SRS 6 MV FFF beam.

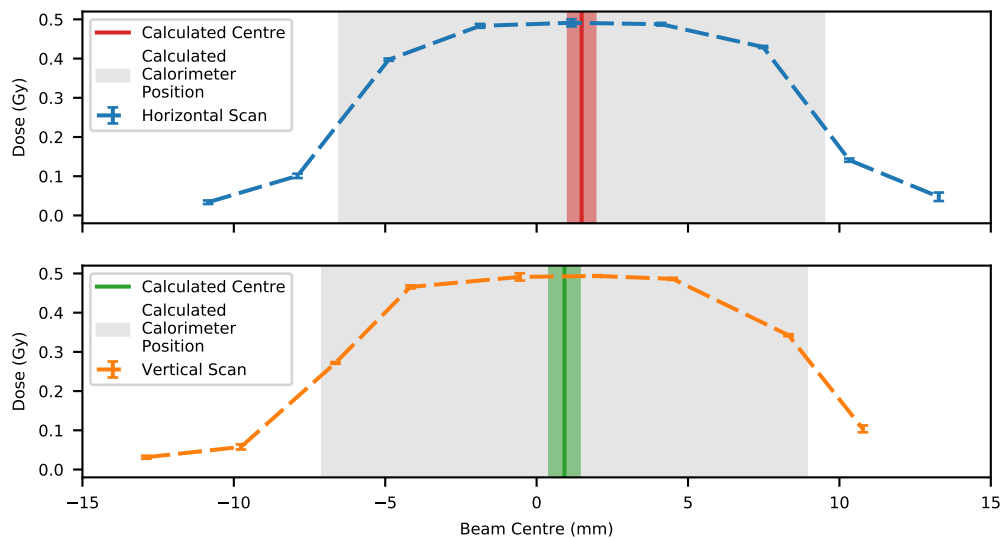


Figure 5.13: Dose profiles in the  $x$  and  $y$  axes when exposing the *NPL proton calorimeter* core with a 4 mm FWHM SRS 6 MV FFF beam.

ing graphite. Throughout this exposure, the "C2" thermistor is not observed to peak like the "C1" thermistor. This is likely as the "C2" thermistor is completely out of the beam and any temperature rise is due to conduction through the graphite.

As shown in Figure 5.14, there is a radiation induced offset in the profiles of the "C1" and "C2" thermistors. Using Equation 5.2 to define the rise time difference ( $\tau_{\Delta}$ ) in terms of the when the "C1" and "C2" thermistor reach 50% of their average beam on dose rate it becomes possible to

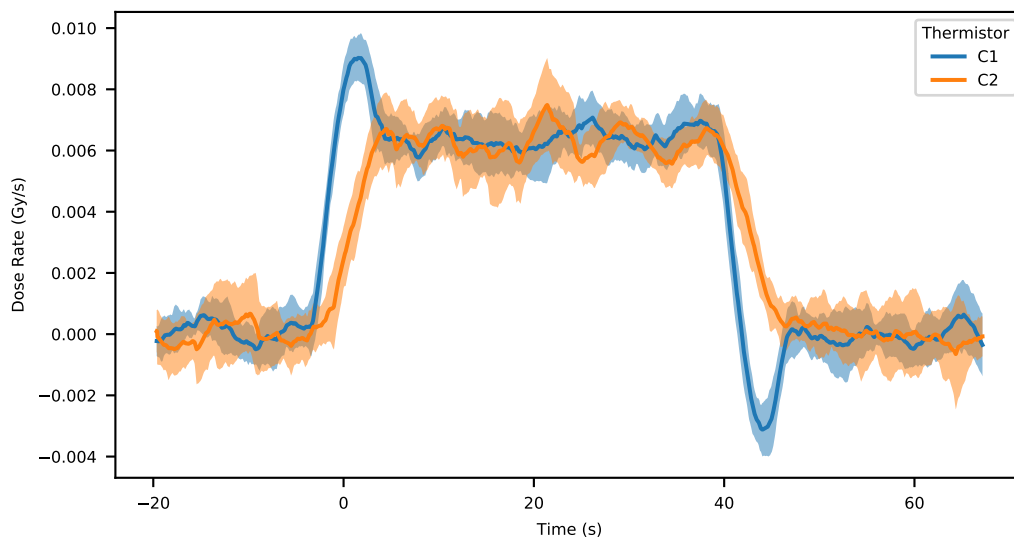


Figure 5.14: Instantaneous dose rate measured by the *NPL proton calorimeter* for an off-centre beam showing the difference in response between the two sensing thermistors.

reconstruct a 2D profile of heat transfer within the *NPL proton calorimeter*.

$$\tau_{\Delta} = \tau_{C1} - \tau_{C2} \quad (5.2)$$

This 2D heat flow measurement is shown in Figure 5.15. The radius of the *NPL proton calorimeter core* is drawn as a black circle to provide context. The measurement points are drawn as solid black circles and are the beam centres, as calculated by the vM2428 detector with the isocentre offset applied. It becomes visible that there is a dividing line bisecting the *core*. This symmetry is expected, given the positions of the two thermistors.

Taking profiles through the horizontal and vertical positions, it becomes possible to perform greater analysis of the rise time difference. These profiles are shown in Figure 5.16. The horizontal scan has a rise time difference of approximately zero for all positions, with a marginally larger standard deviation towards the edges of the *core*. The vertical scan reveals a very linear response correlating beam position and rise time difference.

Using the SciPy algorithm[206], it is possible to calculate the gradient of vertical scan rise time difference to be  $-0.30 \pm 0.11$  s/mm. By calculating the reciprocal, the rise time propagation velocity is calculated to be  $3.29 \pm 0.12$  mm/s. This rise time propagation velocity is comparable to the measured velocity of the moving X-ray beam of  $2.00 \pm 0.01$  mm/s and partially explains the asymmetry in thermistor response and partially explains some of the heat flow effects demonstrated in Section 5.2.4.

This is substantially lower than the expected thermal propagation velocity of graphite, but is an induced effect caused by the dose rate sampling window of 3.2 seconds and the 50% threshold

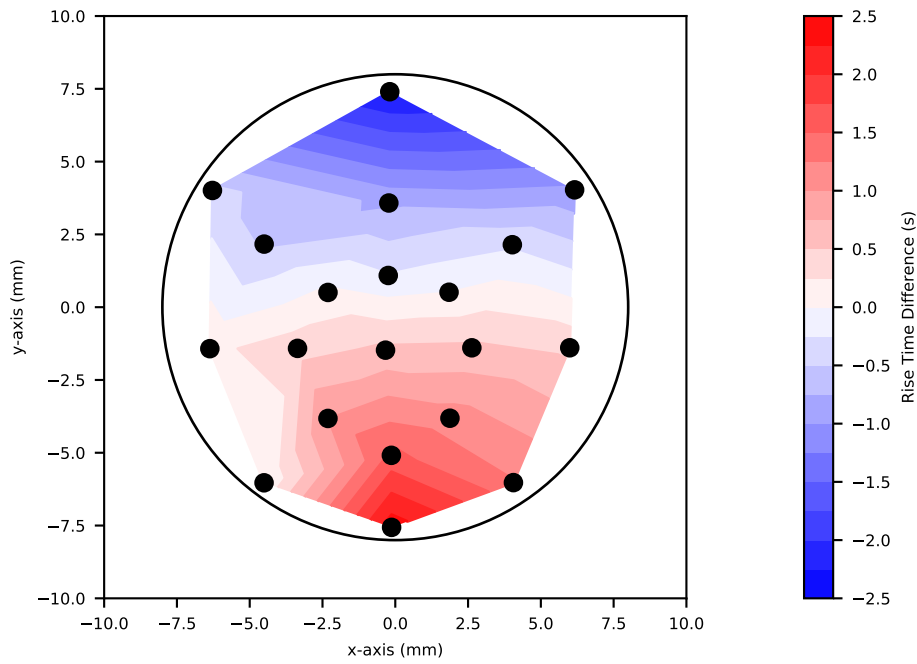


Figure 5.15: Rise time difference as a function of position for the *NPL proton calorimeter*.

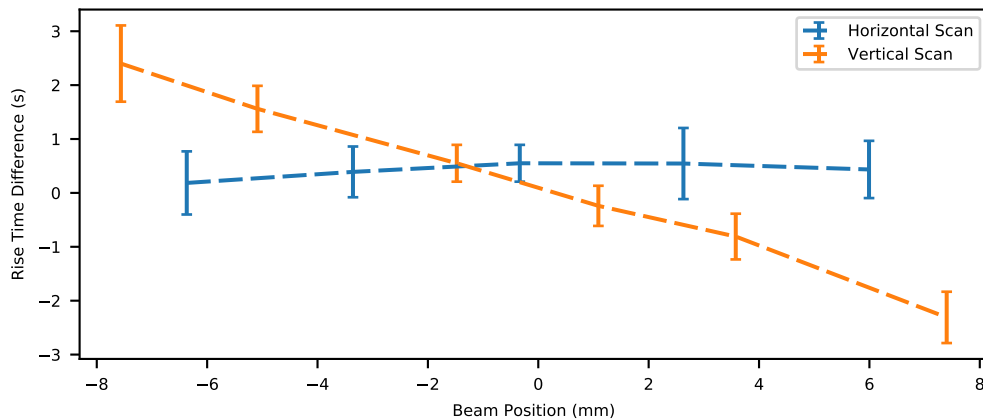


Figure 5.16: Rise time difference profiles of the *NPL proton calorimeter* in the  $x$  and  $y$  axes.

applied to date. Due to the inherent noise of the temperature measurements and low dose rate of the X-ray beam, it was not possible to study dose rate without this window. Despite this, it remains an effective metric for understanding the behaviour of the *NPL proton calorimeter*, and provides quantities that can be compared against simulation (as discussed in Section 5.3).

### 5.2.6 Film Study

After removing the blackout fabric and vM2428 detector PCB, a small study was performed using EBT3 Radiochromic film. This study was to investigate the path and interactions of the X-rays as they passed through the *NPL proton calorimeter*. This is needed to better understand how the radiation propagates and is shaped for further study in section 5.3. To perform this, film

was placed before and after the vM2428 detector and the *NPL proton calorimeter*, as shown in Figure 5.17.

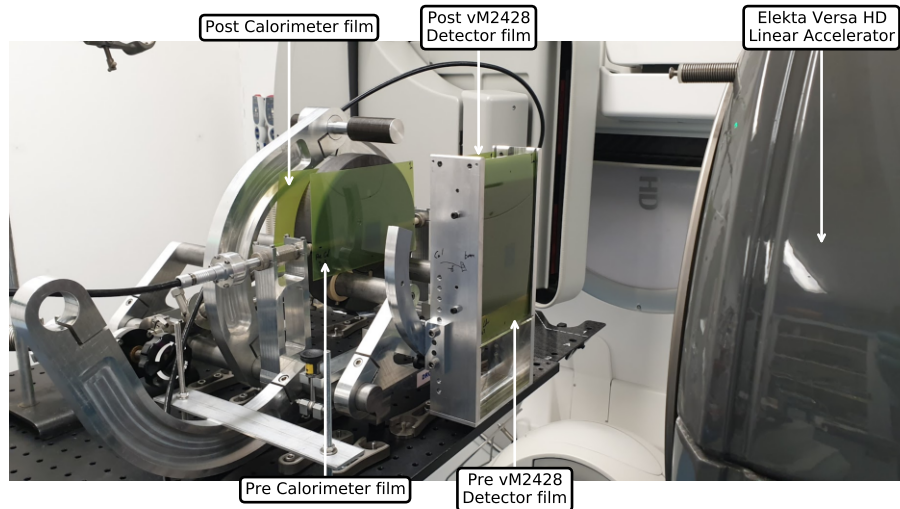


Figure 5.17: Annotated Photograph of the vM2428 Detector with film.

The *NPL proton calorimeter* was exposed with 1000 MU 6 MV FFF X-ray radiation, targeting the centre of the *core* and irradiating all pieces of film simultaneously. Following the procedure recommended by the manufacturer, the EBT3 film was calibrated against an ionisation chamber with the horizontal profiles shown in Figure 5.18. The response of the vM2428 detector was calibrated in terms of dose using the *NPL proton calorimeter* for a 4 mm FWHM beam irradiating the centre of the core. Due to this, it was possible to compare the dose profile of the EBT3 film and the detector.

When comparing the response of the vM2428 detector to the film immediately before, it can be shown that there is good agreement between the two. This is not surprising, confirming previous measurements in this thesis. Comparing the film before and after the vM2428 detector, it is possible to estimate that the intensity of the X-ray beam has reduced by approximately 4%. This reduction is a combination of geometric divergence, and attenuation. By the time the X-rays have reached the *NPL proton calorimeter*, the intensity of the beam has reduced by an additional 40%, although the FWHM has increased from the initial  $3.0 \pm 0.1$  mm to  $3.7 \pm 0.1$  mm. The EBT3 film placed immediately after the *NPL proton calorimeter* reveals that the exit dose profile is much wider, although the peak beam intensity remains approximately constant. It can be concluded from this that the presence of the graphite is causing a non-trivial amount of scatter. Although it is not possible to determine the beam shape in the *core* without Monte Carlo simulations, it can be estimated from these two films. As an alternative visualisation, a 2D reconstruction of the beam profile through the *NPL proton calorimeter* and vM2428 detector can be seen in Figure 5.19.

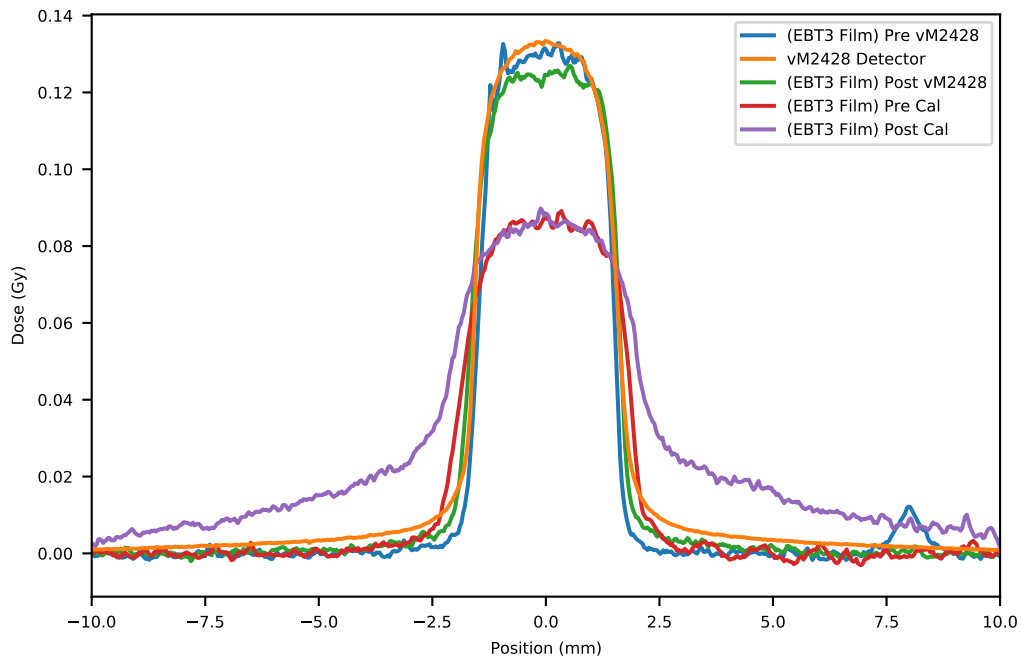


Figure 5.18: Comparison of EBT3 and vM2428 detector dose profiles.

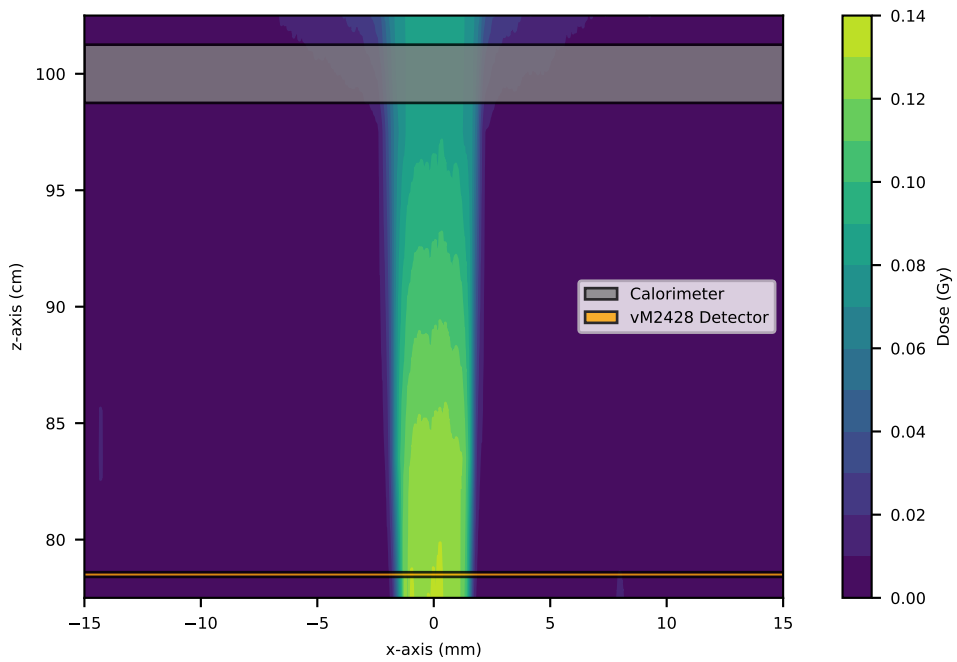


Figure 5.19: Spatial reconstruction of X-Ray dose deposition using EBT3 Film dose profiles.

## 5.3 COMSOL Multiphysics simulations

As demonstrated in this chapter, there is a significant time domain heat flow effect happening within the *NPL proton calorimeter*, impacting the results obtained for the dose determination. To better understand the behaviour and physics processes, a model of the *NPL proton calorimeter* has been constructed.

### 5.3.1 Introduction to COMSOL

The COMSOL Multiphysics software package was chosen to simulate heat flows due to prior experience at the NPL with its modelling capabilities. COMSOL Multiphysics has the ability to simulate many physical interactions, ranging from electrical currents to electrical fatiguing of dielectric materials. It is relevant to this thesis as it has a dedicated Heat Transfer Module[207], capable of simulating conductive, convective, and radiative heat transfer.

### 5.3.2 Prior work

The *NPL proton calorimeter* was previously simulated by L. Petrie in 2016 as part of a doctoral thesis in a collaboration between the University of Surrey, UK, and the NPL[160]. COMSOL Multiphysics simulations conducted as part of this thesis consisted of operating a simplified *NPL proton calorimeter* in quasi-adiabatic mode and providing localised heating to simulate radiation deposition. This model of the calorimeter was composed of four components: a central core, inner jacket, outer jacket, and graphite mantle. The objective of this thesis was to validate whether the *NPL proton calorimeter*, which was initially developed for passive scattered proton beams, was a suitable tool for primary standard dosimetry in Pencil-Beam Scanning.

As part of a series of measurements, the *NPL proton calorimeter* was exposed to proton beams at the Proton Therapy Center, Prague, Czech Republic; and at the Clatterbridge Cancer Centre, Wirral, United Kingdom. Pieces of EBT3 radiochromic film[196] were placed in front of the core to detect and quantify the radiation. The image processing software ImageJ[208] was then used on the processed and calibrated film to obtain parameters of the incident beams.

Simulated radiation induced heat deposition was achieved by localised heating of the calorimeter's voxels. The magnitude of the heating changes per voxel and was based on the depth within the calorimeter (using an appropriate Percentage Depth Dose for the radiation in graphite) and the perpendicular displacement along the axis of the beam (using 2D Gaussian with the previously mentioned beam parameters). An appropriate scaling factor was used to represent the dose rate.

Using this method, stationary and moving proton beams could be simulated. In performing this, confidence in the behaviour of the *NPL proton calorimeter* to Pencil-Beam Scanning was

achieved and the instrument was determined to be a suitable tool for primary standard dosimetry.

The scope of this project was limited. Notably, when simulating and comparing the *NPL proton calorimeter* in response to a moving proton beam, only 1 axis through the centre of the calorimeter core was compared at a time. As discussed in Chapter 2, Pencil-Beam Scanning exposes a complicated 3D shape. For each layer of dose deposited, a complicated 2D shape is delivered with irregular spot weighting. In addition the dose rate is often not constant throughout a delivery, as is the case in the simulated results, although the framework was built into the model to simulate this.

Importantly, this model only functioned in QA mode. When the *NPL proton calorimeter* is used routinely, both modes of operation are used for confirmation and redundancy. Understanding how the heat flow within the calorimeter in ISO mode differs from QA mode is of interest to NPL.

Further to this, there was a lot of simplification of the geometry of the *NPL proton calorimeter*. The PCB ring and internal wires were omitted. The internal thermistors within the calorimeter were also not in the final model, instead the temperature was determined by calculating the temperature at specified coordinates within graphite. This is a suitable approximation to make for slow moving large fields, but needs to be revisited with the recent research interests in high dose rate and spatially fractionated modalities.

#### 5.3.3 Proton calorimeter modelling

With the objectives for a new COMSOL Multiphysics model discussed, the *NPL proton calorimeter* was completely rebuilt in software. This new simulation was built with greater emphasis on optimisation, reducing unnecessary voxels and geometric boundaries. Such efficiencies were necessary as the internal thermistors and wire were represented by physical objects, and their small size caused additional computational overhead. A cross sectional wedge of the COMSOL Multiphysics Calorimeter can be seen in Figure 5.20.

Representing the internal thermistors as physical objects meant that ISO mode could be simulated via a PID based feedback system. Although understanding any differences between the QA mode and ISO mode dose response are beyond the scope of this thesis, the developed model is designed to be as future-proof as possible.

The new simulation was validated against the previous simulation, which was in turn validated using measurements at the Clatterbridge Cancer Centre. This was especially necessary, as updates to the core COMSOL Multiphysics software meant that many of the internal functions had been replaced.

The simulated calorimeter was built to use many of the physical calorimeter's properties, emulating the measured density and internal measurements to high resolution. The temperature de-

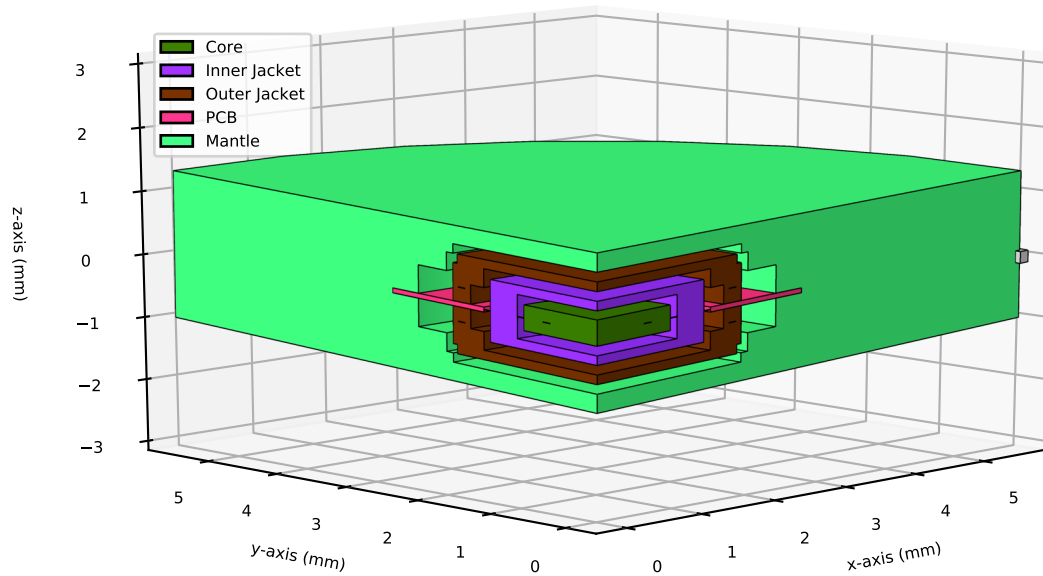


Figure 5.20: Cross section of model of *NPL proton calorimeter* in COMSOL Multiphysics.

pendent specific heat capacity was also incorporated. Although possible, the PID system was disabled for the thermistors embedded in the outer jacket for both QA and ISO mode. The heating thermistors within the outer jacket were instead constrained to always be the target temperature, acting as a heat sink or source as necessary. Doing this provided negligible change in thermal response, but a significant reduction in computational time and improved the response of the internal PID systems when operating in ISO mode. A similar method was used for the previous COMSOL Multiphysics model with the entire outer jacket constrained to a temperature, this new implementation is seen as an advantage as it will allow the outer jacket to experience small changes in temperature as a result of simulated incident radiation.

Further to this, the model was also built to heavily use the MPh[209] Python module which enabled systematic scripting and testing. To facilitate further comparison to the physical calorimeter, all temperature and power outputs from the COMSOL Multiphysics model were wrapped into a file formatted such that the NPL Calorimeter Analysis Software could process.

### 5.3.4 Thermal Conductivity Studies

As demonstrated by the heat flow effects discussed previously, understanding how heat flows through the *NPL proton calorimeter* is very important to know in order to predict future behaviour. As described by Fourier's law of heat conduction, the rate of heat transfer through a material is dependent on the variable  $\alpha$ , the thermal diffusivity (mm/s). This constant is a combination of a material's thermal conductivity,  $k$  (W/m<sup>-1</sup>J<sup>-1</sup>); density,  $\rho$  (kg/m<sup>3</sup>); and the specific

heat capacity,  $c$  (J/kg K). Equation 5.3 links these parameters.

$$\alpha = \frac{k}{\rho c} \tag{5.3}$$

For the batch of graphite used in the *NPL proton calorimeter* the specific heat capacity and density are known to a high degree of precision as they are directly required for determination of absorbed dose to graphite (Equation 2.1). Of the parameters relevant to heat flow within the calorimeter, the only unknown parameter of the graphite is thermal conductivity. Discussions were had with the NPL Temperature & Humidity group on approaching this, but regrettably this is a destructive measurement and it would not be possible to measure in-situ.

It was found in literature that the thermal conductivity of graphite varies between 60-200  $\text{Wm}^{-1}\text{K}^{-1}$ [210]; and is very influenced by the porosity and grain size of the graphite, the graphite temperature and direction of heat gradient[211]. This wide range of thermal conductivity values meant that it was not possible to use an existing value and would need to be calculated via other methods.

A series of simulations were conducted using the described COMSOL Multiphysics model, using a cylindrical heat source of 4 mm diameter. The position of the heat source was moved between the "C1" and "C2" thermistors in steps of 1 mm, which was repeated for a range of thermal conductivity values. The simulated thermistor temperatures were programmatically extracted from COMSOL Multiphysics, and saved into a file format matching the real *NPL proton calorimeter* with 0.2 second time steps. This allowed the NPL Calorimeter Analysis Software program to be used in exactly the same manner for comparability.

Figure 5.21 shows the instantaneous dose rate when heating the simulated calorimeter with a cylindrical beam directly above the "C1" thermistor. The simulated beam provides a uniform heat source depositing an arbitrary 1.30 Gy over 60 seconds. Although the simulated beam only lasts for 60 seconds, the duration appears reduced as the NPL Calorimeter Analysis Software calculates the gradient over a 3.2 second window. It can be seen that for all thermal conductivity values studied, the thermistors temporarily over-shoot in the presence of direct heat deposition before decaying back. When the beam stops, the thermistors again over-shoot with a sharp negative drop of approximately the same magnitude as the first. This behaviour matches the real measurements acquired with the real calorimeter shown previously in Figure 5.2.

The rise time difference between the simulated "C1" and "C2" thermistors were calculated across all of the positions and thermal conductivity values being studied. This result, shown in Figure 5.22, has many similar properties to the physical calorimeter and confirms that there exists a relationship between thermal conductivity and heat wave propagation within the calorimeter

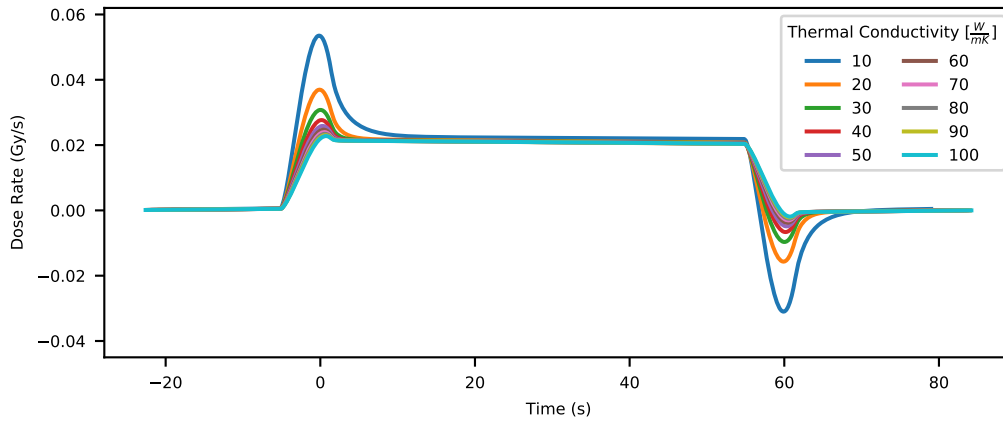


Figure 5.21: Comparison of instantaneous dose rate for various thermal conductivity values.

core. An important difference between this simulated and the physical calorimeter results being that the simulated rise time difference appears to plateau before  $-6$  mm and after  $6$  mm regardless of the thermal conductivity being simulated. This behaviour is expected within the simulation, as the parameter of rise time difference measures the time difference between the two thermistors; once beyond the position of the thermistors this value would become constant. The difference in behaviour with the physical calorimeter is attributed to scattered radiation, as shown previously by Figure 5.18 and Figure 5.19.

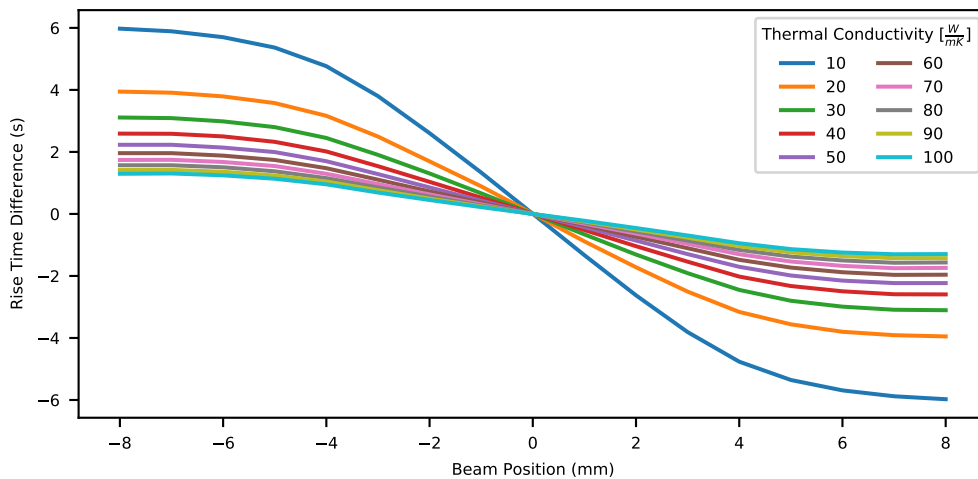


Figure 5.22: Simulation Rise Time comparison for various thermal conductivity values.

The rise time propagation velocity was calculated using only the beams simulated between  $\pm 1$  mm, this region was chosen as it is shown to be linear. The simulated relationship between rise time propagation velocity and thermal conductivity can be seen in Figure 5.23. As shown, there appears to be a linear response between rise time velocity and thermal conductivity. Importantly, this relationship makes sense conceptually and is in agreement with the form of Equation 5.3. When using the previously measured rise time propagation velocity for the physical calorimeter,

$3.29 \pm 0.12$  mm/s, the predicted thermal conductivity is calculated to be  $72 \pm 3$  Wm<sup>-1</sup>K<sup>-1</sup>.

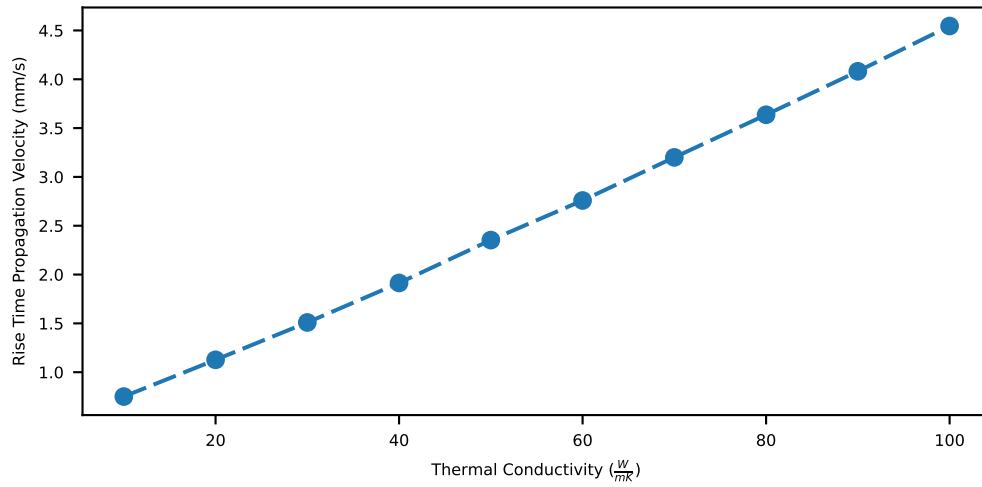


Figure 5.23: Simulated Rise Time Propagation Velocity against Thermal Conductivity.

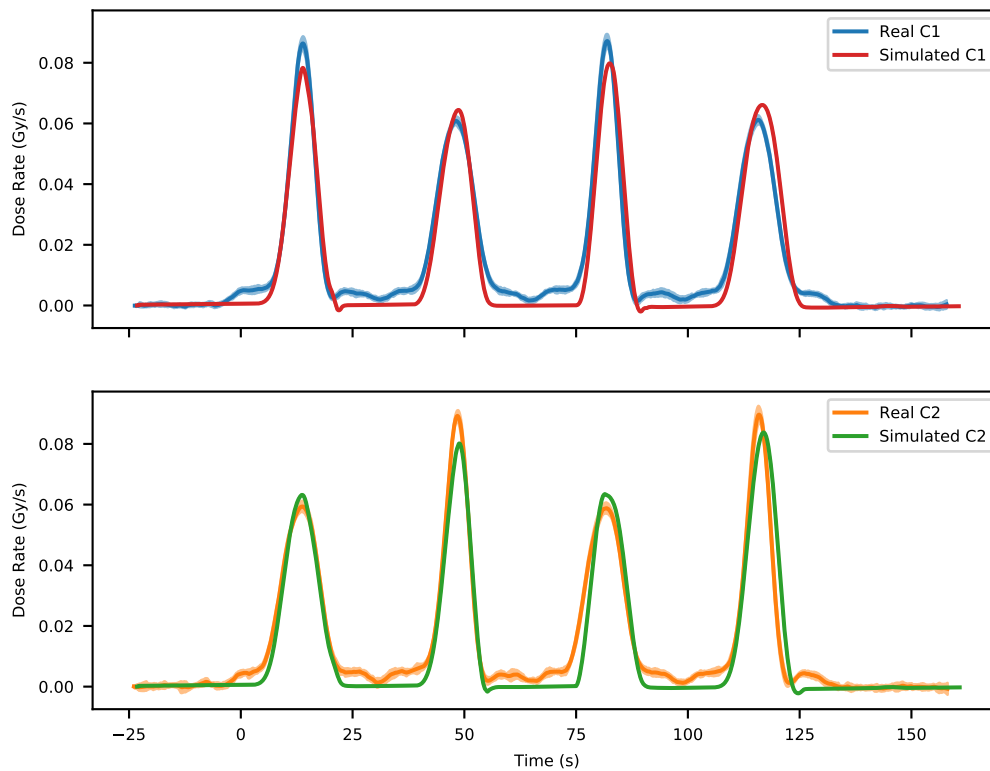


Figure 5.24: Comparison of experimentally measured moving X-ray beam and COMSOL Multiphysics simulated.

The data acquired using the vM2428 detector for the moving radiation beam previously discussed in Section 5.2.4 was parameterised and converted into a file format that COMSOL Multiphysics could open. Using the measured beam position, FWHM, and beam on/off times; it was possible to implement a moving Gaussian heat source using experimental data. The amplitude of

the Gaussian was matched to experimental data, with the results shown in Figure 5.24.

As can be seen, there is good agreement with the experimental data acquired with the *NPL proton calorimeter*. Due to the heat source being a parameterised Gaussian, the dose rate in the *core* resulting from the MLC radiation leakage appears as a constant offset. A localised heat source representing the MLC leak could be added to the simulation to represent this, but the most suitable way would be to use unparameterised data from the vM2428 detector. Despite this drawback, this result was deemed successful enough to have validated the simulation.

By repeating this simulation with the different thermal conductivity values, it was possible to observe the effect on the peak heights. These results can be seen in Figure 5.25. It can be seen that the magnitude of the overshoot is inversely proportional to the thermal conductivity. This overshoot is accompanied by a corresponding undershoot, as shown previously for the stationary beam studies. Interestingly, for a low enough thermal conductivity it becomes possible to observe the direct heat flow and conductive heat flow within the same peak.

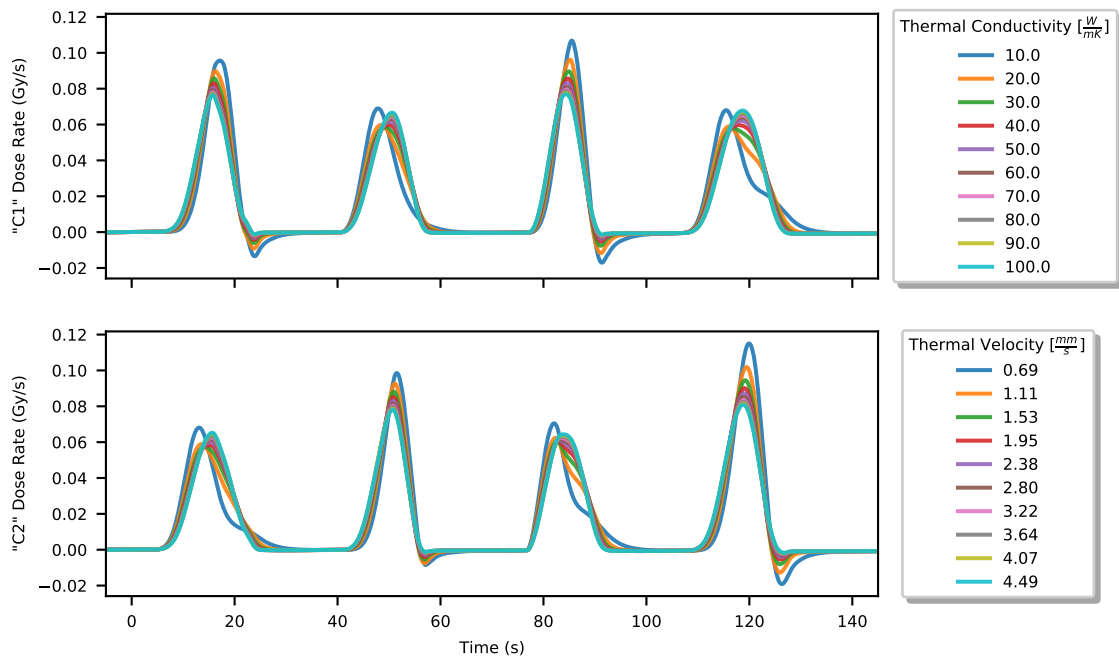


Figure 5.25: Comparison of moving X-ray simulations in COMSOL Multiphysics for various thermal conductivity values.

The ratio of the low:high peaks can be seen in Figure 5.26. It could be expected that for an infinite thermal conductivity, and thus infinite thermal propagation velocity, that the peak ratio tends to 1:1. However as previously described, for a low thermal conductivity there appears to be an increase in peak ratio. This would be due to heat deposited close to a thermistor being unable to dissipate to other areas within the *core* within a given time. A slower moving beam would likely see the peak ratio approach 1:1 for lower values of thermal conductivity as the heat would have

more time to dissipate via conduction.

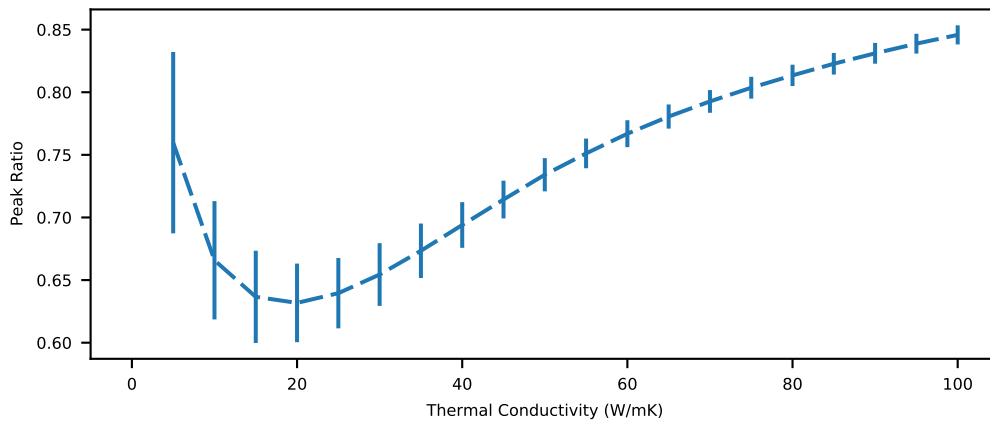


Figure 5.26: Ratio of peaks for moving X-ray simulations in COMSOL Multiphysics for various thermal conductivity values.

With a matched thermal conductivity value, it was possible to measure the thermal propagation velocity in the COMSOL Multiphysics simulation. This was achieved by providing heat energy to a 0.1 mm diameter region at the centre of the *core* for 1 second, and observing the induced change in temperature on the thermistors in 0.25 ms steps. The results of this simulation are shown in Figure 5.27. It can be estimated from this that no change in temperature due to heat conduction can be observed before  $13.5 \pm 0.5$  ms, which can be used to estimate the thermal propagation velocity in graphite to be  $460 \pm 50$  mm/s.

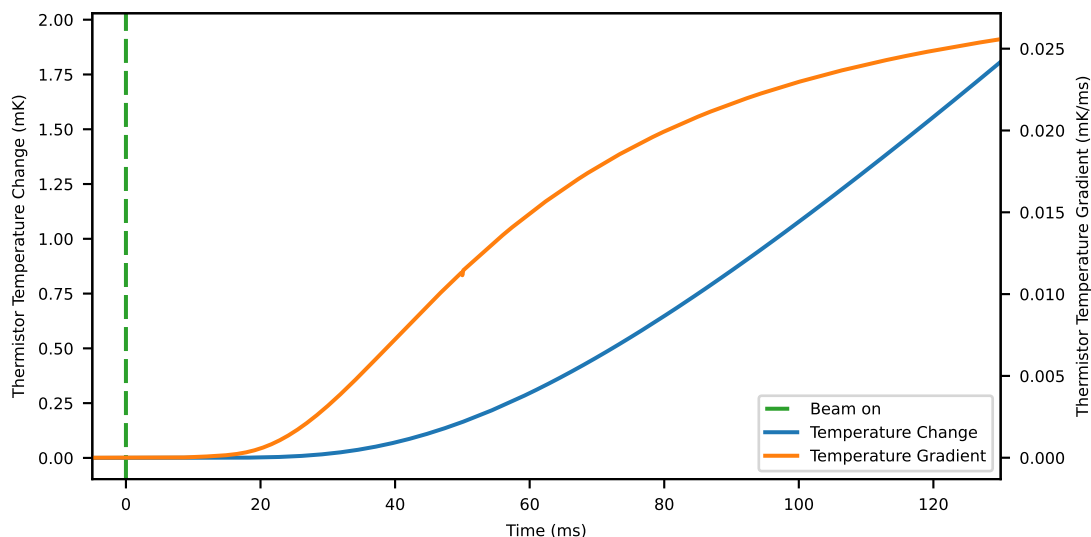


Figure 5.27: Simulated Temperature response of the Calorimeter to small beam positioned at the centre of the *core*.

Using the COMSOL Multiphysics model, a heat flow study with the simulated calorimeter was performed using a rapidly moving heat source emulating PBS. This heat source was a 8 mm FWHM Gaussian, rapidly moved between  $\pm 48$  mm in steps of 4 mm, representing a  $10 \times 10$  cm<sup>2</sup>

field being delivered. Horizontal layers were "painted", with the beam moving vertically down. The positions of the heat source are shown in Figure 5.28.

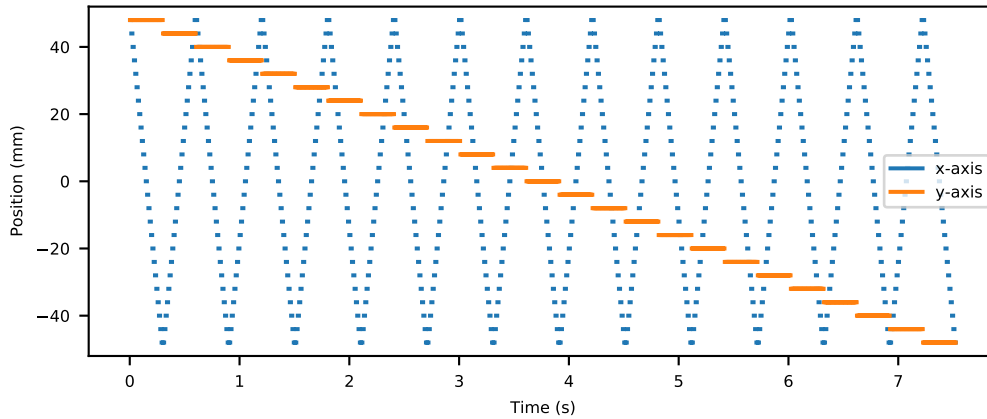


Figure 5.28: Raster scan positions for simulated PBS in COMSOL Multiphysics model.

In true PBS dose is deposited per layer by changing the energy, however for the simulation cylinders were again used depositing heat in all  $z$  positions at once. To represent the rapidly scanning proton beam heat was supplied at each position for 10 ms, with the beam turned off for 1 ms between positions. The amplitude of the Gaussian was scaled such that the total dose delivered to the *core* was approximately 2 Gy, with the entire delivery of 625 spots taking just over 7.5 seconds. To improve the accuracy of the simulation, the time step was reduced from 0.2 seconds (5 Hz) to 1 milliseconds (1000 Hz). Reducing the temporal step size of the simulation by this magnitude was necessary to model the rapidly changing heat flow in the simulated PBS.

Using the simulated thermistors as discussed previously, Figure 5.29 shows the instantaneous dose rate and cumulative dose from the simulation. It can be seen that each of the individual  $y$ -axis positions can be seen as different dose rate peaks. The "C2" thermistor is exposed first in the simulated beam and responds first, as expected, and by the time the first change in dose rate is measured in the "C1" thermistor the "C2" thermistor is already on its second peak. As the heat source is localised, the peaks for the instantaneous dose rate measured in the thermistors are significantly more pronounced than for the entire simulated core.

Figure 5.30 shows the relative surface temperature of the simulated core as the simulated beam passes over. This was calculated by subtracting the average temperature within the core from the 2D surface map produced by COMSOL Multiphysics, and was necessary to enable the heat flow to be visualised on a single scale.

In this figure, it is possible to see the localised temperature distortion in the simulated core as a result of the simulated beam. The direction of the beam in the  $x$  and  $y$  axes are visible as the regions undergoing heating in the simulation experience a very sharp rise in temperature. Despite the relatively slow heat propagation velocity in graphite, the asymmetry in heat deposition

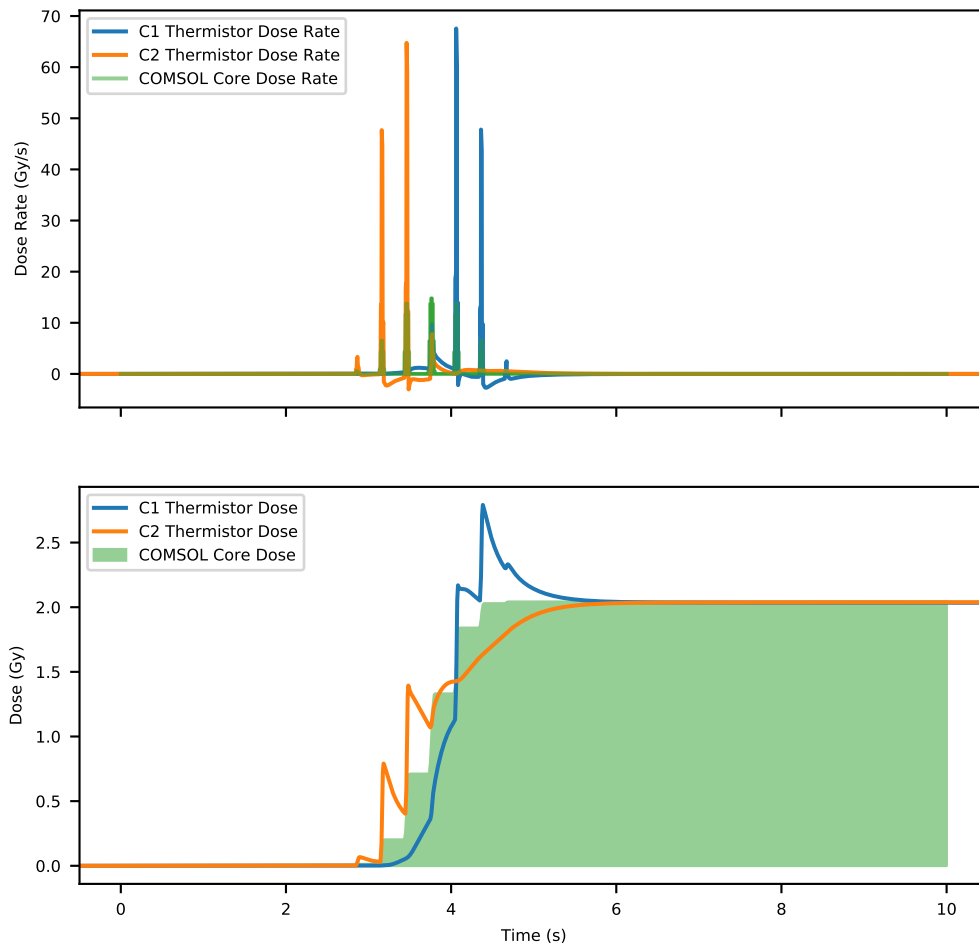
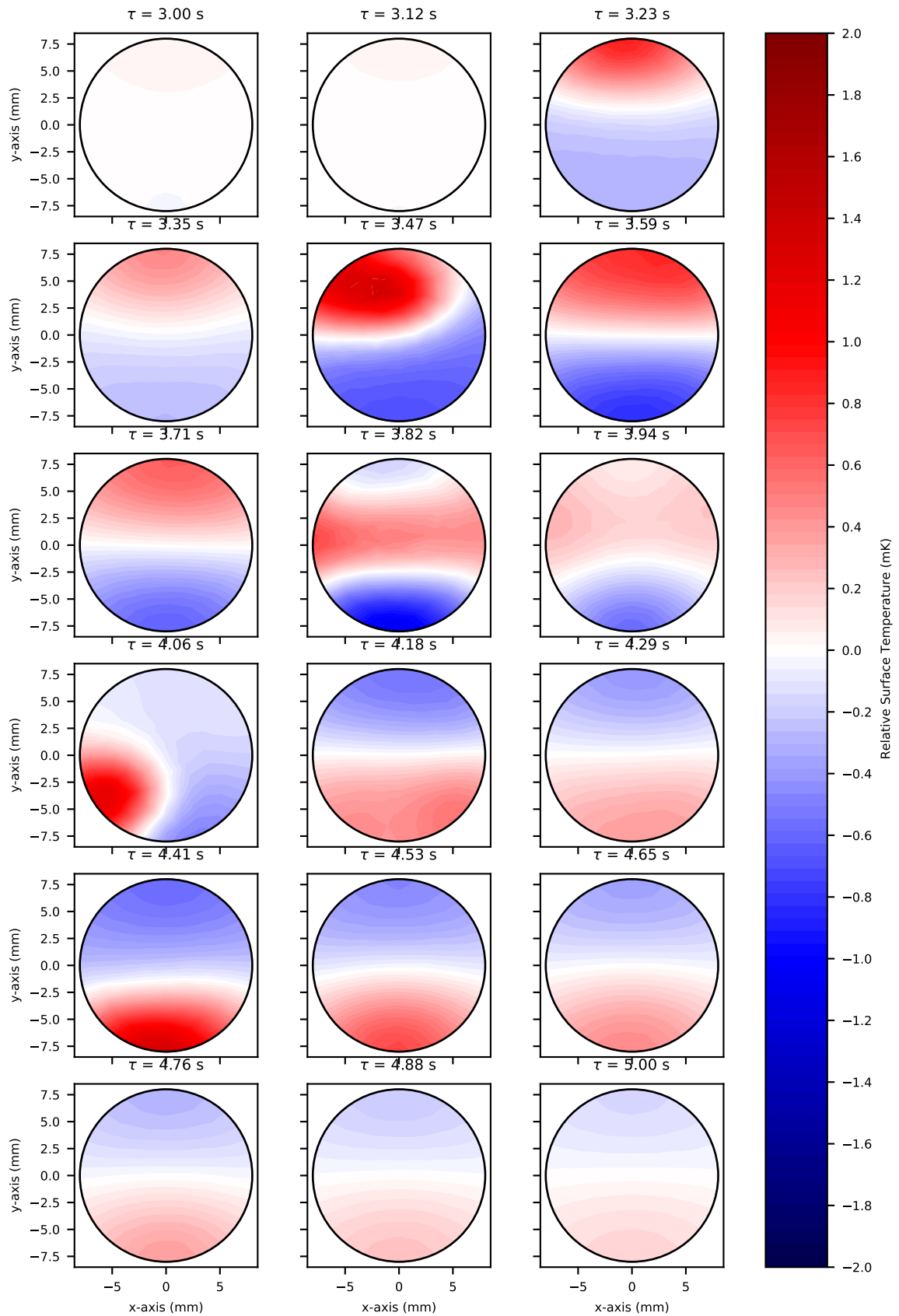


Figure 5.29: Instantaneous dose rate and cumulative dose for simulated PBS study.

becomes negligible as the heat source moves fast enough to compensate .

The effect of changing the direction of the simulated heat source can be seen in Figure 5.31, where the heat source was painted in vertical layers moving from left to right. As with the previous simulation results, the thermistors briefly over-respond as a result of direct heating before rapidly decaying. Although the change is small, it is possible to observe the slight delay between the two thermistors on each pass as the heat source is moved vertically.

Regardless of the beam direction, the dose deposited as determined by the NPL Calorimeter Analysis Software was found to be within 0.5% of the dose as reported by COMSOL Multiphysics. This deviation is within the uncertainty of typical dose measurements using the *NPL proton calorimeter*. The cause of this deviation is likely due to incorrect parameters used for the NPL Calorimeter Analysis Software, which corrects for experimentally measured heat transfer between components. Repeating these measurements for the COMSOL Multiphysics model is possible, but beyond the scope of this thesis at this time.

Figure 5.30: Relative surface temperature of *NPL proton calorimeter* core for simulated PBS.

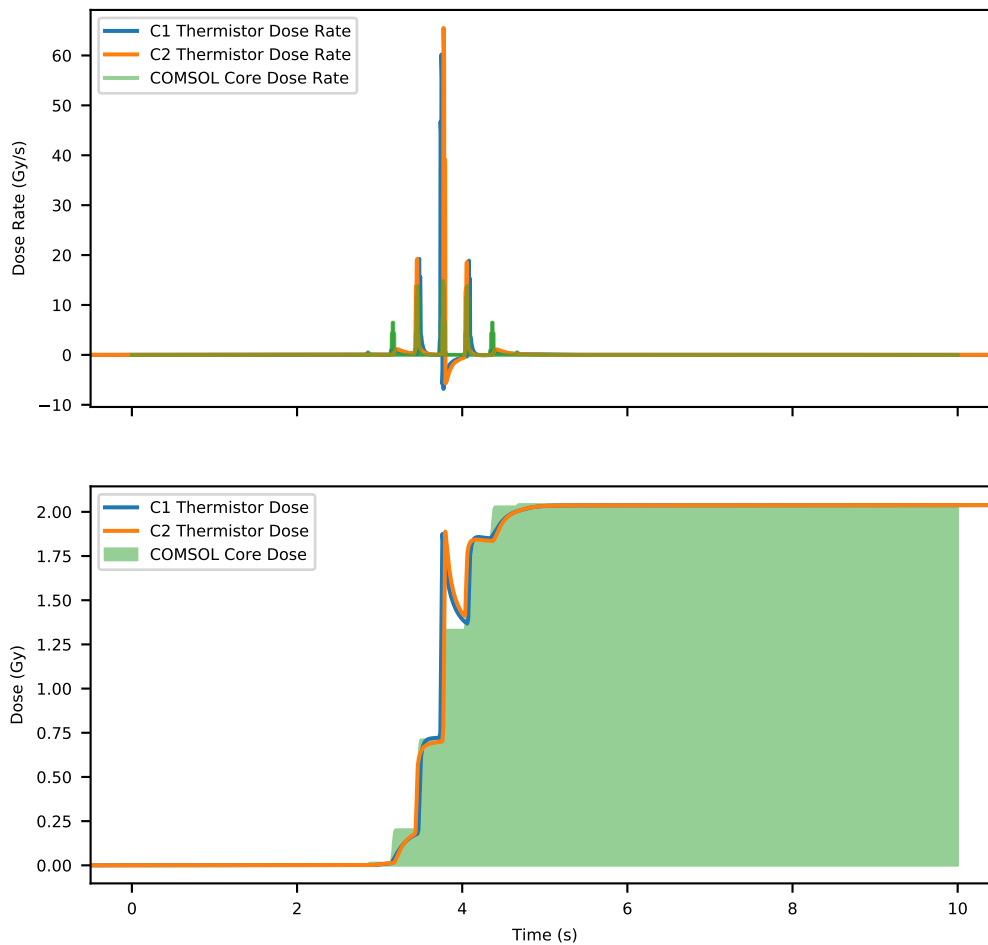


Figure 5.31: Instantaneous dose rate and cumulative dose for simulated PBS study with reversed  $x$  and  $y$  axes beam positions.

## 5.4 Conclusion

In this chapter, the results from experimental studies with the *NPL proton calorimeter* were presented. Using the vM2428 detector, a large format CMOS sensor, it was possible to measure the position, intensity, and FWHM of an X-ray beam in combination with the *NPL proton calorimeter*. Together, it was possible to investigate the effect of localised heating within the *NPL proton calorimeter* graphite core through a series of stationary and dynamic measurements.

The rise time velocity, with a 3.2 second averaging window, through graphite could be measured experimentally to be  $3.29 \pm 0.12$  mm/s. This finite velocity was found to manifest as an asymmetry in instantaneous dose rate when exposing the *NPL proton calorimeter* with a slow moving beam of radiation, when applying a 3.2 averaging window, but appeared to have no impact of cumulative dose. This asymmetry was unexpected and warranted further study to which a model of the *NPL proton calorimeter* was built in COMSOL Multiphysics which was able to replicate this behaviour, providing confidence that it was not an experimental artefact but a core part of the calorimeter response. This model was used to calculate an estimate of the thermal wave propagation velocity

in graphite of  $460 \pm 50$  mm/s.

The COMSOL Multiphysics model was then expanded to simulate the localised heating effects of PBS with a rapidly scanned heat source. It was found that the embedded thermistors would significantly over-respond to direct heating, reporting instantaneous dose rate several times that actually being applied. Again, this did not impact the measurement of the dose deposited within the simulated *core*, providing a measure of confidence for PBS.

To expand this work to be relevant to the clinical practice, the model needs to be expanded to include a *z*-axis component to the deposition of heat, which would enable a PDD to be simulated. From this, it would be possible to investigate radiative heat effects, further expanding on the work by Petrie *et al.*. This was part of the original scope of the thesis, however due to the impact of the "COVID-19" Coronavirus Disease Pandemic, it was not possible to acquire beam time at a clinical facility with the *NPL proton calorimeter*.

## Chapter 6

# Conclusion

It is predicted that up to 50% of people born after 1960 in the UK will develop some form of cancer during their lifetime[40]. Of those patients in the UK receiving therapy, radiotherapy is involved in 27% of all primary cancer treatments[43]. This external beam X-ray radiotherapy is an effective form of tumour control however due to the physical properties of X-rays, it causes additional radiation dose to be deposited in healthy tissue increasing the likelihood of side effects. For paediatric patients in particular this can result in an increased probability of long term consequences, such as a radiation-induced loss of IQ relative to their peers [108]. An alternative form of external beam radiotherapy using protons PBT has been shown to have beneficial effects due to the Bragg peak which can result in a higher dose deposition in the tumour volume whilst minimising dose in healthy tissue. PBT has many challenges associated with it posing challenges for both routine quality-assurance and primary standard dosimetry; demanding new technologies, techniques, and innovations. With the construction of new NHS and private healthcare radiotherapy facilities in the UK for PBT, there is more pressure than ever to ensure that patients receiving cancer therapies receive the best quality care possible.

This thesis has investigated the suitability of SSD and CMOS detectors for a combined system with the *NPL proton calorimeter*, in order to enhance the UK Primary Standard for Absorbed Dose for Proton Radiotherapy. Such a combined system would be able to provide a primary standard measurement of the integral dose deposited from a proton pencil beam; whilst simultaneously measuring the beam position, size, and uniformity. It would be possible to use the data acquired from the silicon detector to conduct independent simulations of the radiation propagation and internal heat flow, providing a level of confidence in complex radiation therapies.

In Chapter 3, the PRAVDA tracker unit was evaluated in an Elekta Synergy Linac. The three non-orthogonal planes of the detector, whilst optimised for pCT, are redundant for X-ray beam therapy and PBT, and required the development of a reconstruction algorithm (Appendix A.1)

in order to reconstruct the incident dose. Although it was found that the detector was able to calculate beam centre within  $\pm 0.1$  mm of expected, a tolerance that is clinically acceptable, the maximum region that could be used for beam monitoring was limited due to the relative small active area of the SSDs that composed the detector. The reconstruction algorithms presented were not cable of reconstructing the 2D dose deposition in a manner that would be clinically acceptable, although this could potentially be overcome with Deep Learning as has been performed for xCT[212]. Unfortunately, damage to the detector during transportation prevented further research into the application of the PRaVDA tracker unit to proton beams of clinically relevant energies.

The use of the vM1212 and vM2428 large-format CMOS detectors for 2D dose reconstruction of X-ray and proton beams was investigated in Chapter 4. These detectors were designed for X-ray imaging, and not optimised for the harsh ionising radiation environment of external beam radiotherapy. Regardless, it was found that the CMOS detectors were able to obtain 2D dose measurements comparable to EBT3 Gafchromic film, a detector used routinely in the clinical environment. The CMOS detectors were able to obtain not only the beam position, but able to acquire measurements of the 2D uniformity of the incident beam on a frame by frame basis, something not possible with SSD detectors. Although the frame rate of the detectors was lower than that of the PRaVDA tracker unit, there is no requirement for a certain number of frames for superposition in order to acquire a 1D profile, resulting in the possibility of pulse by pulse dosimetry using CMOS detectors. This could be of benefit to the "FLASH" radiotherapy modality in the future, although at present the current full-well of the detectors would not be sufficiently large enough to prevent saturation of the detector. Such a saturation would not be entirely unexpected, given that the detector was designed for diagnostic imaging with much lower dose rates. With new silicon detectors for radiotherapy applications coming to market, such as the myQA SRS by IBA Dosimetry[213] it is likely that there are to be further applications of CMOS detectors to radiotherapy in the future. The continued development of CMOS pixel designs with greater radiation tolerance, such as the MALTA pixel detector[214] offers one such possibility.

The use of CMOS detectors for dosimetry in spatially fractionated radiotherapy has been highlighted in this thesis, and is discussed in Chapter 4. This work, also presented in Appendix B.2 and B.2, has shown that CMOS detectors are viable instruments for microbeam dosimetry, able to acquire real-time beam information at an accuracy again comparable to radiochromic film. Although the pixels of the vM1212 and vM2428 detectors are too large ( $50 \mu\text{m}$ ) for the smallest microbeams used for preclinical research ( $25 \mu\text{m}$ )[215], there exists other CMOS pixel designs that could be used or adapted. This could be combined with a pixel with a high tolerance to ionising radiation, for an instrument truly optimised for microbeam dosimetry. In the short term

---

however, such an instrument is unlikely to be developed as it would not be economically viable due to the current preclinical status of microbeam radiotherapy.

A proof of principle investigation combining the vM2428 detector with the *NPL proton calorimeter* was described in Chapter 5. Here it is demonstrated that it is possible to synchronise detection of incident radiation on both devices; enabling the acquisition of beam information of stationary and dynamic beams, and integral dose rates from the calorimeter. Using beam position information as acquired using the CMOS detector, it was shown that not only was there a difference in spatial response when irradiating different points within the core; but that there is a difference in temporal response, attributed to internal heat flow. A difference in temperature response of thermistors was experimentally measured which, when averaged over a 3.2 second window, propagates through the graphite at  $3.29 \pm 0.12$  mm/s. An investigation with a moving beam of radiation provided unexpected integral dose rates as recorded on the calorimeter, where it was implied that the direction of beam travel could impact the result. Using the recorded data of the radiation as acquired by the vM2428 detector, no asymmetry was observed implying this could be due to the internal heat flow within the *NPL proton calorimeter*.

To better understand the physics processes occurring, a model of the *NPL proton calorimeter* was built in the COMSOL Multiphysics finite element modelling software. This model was capable of processing parameterised data from the vM2428 detector, allowing the measurement to be simulated using real data. A graphite thermal conductivity value of  $72 \pm 3$  Wm<sup>-1</sup>K<sup>-1</sup> was found to replicate the asymmetry observed for the dynamic beam, confirming that this was an internal heat flow effect. This value was used to estimate the heat flow propagation velocity of graphite to be  $460 \pm 50$  mm/s. The model was then expanded to simulate PBS where it was found that despite significant instantaneous dose rates, the cumulative dose reported by the simulated thermistors was within 0.5% of that deposited by the COMSOL Multiphysics software. Although beyond the scope of the thesis, the model is built in such a way that it can be used for future investigations studying the differences between the QA and ISO modes of operation; the impact of the internal PCB; and the effect of beam position uncertainty on cumulative dose.

This thesis has demonstrated the potential of a system composing of a *NPL proton calorimeter* and a CMOS detector, although for use in a routine proton clinical environment the tolerance to radiation induced "*Bulk Damage*" (Section 2.3.6) must be improved. It is recommended that future studies using the combined system be investigated in PBT facilities. An additional avenue of research would be to investigate the 2D dose signal recorded by the CMOS detector in the context of verifying Monte Carlo simulations, providing greater confidence to the shape and position of the Bragg peaks. This could also be incorporated into the COMSOL Multiphysics model, simulating 3D heat flow effects. Such 3D heat flow studies would certainly be of interest if performing calorimetry

in spatially fractionated beams.

A possibility for the future is a pixelated detector could record the delivery of a scanned pencil beam, enabling Monte Carlo simulations of each beamlet, which would be fed into COMSOL Multiphysics for heat flow simulations. A chain of software in this manner would be able to obtain per-measurement correction factors for heat flow within the *NPL proton calorimeter*. This has the potential to reduce the uncertainty of the absorbed dose measurement, in addition to providing verification of the beam delivery.

# References

- [1] ‘Report 85: Fundamental quantities and units for ionizing radiation.’ eng. In: *Journal of the ICRU* 11.1 (Apr. 2011), pp. 1–31. ISSN: 1742-3422 (Electronic). DOI: 10.1093/jicru/ndr011.
- [2] N. Petoussi-Henss, W.E. Bolch, K.F. Eckerman et al. ‘Annals of the ICRP’. In: *Annals of the ICRP* 6.1 (1981), p. 1. ISSN: 01466453. DOI: 10.1016/0146-6453(81)90127-5.
- [3] COMSOL Multiphysics. *About COMSOL*. URL: <https://uk.comsol.com/company>.
- [4] Michael Joiner and Albert van der Kogel, eds. *Basic Clinical Radiobiology*. 4th. London: CRC Press, 2009. ISBN: 9780429190896. DOI: 10.1201/b15450.
- [5] National Instruments. *What is LabVIEW?* URL: <https://www.ni.com/en-gb/shop/labview.html>.
- [6] Dirk P. Kroese, Tim Brereton, Thomas Taimre et al. ‘Why the Monte Carlo method is so important today’. In: *Wiley Interdisciplinary Reviews: Computational Statistics* 6.6 (2014), pp. 386–392. ISSN: 19390068. DOI: 10.1002/wics.1314.
- [7] J Daintith. *A Dictionary of Physics*. Oxford Paperback Reference. OUP Oxford, 2009. ISBN: 9780199233991. URL: <https://books.google.co.uk/books?id=N2PEAQAACAAJ>.
- [8] Martyn Sené, Ian Gilmore and Jan Theodoor Janssen. ‘Metrology is key to reproducing results’. In: *Nature* 547.7664 (2017), pp. 397–399. ISSN: 14764687. DOI: 10.1038/547397a.
- [9] Nature Methods. ‘Better research through metrology’. In: *Nature Methods* 15.6 (2018), p. 395. ISSN: 15487105. DOI: 10.1038/s41592-018-0035-x.
- [10] Robert Kaarls. ‘Metrology, essential to trade, industry and society’. In: *Accreditation and Quality Assurance* 12.8 (2007), pp. 435–437. ISSN: 1432-0517. DOI: 10.1007/s00769-007-0301-6. URL: <https://doi.org/10.1007/s00769-007-0301-6>.
- [11] Ian Mills, Tomislav Cvitas, Klaus Homann et al. *Quantities, Units and Symbols in Physical Chemistry*. 2nd. Oxford, United Kingdom, 1993. ISBN: 9780123864543. DOI: 10.1016/B978-0-12-386454-3.01021-6.

- 
- [12] National Physical Laboratory. *Differences between metrology and measurement - NPL*. URL: <https://www.npl.co.uk/resources/q-a/the-difference-between-metrology-and-measurement>.
- [13] EURAMET. *EMPIR Call Process List, List 1a: EURAMET NMIs and DIs*. Tech. rep. EURAMET, 2019. URL: <https://msu.euramet.org/downloads/documents/List1a.pdf>.
- [14] *EURAMET - European Association of National Metrology Institutes*. URL: <https://www.euramet.org/>.
- [15] *Kibble balance - NPL*. URL: <https://www.npl.co.uk/kibble-balance>.
- [16] *Josephson primary standard for voltage - NPL*. URL: <https://www.npl.co.uk/products-services/quantum-technology/josephson-voltage-standard>.
- [17] M Stock, S Davidson, H Fang et al. ‘Maintaining and disseminating the kilogram following its redefinition’. In: *Metrologia* 54.6 (Oct. 2017), S99. ISSN: 0026-1394. DOI: 10.1088/1681-7575/AA8D2D.
- [18] A D Ritchie. *Scientific method: An Inquiry into the Character and Validity of Natural Laws*. International Library of Philosophy. Taylor & Francis, 2014. ISBN: 9781317830030. URL: <https://books.google.co.uk/books?id=Z-vgAwAAQBAJ>.
- [19] Ian Farrance and Robert Frenkel. *Uncertainty of measurement: A review of the rules for calculating Uncertainty components through functional relationships*. 2012.
- [20] Department of Health and Social Care. *Government commits £250 million for innovative cancer treatment to save lives and reduce side effects*. 2013. URL: <https://www.gov.uk/government/news/government-commits-250-million-for-innovative-cancer-treatment-to-save-lives-and-reduce-side-effects>.
- [21] Rutherford Cancer Centres. *First for high energy proton therapy in the UK*. 2018. URL: <https://www.therutherford.com/news/first-cancer-patient-treated-with-high-energy-proton-therapy-in-the-uk/>.
- [22] S. Flynn, T. Price, S. Galer et al. ‘Characterisation of a megavolt X-Ray therapeutic beam using non-orthogonal strip detectors for future enhanced primary standard dosimetry’. In: *Journal of Instrumentation* 14.09 (Sept. 2019), T09007–T09007. ISSN: 1748-0221. DOI: 10.1088/1748-0221/14/09/T09007. URL: [http://iopscience.iop.org/1748-0221/14/09/T09007?utm\\_source=researcher\\_app&utm\\_medium=referral&utm\\_campaign=RESR\\_MRKT\\_Researcher\\_inbound%20https://iopscience.iop.org/article/10.1088/1748-0221/14/09/T09007](http://iopscience.iop.org/1748-0221/14/09/T09007?utm_source=researcher_app&utm_medium=referral&utm_campaign=RESR_MRKT_Researcher_inbound%20https://iopscience.iop.org/article/10.1088/1748-0221/14/09/T09007).

## REFERENCES

---

- [23] Wei-jie Guan, Zheng-yi Ni, Yu Hu et al. ‘Clinical Characteristics of Coronavirus Disease 2019 in China’. In: *New England Journal of Medicine* 382.18 (2020), pp. 1708–1720. ISSN: 0028-4793. DOI: 10.1056/nejmoa2002032.
- [24] Eva Bianconi, Allison Piovesan, Federica Facchin et al. ‘An estimation of the number of cells in the human body’. In: *Annals of Human Biology* 40.6 (2013), pp. 463–471. ISSN: 03014460. DOI: 10.3109/03014460.2013.807878.
- [25] S. C. Rastogi. *Cell Biology*. Second Edi. New Delhi: New Age International (P) Limited Publishers, 2002. ISBN: 9788122413977. URL: <https://books.google.co.uk/books?id=h6Hj53zCtcoC>.
- [26] Nigel Chaffey. *Molecular biology of the cell*. eng. 4th Editio. Vol. 91. 3. New York: Oxford University Press, Feb. 2003, p. 401. DOI: 10.1093/aob/mcg023. URL: <https://www.ncbi.nlm.nih.gov/pmc/articles/PMC4244961/>.
- [27] Frederica P. Perera. ‘Environment and cancer: Who are susceptible?’ In: *Science* 278.5340 (1997), pp. 1068–1073. ISSN: 00368075. DOI: 10.1126/science.278.5340.1068.
- [28] Anthony Tubbs and André Nussenzweig. ‘Endogenous DNA Damage as a Source of Genomic Instability in Cancer’. eng. In: *Cell* 168.4 (Feb. 2017), pp. 644–656. ISSN: 1097-4172. DOI: 10.1016/j.cell.2017.01.002. URL: <https://pubmed.ncbi.nlm.nih.gov/28187286%20https://www.ncbi.nlm.nih.gov/pmc/articles/PMC6591730/>.
- [29] Jan H J Hoeijmakers. ‘DNA damage, aging, and cancer.’ eng. In: *The New England journal of medicine* 361.15 (Oct. 2009), pp. 1475–1485. ISSN: 1533-4406 (Electronic). DOI: 10.1056/NEJMra0804615.
- [30] Stephen P. Jackson and Jiri Bartek. ‘The DNA-damage response in human biology and disease’. In: *Nature* 461.7267 (2009), pp. 1071–1078. ISSN: 00280836. DOI: 10.1038/nature08467.
- [31] Vincent Pagès and Robert P.P. Fuchs. ‘How DNA lesions are turned into mutations within cells?’ In: *Oncogene* 21 (2002), pp. 8957–8966. ISSN: 09509232. DOI: 10.1038/sj.onc.1206006.
- [32] Abel Gonzalez-Perez, Radhakrishnan Sabarinathan and Nuria Lopez-Bigas. ‘Local Determinants of the Mutational Landscape of the Human Genome’. In: *Cell* 177.1 (2019), pp. 101–114. ISSN: 10974172. DOI: 10.1016/j.cell.2019.02.051. URL: <https://doi.org/10.1016/j.cell.2019.02.051>.
- [33] H Lodish, A Berk, SL Zipursky et al. *Molecular Cell Biology*. 4th Editio. New York: W. H. Freeman and Company, 2000. ISBN: 0-7167-3136-3. URL: <https://www.ncbi.nlm.nih.gov/books/NBK21554/>.

- [34] Aziz Sancar, Laura A. Lindsey-Boltz, Keziban Ünsal-Kaçmaz et al. 'Molecular mechanisms of mammalian DNA repair and the DNA damage checkpoints'. In: *Annual Review of Biochemistry* 73 (2004), pp. 39–85. ISSN: 00664154. DOI: 10.1146/annurev.biochem.73.011303.073723.
- [35] Christopher J. Lord and Alan Ashworth. 'The DNA damage response and cancer therapy'. In: *Nature* 481.7381 (2012), pp. 287–294. ISSN: 00280836. DOI: 10.1038/nature10760.
- [36] J Ater, Nj Tarbell and E Laws Jr. 'Optic nerve, chiasmal, and hypothalamic tumors'. In: *Cancer in the Nervous System, ed* (2002), pp. 158–170. URL: [http://soc-neuro-onc.org/levin/Levin\\_ch05\\_p158-170.pdf](http://soc-neuro-onc.org/levin/Levin_ch05_p158-170.pdf).
- [37] Angelo Fortunato, Amy Boddy, Diego Mallo et al. 'Natural selection in cancer biology: From molecular snowflakes to trait hallmarks'. In: *Cold Spring Harbor Perspectives in Medicine* 7.2 (2017), pp. 1–14. ISSN: 21571422. DOI: 10.1101/cshperspect.a029652.
- [38] Aisha Patel. 'Benign vs Malignant Tumors'. In: *JAMA Oncology* 6.9 (2020), p. 1488. ISSN: 23742445. DOI: 10.1001/jamaoncol.2020.2592.
- [39] M J Lind. 'Cancer and Its Management 4th Edition'. In: *British Journal of Cancer* 91.10 (2004), p. 1851. ISSN: 1532-1827. DOI: 10.1038/sj.bjc.6602210. URL: <https://doi.org/10.1038/sj.bjc.6602210>.
- [40] C R Smittenaar, K A Petersen, K Stewart et al. 'Cancer incidence and mortality projections in the UK until 2035'. In: *British Journal of Cancer* 115.9 (Oct. 2016), pp. 1147–1155. ISSN: 0007-0920. DOI: 10.1038/bjc.2016.304. URL: <http://www.ncbi.nlm.nih.gov/pubmed/27727232> <http://www.pubmedcentral.nih.gov/articlerender.fcgi?artid=PMC5117795> <http://www.nature.com/articles/bjc2016304>.
- [41] J Maddams, M Utley and H Møller. 'Projections of cancer prevalence in the United Kingdom, 2010-2040.' In: *British journal of cancer* 107.7 (Sept. 2012), pp. 1195–202. ISSN: 1532-1827. DOI: 10.1038/bjc.2012.366. URL: <http://www.ncbi.nlm.nih.gov/pubmed/22892390>.
- [42] World Health Organization. *Cancer*. URL: <https://www.who.int/news-room/fact-sheets/detail/cancer>.
- [43] *CancerData*. URL: <https://www.cancerdata.nhs.uk/treatments>.
- [44] *Radiotherapy - NHS*. 2017. URL: <https://www.nhs.uk/conditions/radiotherapy/>.
- [45] Geoff Delaney, Susannah Jacob, Carolyn Featherstone et al. *The role of radiotherapy in cancer treatment: Estimating optimal utilization from a review of evidence-based clinical guidelines*. Sept. 2005. DOI: 10.1002/cncr.21324.

## REFERENCES

---

- [46] M. Abdel-Wahab, E. Fidarova and A. Polo. ‘Global Access to Radiotherapy in Low- and Middle-income Countries’. In: *Clinical Oncology* 29.2 (2017), pp. 99–104. ISSN: 14332981. DOI: 10.1016/j.clon.2016.12.004. URL: <http://dx.doi.org/10.1016/j.clon.2016.12.004>.
- [47] National Cancer Institute. *Definition of solid tumor - NCI Dictionary of Cancer Terms*. URL: <https://www.cancer.gov/publications/dictionaries/cancer-terms/def/solid-tumor>.
- [48] Joe Cullen, David Drabble, Cristina Castellanos et al. *Recommendations for achieving a world-class radiotherapy service in the UK*. Tech. rep. The Tavistock Institute, 2014. URL: [http://www.tavistockinstitute.org/wp-content/uploads/2014/05/Tavistock\\_Projects\\_Recommendations-for-achieving-a-world-class-radiotherapy-service-in-the-UK-.pdf](http://www.tavistockinstitute.org/wp-content/uploads/2014/05/Tavistock_Projects_Recommendations-for-achieving-a-world-class-radiotherapy-service-in-the-UK-.pdf).
- [49] *All Party Parliamentary Group for Radiotherapy Manifesto for Radiotherapy Improving cancer survival with a modern world-class radiotherapy service*. Tech. rep. URL: <https://www.england.nhs.uk/wp-content/uploads/2013/06/b01-radiotherapy.pdf>.
- [50] *Cancer survival rates ‘threatened by rising cost’ - NHS*. URL: <https://www.nhs.uk/news/cancer/cancer-survival-rates-threatened-by-rising-cost/>.
- [51] William Herschel. ‘XIV. Experiments on the refrangibility of the invisible rays of the sun’. In: *Philosophical Transactions of the Royal Society of London* 90 (1800), pp. 284–292. DOI: <https://doi.org/10.1098/rstl.1800.0015>.
- [52] Arthur Stanton. ‘Wilhelm Conrad Röntgen on a new kind of rays: translation of a paper read before the Würzburg Physical and Medical Society’. In: *Nature* 53 (1895), pp. 274–276.
- [53] Richard F. Mould. ‘Leopold Freund (1868-1943) & priority for X-ray therapy for benign disease’. In: *Nowotwory* 69.5-6 (2019), pp. 187–190. ISSN: 23002115. DOI: 10.5603/NJO.2019.0033.
- [54] G. Fuchs and J. Hofbauer. ‘Das Spätresultat einer von 70 Jahren durchgeführten Röntgenbestrahlung.’ In: *Strahlentherapie* 139 (1966), pp. 161–166.
- [55] Joseph Belot. *Radiotherapy in Skin Disease*. Rebman, 1905, p. 463. URL: <https://books.google.co.uk/books?id=WvA0AQAAMAAJ>.
- [56] Ralston Paterson. ‘Roentgen-Ray Treatment of Primary Carcinoma of the Lung’. In: *The British Journal of Radiology* 1.3 (Mar. 1928), pp. 90–96. ISSN: 0007-1285. DOI: 10.1259/0007-1285-1-3-90. URL: <https://doi.org/10.1259/0007-1285-1-3-90>.

- [57] Gösta Forssell. 'Radiotherapy of Malignant Tumours in Sweden'. In: *The British Journal of Radiology* 3.29 (May 1930), pp. 198–234. ISSN: 0007-1285. DOI: 10.1259/0007-1285-3-29-198. URL: <https://doi.org/10.1259/0007-1285-3-29-198>.
- [58] Robert R. Wilson. 'Radiological use of fast protons.' In: *Radiology* 47.5 (1946), pp. 487–491. ISSN: 00338419. DOI: 10.1148/47.5.487.
- [59] Omar Desouky, Nan Ding and Guangming Zhou. 'Targeted and non-targeted effects of ionizing radiation'. In: *Journal of Radiation Research and Applied Sciences* 8.2 (Apr. 2015), pp. 247–254. ISSN: 1687-8507. DOI: 10.1016/J.JRRAS.2015.03.003. URL: <https://www.sciencedirect.com/science/article/pii/S1687850715000333>.
- [60] William C. Dewey, Clifton C. Ling and Raymond E. Meyn. 'Radiation-induced apoptosis: Relevance to radiotherapy'. In: *International Journal of Radiation Oncology\*Biophysics* 33.4 (Nov. 1995), pp. 781–796. ISSN: 03603016. DOI: 10.1016/0360-3016(95)00214-8. URL: <http://www.ncbi.nlm.nih.gov/pubmed/7591884><http://linkinghub.elsevier.com/retrieve/pii/0360301695002148>.
- [61] David Eriksson and Torgny Stigbrand. 'Radiation-induced cell death mechanisms'. In: *Tumor Biology* 31.4 (Aug. 2010), pp. 363–372. ISSN: 1010-4283. DOI: 10.1007/s13277-010-0042-8. URL: <http://www.ncbi.nlm.nih.gov/pubmed/20490962><http://link.springer.com/10.1007/s13277-010-0042-8>.
- [62] N. Chatterjee and G. C. Walker. 'Mechanisms of DNA damage, repair, and mutagenesis. Environmental and molecular mutagenesis'. In: *Physiology & behavior* 58.5 (2017), pp. 235–263. DOI: 10.1002/em.22087.Mechanisms.
- [63] Alexandru Daşu, Iuliana Toma-Daşu, Jörgen Olofsson et al. 'The use of risk estimation models for the induction of secondary cancers following radiotherapy'. In: *Acta Oncologica* 44.4 (2005), pp. 339–347. ISSN: 0284186X. DOI: 10.1080/02841860510029833.
- [64] Gunjesh Kumar Singh, Vikas Yadav, Pragya Singh et al. 'Radiation-Induced Malignancies Making Radiotherapy a "Two-Edged Sword": A Review of Literature'. In: *World Journal of Oncology* 8.1 (2017), pp. 1–6. ISSN: 1920-4531. DOI: 10.14740/wjon996w.
- [65] Andrea K. Ng, Lisa B. Kenney, Ethel S. Gilbert et al. 'Secondary Malignancies Across the Age Spectrum'. In: *Seminars in Radiation Oncology* 20.1 (2010), pp. 67–78. ISSN: 10534296. DOI: 10.1016/j.semradonc.2009.09.002.
- [66] RS Sherif, WM Elshemey and EM Attalla. 'The risk of secondary cancer in pediatric medulloblastoma patients due to three-dimensional conformal radiotherapy and intensity-modulated radiotherapy'. In: *Indian J Cancer* 55.4 (2018), pp. 372–376.

## REFERENCES

---

- [67] S.V Gupta. *Units of Measurement: Past, Present and Future: International System of Units*. Ed. by Robert Hull, R. M. Osgood Jr, Jürgen Parisi et al. Vol. 145. 4. Springer, 2009. ISBN: 978-3-642-00737-8. DOI: 10.1007/978-3-642-00738-5.
- [68] *Dosimetry in Diagnostic Radiology: An International Code of Practice*. Technical Reports Series 457. Vienna: INTERNATIONAL ATOMIC ENERGY AGENCY, 2007. ISBN: 92-0-115406-2. URL: <https://www.iaea.org/publications/7638/dosimetry-in-diagnostic-radiology-an-international-code-of-practice>.
- [69] G. A. Carlsson. ‘Definition of energy imparted. A new formulation adapted to exact solutions of the absorbed dose equation under nonequilibrium conditions’. In: *Radiation Research* 77.2 (Oct. 1979), pp. 209–220. ISSN: 00337587. DOI: 10.2307/3575133. URL: <http://www.jstor.org/stable/3575133>.
- [70] David Martínez-martín, Gotthold Fläschner, Benjamin Gaub et al. ‘Inertial picobalance reveals fast mass fluctuations in mammalian cells’. In: *Nature Publishing Group* 550.7677 (2017), pp. 500–505. ISSN: 0028-0836. DOI: 10.1038/nature24288. URL: <http://dx.doi.org/10.1038/nature24288>.
- [71] Marie Catherine Vozenin, Pauline De Fornel, Kristoffer Petersson et al. ‘The Advantage of FLASH Radiotherapy Confirmed in Mini-pig and Cat-cancer Patients’. In: *Clinical Cancer Research* 25.1 (2019), pp. 35–42. ISSN: 15573265. DOI: 10.1158/1078-0432.CCR-17-3375.
- [72] Stephen J. McMahon and Kevin M. Prise. ‘Mechanistic modelling of radiation responses’. In: *Cancers* 11.2 (2019). ISSN: 20726694. DOI: 10.3390/cancers11020205.
- [73] The Royal College of Radiologists. ‘Radiotherapy dose fractionation, third edition’. In: *Clinical Oncology* December (2019), p. 17. ISSN: 0007-1285. URL: [https://www.rcr.ac.uk/system/files/publication/field\\_publication\\_files/bfco163\\_dose\\_fractionation\\_2nd\\_ed\\_march2017.pdf](https://www.rcr.ac.uk/system/files/publication/field_publication_files/bfco163_dose_fractionation_2nd_ed_march2017.pdf).
- [74] Punit Kaur, Mark D. Hurwitz, Sunil Krishnan et al. ‘Combined hyperthermia and radiotherapy for the treatment of cancer’. In: *Cancers* 3.4 (2011), pp. 3799–3823. ISSN: 20726694. DOI: 10.3390/cancers3043799.
- [75] Albrecht M. Kellerer. *The Dosimetry of Ionizing Radiation: Fundamentals of Microdosimetry*. Ed. by Kenneth R. Kase Kase, Bengt E. Bjärngard and Frank H. Attix. Vol. 1. Academic Press, 1985, pp. 78–163. DOI: 10.1016/0883-2889(91)90233-q.
- [76] J W Rohlfs. *Modern Physics from  $[\alpha]$  to  $Z^\infty$* . Wiley, 1994. ISBN: 9780471021261. URL: <https://books.google.co.uk/books?id=c0Z4QgAACAAJ>.

- [77] ‘Report 90’. In: *Journal of the International Commission on Radiation Units and Measurements* 14.1 (Nov. 2014), NP–NP. ISSN: 1473-6691. DOI: 10.1093/jicru/ndw043. URL: <https://doi.org/10.1093/jicru/ndw043>.
- [78] J.H. Hubbell and S.M. Seltzer. *X-Ray Mass Attenuation Coefficients / NIST*. 2004. DOI: 10.18434/T4D01F. URL: <https://www.nist.gov/pml/x-ray-mass-attenuation-coefficients>.
- [79] International Atomic Energy Agency. ‘Radiation Oncology Physics: A Handbook for Teachers and Students’. In: Vienna, Austria: IAEA, 2005. ISBN: 92-0-107304-6. URL: <https://www.iaea.org/publications/7086/radiation-oncology-physics>.
- [80] IAEA TRS 398. *Absorbed Dose Determination in External Beam Radiotherapy*. Technical Reports Series 398. Vienna: INTERNATIONAL ATOMIC ENERGY AGENCY, 2000, pp. 1–229. ISBN: 978-92-0-105807. DOI: 10.1097/00004032-200111000-00017. URL: <http://www-pub.iaea.org/books/IAEABooks/5954/Absorbed-Dose-Determination-in-External-Beam-Radiotherapy>.
- [81] NHS England. *NHS England launches biggest upgrade to NHS cancer treatment in 15 years*. URL: <https://www.england.nhs.uk/2016/10/radiotherapy-fund/>.
- [82] European Coordination Committee and Healthcare I T Industry. ‘RADIOTHERAPY AGE PROFILE & DENSITY December 2019 Edition’. In: December (2019).
- [83] Nathalie Mikhailova. *Safely embracing the growing power of radiotherapy*. Vienna, Austria, 2019.
- [84] C. Victor Levin, Brahim El Gueddari and Ahmed Meghzifene. ‘Radiation therapy in Africa: Distribution and equipment’. In: *Radiotherapy and Oncology* 52.1 (1999), pp. 79–83. ISSN: 01678140. DOI: 10.1016/S0167-8140(99)00069-9.
- [85] Surbhi Grover, Melody J. Xu, Alyssa Yeager et al. ‘A Systematic Review of Radiotherapy Capacity in Low- and Middle-Income Countries’. In: *Frontiers in Oncology* 4.January (2015), pp. 1–11. ISSN: 2234-943X. DOI: 10.3389/fonc.2014.00380.
- [86] Jack Copeland and Andre A. Haeff. ‘The true history of the traveling wave tube’. In: *IEEE Spectrum* 52.9 (2015), pp. 38–43. ISSN: 00189235. DOI: 10.1109/MSPEC.2015.7226611.
- [87] Supriya Mallick, Goura K. Rath and Rony Benson. *Practical radiation oncology*. 2019, pp. 1–300. ISBN: 9789811500732. DOI: 10.1007/978-981-15-0073-2.
- [88] Frank Herbert Attix. *Introduction to Radiological Physics and Radiation Dosimetry*. Weinheim, Germany: Wiley-VCH Verlag GmbH, Nov. 1986. ISBN: 9783527617135. DOI: 10.1002/9783527617135. URL: <http://doi.wiley.com/10.1002/9783527617135>.

- [89] Abdulhamid Chaikh, Jarkko Ojala, Catherine Khamphan et al. ‘Dosimetrical and radiobiological approach to manage the dosimetric shift in the transition of dose calculation algorithm in radiation oncology: How to improve high quality treatment and avoid unexpected outcomes?’ In: *Radiation Oncology* 13.1 (2018), pp. 1–11. ISSN: 1748717X. DOI: 10.1186/s13014-018-1005-2.
- [90] *Accuracy Requirements and Uncertainties in Radiotherapy*. Human Health Series 31. Vienna: INTERNATIONAL ATOMIC ENERGY AGENCY, 2016. ISBN: 978-92-0-100815-2. URL: <https://www.iaea.org/publications/10668/accuracy-requirements-and-uncertainties-in-radiotherapy>.
- [91] A. Mesbahi, N. Rasouli, M. Mohammadzadeh et al. ‘Comparison of Radiobiological Models for Radiation Therapy Plans of Prostate Cancer: Three-dimensional Conformal versus Intensity Modulated Radiation Therapy’. eng. In: *Journal of biomedical physics & engineering* 9.3 (June 2019), pp. 267–278. ISSN: 2251-7200. DOI: 10.31661/jbpe.v9i3Jun.655. URL: <https://pubmed.ncbi.nlm.nih.gov/31341872/><https://www.ncbi.nlm.nih.gov/pmc/articles/PMC6613163/>.
- [92] W Schlegel and P Kneschaurek. ‘Inverse radiotherapy planning’. ger. In: *Strahlentherapie und Onkologie : Organ der Deutschen Rontgengesellschaft ... [et al]* 175.5 (May 1999), pp. 197–207. ISSN: 0179-7158 (Print). DOI: 10.1007/BF02742396.
- [93] Neil G Burnet, Simon J Thomas, Kate E Burton et al. ‘Defining the tumour and target volumes for radiotherapy.’ In: *Cancer imaging : the official publication of the International Cancer Imaging Society* 4.2 (Oct. 2004), pp. 153–61. ISSN: 1470-7330. DOI: 10.1102/1470-7330.2004.0054. URL: <http://www.ncbi.nlm.nih.gov/pubmed/18250025><http://www.pubmedcentral.nih.gov/articlerender.fcgi?artid=PMC1434601>.
- [94] Enzhuo M Quan, Xiaoqiang Li, Yupeng Li et al. ‘A comprehensive comparison of IMRT and VMAT plan quality for prostate cancer treatment’. eng. In: *International journal of radiation oncology, biology, physics* 83.4 (July 2012), pp. 1169–1178. ISSN: 1879-355X. DOI: 10.1016/j.ijrobp.2011.09.015. URL: <https://pubmed.ncbi.nlm.nih.gov/22704703/><https://www.ncbi.nlm.nih.gov/pmc/articles/PMC3805837/>.
- [95] May Teoh, C. H. Clark, K. Wood et al. ‘Volumetric modulated arc therapy: A review of current literature and clinical use in practice’. In: *British Journal of Radiology* 84.1007 (2011), pp. 967–996. ISSN: 00071285. DOI: 10.1259/bjr/22373346.
- [96] Andrew Wu, G Lindner, A H Maitz et al. ‘Physics of gamma knife approach on convergent beams in stereotactic radiosurgery’. In: *International Journal of Radiation Oncology\*Biological\*Physics* 18.4 (1990), pp. 941–949. ISSN: 0360-3016. DOI: <https://doi.org/>

- 10.1016/0360-3016(90)90421-F. URL: <http://www.sciencedirect.com/science/article/pii/036030169090421F>.
- [97] Martin Kocher, Andrea Wittig, Marc Dieter Piroth et al. ‘Stereotactic radiosurgery for treatment of brain metastases: A report of the DEGRO Working Group on Stereotactic Radiotherapy’. In: *Strahlentherapie und Onkologie* 190.6 (2014), pp. 521–532. ISSN: 1439099X. DOI: 10.1007/s00066-014-0648-7.
- [98] Accuray. *Accuray: Innovators of Radiation Therapy for Cancer*. URL: <https://www accuray.com/company/>.
- [99] *CyberKnife - How it Works | CyberKnife*. URL: <https://cyberknife.com/cyberknife-how-it-works/>.
- [100] Elekta. *About Elekta*. URL: <https://www.elekta.com/company/>.
- [101] *Gamma Knife Treatment Process*. URL: <https://www.elekta.com/patients/gammaknife-treatment-process/>.
- [102] M J Berger, M Inokuti, H H Anderson et al. ‘Report 37’. In: *Journal of the International Commission on Radiation Units and Measurements* os19.2 (Apr. 2016), NP–NP. ISSN: 1473-6691. DOI: 10.1093/jicru/os19.2.Report37. URL: <https://doi.org/10.1093/jicru/os19.2.Report37>.
- [103] Andrew Brown and Herman Suit. ‘The centenary of the discovery of the Bragg peak’. In: *Radiotherapy and Oncology* 73.3 (Dec. 2004), pp. 265–268. ISSN: 0167-8140. DOI: 10.1016/J.RADONC.2004.09.008. URL: <https://www.sciencedirect.com/science/article/pii/S0167814004004499?via%3Dihub>.
- [104] Bijan Arjomandy, Narayan Sahoo, X. Ronald Zhu et al. ‘An overview of the comprehensive proton therapy machine quality assurance procedures implemented at the University of Texas M. D. Anderson Cancer Center Proton Therapy Center-Houston’. In: *Medical Physics* 36.6 (2009), pp. 2269–2282. ISSN: 00942405. DOI: 10.1118/1.3120288.
- [105] *khpeek/spread-out-Bragg-peak*. URL: <https://github.com/khpeek/spread-out-Bragg-peak>.
- [106] NIST. *Stopping-Power & Range Tables for Electrons, Protons, and Helium Ions*. DOI: 10.18434/T4NC7P. URL: <https://www.nist.gov/pml/stopping-power-range-tables-electrons-protons-and-helium-ions>.
- [107] Pedro Andreo, David T Burns, Alan E Nahum et al. *Fundamentals of ionizing radiation dosimetry*. English. Weinheim, Germany, 2017. URL: <https://search.ebscohost.com/login.aspx?direct=true&scope=site&db=nlebk&db=nlabk&AN=1535812>.

## REFERENCES

---

- [108] Lisa S Kahalley, M Douglas Ris, David R Grosshans et al. ‘Comparing Intelligence Quotient Change After Treatment With Proton Versus Photon Radiation Therapy for Pediatric Brain Tumors.’ eng. In: *Journal of clinical oncology : official journal of the American Society of Clinical Oncology* 34.10 (Apr. 2016), pp. 1043–1049. ISSN: 1527-7755 (Electronic). DOI: 10.1200/JCO.2015.62.1383.
- [109] M. M. Kligerman, W. C. Black, J. M. Yuhas et al. ‘Current status of clinical pion radiotherapy’. In: *Radiology* 125.2 (1977), pp. 489–492. ISSN: 00338419. DOI: 10.1148/125.2.489.
- [110] Niels Bassler, Jan Alsner, Gerd Beyer et al. ‘Antiproton radiotherapy’. In: *Radiotherapy and Oncology* 86.1 (2008), pp. 14–19. ISSN: 01678140. DOI: 10.1016/j.radonc.2007.11.028.
- [111] N. V. Mokhov and A. Van Ginneken. ‘Muons versus hadrons for radiotherapy’. In: *Proceedings of the IEEE Particle Accelerator Conference* 4 (1999), pp. 2525–2527. DOI: 10.1109/pac.1999.792754.
- [112] Christian P Karger and Peter Peschke. ‘RBE and related modeling in carbon-ion therapy’. In: *Physics in Medicine & Biology* 63.1 (2017), 01TR02. ISSN: 1361-6560. DOI: 10.1088/1361-6560/aa9102. URL: <http://dx.doi.org/10.1088/1361-6560/aa9102>.
- [113] Cary Zeitlin and Chiara La Tessa. ‘The role of nuclear fragmentation in particle therapy and space radiation protection’. In: *Frontiers in Oncology* 6.MAR (2016), pp. 1–13. ISSN: 2234943X. DOI: 10.3389/fonc.2016.00065.
- [114] Yoshihisa Takada, Takeshi Himukai, Kenji Takizawa et al. ‘The basic study of a bi-material range compensator for improving dose uniformity for proton therapy’. In: *Physics in Medicine and Biology* 53.19 (2008), pp. 5555–5569. ISSN: 00319155. DOI: 10.1088/0031-9155/53/19/019.
- [115] Hui Liu and Joe Y. Chang. ‘Proton therapy in clinical practice’. In: *Chinese Journal of Cancer* 30.5 (2011), pp. 315–326. ISSN: 1944446X. DOI: 10.5732/cjc.010.10529.
- [116] Sang Eun Han, Gyuseong Cho and Se Byeong Lee. ‘An Assessment of the Secondary Neutron Dose in the Passive Scattering Proton Beam Facility of the National Cancer Center’. In: *Nuclear Engineering and Technology* 49.4 (2017), pp. 801–809. ISSN: 2234358X. DOI: 10.1016/j.net.2016.12.003. URL: <http://dx.doi.org/10.1016/j.net.2016.12.003>.
- [117] Eros Pedroni, Reinhard Bacher, Hans Blattmann et al. ‘The 200-Mev proton therapy project at the Paul Scherrer Institute: Conceptual design and practical realization’. In: *Medical Physics* 22.1 (1995), pp. 37–53. ISSN: NA. DOI: 10.1118/1.597522.
- [118] PTCOG. *Facilities under Construction*. URL: <https://www.ptcog.ch/index.php/facilities-under-construction>.

- [119] Radhe Mohan and David Grosshans. ‘Proton therapy – Present and future’. In: *Advanced Drug Delivery Reviews* 109.1 (2017), pp. 26–44. ISSN: 0169-409X. DOI: <https://doi.org/10.1016/j.addr.2016.11.006>. URL: <http://www.sciencedirect.com/science/article/pii/S0169409X16303192>.
- [120] Xuanfeng Ding, Xiaoqiang Li, An Qin et al. ‘Have we reached proton beam therapy dosimetric limitations? – A novel robust, delivery-efficient and continuous spot-scanning proton arc (SPArc) therapy is to improve the dosimetric outcome in treating prostate cancer’. In: *Acta Oncologica* 57.3 (Mar. 2018), pp. 435–437. ISSN: 0284-186X. DOI: 10.1080/0284186X.2017.1358463. URL: <http://www.ncbi.nlm.nih.gov/pubmed/28774218><https://www.tandfonline.com/doi/full/10.1080/0284186X.2017.1358463>.
- [121] Particle Therapy Co-Operative Group (PTCOG). *Facilities in Operation*. URL: <https://www.ptcog.ch/index.php/facilities-in-operation>.
- [122] G. Klimpki, Y. Zhang, G. Fattori et al. ‘The impact of pencil beam scanning techniques on the effectiveness and efficiency of rescanning moving targets’. In: *Physics in Medicine and Biology* 63.14 (2018). ISSN: 13616560. DOI: 10.1088/1361-6560/aacd27.
- [123] Juan Yu, Chris J. Beltran and Michael G. Herman. ‘Implication of spot position error on plan quality and patient safety in pencil-beam-scanning proton therapy’. In: *Medical Physics* 41.8Part1 (July 2014), p. 081706. ISSN: 00942405. DOI: 10.1118/1.4885956. URL: <http://doi.wiley.com/10.1118/1.4885956>.
- [124] Stephen Peterson, Jerimy Polf, George Ciangaru et al. ‘Variations in proton scanned beam dose delivery due to uncertainties in magnetic beam steering’. In: *Medical Physics* 36.8 (July 2009), pp. 3693–3702. ISSN: 00942405. DOI: 10.1118/1.3175796. URL: <http://www.ncbi.nlm.nih.gov/pubmed/19746802><http://doi.wiley.com/10.1118/1.3175796>.
- [125] Satomi Shiraishi, Michael G. Herman and Keith M. Furutani. ‘Measurement of Dispersion of a Clinical Proton Therapy Beam’. In: (Apr. 2018). URL: <https://arxiv.org/abs/1805.00080>.
- [126] E Ford, R Emery, D Huff et al. ‘An image-guided precision proton radiation platform for preclinical *in vivo* research’. In: *Physics in Medicine and Biology* 62.1 (Jan. 2017), pp. 43–58. ISSN: 0031-9155. DOI: 10.1088/1361-6560/62/1/43. URL: <http://stacks.iop.org/0031-9155/62/i=1/a=43?key=crossref.97c9fc3110cf967a70699619f367fcb0>.
- [127] O Actis, D Meer, S König et al. ‘A comprehensive and efficient daily quality assurance for PBS proton therapy’. In: *Physics in Medicine and Biology* 62.5 (Mar. 2017), pp. 1661–1675. ISSN: 0031-9155. DOI: 10.1088/1361-6560/aa5131. URL: <http://www.ncbi.nlm.nih.gov/pubmed/28774218>.

## REFERENCES

---

- gov/pubmed/28166055%20http://stacks.iop.org/0031-9155/62/i=5/a=1661?key=crossref.4c353196c61ce5801f66b9a1c808d3ea.
- [128] M A Stevens, J R Turner, R P Hugtenburg et al. ‘High-resolution dosimetry using radiochromic film and a document scanner’. In: *Physics in Medicine and Biology* 41.11 (Nov. 1996), pp. 2357–2365. ISSN: 0031-9155. DOI: 10.1088/0031-9155/41/11/008. URL: <http://stacks.iop.org/0031-9155/41/i=11/a=008?key=crossref.de94f73ea9f7ea3dc309da3cac2d6807>.
- [129] *Garchromic EBT Films - GAFchromic™*. URL: <http://www.gafchromic.com/gafchromic-film/radiotherapy-films/EBT/index.asp>.
- [130] David Laws. *13 Sextillion & Counting: The Long & Winding Road to the Most Frequently Manufactured Human Artifact in History - CHM*. 2018. URL: <https://computerhistory.org/blog/13-sextillion-counting-the-long-winding-road-to-the-most-frequently-manufactured-human-artifact-in-history/?key=13-sextillion-counting-the-long-winding-road-to-the-most-frequently-manufactured-human-artifact-in-history>.
- [131] Gerhard Lutz. *Semiconductor Radiation Detectors*. Second Edi. New York: Springer, 1999. ISBN: 978-3-540-71678-5.
- [132] W. Fulop. ‘Calculation of avalanche breakdown voltages of silicon p-n junctions’. In: *Solid State Electronics* 10.1 (1967), pp. 39–43. ISSN: 00381101. DOI: 10.1016/0038-1101(67)90111-6.
- [133] Y. Sun, S. A. Boggs and R. Ramprasad. ‘The intrinsic electrical breakdown strength of insulators from first principles’. In: *Applied Physics Letters* 101.13 (2012). ISSN: 00036951. DOI: 10.1063/1.4755841.
- [134] William R Leo. *W. R. Leo. Techniques for Nuclear and Particle Physics Experiments. Springer-Verlag, , 1987*. Second Rev. Berlin: Springer-Verlag, 1994. ISBN: 978-3-540-57280-0. DOI: 10.1007/978-3-642-57920-2.
- [135] George C Messenger and Milton S Ash. *The Effects of Radiation on Electronic Systems*. New York: Van Nostrand Reinhold, 1986. ISBN: 9780442239527.
- [136] A. Neugroschel. ‘Minority-Carrier Diffusion Coefficients and Mobilities in Silicon’. In: *IEEE Electron Device Letters* 6.8 (1985), pp. 425–427. ISSN: 15580563. DOI: 10.1109/EDL.1985.26178.

- [137] Jeremy A Davis, Jason R Paino, Andrew Dipuglia et al. ‘Characterisation and evaluation of a PNP strip detector for synchrotron microbeam radiation therapy’. In: *Biomedical Physics & Engineering Express* 4.4 (June 2018), p. 044002. ISSN: 2057-1976. DOI: 10.1088/2057-1976/aab10c. URL: <http://stacks.iop.org/2057-1976/4/i=4/a=044002?key=crossref.9f17108c35b54e617978b404c21e2209>.
- [138] Rolf Unbehauen and Andrzej Cichocki. ‘CMOS Analog-to-Digital and Digital-to-Analog Conversion Systems BT - MOS Switched-Capacitor and Continuous-Time Integrated Circuits and Systems: Analysis and Design’. In: ed. by Rolf Unbehauen and Andrzej Cichocki. Berlin, Heidelberg: Springer Berlin Heidelberg, 1989, pp. 555–627. ISBN: 978-3-642-83677-0. DOI: 10.1007/978-3-642-83677-0\_{\\_}7. URL: [https://doi.org/10.1007/978-3-642-83677-0\\_7](https://doi.org/10.1007/978-3-642-83677-0_7).
- [139] F Wanlass and C Sah. ‘Nanowatt logic using field-effect metal-oxide semiconductor triodes’. In: *1963 IEEE International Solid-State Circuits Conference. Digest of Technical Papers*. Vol. VI. 1963, pp. 32–33. ISBN: VO - VI. DOI: 10.1109/ISSCC.1963.1157450.
- [140] P Zhang. *Advanced Industrial Control Technology*. Jan. 2010. ISBN: 978-1-4377-7807-6. DOI: 10.1016/C2009-0-20337-0.
- [141] Savvas G. Chamberlain. ‘Photosensitivity and Scanning of Silicon Image Detector Arrays’. In: *IEEE Journal of Solid-State Circuits* 4.6 (1969), pp. 333–342. ISSN: 1558173X. DOI: 10.1109/JSSC.1969.1050032.
- [142] L. Servoli, D. Biagetti, S. Meroli et al. ‘Use of a standard CMOS imager as position detector for charged particles’. In: *Nuclear Physics B - Proceedings Supplements* 215.1 (2011), pp. 228–231. ISSN: 09205632. DOI: 10.1016/j.nuclphysbps.2011.04.016. URL: <http://dx.doi.org/10.1016/j.nuclphysbps.2011.04.016>.
- [143] R. Wunstorf, H. Feick, E. Fretwurst et al. ‘Damage-induced surface effects in silicon detectors’. In: *Nuclear Instruments and Methods in Physics Research, Section A: Accelerators, Spectrometers, Detectors and Associated Equipment* 377.2-3 (1996), pp. 290–297. ISSN: 01689002. DOI: 10.1016/0168-9002(96)00218-5.
- [144] Hartmut F.W. Sadrozinski. ‘Silicon microstrip detectors in high luminosity application’. In: *IEEE Transactions on Nuclear Science* 45.3 PART 1 (1998), pp. 295–302. ISSN: 00189499. DOI: 10.1109/23.682397.
- [145] S. C. Lillicrap, B. Owen, J. R. Williams et al. ‘Code of Practice for high-energy photon therapy dosimetry based on the NPL absorbed dose calibration service’. In: *Physics in Medicine and Biology* 35.10 (1990), pp. 1355–1360. ISSN: 0031-9155. DOI: 10.1088/0031-9155/35/10/301. URL: <http://dx.doi.org/10.1088/0031-9155/35/10/301>.

## REFERENCES

---

- [146] David J Eaton, Graham A Bass, Paul Booker et al. ‘IPEM code of practice for high-energy photon therapy dosimetry based on the NPL absorbed dose calibration service.’ eng. In: *Physics in medicine and biology* (June 2020). ISSN: 1361-6560 (Electronic). DOI: 10.1088/1361-6560/ab99e3.
- [147] Matthew Bolt, Catharine H. Clark, Andrew Nisbet et al. ‘Quantification of the uncertainties within the radiotherapy dosimetry chain and their impact on tumour control’. In: *Physics and Imaging in Radiation Oncology* 19 (July 2021), pp. 33–38. ISSN: 24056316. DOI: 10.1016/j.phro.2021.06.004.
- [148] Jérémie Vū Bezin, Rodrigue S. Allodji, Jean Pierre Mège et al. ‘A review of uncertainties in radiotherapy dose reconstruction and their impacts on dose-response relationships’. In: *Journal of Radiological Protection* 37.1 (2017), R1–R18. ISSN: 13616498. DOI: 10.1088/1361-6498/aa575d.
- [149] Thomas Bortfeld and Harald Paganetti. ‘The biologic relevance of daily dose variations in adaptive treatment planning’. In: *International Journal of Radiation Oncology Biology Physics* 65.3 (2006), pp. 899–906. ISSN: 03603016. DOI: 10.1016/j.ijrobp.2006.02.036.
- [150] M W Chase. *NIST-JANAF Thermochemical Tables*. Fourth Edi. Vol. 9. Gaithersburg, Maryland: American Chemical Society; American Institute of Physics; National Institute of Standards and Technology, 1998, p. 1. ISBN: 1-56396-831-2. DOI: 10.18434/T42S31.
- [151] Vsl.nl. *The new VSL water calorimeter – ready for the future*. URL: <https://www.vsl.nl/en/new-vsl-water-calorimeter-ready-future>.
- [152] Steve R. Domen. *Calorimeter*. 1972. URL: <https://patents.google.com/patent/US3665762A/en>.
- [153] R. C. Murty. ‘Effective atomic numbers of heterogeneous materials’. In: *Nature* 207.4995 (1965), pp. 398–399. ISSN: 00280836. DOI: 10.1038/207398a0.
- [154] James Renaud, Arman Sarfehnia, Julien Bancheri et al. ‘Aerrow: A probe-format graphite calorimeter for absolute dosimetry of high-energy photon beams in the clinical environment’. In: *Medical Physics* 45.1 (2018), pp. 414–428. ISSN: 00942405. DOI: 10.1002/mp.12669.
- [155] Ana Lourenço, Russell Thomas, Hugo Bouchard et al. ‘Experimental and Monte Carlo studies of fluence corrections for graphite calorimetry in low- and high-energy clinical proton beams’. In: *Medical Physics* 43.7 (June 2016), pp. 4122–4132. ISSN: 00942405. DOI: 10.1118/1.4951733. URL: <http://www.ncbi.nlm.nih.gov/pubmed/27370132%20http://doi.wiley.com/10.1118/1.4951733>.
- [156] *Roos Electron Chamber - PTW Freiburg GmbH*. URL: <https://www.ptwdosimetry.com/en/products/roos-electron-chamber/>.

- [157] Keithley Instruments. ‘Model 2182 / 2182A Nanovoltmeter User ’ s Manual’. In: June (2004). ISSN: 1448-5028, 1448-5028.
- [158] Stuart Bennett. ‘A Brief History of Automatic Control’. In: *IEEE Control Systems* 16.3 (1996), pp. 17–25. ISSN: 1066033X. DOI: 10.1109/37.506394.
- [159] Stefan Bartzsch, Johanna Lott, Katrin Welsch et al. ‘Micrometer-resolved film dosimetry using a microscope in microbeam radiation therapy’. In: *Medical Physics* 42.7 (June 2015), pp. 4069–4079. ISSN: 00942405. DOI: 10.1118/1.4922001. URL: <http://doi.wiley.com/10.1118/1.4922001>.
- [160] L M Petrie. ‘Characterisation of a Graphite Calorimeter in Scanned Proton Beams’. PhD thesis. 2016. URL: [http://epubs.surrey.ac.uk/812801/1/Final\\_Thesis\\_with\\_Corrections.pdf](http://epubs.surrey.ac.uk/812801/1/Final_Thesis_with_Corrections.pdf).
- [161] L. Arnold, J. Baudot, D. Bonnet et al. ‘The STAR silicon strip detector (SSD)’. In: *Nuclear Instruments and Methods in Physics Research, Section A: Accelerators, Spectrometers, Detectors and Associated Equipment* 499.2-3 (2003), pp. 652–658. ISSN: 01689002. DOI: 10.1016/S0168-9002(02)01963-0.
- [162] Pauline Fournier, Iwan Cornelius, Mattia Donzelli et al. ‘X-Tream quality assurance in synchrotron X-ray microbeam radiation therapy’. In: *Journal of Synchrotron Radiation* 23.5 (Sept. 2016), pp. 1180–1190. ISSN: 1600-5775. DOI: 10.1107/S1600577516009322. URL: <http://scripts.iucr.org/cgi-bin/paper?S1600577516009322>.
- [163] Michela Esposito, Chris Waltham, Jonathan T. Taylor et al. ‘PRaVDA: The first solid-state system for proton computed tomography’. In: *Physica Medica* 55 (Nov. 2018), pp. 149–154. ISSN: 1120-1797. DOI: 10.1016/J.EJMP.2018.10.020. URL: <https://www.sciencedirect.com/science/article/pii/S1120179718313073>.
- [164] J. B. Farr, A. E. Mascia, W. C. Hsi et al. ‘Clinical characterization of a proton beam continuous uniform scanning system with dose layer stacking’. In: *Medical Physics* 35.11 (2008), pp. 4945–4954. ISSN: 00942405. DOI: 10.1118/1.2982248.
- [165] J T Taylor, C Waltham, T Price et al. ‘A new silicon tracker for proton imaging and dosimetry.’ In: *Nuclear instruments & methods in physics research. Section A, Accelerators, spectrometers, detectors and associated equipment* 831 (Sept. 2016), pp. 362–366. ISSN: 0168-9002. DOI: 10.1016/j.nima.2016.02.013. URL: <http://www.ncbi.nlm.nih.gov/pubmed/27667884>.
- [166] Peter R. Almond, Peter J. Biggs, B. M. Coursey et al. ‘AAPM’s TG-51 protocol for clinical reference dosimetry of high-energy photon and electron beams’. In: *Medical Physics* 26.9 (1999), pp. 1847–1870. ISSN: 00942405. DOI: 10.1118/1.598691.

- [167] Lang Yang, Annabel C Burton, Mike Bradburn et al. ‘Distribution of bone density in the proximal femur and its association with hip fracture risk in older men: the osteoporotic fractures in men (MrOS) study’. eng. In: *Journal of bone and mineral research : the official journal of the American Society for Bone and Mineral Research* 27.11 (Nov. 2012), pp. 2314–2324. ISSN: 1523-4681. DOI: 10.1002/jbmr.1693. URL: <https://pubmed.ncbi.nlm.nih.gov/22729872%20https://www.ncbi.nlm.nih.gov/pmc/articles/PMC3474863/>.
- [168] Zhouguang Hui, Xiaodong Zhang, George Starkschall et al. ‘Effects of interfractional motion and anatomic changes on proton therapy dose distribution in lung cancer’. eng. In: *International journal of radiation oncology, biology, physics* 72.5 (Dec. 2008), pp. 1385–1395. ISSN: 1879-355X. DOI: 10.1016/j.ijrobp.2008.03.007. URL: <https://pubmed.ncbi.nlm.nih.gov/18486357%20https://www.ncbi.nlm.nih.gov/pmc/articles/PMC3401022/>.
- [169] Lauri Koivula, Leonard Wee and Juha Korhonen. ‘Feasibility of MRI-only treatment planning for proton therapy in brain and prostate cancers: Dose calculation accuracy in substitute CT images’. In: *Medical Physics* 43.8 (2016), pp. 4634–4642. ISSN: 00942405. DOI: 10.1118/1.4958677.
- [170] X. Yang, Y. Lei, H.K.G. Shu et al. ‘A Learning-Based Approach to Derive Electron Density from Anatomical MRI for Radiation Therapy Treatment Planning’. In: *International Journal of Radiation Oncology\*Biological\*Physics* 99.2 (2017), S173–S174. ISSN: 03603016. DOI: 10.1016/j.ijrobp.2017.06.437. URL: <http://dx.doi.org/10.1016/j.ijrobp.2017.06.437>.
- [171] Charles-Antoine Collins-Fekete, Lennart Volz, Stephen K N Portillo et al. ‘A theoretical framework to predict the most likely ion path in particle imaging’. In: *Physics in Medicine and Biology* 62.5 (2017), pp. 1777–1790. ISSN: 0031-9155. DOI: 10.1088/1361-6560/aa58ce. URL: <http://dx.doi.org/10.1088/1361-6560/aa58ce>.
- [172] *PRaVDA*. 2016. URL: <http://www.pravda.uk.com/>.
- [173] Helmuth Spieler. *Semiconductor Detector Systems*. Oxford science publications. OUP Oxford, 2005. ISBN: 9780198527848. URL: <https://books.google.co.uk/books?id=qIXjBAAAQBAJ>.
- [174] G. Poludniowski, N. M. Allinson and P. M. Evans. ‘Proton computed tomography reconstruction using a backprojection-then-filtering approach’. In: *Physics in Medicine and Biology* 59.24 (2014), pp. 7905–7918. ISSN: 13616560. DOI: 10.1088/0031-9155/59/24/7905.
- [175] Willhelm Burger and Mark J. Burge. *Digital Image Processing*. Ed. by David Gries and Fred B. Schneider. 2nd. London, 2016. ISBN: 978-1-4471-6683-2. DOI: 10.1007/978-1-4471-6684-9.

- [176] M Rodriguez, J Sempau and L Brualla. ‘PRIMO: A graphical environment for the Monte Carlo simulation of Varian and Elekta linacs’. In: *Strahlentherapie und Onkologie* 189.10 (2013), pp. 881–886. ISSN: 1439-099X. DOI: 10.1007/s00066-013-0415-1. URL: <https://doi.org/10.1007/s00066-013-0415-1>.
- [177] H. Beauvais, A. Bridier and A. Dutreix. ‘Characteristics of contamination electrons in high energy photon beams’. In: *Radiotherapy and Oncology* 29.3 (Dec. 1993), pp. 308–316. ISSN: 0167-8140. DOI: 10.1016/0167-8140(93)90149-3.
- [178] Yuhi Suda, Masatsugu Hariu, Ryohei Yamauchi et al. ‘Direct energy spectrum measurement of X- ray from a clinical linac’. In: *Journal of Applied Clinical Medical Physics* n/a.n/a (2021), pp. 1–10. ISSN: 1526-9914. DOI: <https://doi.org/10.1002/acm2.13354>. URL: <https://doi.org/10.1002/acm2.13354>.
- [179] Phoenix Dosimetry. *Bart’s Solid Water for Electrons and Photons*. URL: <https://phoenix-dosimetry.co.uk/solid-water-and-bolus-material/>.
- [180] Lorenzo Brualla, Miguel Rodriguez, Josep Sempau et al. ‘PENELOPE/PRIMO-calculated photon and electron spectra from clinical accelerators’. In: *Radiation Oncology* 14.1 (2019), pp. 1–10. ISSN: 1748717X. DOI: 10.1186/s13014-018-1186-8.
- [181] William H. Hinson, William T. Kearns, Allan F. DeGuzman et al. ‘Photon spectral characteristics of dissimilar 6 MV linear accelerators’. In: *Medical Physics* 35.5 (2008), pp. 1698–1702. ISSN: 00942405. DOI: 10.1118/1.2900001.
- [182] F. Sánchez-Doblado, G. H. Hartmann, J. Pena et al. ‘A new method for output factor determination in MLC shaped narrow beams’. In: *Physica Medica* 23.2 (2007), pp. 58–66. ISSN: 11201797. DOI: 10.1016/j.ejmp.2007.03.002.
- [183] *Pyramid - Product - IC128-25LC-2I*. URL: <http://www.ptcusa.com/products/44>.
- [184] *Datasheet PSI System Controls and Diagnostics Pyramid Technical Consultants Integrated Dosimetry and Position Sensing Ionization Chamber with Dual Redundant Dose Measurement*. Tech. rep. URL: [http://www.ptcusa.com/files/datasheet/IC128-25LC-2I\\_DS\\_190605.pdf](http://www.ptcusa.com/files/datasheet/IC128-25LC-2I_DS_190605.pdf).
- [185] I Sedgwick, D Das, N Guerrini et al. ‘LASSENA: A 6.7 Megapixel, 3-sides Buttable Wafer-Scale CMOS Sensor using a novel grid- addressing architecture’. In: *Proc. Int. Image Sensor Workshop* (2013), pp. 3–6.
- [186] *vivaMOS image sensors*. URL: <https://www.vivamos.co.uk/>.
- [187] Nordson DAGE. *Nordson X-ray Technologies Product Range*. URL: <https://www.nordson.com/en/divisions/dage/nordson-x-ray-technologies>.

## REFERENCES

---

- [188] W. Snoeys, F. Faccio, M. Burns et al. ‘Layout techniques to enhance the radiation tolerance of standard CMOS technologies demonstrated on a pixel detector readout chip’. In: *Nuclear Instruments and Methods in Physics Research Section A: Accelerators, Spectrometers, Detectors and Associated Equipment* 439.2-3 (Jan. 2000), pp. 349–360. ISSN: 0168-9002. DOI: 10.1016/S0168-9002(99)00899-2. URL: <https://www.sciencedirect.com/science/article/pii/S0168900299008992>.
- [189] D. N. Slatkin, P. Spanne, F. A. Dilmanian et al. ‘Microbeam radiation therapy’. In: *Medical Physics* 19.6 (Nov. 1992), pp. 1395–1400. ISSN: 00942405. DOI: 10.1118/1.596771. URL: <http://doi.wiley.com/10.1118/1.596771>.
- [190] Audrey Bouchet, Raphaël Serduc, Jean Albert Laissue et al. ‘Effects of microbeam radiation therapy on normal and tumoral blood vessels’. In: *Physica Medica* 31.6 (Sept. 2015), pp. 634–641. ISSN: 1120-1797. DOI: 10.1016/J.EJMP.2015.04.014. URL: <https://www.sciencedirect.com/science/article/pii/S1120179715001088>.
- [191] Raphaël Serduc, Thomas Christen, Jean Laissue et al. ‘Brain tumor vessel response to synchrotron microbeam radiation therapy: a short-term *in vivo* study’. In: *Physics in Medicine and Biology* 53.13 (July 2008), pp. 3609–3622. ISSN: 0031-9155. DOI: 10.1088/0031-9155/53/13/015. URL: <http://stacks.iop.org/0031-9155/53/i=13/a=015?key=crossref.435118fcd0ec724083ec7fb93b481a0a>.
- [192] Jeffrey C Crosbie, Robin L Anderson, Kai Rothkamm et al. ‘Tumor Cell Response to Synchrotron Microbeam Radiation Therapy Differs Markedly From Cells in Normal Tissues’. In: *International Journal of Radiation Oncology\*Biophysics* 77.3 (2010), pp. 886–894. ISSN: 0360-3016. DOI: <https://doi.org/10.1016/j.ijrobp.2010.01.035>. URL: <http://www.sciencedirect.com/science/article/pii/S0360301610001355>.
- [193] Kevin M. Prise, Giuseppe Schettino, Melvyn Folkard et al. ‘New insights on cell death from radiation exposure’. In: *Lancet Oncology* 6.7 (2005), pp. 520–528. ISSN: 14702045. DOI: 10.1016/S1470-2045(05)70246-1.
- [194] Cristian Fernandez-Palomo, Elke Bräuer-Krisch, Jean Laissue et al. ‘Use of synchrotron medical microbeam irradiation to investigate radiation-induced bystander and abscopal effects *in vivo*’. In: *Physica Medica* 31.6 (Sept. 2015), pp. 584–595. ISSN: 1120-1797. DOI: 10.1016/J.EJMP.2015.03.004. URL: <https://www.sciencedirect.com/science/article/pii/S1120179715000642>.
- [195] Rachel Delorme, Joao Seco, Joao Seca et al. ‘Proposal of a Chemical Mechanism for Mini-Beam and Micro-Beam Efficacy’. In: 8.October (2020), pp. 1–11. DOI: 10.3389/fphy.2020.564836. URL: [www.frontiersin.org](http://www.frontiersin.org).

- [196] *GAFCHROMIC™ DOSIMETRY MEDIA, TYPE EBT-3*. Tech. rep. URL: [www.FilmQAPro.com](http://www.FilmQAPro.com).
- [197] Samuel Flynn, Tony Price, Philip P. Allport et al. ‘Evaluation of a pixelated large format CMOS sensor for x-ray microbeam radiotherapy’. In: *Medical Physics* 47.3 (2020), pp. 1305–1316. ISSN: 00942405. DOI: 10.1002/mp.13971. URL: <https://aapm.onlinelibrary.wiley.com/doi/abs/10.1002/mp.13971>.
- [198] Samuel Flynn, Tony Price, Philip P Allport et al. ‘First demonstration of real-time in-situ dosimetry of X-ray microbeams using a large format CMOS sensor’. In: *Nuclear Inst. and Methods in Physics Research, A* 978. February (2020), p. 164395. ISSN: 0168-9002. DOI: 10.1016/j.nima.2020.164395. URL: <https://doi.org/10.1016/j.nima.2020.164395>.
- [199] *Samtec*. URL: <https://www.samtec.com/>.
- [200] *Blackout and Laser Safety Materials*. URL: [https://www.thorlabs.com/newgrouppage9.cfm?objectgroup\\_id=190](https://www.thorlabs.com/newgrouppage9.cfm?objectgroup_id=190).
- [201] L Beck, J J Velthuis, S Fletcher et al. ‘Using a TRAPS upstream transmission detector to verify multileaf collimator positions during dynamic radiotherapy delivery’. In: *Applied Radiation and Isotopes* 156 (2020), p. 108951. ISSN: 0969-8043. DOI: <https://doi.org/10.1016/j.apradiso.2019.108951>. URL: <https://www.sciencedirect.com/science/article/pii/S0969804319307821>.
- [202] Inc. Varian Medical Systems. *Varian Installs ProBeam Cyclotron at UCLH Proton Beam Therapy Center*. 2018. URL: <https://www.varian.com/en-gb/node/6633>.
- [203] A Roth, E Akcöltekin, O Boldt et al. ‘ENERGY REDUCTION OF VARIAN’S ProBeam 250 MeV CYCLOTRON TO 226 MeV’. In: (2019). DOI: 10.18429/JACoW-Cyclotrons2019-FRA03.
- [204] *Blackout and Laser Safety Materials*. URL: [https://www.thorlabs.com/newgrouppage9.cfm?objectgroup\\_id=190&pn=BK5](https://www.thorlabs.com/newgrouppage9.cfm?objectgroup_id=190&pn=BK5).
- [205] B Marchand, D Prieels, B Bauvir et al. ‘IBA proton pencil beam scanning: an innovative solution for cancer treatment’. In: *Proceedings of EPAC* (2000), pp. 2539–2541. URL: <http://accelconf.web.cern.ch/Accelconf/e00/PAPERS/WEP4B20.pdf>.
- [206] Pauli Virtanen, Ralf Gommers, Travis E Oliphant et al. ‘SciPy 1.0: Fundamental Algorithms for Scientific Computing in Python’. In: *Nature Methods* 17 (2020), pp. 261–272. DOI: <https://doi.org/10.1038/s41592-019-0686-2>.
- [207] COMSOL Multiphysics. *Heat Transfer Module User’s Guide*. 2015.
- [208] *Introduction*. URL: <https://imagej.nih.gov/ij/docs/intro.html>.

## REFERENCES

---

- [209] John Hennig. ‘MPh 1.0.4’. In: (2021). URL: <https://pypi.org/project/MPh/>.
- [210] Donald M. McEligot, W. David Swank, David L. Cottle et al. ‘Thermal Properties of G-348 Graphite’. In: May (2016), p. 23. URL: <https://www.osti.gov/servlets/purl/1330693>.
- [211] Giorgia Fugallo, Andrea Cepellotti, Lorenzo Paulatto et al. ‘Thermal conductivity of graphene and graphite: Collective excitations and mean free paths’. In: *Nano Letters* 14.11 (2014), pp. 6109–6114. ISSN: 15306992. DOI: 10.1021/nl502059f.
- [212] Ge Wang, Jong Chul Ye and Bruno De Man. ‘Deep learning for tomographic image reconstruction’. In: *Nature Machine Intelligence* 2.12 (2020), pp. 737–748. ISSN: 2522-5839. DOI: 10.1038/s42256-020-00273-z. URL: <https://doi.org/10.1038/s42256-020-00273-z>.
- [213] IBA Dosimetry. *myQA SRS*. URL: <https://www.iba-dosimetry.com/product/myqa-srs/>.
- [214] L. S. Argemi, I. A. Asensi, I. Berdalovic et al. ‘The MALTA CMOS pixel detector prototype for the ATLAS Pixel ITk’. In: *Proceedings of Science* 348.October (2018), pp. 0–10. ISSN: 18248039. DOI: 10.22323/1.348.0014.
- [215] Raphaël Serduc, Audrey Bouchet, Elke Bräuer-Krisch et al. ‘Synchrotron microbeam radiation therapy for rat brain tumor palliation—influence of the microbeam width at constant valley dose’. In: *Physics in Medicine and Biology* 54.21 (Nov. 2009), pp. 6711–6724. ISSN: 0031-9155. DOI: 10.1088/0031-9155/54/21/017. URL: <http://stacks.iop.org/0031-9155/54/i=21/a=017?key=crossref.0b4cc3eea4f6fa33d89dfd210926eab6>.
- [216] *PyMedPhys*. URL: <https://pymedphys.com/>.
- [217] Janusz Winięcki, Tomasz Morgaś, Karolina Majewska et al. ‘The gamma evaluation method as a routine QA procedure of IMRT’. In: *Reports of Practical Oncology and Radiotherapy* 14.5 (2009), pp. 162–168. ISSN: 15071367. DOI: 10.1016/S1507-1367(10)60031-4.

# Appendices

# Appendix A

## PRAVDA tracker reconstruction algorithms

### A.1 Reconstruction algorithms

Unlike the pCT algorithm which is capable of reconstructing the particle (and thus the tracks) of individual particles, the profile acquired by the trackers in treatment mode meant new algorithms had to be developed, referred to as the "Fast" and "Slow" algorithms. Both reconstruction algorithms were written in LabVIEW. This programming language was chosen as the data acquisition software provided by aSpect Systems GmbH for data acquisition in pCT and therapeutic mode was also written in LabVIEW.

#### A.1.1 Fast reconstruction algorithm

##### A.1.1.1 Projection method

The algorithm projects the three profiles acquired by the trackers into a 2D space. Each plane is assigned a gradient ( $m_{x,u,v}$ ) representing the line tangentially intersecting all the strip channels. It is assumed that the centre of each strip plane is aligned. Equation A.1 governs the position along the centre of the strip channels.

$$y_i = m_{x,u,v}x_i \tag{A.1}$$

For an arbitrary point in 2D space ( $x_i, y_i$ ) there exists a line connecting each plane with a gradient that is perpendicular to the gradient assigned to the plane ( $m_{x,u,v}$ ). The equation governing this is A.2.

$$y_{tangent} = \frac{-1}{m_{x,u,v}}x_i + c_{x,u,v} \tag{A.2}$$

Equating A.1 and A.2 to eliminate the variable  $c_{x,u,v}$ , A.3 determines the projection in the x-axis along the strips for each plane for the arbitrary point  $(x_i, y_i)$ .

$$x_{x,u,v} = \left( \frac{\frac{x_i}{m_{x,u,v}} + y_i}{m_{x,u,v} + \frac{1}{m_{x,u,v}}} \right) \quad (\text{A.3})$$

Equating A.1 and A.3 determines the projection in the y-axis for each plane (A.4).

$$y_{x,u,v} = \left( \frac{\frac{x_i}{m_{x,u,v}} + y_i}{m_{x,u,v} + \frac{1}{m_{x,u,v}}} \right) m_{x,u,v} \quad (\text{A.4})$$

The displacement along each axis (relative to the origin) is calculated with A.5, where the appropriate sign is chosen by evaluating  $x_i - x_{x,u,v}$ . The index of the slit is determined by subtracting 512, as the strip index does not start in the centre of the strip plane.

$$d_i = \pm \sqrt{x_{x,u,v}^2 + y_{x,u,v}^2} \quad (\text{A.5})$$

The value assigned to the projection matrix at coordinates  $(x_i, y_i)$  is given by indexing all of the strip layers and summing the values. Exception cases have to be made in the event that the strip layers are aligned at 0, or 90°, in which circumstance the algorithm takes the appropriate x or y index accordingly. Figure A.1 graphically demonstrates the projection method.

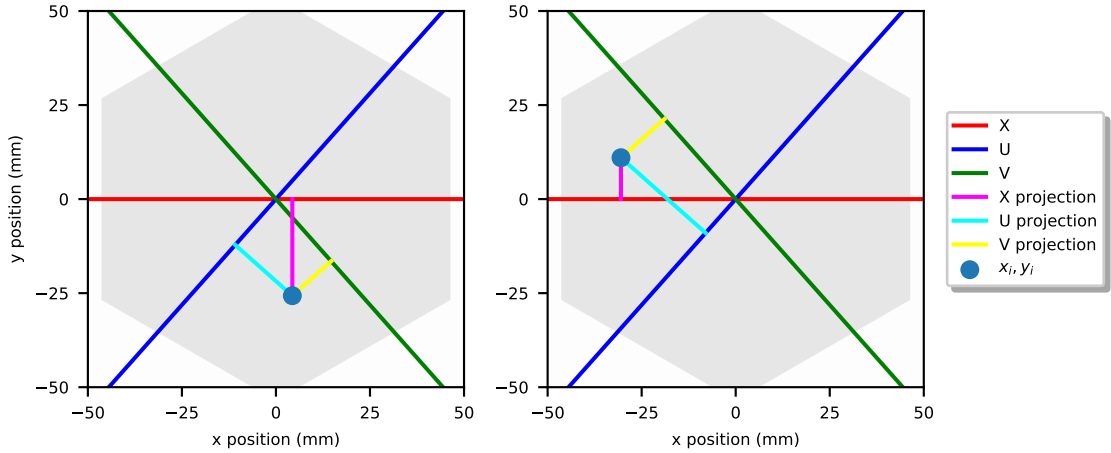


Figure A.1: Diagram of PRAVDA reconstruction algorithm.

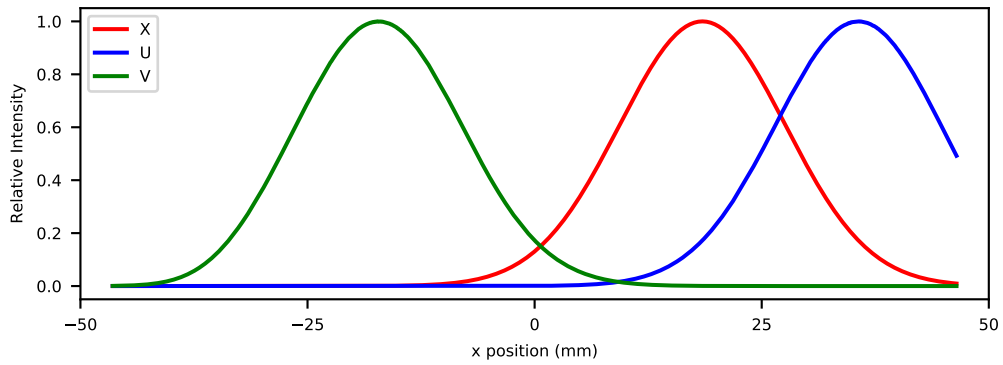


Figure A.2: Simulated Gaussian profiles on the PRAVDA tracker layers with a 20 mm FWHM, centred at  $X = 18.5$  mm,  $U = 35.7$  mm and  $V = -17.2$  mm.

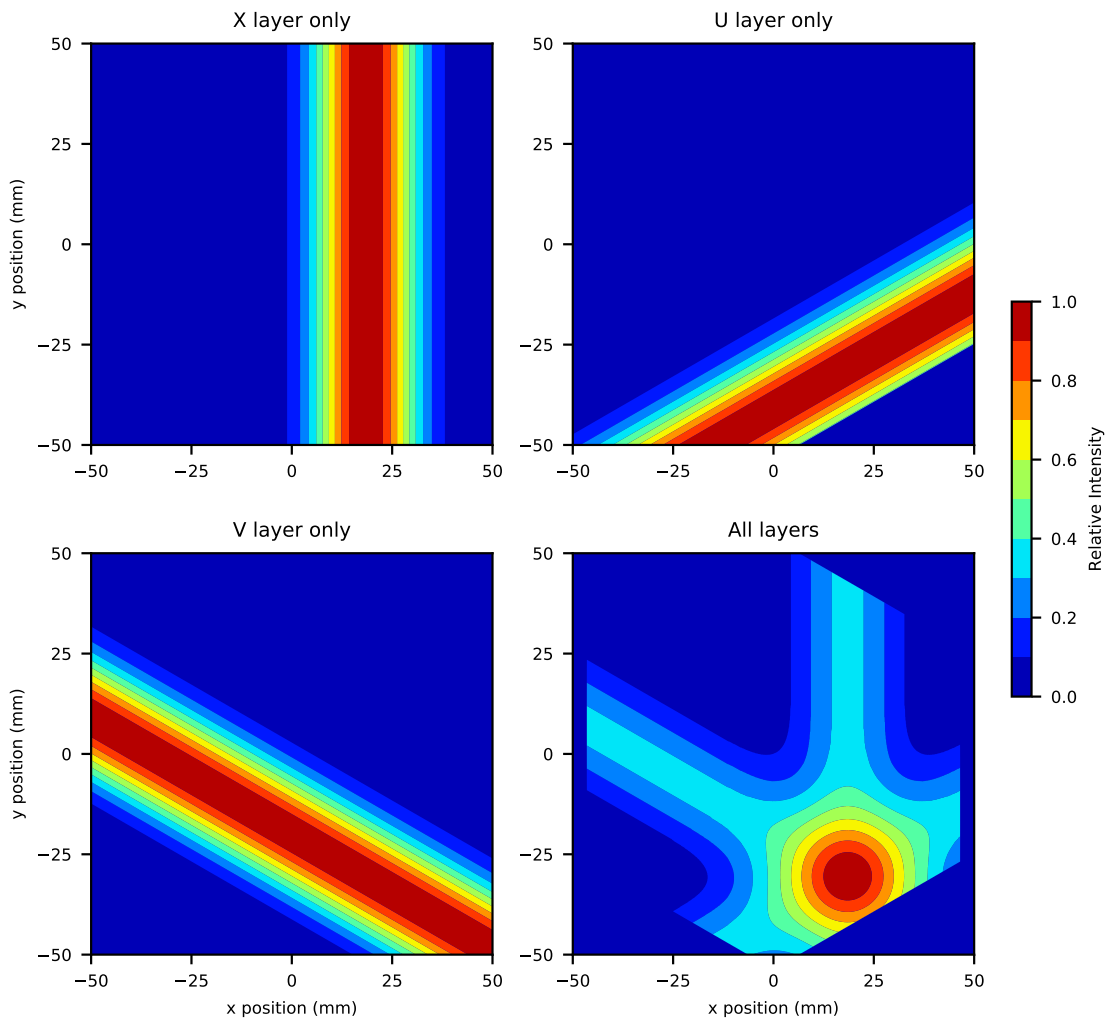


Figure A.3: Layer by layer reconstruction of the simulated Gaussian profiles for the PRAVDA tracker shown in Figure A.2.

### A.1.1.2 Beam Centre Validation

The PRAVDA tracker algorithm for treatment mode reconstruction was validated by the development of a secondary program to determine its limitations. A validation algorithm was developed (again developed in LabVIEW, to enable use of the same code) and carries out the reconstruction algorithm in reverse, using an input 2D image or array and determining the projection on each of the tracker layers. Using this, incident beams of different sizes, shapes and locations can be investigated. Figure A.4 shows a simulated 2D Gaussian with a FWHM of 20 mm and the reconstructed beam. Figure A.5 shows a physically impossible square beam of  $20 \times 20 \text{ mm}^2$  (both positioned at (0 mm, 0 mm)).

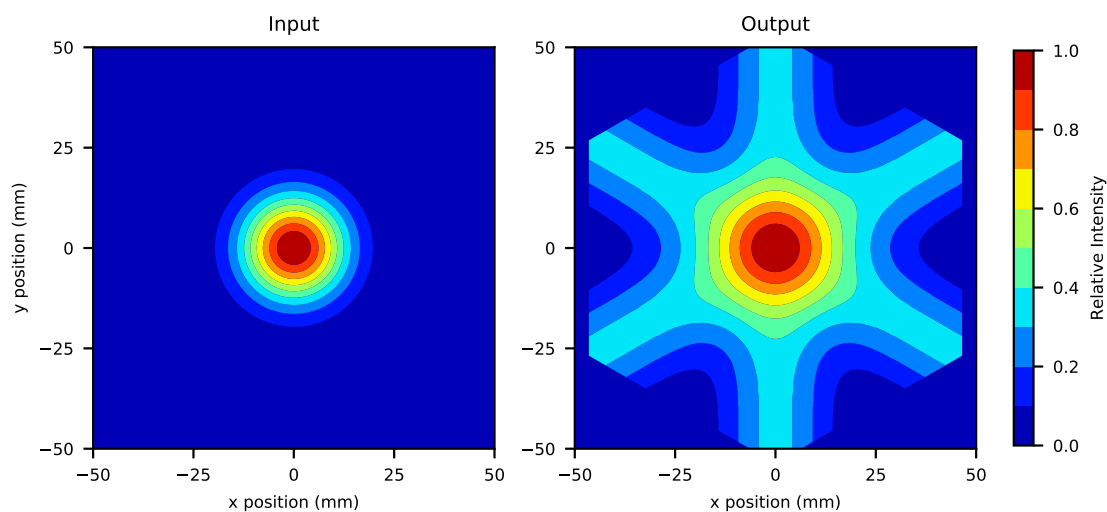


Figure A.4: Demonstration of the validation algorithm for a 2D Gaussian with 20 mm FWHM.

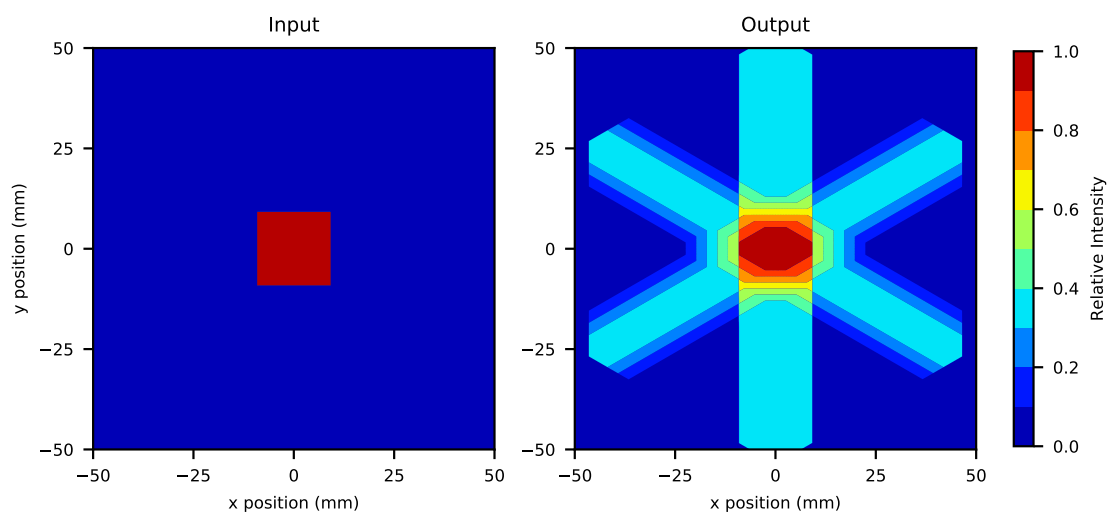


Figure A.5: Demonstration of validation algorithm for a  $20 \times 20 \text{ mm}^2$  square.

### A.1.1.3 Effect of threshold cutoff

To determine the centre of the reconstructed projection a centre of mass function is fitted, however as a result of the streaking artefacts resulting from the projection method this method results in inaccurate values. To account for this, a 50% threshold filter was applied. This value was chosen after simulations (Figure A.6) showing that it required to be at least 33% (due to the three layers), and due to the historic use of 50% dose maximum to determine field sizes in conventional flattening field external beam radiotherapy.

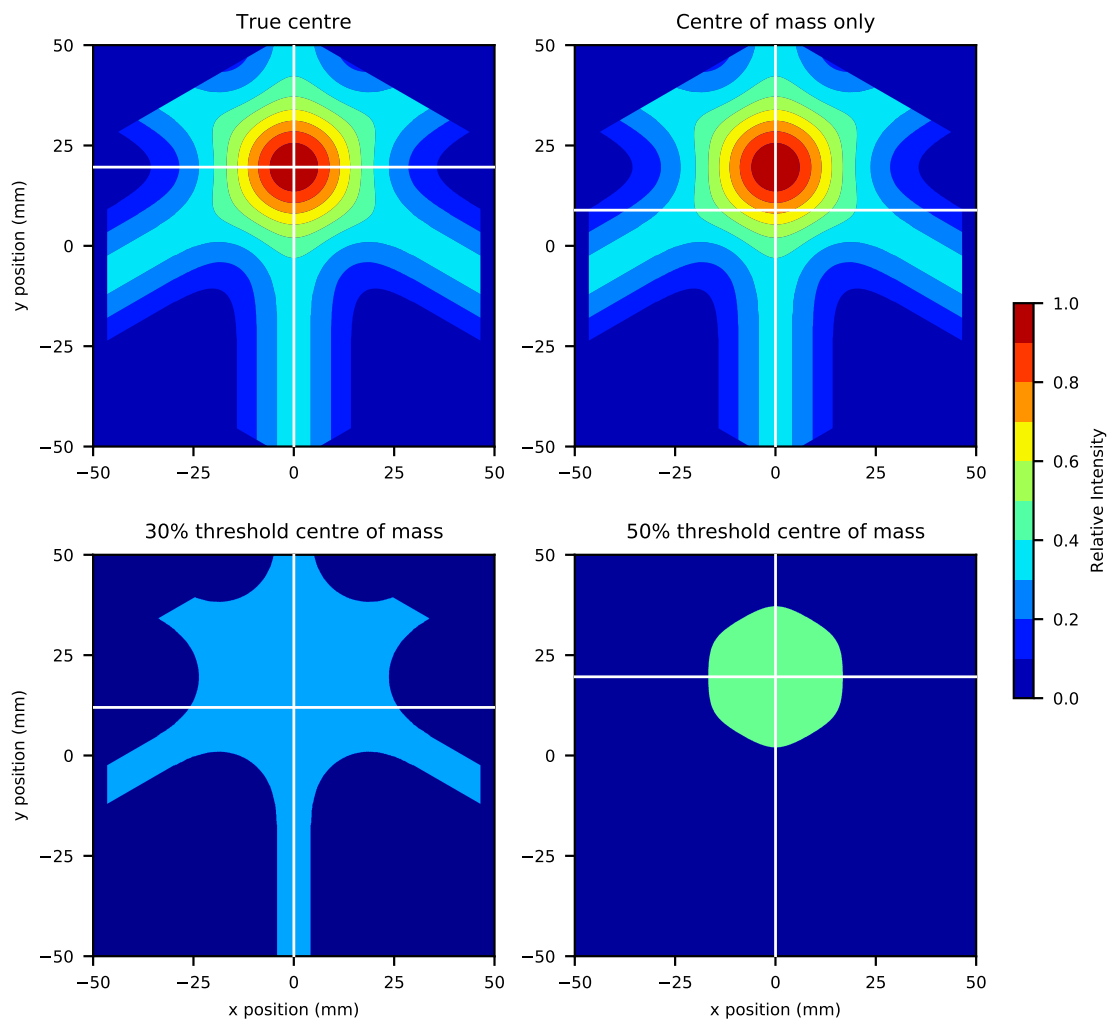


Figure A.6: Determining the beam centre of the reconstructed beam projection.

The effect of changing this threshold value on the reconstructed beam centre can be seen in Figure A.7, where there is a significant reduction in the position error (defined as the displacement between the centre of the incident and reconstructed beams) above 33%. Increasing the threshold to above 50% results in no significant reduction in position error, and is likely to make the reconstruction more sensitive to noise.

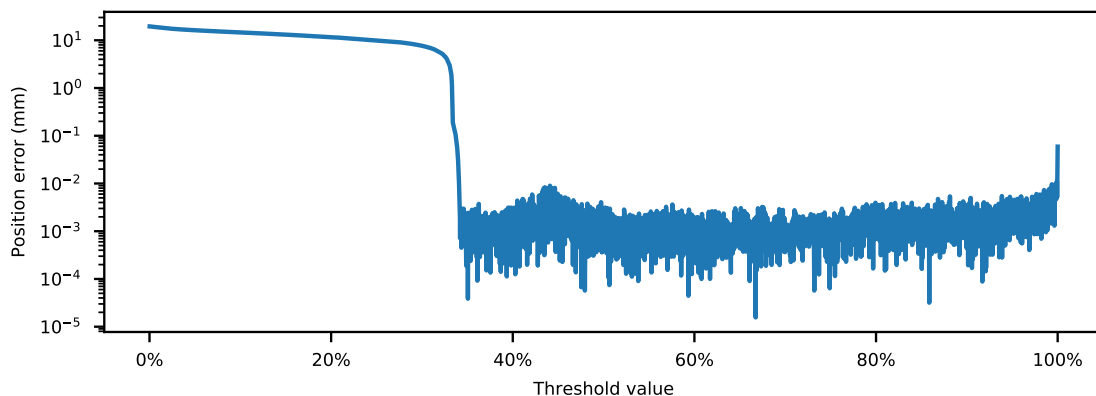


Figure A.7: Position error of the reconstructed beam centre for different threshold values.

#### A.1.1.4 Gamma Evaluation

A quantitative quantification of the reconstructed beam was performed using a gamma evaluation with the open source PyMedPhys Python module[216]. The gamma evaluation method compares a reference profile ( $D_r$ ) to a second dose profile( $D_e$ ). In clinical use, this is used for verifying predicted and measured dose distributions in routine quality assurance[217]. Typical clinical requirements in IMRT are that the delivered beam at each point within the dose profile should be within 3% of the expected or within 3 mm of a pixel that is the correct dose.

The function used to compute this is equation A.6, where the dose difference  $\delta(\vec{r}_e, \vec{r}_r)$  is defined in equation A.7 and the spatial difference ( $r(\vec{r}_e, \vec{r}_r)$ ) is defined in equation A.8.

$$\Gamma(\vec{r}_e, \vec{r}_r) = \sqrt{\frac{\delta^2(\vec{r}_e, \vec{r}_r)}{\Delta D^2} + \frac{r^2(\vec{r}_e, \vec{r}_r)}{\Delta d^2}} \quad (\text{A.6})$$

$$\delta(\vec{r}_e, \vec{r}_r) = D_e(\vec{r}_e) - D_r(\vec{r}_r) \quad (\text{A.7})$$

$$r(\vec{r}_e, \vec{r}_r) = |\vec{r}_e - \vec{r}_r| \quad (\text{A.8})$$

The gamma index of the reference point ( $\gamma(\vec{r}_r)$ ) is determined after sampling the surrounding pixels to determine the local gamma evaluations and finding the minimum value (equation A.9). A pixel is determined to have passed the gamma evaluation if  $\gamma(\vec{r}_r) \leq 1$ .

$$\gamma(\vec{r}_r) = \min\{\Gamma(\vec{r}_e, \vec{r}_r)\} \forall \{\vec{r}_e\} \quad (\text{A.9})$$

The gamma passing criteria for comparing predicted measured and predicted dose profiles is typically that 95% of pixels have a gamma evaluation of less than or equal to 1. To avoid weighting

this value to low dose regions which may have low impact, a dose threshold of 20% is typically applied, ignoring values below that.

The computed gamma evaluation for the "Fast" algorithm reconstructing a  $25 \times 15 \text{ mm}^2$  ellipsoid is shown in figure A.8. The gamma passing rate is 8.69%, which would not be clinically acceptable. The reconstruction method results in "smeared" artefacts in the 2D reconstruction of relative intensity (100/n)%, where n is the number of layers.

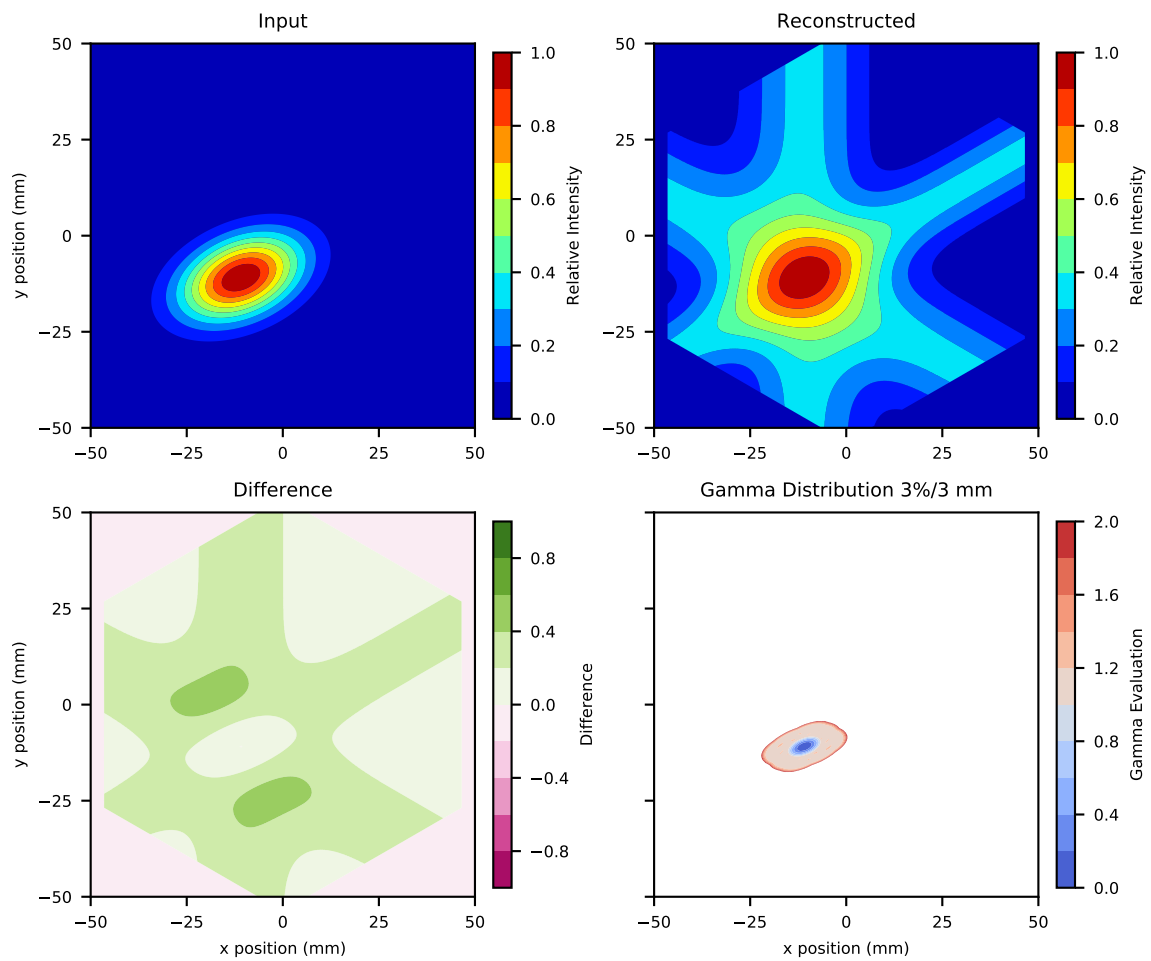


Figure A.8: Gamma evaluation of the "Fast" reconstruction algorithm with 3%/3mm parameters and a 20% dose cutoff.

### A.1.2 Slow reconstruction algorithm

As described, the "Slow" reconstruction method aims to reconstruct incident radiation field as accurately as possible.

### A.1.2.1 Projection method

The "Slow" reconstruction method begins with the assumption that the incident beam is "Gaussian-like". The reconstructed beam centre from the "Fast" reconstruction is used to create a pivot point. The profiles from the separate strip planes are then reevaluated, to determine the channel either side of the centre that matches a target percentage (such as 66%). This process can be seen in Figure A.9.

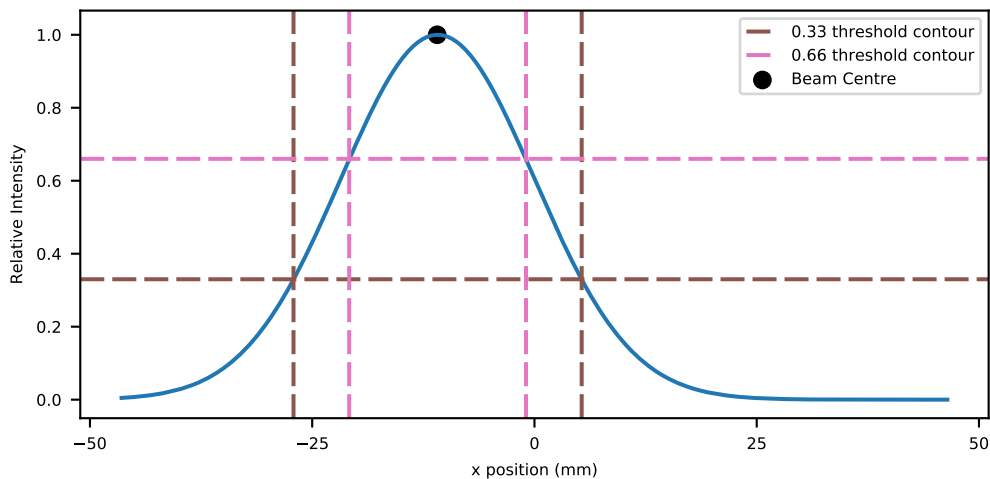


Figure A.9: "Slow" Reconstruction Algorithm step 1: Identifying the 1D positions of the threshold.

The determined points are then projected from the pivot point in a plane that is parallel to the plane of the SSD. Repeating this for each plane, results in a set of positions as seen in the left plot of Figure A.10. An additional step then takes place to interpolate between these fixed positions, to convert the hexagonal polygon into a shape with smooth edges. Pixels within this defined area are assigned the value of the target percentage. The process is repeated for a number of target percentages, to build up 2D intensity profile.

A "Slow" reconstruction of the same incident off-centre ellipsoid as shown for Figure A.8 can be seen in Figure A.11. As result of processing, the gamma passing rate (3%/3mm, 20% cutoff) of the reconstruction was increased to 36.47%. Whilst this represents a significant increase, it is still significantly lower than would be desired clinically.

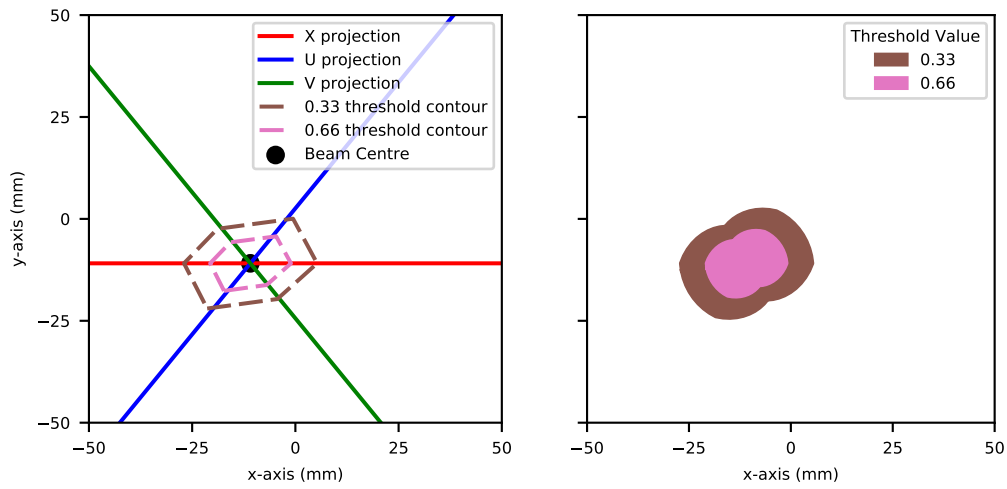


Figure A.10: "Slow" Reconstruction Algorithm Step 2: Defining 2D threshold contours

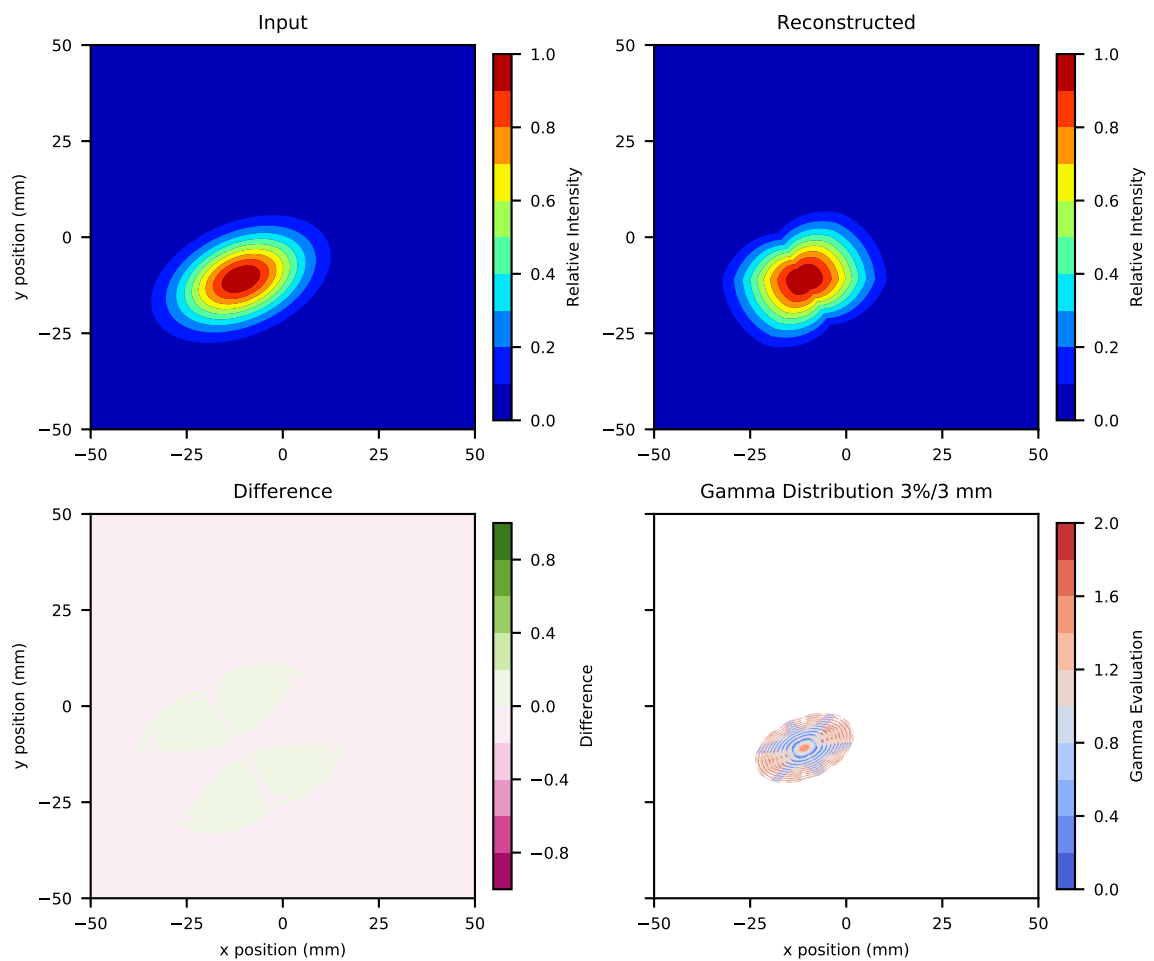


Figure A.11: Gamma evaluation of the "Slow" reconstruction algorithm with 3%/3mm parameters and a 20% dose cutoff.

# Appendix B

## Presentations and Publications

### B.1 Poster presentations

- *First demonstration of real-time in-situ dosimetry of x-ray microbeams using a large format CMOS sensor*  
12th International "Hiroshima" Symposium on the Development and Application of Semiconductor Tracking Detectors (HSTD12), 2019, Hiroshima, Japan
- *Proof of concept investigation for in-vivo verification of microbeam radiotherapy using high resolution pixelated detectors*  
International Congress on Radiation Research, 2019, Manchester, United Kingdom
- *Therapeutic dose rate reconstruction of X-Ray beams using strip detectors for enhanced primary standard dosimetry*  
Proton Physics Research and Implementation Group, 2019, London, United Kingdom

### B.2 First-author publications

- Characterisation of a megavolt X-Ray therapeutic beam using non-orthogonal strip detectors for future enhanced primary standard dosimetry, 2019, Journal of Instrumentation[22]
- Evaluation of a pixelated large format CMOS sensor for x-ray microbeam radiotherapy, 2020, AAPM Medical Physics[197]
- First demonstration of real-time in-situ dosimetry of X-ray microbeams using a large format CMOS sensor, 2020, NIMA[198]

## TECHNICAL REPORT

## Characterisation of a megavolt X-Ray therapeutic beam using non-orthogonal strip detectors for future enhanced primary standard dosimetry

S. Flynn,<sup>a,b,1</sup> T. Price,<sup>a,b</sup> S. Galer,<sup>b</sup> R. Thomas,<sup>b</sup> J. Cotterill,<sup>a</sup> M. Chiesa,<sup>c</sup> C. Waltham,<sup>d</sup> J. Taylor,<sup>e</sup> A. Smith<sup>e</sup> and P. Allport<sup>a</sup>

<sup>a</sup>*School of Physics and Astronomy, University of Birmingham, Edgbaston Park Road, Birmingham B15 2TT, U.K.*

<sup>b</sup>*Medical Radiation Science, National Physical Laboratory, Hampton Road, Teddington TW11 0WL, U.K.*

<sup>c</sup>*Dipartimento di Fisica, Università degli Studi di Pavia, Via Bassi 6, 27100 Pavia PV, Italy*

<sup>d</sup>*Laboratory of Vision Engineering, School of Computer Science, University of Lincoln, Lincoln LN6 7TS, U.K.*

<sup>e</sup>*Department of Physics, University of Liverpool, Oxford Street, Liverpool L69 7ZE, U.K.*

E-mail: [sam.flynn@npl.co.uk](mailto:sam.flynn@npl.co.uk)

**ABSTRACT:** The National Physical Laboratory (NPL) provides traceable high accuracy measurements for absorbed dose via primary standard graphite calorimeters. Patients undergoing radiotherapy for cancer treatments in the U.K. receive a dose that is traceable to these devices. In the case of hadron radiotherapy, reducing the uncertainty of these measurements requires the addition of spatial information to understand not only the integral dose delivered, but where the energy is deposited locally.

The PRaVDA consortium developed strip detectors able to track individual protons at low rates for proton computed tomography. For calorimetry at clinical dose rates only real-time spot location is required, which could be projected to reconstruct a 2D visualisation from which the beam centre can be determined.

This work reports on a proof-of-concept trial carried out using 6 MV X-rays using an Elekta Synergy linear accelerator. We show how the beam positions can be determined within  $\pm 0.5$  mm of the expected radiation beam position, which is similar to the tolerances of the field defining multileaf collimator within the linear accelerator treatment head.

The trial will be extended to perform measurements in a clinical proton beam alongside the NPL graphite proton calorimeter.

**KEYWORDS:** Instrumentation for gamma-electron therapy; Algorithms and Software for radiotherapy; Dosimetry concepts and apparatus; Instrumentation for hadron therapy

Corresponding author.

---

## Contents

<b>1</b>	<b>Introduction</b>	<b>1</b>
1.1	Graphite calorimetry at the National Physical Laboratory	1
1.2	Silicon tracker development by PRaVDA	2
<b>2</b>	<b>Method</b>	<b>2</b>
2.1	Exposures performed	2
2.2	Reconstruction algorithm	2
<b>3</b>	<b>Results</b>	<b>3</b>
3.1	Pulse detection	3
3.2	Static irradiations	3
3.3	Moving irradiations	5
<b>4</b>	<b>Discussion</b>	<b>6</b>
<b>5</b>	<b>Conclusions</b>	<b>6</b>

---

## 1 Introduction

In the U.K. there are an estimated 2.5 million people living with cancer, a figure expected to rise to 4 million by 2030 [1]. Proton radiotherapy is commonly used in specialist cancer cases where the dose sparing effect of the energy loss of protons being greatest at the end of their range (the “Bragg peak”) can be exploited to reduce damage to healthy cells around the primary tumour volume. However, due to errors associated with delivering the beam during modern pencil beam spot-scanning treatments, hotspots within the delivery volume of approximately 4% can arise from a single spot delivered 1 mm off target [2]. This has motivated the development of proton computed tomography (pCT) to reduce uncertainties by directly mapping the proton stopping power within the patient.

### 1.1 Graphite calorimetry at the National Physical Laboratory

The suite of primary standard graphite calorimeters at the National Physical Laboratory (NPL) provide traceable absorbed dose measurements in the United Kingdom for X-ray and proton radiotherapy. These devices are irradiated using clinical radiation beams in lieu of a patient and directly measure the temperature rise (of the order mK) due to radiation interactions using calibrated thermistors embedded within the graphite. Using the measured energy change combined with relevant correction factors the total absorbed dose can be determined with very low uncertainty. An incident radiation beam covering multiple components within the calorimeter would cause differing temperature rises (due to the differing specific heat capacities). This is accounted for by large-scale

modelling of temperature and heat flows [3] which, by also including detailed additional positional information of the beam, allows even more accurate heat flow corrections to be applied, reducing the overall uncertainty.

## 1.2 Silicon tracker development by PRAVDA

To investigate pCT, the PRAVDA collaboration developed silicon strip detectors (SSDs) capable of resolving the signal for individual protons in order to resolve their position for path reconstruction. The SSDs consist of 150  $\mu\text{m}$  thick n-in-p silicon with  $2 \times 1024$  channels (90.8  $\mu\text{m}$  pitch) for an active area of  $93 \times 96 \text{ mm}^2$  split into two regions of active area  $93 \times 48 \text{ mm}^2$ . Each tracker unit consists of three pairs of SSDs rotated by  $60^\circ$  with respect to each other in a (X-U-V) configuration. The each ASIC has two tunable thresholds for both high and low particle fluence environments. In addition to pCT mode (where the ASICs read out at the 26 MHz repetition rate of the cyclotron for a maximum of eight channels per cycle, as described in [4]), the ASICs are capable of operating in “Treatment mode”, a modality which has not been investigated until now. In this mode all channels are read at a maximum 6 kHz repetition rate with the charge deposited on each strip integrating between measurements. This mode is not capable of recording the signals of individual protons, but could instead measure projections of the incident radiation beam in each of the planes.

## 2 Method

To evaluate the interaction between the PRAVDA tracker and a high dose rate beam, an exposure was performed at the National Physical Laboratory using an Elekta Synergy Linac delivering 6 MV X-ray beams. Although the aim of this collaboration is to reduce the associated spatial uncertainty of proton beams, both the proton calorimeter and the PRAVDA tracker unit should respond to X-ray beams in a similar manner as energy is deposited within the detectors.

### 2.1 Exposures performed

The tracker was set up at the linear accelerator’s isocentre with 5 cm of water equivalent solid water plastic following the IAEA code of practice for X-ray dosimetry [5]. The PRAVDA tracker was tested with a  $2.0 \times 2.0 \text{ cm}^2$  6 MV X-ray beam, which was moved by changing the leaves of the Multileaf Collimator as well as rotating the linear accelerator head.

### 2.2 Reconstruction algorithm

The developed algorithm is capable of projecting the response for each channel onto a 2D space. This is achieved by determining the strip channel position in each plane for each given point in space within the active area (as can be seen in figure 1(a)) and summing the strip response for the associated channels in each plane. To compute the beam centre a function was applied to the resulting 2D array to discard any results below 50% of the maximum value and normalise those above. The 50% filter minimises the influence of the banded artefacts that can be seen in figure 1(b). A medium rank filter can be applied to the X-U-V profiles, removing the influence of oversensitive or masked channels before normalising each plane’s response to account for global calibration differences in each plane (as seen in figure 3).

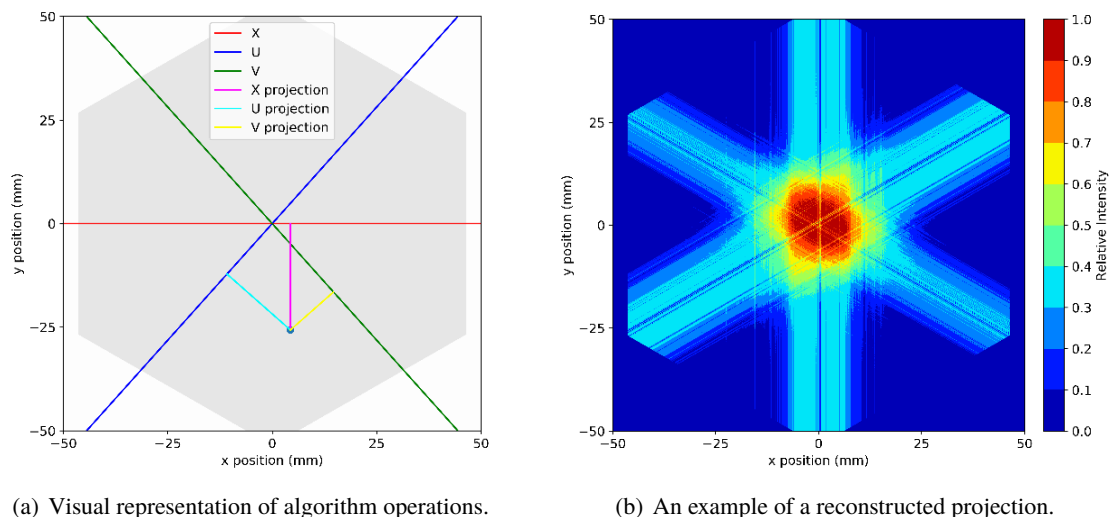


**Figure 1.** The reconstruction algorithm determines the projection of each of the three strips for each point in space, rather than calculate each intersection between the strip channels.

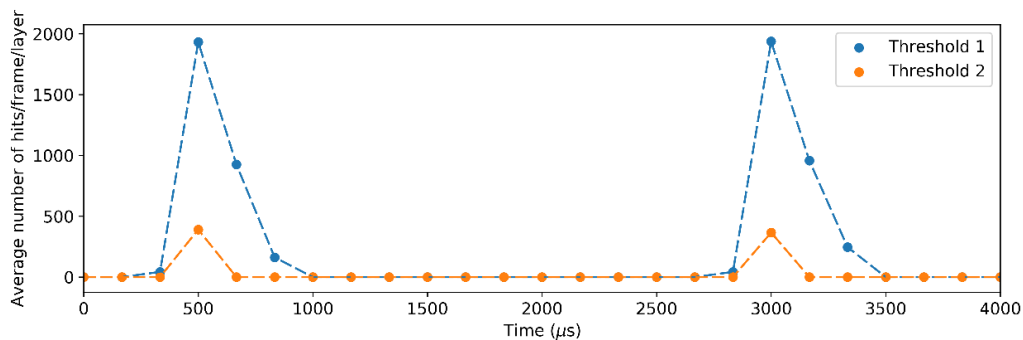


**Figure 2.** The PRaVDA tracker was able to detect individual pulses from the Elekta Synergy Linear Accelerator.

Only positions that are present on all three planes are reconstructed using the algorithm. Points that are out of these limits are ignored, creating the sharp hexagonal background that can be seen in figure 1(a) and figure 1(b).

### 3 Results

#### 3.1 Pulse detection

The PRaVDA tracker was found to be able to detect X-rays from the linear accelerator, with the high measurement rate of the detector enabling individual linac pulses to be detected as can be seen in figure 2. Using the signal deposited on the two thresholds, the pulse width can be estimated at 300–700  $\mu\text{s}$ , comparable to previous work by [6] but with significantly lower temporal resolution. The threshold levels were manually tuned to prevent saturation.

#### 3.2 Static irradiations

Figure 3 shows the processed tracker response to an X-ray beam. It can be observed that the strips in the X plane (with the same orientation as the square field) measure a beam profile similar to that

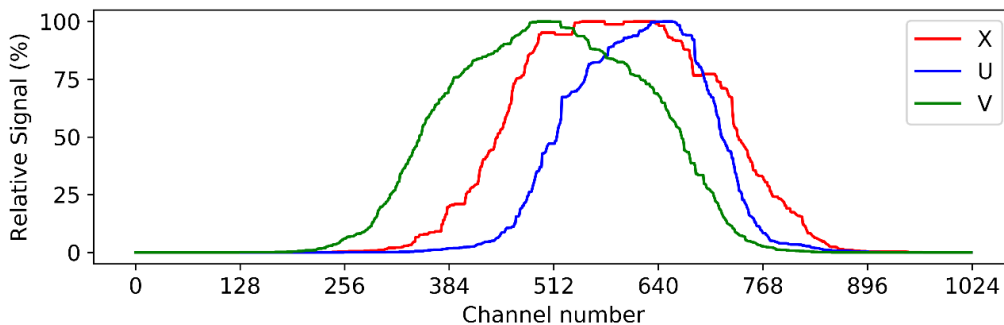


**Figure 3.** The PRaVDA tracker processed channel response to a clinical dose rate 6 MV  $20 \times 20$  mm<sup>2</sup> square X-ray incident beam, irradiating off centre.

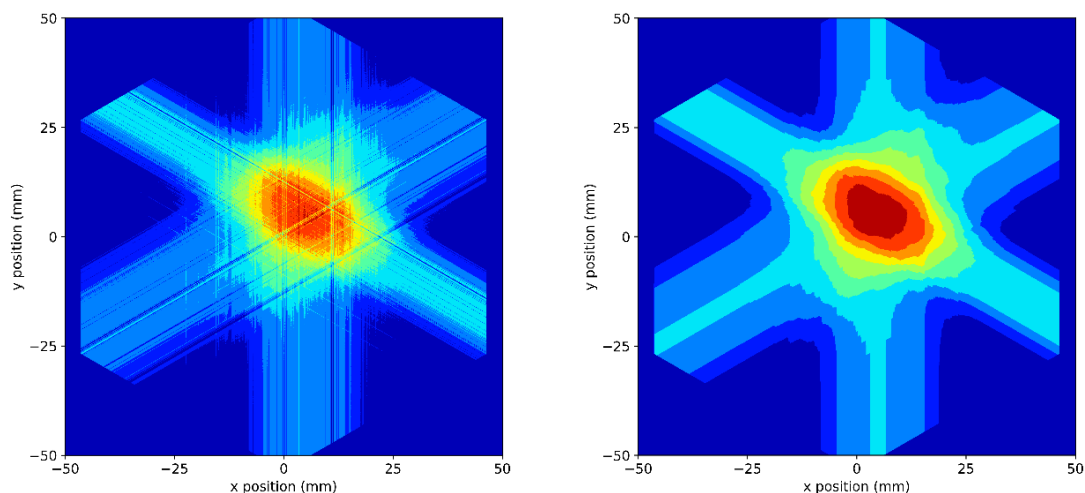
when using standard radiotherapy equipment. The U and V planes (oriented  $60^\circ$  and  $120^\circ$  to the square X-ray beam) capture a projected profile that is narrower.

The algorithm developed is able to accurately reconstruct the centre of the beam for a multitude of positions, providing that the entire beam profile is contained the three planes of silicon strip detectors. Under these circumstances, the calculated beam centre was found to consistently be within 0.5 mm of the expected position.

Beam reconstruction was found only to be possible when the entire beam profile was captured by the strip detectors. As a beam with FWHM of approximately 20 mm was used, this would limit the region within the active area capable of successfully reconstructing a beam to a circle with radius 30 mm. For smaller incident beams (as in the case of clinical proton beams with beam size approximately  $7$  mm  $\sigma$ ), this reconstruction area is expected to increase consequently. Further investigations are planned to verify this. The repeatability of the multileaf collimators in delivering a fixed beam was investigated by comparing several different reconstructed beams. It was found that all beam centres of the same position were within  $\pm 0.5$  mm of each other, well within the expected tolerance of the linear accelerator.

By irradiating with complex field shapes (when the field was no longer a simple square) with the multileaf collimator, it was found that the developed algorithm was unable to reconstruct many features of the incident beam. This was expected, due to the signal being spatially integrated over the strip detector, however the beam centre for each of these was found to agree. Having more than three planes would allow for a more representative reconstruction of the field edges and shape but would not provide additional information regarding the internal beam structure — a fundamental limitation of using strip detectors.

It was found that processing the silicon strip detector channel responses to remove the noise generally had a minimal effect on positional accuracy due to the relatively few number of channels generating erroneous readings. As only the overall signal profile was required to calculate the beam centre, large differences between adjacent strips could be dismissed. Typical differences between the beam centres calculated using raw and processed data were less than 0.3 mm, however the processed values were consistently closer to the expected positions. An example of this can be seen in figure 4.



(a) Raw signal reconstruction: the calculated centre is  $(4.8 \pm 0.1 \text{ mm}, 5.4 \pm 0.1 \text{ mm})$ .

(b) Processed signal reconstruction: the calculated centre is  $(5.0 \pm 0.1 \text{ mm}, 5.5 \pm 0.1 \text{ mm})$ .

**Figure 4.** Comparison of raw (a) and processed (b) reconstructions of an X-ray beam  $20 \times 20 \text{ mm}^2$  square X-ray incident beam at  $(5.0 \text{ mm}, 5.0 \text{ mm})$ . The tracker was found to be positioned  $0.5 \text{ mm}$  offset in the Y axis across all measurements. The same colourbar scale is used as in figure 1(b).

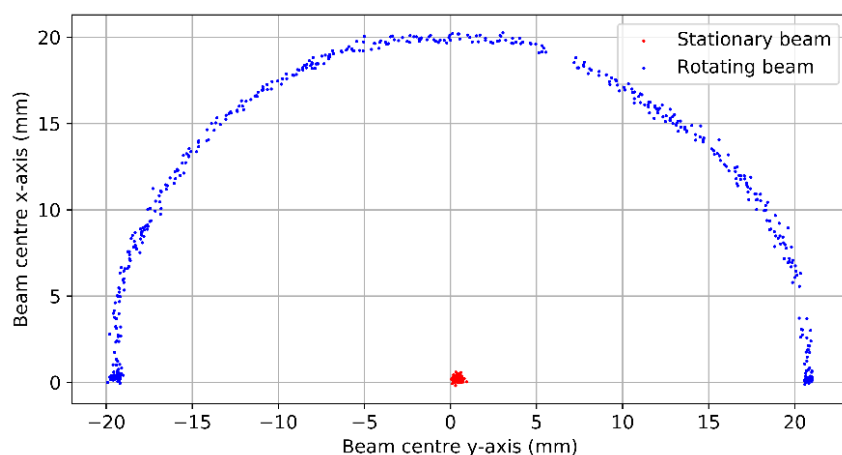


**Figure 5.** Reconstructed centres of a stationary X-ray beam and a rotating X-ray beam with arc  $20 \text{ mm}$  as measured by the PRaVDA tracker and reconstructed using the developed algorithm. The gaps present in the arc are due to a dead time that occurs between the PRaVDA taking successive measurements.

### 3.3 Moving irradiations

By subdividing the 10,000 frames obtained by the detector in each measurement it is possible to create multiple consecutive reconstructions using the developed algorithm from the same measurement. Analysis of a moving radiation field could be achieved this way. A radiation field positioned at  $(0 \text{ mm}, 20 \text{ mm})$  using the multileaf collimator was moved in an arc by rotating the collimator between  $0^\circ$  and  $180^\circ$ . Figure 5 shows the result obtained from this when taking 10 consecutive measurements. The calculated radius of this arc was determined to be  $20.04 \pm 0.36 \text{ mm}$ .

## 4 Discussion

The irradiations provided by the Synergy linear accelerator were all carried out using a flattening field filter, designed to provide uniform beams. Further investigation is required to determine the validity of the algorithm to non-uniform beams, this could be achieved by de-tuning the linear accelerator's internal steering mechanism to create an asymmetrical beam or introducing a device to perturb the beam such as a mechanical wedge. All of the results presented were performed using simple beam shapes for initial verification of the PRaVDA tracker, the abundance of complex field shapes used in modern Volume Modulated Arc Therapy (VMAT) would indicate that silicon strip detectors are not suitable for X-ray radiotherapy. Complex fields would require the use of pixelated detectors such as the ACHILLES as has been done by [7], however simple Gaussian beams as used in modern proton beam therapies are ideal candidates for the detectors described here.

The use of silicon strip detectors for beam monitoring in radiotherapy has been explored by the international community [8, 9], however the PRaVDA tracker is novel due to its large active area and non-orthogonal layer orientation. When compared to commercial transmission detectors for proton beam monitoring (such as the IC128-25LC-2I detector by Pyramid [10]), the PRaVDA tracker has superior resolution but suffers from thicker water equivalent material, smaller active area and lower refresh rate. With further optimization in future iterations, these issues could be resolved in future revisions of the PRaVDA tracker unit.

## 5 Conclusions

The investigation demonstrated that high dose rate X-ray beams could be monitored using the three planes of silicon strip detectors that make up the PRaVDA tracker when operated in "Treatment Mode". It was determined that calculating many basic features of the beam (such as width, MLC positions) beyond beam centre could not be determined however this is to be expected when using strip sensors.

The resolution at which the developed algorithm can detect changes in beam position is small enough to enable the use of the PRaVDA tracker to benefit the NPL graphite calorimeter for absorbed dose in proton beam therapy by both reducing the energy uncertainty and adding beam profile information. Further experiments are planned in order to investigate this further and use the beam profile information of the PRaVDA tracker as a direct input for heat-flow modelling within the calorimeter.

## Acknowledgments

The authors wish to thank aSpect Systems GmbH for their continued support of the PRaVDA project, without which this investigation would not be possible.

This work was supported by the Science and Technology Facilities grant number ST/P002552/1.

## References

- [1] J. Maddams, M. Utley and H. Møller, *Projections of cancer prevalence in the United Kingdom, 2010-2040*, *Br. J. Cancer* **107** (2012) 1195.

- [2] J. Yu, C.J. Beltran and M.G. Herman, *Implication of spot position error on plan quality and patient safety in pencil-beam-scanning proton therapy*, *Med. Phys.* **41** (2014) 081706.
- [3] L.M. Petrie, *Characterisation of a graphite calorimeter in scanned proton beams* (2016).
- [4] J.T. Taylor et al., *A new silicon tracker for proton imaging and dosimetry*, *Nucl. Instrum. Meth. A* **831** (2016) 362.
- [5] *Absorbed Dose Determination in External Beam Radiotherapy*, IAEA TRS 398 2000, International Atomic Energy Agency, Vienna, Austria.
- [6] J.J. Velthuis et al., *Toward pulse by pulse dosimetry using an SC CVD diamond detector*, *IEEE Trans. Radiat. Plasma Med. Sci.* **1** (2017) 527.
- [7] R.F. Page et al., *Using a monolithic active pixel sensor for monitoring multileaf collimator positions in intensity modulated radiotherapy*, *IEEE Trans. Nucl. Sci.* **61** (2014) 74.
- [8] M. Povoli et al., *Thin silicon strip detectors for beam monitoring in micro-beam radiation therapy*, *2015 JINST* **10** P11007.
- [9] M. Bouterfa and D. Flandre, *Validation of a novel ultra-thin silicon strip detector for hadron therapy beam monitoring* *J. Circ. Syst. Comput.* **22** (2013) 1340018.
- [10] Anon Pyramid, *Product IC128-25LC-2I*, <http://www.ptcusa.com/products/44>.



# Evaluation of a pixelated large format CMOS sensor for x-ray microbeam radiotherapy

Samuel Flynn<sup>a)</sup> and Tony Price

*School of Physics and Astronomy, University of Birmingham, Birmingham B15 2TT, UK  
Medical Physics Department, National Physical Laboratory, Teddington TW11 0LW, UK*

Philip P. Allport

*School of Physics and Astronomy, University of Birmingham, Birmingham B15 2TT, UK*

Ileana Silvestre Patallo

*Medical Physics Department, National Physical Laboratory, Teddington TW11 0LW, UK  
UCL Cancer Institute, University College London, London WC1E 6AG, UK*

Russell Thomas, and Anna Subiel

*Medical Physics Department, National Physical Laboratory, Teddington TW11 0LW, UK*

Stefan Bartzsch

*Helmholtz Centre Munich, Institute for Radiation Medicine, Munich 85764, Germany  
School of Medicine, Klinikum rechts der Isar, Department of Radiation Oncology, Technical University of Munich, Munich 80333, Germany*

Franziska Treibel, and Mabroor Ahmed

*School of Medicine, Klinikum rechts der Isar, Department of Radiation Oncology, Technical University of Munich, Munich 80333, Germany*

Jon Jacobs-Headspith, Tim Edwards, Isaac Jones, and Dan Cathie

*vivaMOS Ltd, Southampton SO16 7NP, UK*

Nicola Guerrini, and Iain Sedgwick

*Rutherford Appleton Laboratory, Didcot OX11 0QX, UK*

(Received 16 August 2019; revised 6 December 2019; accepted for publication 6 December 2019; published xx xxxx xxxx)

**Purpose:** Current techniques and procedures for dosimetry in microbeams typically rely on radiochromic film or small volume ionization chambers for validation and quality assurance in 2D and 1D, respectively. Whilst well characterized for clinical and preclinical radiotherapy, these methods are non-instantaneous and do not provide real time profile information. The objective of this work is to determine the suitability of the newly developed vM1212 detector, a pixelated CMOS (complementary metal-oxide-semiconductor) imaging sensor, for *in situ* and *in vivo* verification of x-ray microbeams.

**Methods:** Experiments were carried out on the vM1212 detector using a 220 kVp small animal radiation research platform (SARRP) at the Helmholtz Centre Munich. A 3 x 3 cm<sup>2</sup> square piece of EBT3 film was placed on top of a marked nonfibrous card overlaying the sensitive silicon of the sensor. One centimeter of water equivalent bolus material was placed on top of the film for build-up. The response of the detector was compared to an Epson Expression 10000XL flatbed scanner using FilmQA Pro with triple channel dosimetry. This was also compared to a separate exposure using 450 μm of silicon as a surrogate for the detector and a Zeiss Axio Imager 2 microscope using an optical microscopy method of dosimetry. Microbeam collimator slits with range of nominal widths of 25, 50, 75, and 100 μm were used to compare beam profiles and determine sensitivity of the detector and both film measurements to different microbeams.

**Results:** The detector was able to measure peak and valley profiles in real-time, a significant reduction from the 24 hr self-development required by the EBT3 film. Observed full width at half maximum (FWHM) values were larger than the nominal slit widths, ranging from 130 to 190 μm due to divergence. Agreement between the methods was found for peak-to-valley dose ratio (PVDR), peak to peak separation and FWHM, but a difference in relative intensity of the microbeams was observed between the detectors.

**Conclusions:** The investigation demonstrated that pixelated CMOS sensors could be applied to microbeam radiotherapy for real-time dosimetry in the future, however the relatively large pixel pitch of the vM1212 detector limit the immediate application of the results. © 2019 American Association of Physicists in Medicine [https://doi.org/10.1002/mp.13971]

Key words: CMOS detectors, compact microbeam sources, dosimetry, microbeam radiation therapy

## 1. INTRODUCTION

### 1.A. Microbeam radiotherapy

Microbeam radiotherapy (MRT) is a novel type of spatially fractionated therapy which is defined by narrow beams of radiation (typically  $<100\ \mu\text{m}$ ) that can selectively irradiate portions of the target volume.<sup>1</sup> To cover the entire target volume, microbeams are delivered in a grid pattern in which multiple quasi-parallel rectangular beams, with typical centre-to-centre distances of 200–400  $\mu\text{m}$ . Crucially the entire target volume is not irradiated uniformly, with regions of very high dose microbeam "peaks" separated by very low dose valleys.

Preclinical studies have indicated that this dose pattern has a greater efficacy than that of a single uniform field.<sup>2</sup> Whilst the exact mechanism for preferential effect tumor is not fully understood and is likely a combination of effects. Possible mechanisms under investigation are preferential damage to vascular tissue in tumors,<sup>3–5</sup> and radiation-induced bystander and abscopal effects.<sup>6,7</sup>

### 1.B. Current verification methods

The very small size and high dose gradients of microbeams present a significant challenge to most standard detectors. That combined with high dose rates at synchrotrons adds to the complexity when working towards accurate dosimetry for microbeam radiotherapy.

Stereotactic radiotherapy treatments (with radiation fields sizes typically between 0.4 and 30 mm<sup>8</sup>) have strict requirements on the geometrical and dosimetric accuracy from dose calculations to delivery of  $\pm 5\%$  ( $k = 2$ ).<sup>9</sup> Microbeam irradiations are a step forward in terms of complexity and at present there is no dosimetry protocol or recommendations for dosimetry of irradiations with such beam configurations.<sup>10</sup>

Much of the ongoing research in the community is dedicated to optimizing irradiation configurations in order to obtain the best therapeutic outcomes, with peak to peak distance,<sup>11</sup> full-width at half maximum (FWHM)<sup>12</sup> and the peak-to-valley dose ratio (PVDR)<sup>13,14</sup> being of particular interest.

Due to the very small scales involved in microbeam radiotherapy, conventional radiotherapy equipment for beam profile acquisition (like small volume ionization chambers) are unable to resolve the individual microbeam peaks<sup>9</sup>. Scanning other types of small volume detectors through a microbeam peak has been previously performed with success by using a MOSFET dosimeter<sup>15,16</sup> or with a commercial PTW (Physikalisch-Technische Werkstätten GmbH, Freiburg, Germany) microdiamond detector,<sup>17</sup> with resolutions of 1  $\mu\text{m}$ .<sup>18</sup> This method has shown good agreement with radiochromic film,<sup>19</sup> however the measurements are acquired point by point and therefore the shape of the profiles are not shown instantaneously which limits its use for *in vivo* dosimetry or *in situ* verification. The same applies to the use of scintillating fibers, as shown by Archer *et al.*<sup>20</sup>

Various groups have developed silicon strip detectors capable of quantifying parameters of the microbeam field.<sup>21–23</sup> Whilst hybrid strip detectors (with separate sensor and readout) can offer greater resistance to radiation than monolithic pixelated detectors, strip detectors do not provide detailed information about the 2D profile of the radiation field and, therefore, will be more sensitive to angular misalignment.

A method of obtaining 2D relative dose distributions of microbeams was developed by Bartzsch *et al.*<sup>24</sup> using optical microscopy and EBT3 films,<sup>25</sup> which when using a microscope is technically capable of spatial resolutions better than 1  $\mu\text{m}$ . Due to film grain inhomogeneities this is reduced to 5  $\mu\text{m}$  in practice. This method builds on existing techniques for film dosimetry. Radiochromic films have a relatively large dose range (0.1 cGy–10 Gy for EBT3<sup>26</sup>), however the analysis process is slow, requiring a minimum of 24 hr for self-development post-irradiation.<sup>27</sup> At lower dose levels (less than 0.1 Gy<sup>28,29</sup>) noise becomes more significant. This typically necessitates two separate sets of irradiations for the same set of microbeams, in order to be able to increase the accuracy of the assessment of the dose distribution in the regions with lower dose range (valleys) without saturating the high dose region of the microbeam peaks.

This investigation was carried out to evaluate the suitability of the newly developed vM1212 detector for its use in the analysis of preclinical radiotherapy microbeams, using the custom built multi-slit collimator at the Helmholtz Zentrum München, Germany. The objective was to quantify microbeam parameters and to compare the results of the analysis of the same deliveries to EBT3 films, using the optical microscopy method.<sup>24</sup>

## 2. MATERIALS AND METHODS

### 2.A. vM1212 pixelated detector

The vM1212 pixelated detector is a large format CMOS (complementary metal–oxide–semiconductor) imaging sensor with 50  $\mu\text{m}$  pixel pitch originally designed for medical and scientific x-ray imaging by the CMOS Sensor Design Group at the Rutherford Appleton Laboratory<sup>30</sup> and is now licensed and manufactured into a full detector assembly by vivaMOS Ltd. The active area of the vM1212 detector is approximately  $6 \times 6\ \text{cm}^2$  ( $1204 \times 1248$  pixels) and is sufficiently large to capture the entire radiation field of the microbeam multislit collimator in a single instance.

The small pixel pitch and predicted resistance to damage caused by high levels of ionizing radiation justified a proof of principle investigation to determine the response of the detector to microbeam radiation.

### 2.B. Methodology

A SARRP (Small Animal Radiation Research Platform) x-ray irradiator at the Helmholtz Zentrum München was used

for this investigation. The irradiation parameters were set to 220 kVp (0.67 mm Cu HVL); 2.8 mA; and fine focus (effective beam source size of 0.4 mm<sup>31</sup>).

The tungsten microbeam multislit collimator consisted of three levels of fifty one 100- $\mu$ m slits (7 mm total thickness), with a slit-to-slit separation of 400  $\mu$ m. The first and third levels are in a fixed alignment, whilst the second central level is controlled by two motorized translation stages. When fully open, the transmission gap is 100  $\mu$ m, but the finest step resolution of the piezoelectric pistons enables variable slit widths between 0 and 100  $\mu$ m to be investigated to an accuracy of 0.5  $\mu$ m. The collimator was mounted at a distance of 21.2 cm from the source, with additional lead shielding to prevent radiation damage to the electronics as shown in Fig. 1(a).

In order to obtain robust and safe positioning, the vM1212 detector had to be mounted at a source to surface distance (SSD) of 29 cm, 6.8 cm from the surface of the microbeam collimator. To achieve conditions similar to the ones used for small animal irradiations a 1 cm slab of tissue-equivalent flexible bolus material with density of 1.03 g/cm<sup>32</sup> (trimmed to 7  $\times$  7 cm<sup>2</sup>) was placed on top of the EBT3 film. The vM1212 detector was used without scintillating material to maximize the potential spatial resolution. To enable a direct comparison between the EBT3 film and the vM1212 detector,

EBT3 film pieces were placed on top of the active area of the sensor, separated by a thin layer of a nonfibrous card which had been marked for repeatable alignment [Fig. 1(b)].

The EBT3 films irradiated simultaneously to the vM1212 detector were scanned using an Epson Expression 10000XL flatbed scanner (1400 dpi) and calibrated using FilmQA Pro with triple channel dosimetry.<sup>33,34</sup> Due to time constraints during the experiment, it was not possible to irradiate a second set of films for their analysis with optical microscopy. Those irradiations were performed in an independent experiment following the same irradiation conditions: source-surface distance, same bolus material and nonfibrous card, but using 450  $\mu$ m of silicon simulating the thickness of the detector. This second set of films was scanned using a ZEISS Axio Imager 2 optical microscope<sup>35</sup> on 5X magnification for a pixel resolution of 1.29  $\mu$ m.

Prior to the film irradiations, the output (Gy/min) was measured in reference conditions for SARRP absolute calibration. Measurements were performed with the SARRP open field at Source Surface Distance (SSD) of 33 cm and at 2 cm depth in WT1 water equivalent slab phantom, with 3 cm of backscatter material. Two independent measurements of the SARRP output were performed, one with the local dosimetry system (PTW 30010 ionization chamber), traceable to the PTW-Freiburg SSDL Calibration Laboratory and with a National Physical Laboratory (NPL) secondary standard system (PTW 30012 ionization chamber), traceable to the NPL primary standard for medium energy x-rays. Both ionization chambers used a local PTW Unidos TW1001 electrometer for dosimetry. Following output measurements and in order to obtain a calibration curve, a set of nine films were irradiated in the same reference conditions, with doses ranging from 0 to 14 Gy.

For consistency throughout the investigation, the same integration time, 28 ms, was always used on the vM1212 detector. This ensured that all the performed measurements were all in the linear response region for the pixels and prevented saturation of the detector. The results obtained using the vM1212 detector were corrected by averaging over a number of frames to reduce noise, subtracting a dark image to account for dark current in the pixels and calibrating the pixel response values against measurements with the NPL ionization chamber under the same conditions.

Direct comparison between the EBT3 films and the different acquisitions with vM1212 detector were carried out for 25, 50, 75, and 100  $\mu$ m slit widths. All the slits were irradiated with 240 s of exposure with the exception of the 25  $\mu$ m slit width which was irradiated with 480 s, to increase the dose and therefore to reduce the level of noise for the films measurements in such narrow beams.

Finally, to understand the difference in spatial response between the vM1212 detector and the two methods of EBT3 film scanning, the modulation transfer function (MTF) was measured for each. The modulation transfer function of the vM1212 detector was measured following BS EN 62220-1-3:2008<sup>36</sup> and using the COQ analysis software written by Donini *et al.*<sup>37</sup>. The MTF of the Epson Expression 10000XL

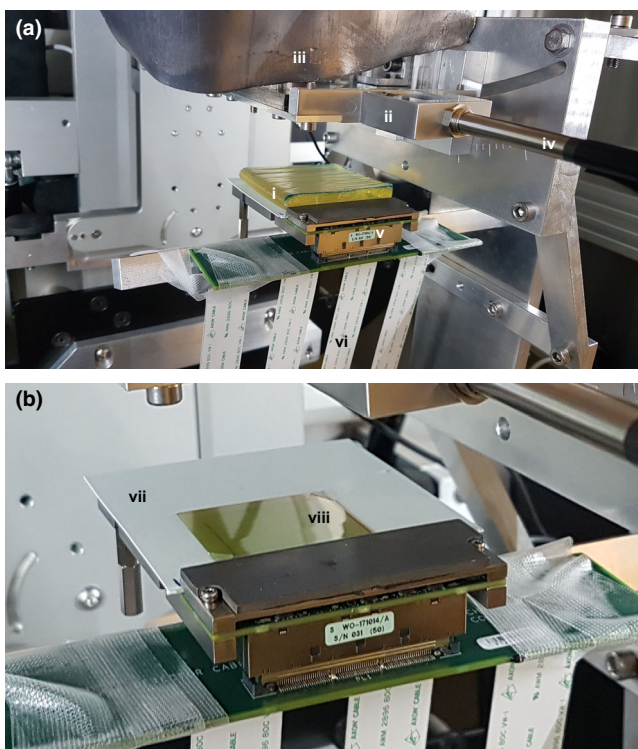


FIG. 1. Experimental set up: (a) vM1212 detector with 1 cm of water equivalent build-up, (b) vM1212 detector with aligned EBT3 film. (i) Lead shield to protect collimator electronics; (ii) Microbeam collimator; (iii) 1 cm of water equivalent bolus; (iv) Cable for microbeam collimator; (v) vM1212 detector; (vi) Ribbon cables for vM1212 detector; (vii) Nonfibrous card with alignment points; (viii) 3  $\times$  3 cm<sup>2</sup> square of EBT3 film.

scanner at 1400 dpi scanning resolution was measured using a sharp flat edge positioned over a piece of unexposed EBT3 film at an angle of  $4^\circ$ . Again using the COQ analysis software, the edge spread function was calculated allowing the modulation transfer function to be determined. The MTF of the Zeiss Axio Imager 2 was measured with the Xradia resolution sample (provided by Zeiss), which contained a pattern of lines with known width and separation. The largest line width on this pattern was  $32\ \mu\text{m}$  (period =  $64\ \mu\text{m}$ ), and as such the smallest resolution measurable with this resolution sample was 15.6 line pairs/mm (1/0.064 mm).

### 3. RESULTS

#### 3.A. Profile measurements

It was found that the vM1212 detector was able to capture the entire radiation field as defined by the collimator, as can be seen in Fig. 2(b). To create the microbeam collimator slits in tungsten, 0.3 mm diameter holes had to be drilled into the tungsten, allowing for wire erosion to mill out the  $100\ \mu\text{m}$  wide slits. This detail can be recognized on both detectors (film and vM1212 detector) and was used for alignment purposes. All profile comparisons presented are aligned relative

to the central 26th peak. By comparing vertical profiles from the EBT3 film methods with vertical profiles taken using the vM1212 detector we were able to observe that the alternating pattern of peaks and valleys of the microbeam collimator are well correlated between the different detectors. The larger SSD required to mount the vM1212 detector and the maximum scanning size of the EBT3 film possible with the microscope reduced the number of peaks that could be recorded using this method to approximately 40 (reduced from 51 physical slits on the collimator).

The  $100\ \mu\text{m}$  slit profiles' comparison can be seen in Fig. 3(a), where an agreement in terms of alignment of the peaks between the three detector methods can be observed. The vM1212 detector and the Epson Expression 10000XL under respond in terms of peak dose by approximately 30%; however there is relatively good agreement of the location of the microbeam peak center values [Fig. 3(b)]. As shown in Fig. 4, relative to the Zeiss Axio Imager 2, the valley doses are over reported by the Epson Expression 10000XL (with scanning resolution at 1400 dpi) by approximately 25% (15 mGy/min), whilst the vM1212 detector over reports by less than 5% (5 mGy/min). The average deviation between corresponding peak centers for the vM1212 detector and the Epson Expression 10000XL measurement was  $18.5\ \mu\text{m}$ ,

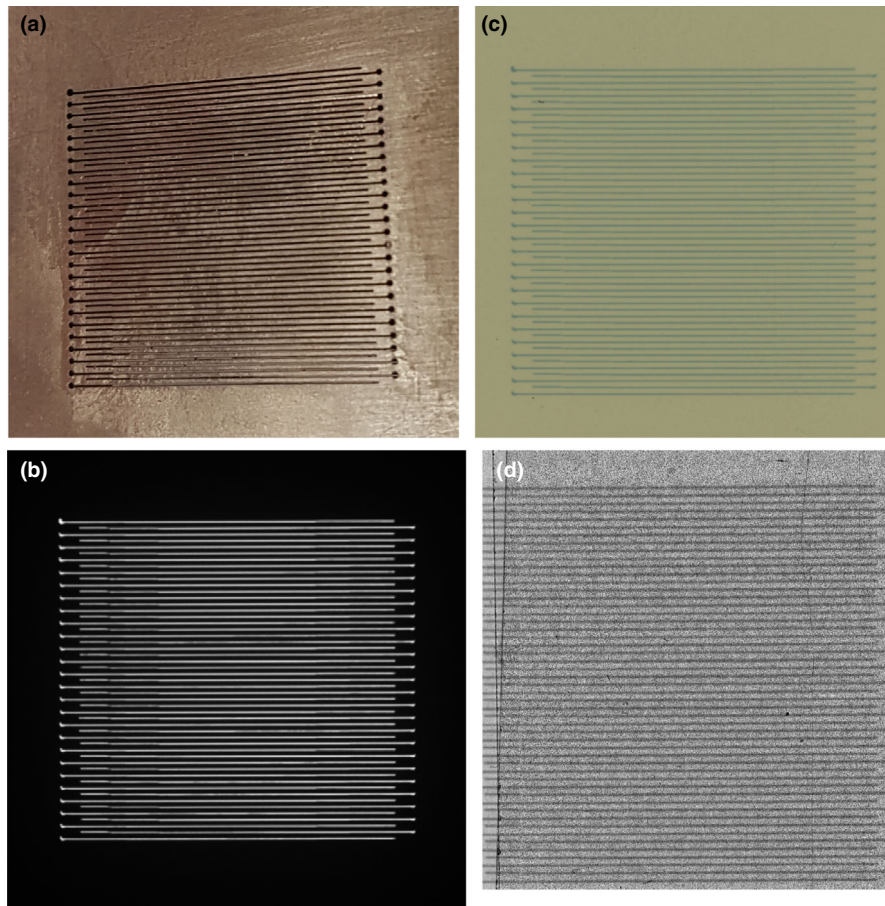


FIG. 2. (a) Photograph of microbeam collimator slits. (b) vM1212 detector image (cropped). (c) Scan of exposed EBT3 film using the Epson Expression 10000XL scanner ( $100\ \mu\text{m}$  slit width). (d) Scan of exposed EBT3 film using Zeiss Axio Imager 2.

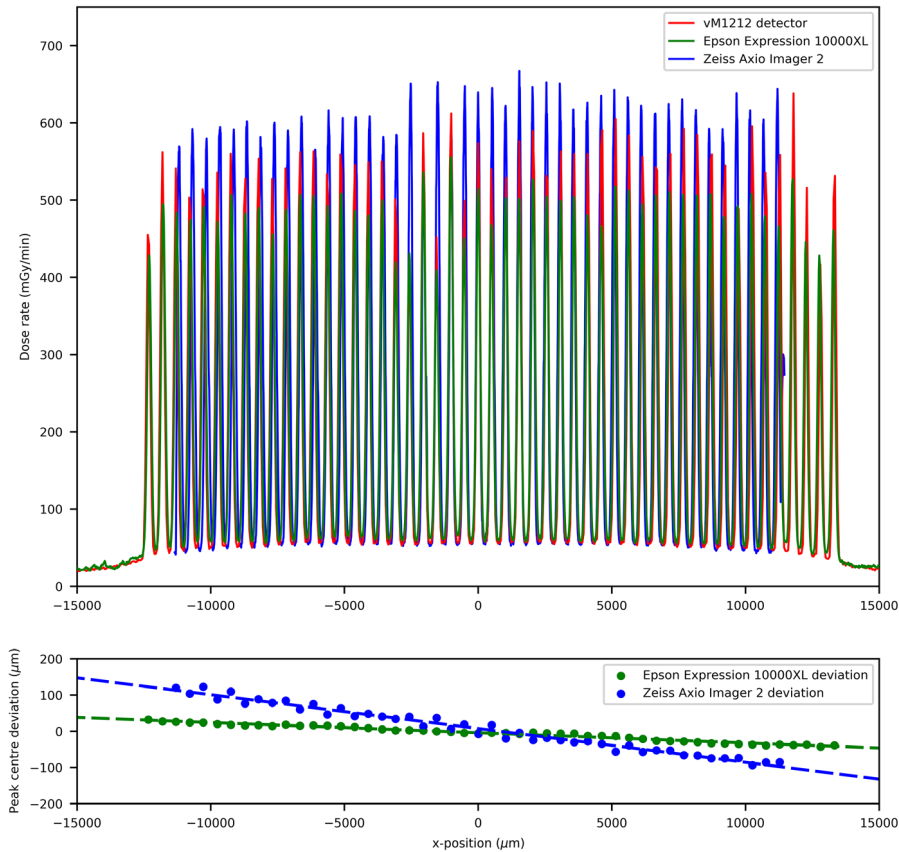


Fig. 3. (a) 100 μm slit width profile comparison, (b) Microbeam peak deviation between the vM1212 detector and the two EBT3 film methods.

whilst for the Zeiss Axio Imager 2 measurement was found to be 55.3 μm. As shown in Fig. 5 for the 26th central peak, the profile resolved on all three detector methods appears to be Gaussian.

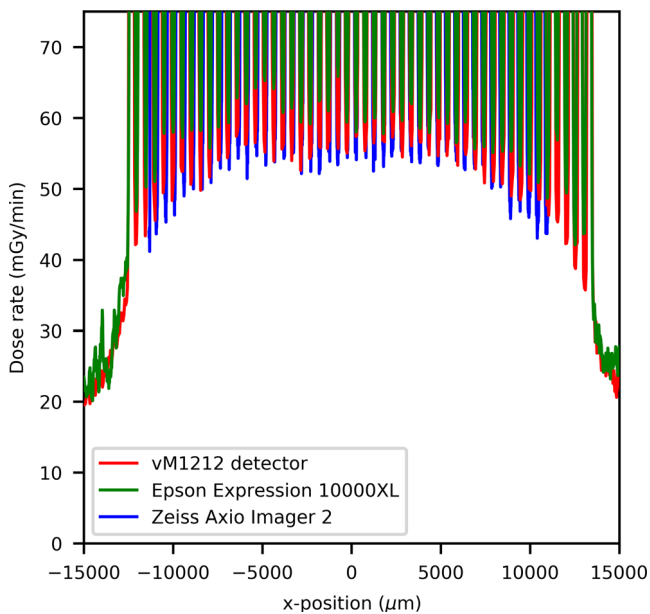


Fig. 4. 100 μm slit width valley profile comparison.

For the 25 μm slit width comparison (Fig. 6) the agreement between the EBT3 films and the vM1212 detector becomes worse as there is a strong disagreement for dose rate values between the scan performed by the Zeiss Axio Imager 2 and the other methods. This deviation is likely due to spatial averaging within the vM1212 detector and the Epson Expression 10000XL, however it is also possible that this deviation was introduced by misalignment during the Zeiss Axio Imager 2 exposure as it was performed at a later date. The lower measured dose rate is not consistent across the microbeam profiles as shown for the central peak (Fig. 7), where the dose rate measured by the vM1212 detector and Epson Expression 10000XL EBT3 film is approximately 20% of the dose rate measured by the Zeiss Axio Imager 2. For the Epson Expression 10000XL and the vM1212, the dose rate measured for the 27th peak (Fig. 7) is better but still measures only 40% relative to the Zeiss Axio Imager 2. Valley profiles for the 25 μm slit measured all of the detectors are again inconsistent, with approximate differences relative to the Zeiss Axio Imager 2 of 40% and 20% for the vM1212 detector and Epson Expression 10000XL, respectively. This peak specific under response not observed in the Zeiss Axio Imager 2 measurement is suspected to be due to a combination of manufacturing tolerances on the machined microbeam slits and repeatability issues of the microbeam setup.

Figures 7, 8 and 8 show a profile comparisons with a Gaussian fit applied between the three detectors for the 26th

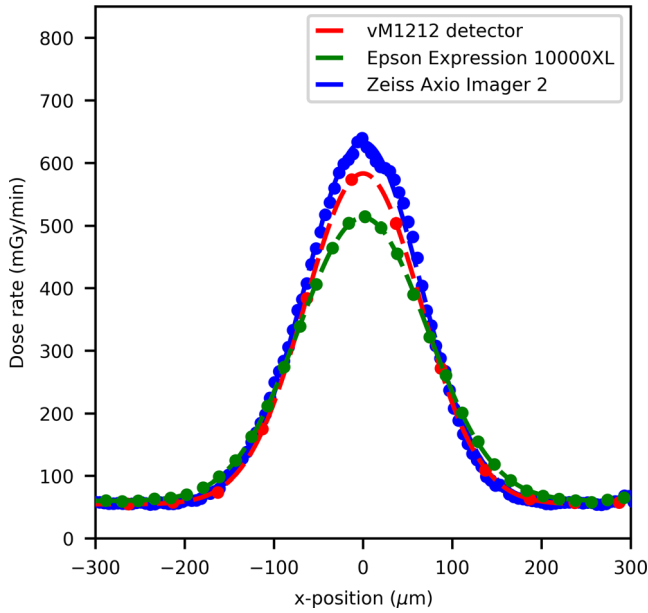


FIG. 5. 100  $\mu\text{m}$  slit width profile comparison of the 26th central peak.

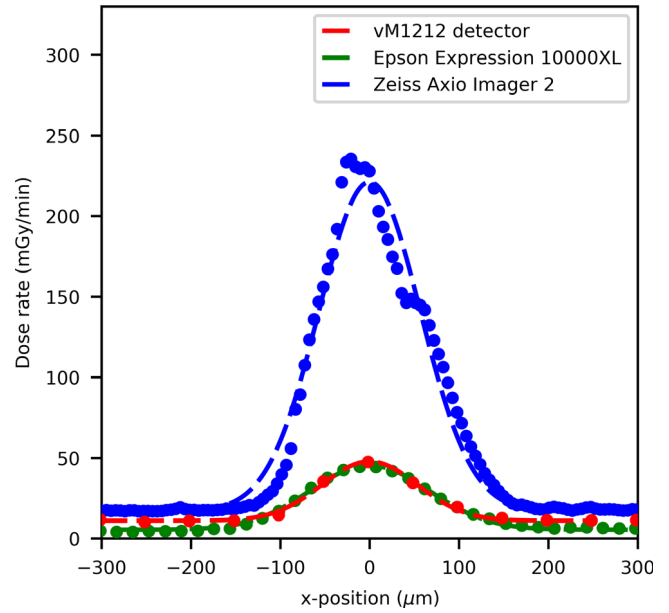


FIG. 7. 25  $\mu\text{m}$  slit width peak profile comparison of the 26th central peak.

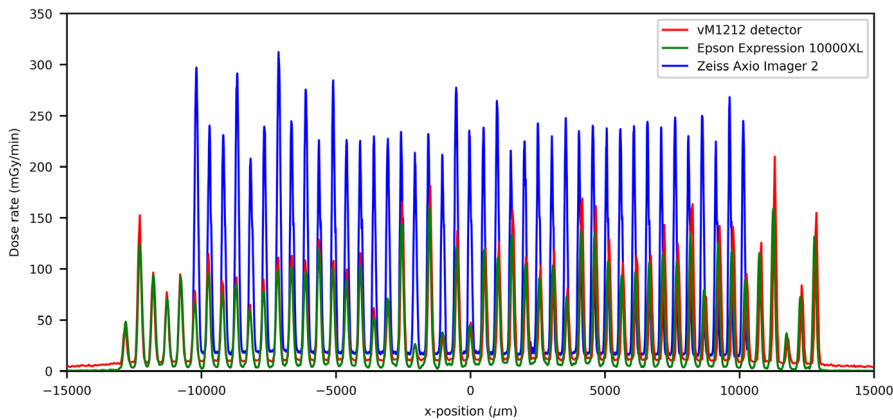


FIG. 6. 25  $\mu\text{m}$  slit width profile comparison.

(central) and 27th peak, respectively. A stitching artifact between the high dose valley irradiation and the low dose peak measurement can be seen in Fig. 8 in the Zeiss Axio Imager 2 dose profile at approximately 50  $\mu\text{m}$ . The centers of the 27th microbeam peak (relative to the 26th central peak) can be calculated to be 550, 514, and 488  $\mu\text{m}$  for the vM1212 detector, Epson Expression 10000XL and Zeiss Axio Imager 2 respectively.

The peak to peak separation could be measured across the three detection methods for all measured slit widths, as shown in Table I. It can be shown that the three methods agree within the uncertainties calculated. Using the inverse square law and the differences between the measured peak to peak separations, it can be estimated that the EBT3 films for the Epson Expression 10000XL and Zeiss Axio Imager 2 measurements were positioned  $0.5 \pm 0.2 \text{ mm}$  and  $2.4 \pm 0.2 \text{ mm}$  closer respectively to the x-ray source than

the vM1212 detector measurement. As the measurements for the Epson Expression 10000XL were taken concurrently with the vM1212 detector, this difference can be attributed to the thickness of the nonfibrous card which was independently measured with a digital caliper to be  $0.53 \pm 0.01 \mu\text{m}$ . The 2.4 mm deviation of the Zeiss Axio Imager 2 measurement is likely due to setup misalignment.

It was also found that the vM1212 detector was still able to detect and identify each of the 51 peaks when the microbeam collimator is fully closed (set to 0  $\mu\text{m}$  slit width) (Fig. 9). Profiles resulting from this leakage are used in Sections 3.B FWHM measurements and 3.C Peak and Valley Measurements.

Using the vM1212 detector it is possible to take real time horizontal profiles of the microbeam collimator. A comparison between the methods averaged across all recorded peaks for the 100  $\mu\text{m}$  slit width can be seen in Fig. 10, which again

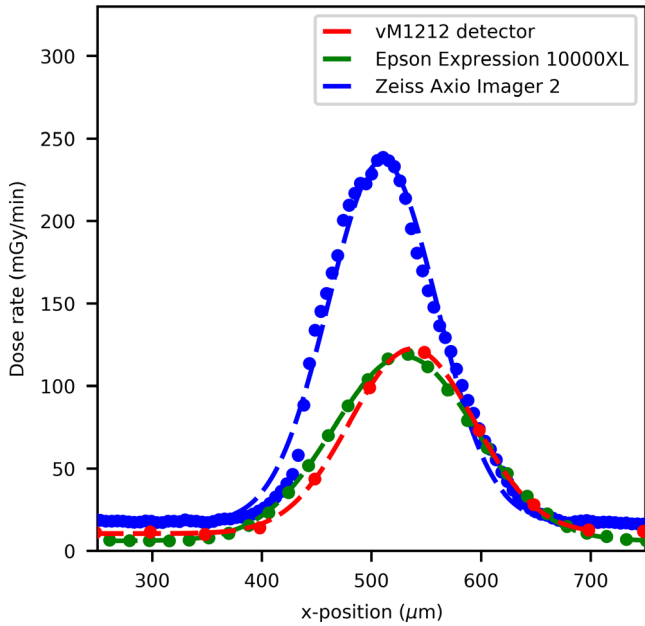


FIG. 8. 25  $\mu\text{m}$  slit width peak profile comparison of the 27th peak.

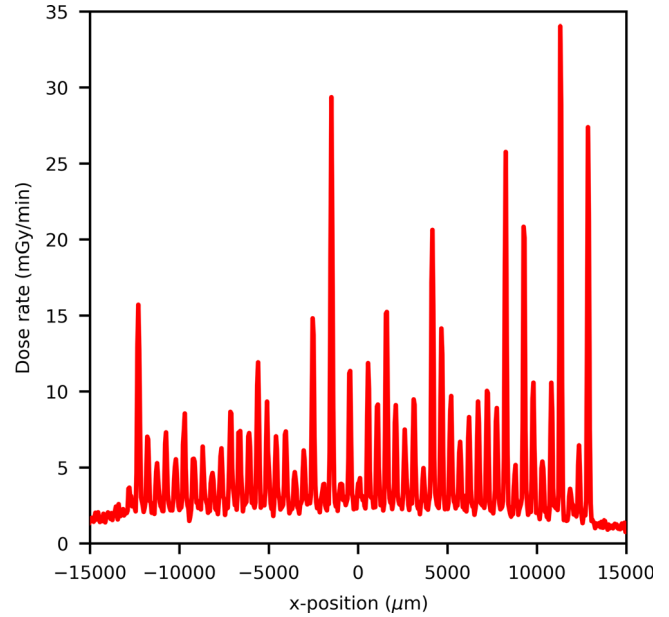


FIG. 9. Radiation leakage through the collimator at 0  $\mu\text{m}$  slit width as measured by the vM1212 detector.

TABLE I. Measured peak to peak separation as measured on the three detectors. Statistical uncertainty corresponds to one standard deviation.

Nominal slit width ( $\mu\text{m}$ )	Measured peak to peak separation ( $\mu\text{m}$ )		
	vM1212 detector	Epson Expression 10000XL	Zeiss Axio Imager 2
25	$513.4 \pm 13.9$	$512.0 \pm 11.3$	$508.3 \pm 9.9$
50	$512.9 \pm 10.1$	$511.7 \pm 9.7$	$508.9 \pm 9.1$
75	$512.6 \pm 9.2$	$511.9 \pm 10.1$	$508.3 \pm 8.6$
100	$512.4 \pm 9.5$	$511.8 \pm 9.6$	$508.5 \pm 9.8$

shows the approximately 30% under response of the vM1212 detector and Epson Expression 10000XL measurements relative to the Zeiss Axio Imager 2 measurement. The sharp vertical peaks at 13,000 and 41,000  $\mu\text{m}$  are due to the 0.3 mm diameter holes seen in Fig. 2. It can be seen in all three methods that the radiation intensity does not follow a smooth profile across the collimator as one might expect, although it is beyond the scope of this paper to discuss any therapeutic impact this may have.

### 3.B. FWHM measurements

An averaged FWHM comparison between the Zeiss Axio Imager 2 and the vM1212 detector for each of the slits can be seen in Fig. 11. The error bars shown represent one standard deviation of uncertainty for the microbeam peaks.

A linear relationship between the FWHMs is observed; however, there is a large deviation between FWHMs within a measurement. This can be attributed to a significant trend in the FWHM as a function of vertical position that was undetectable at the time of the experiment that can be seen in both

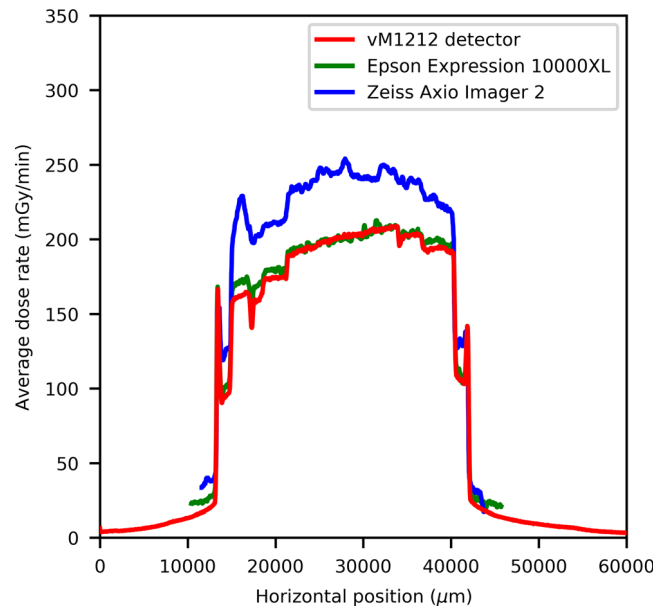


FIG. 10. Horizontal profile of the 100  $\mu\text{m}$  slit width.

the vM1212 detector results (Fig. 12) and the analyzed EBT3 films (not shown). This is most probably due to the angle of the beam after it is produced at the tungsten target, within the x-ray tube, known as heel effect. This effect would have become more dominant due to the larger SSD and was not observed on past measurements using the microbeam collimator.

Such a difference in beam FWHM across the beam profile would have had a significant impact on patient outcome, as described by Serduc *et al.*<sup>12</sup>. For *in vivo*

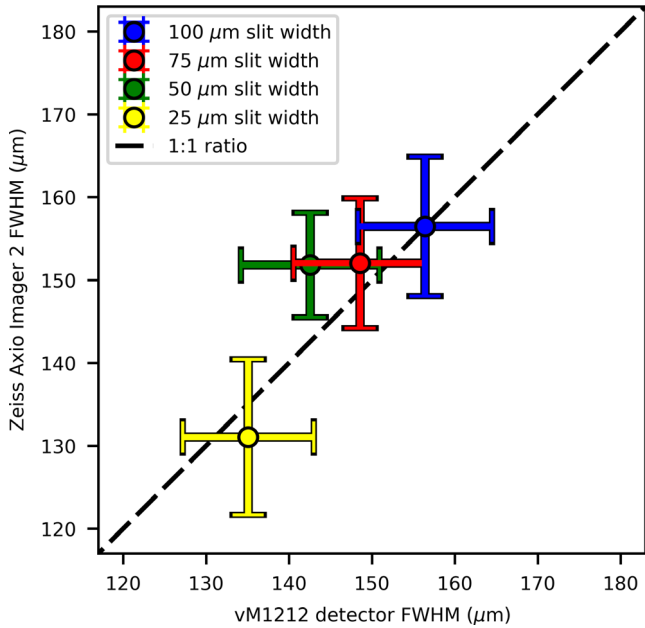


FIG. 11. FWHM comparison between Zeiss Axio Imager 2 and the vM1212 detector. A 1:1 ratio has been added to guide the eye.

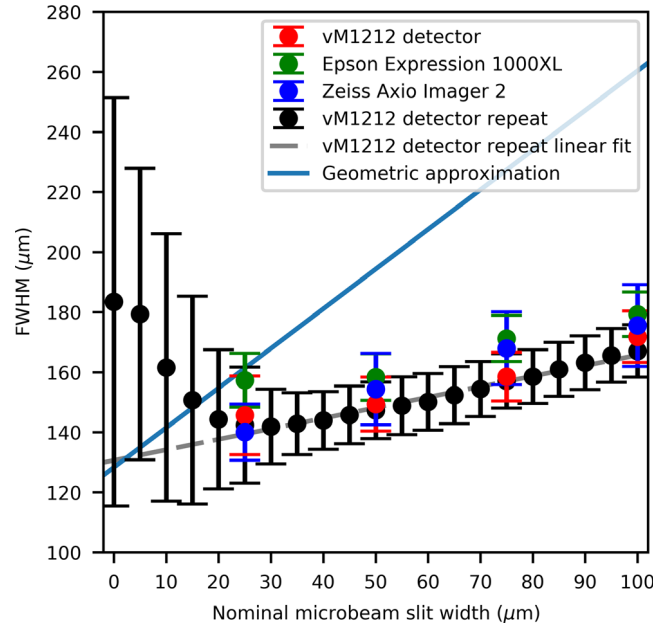


FIG. 13. Comparing the microbeam slit width to observed FWHM.

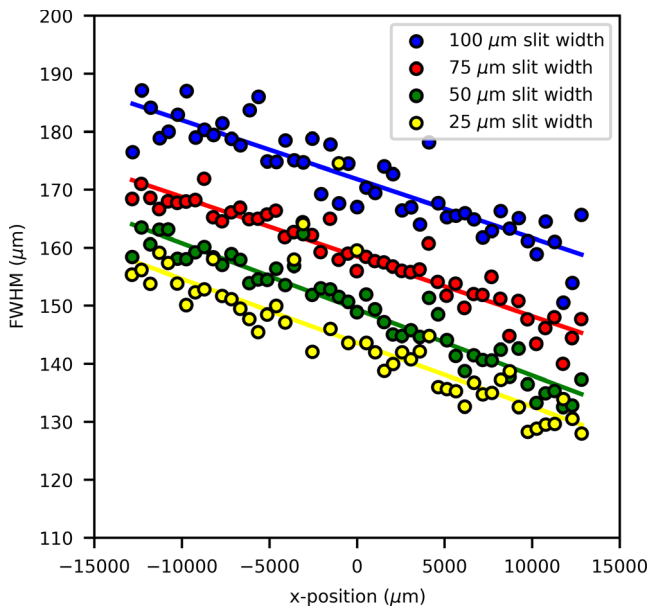


FIG. 12. FWHM trend as measured by the vM1212 detector.

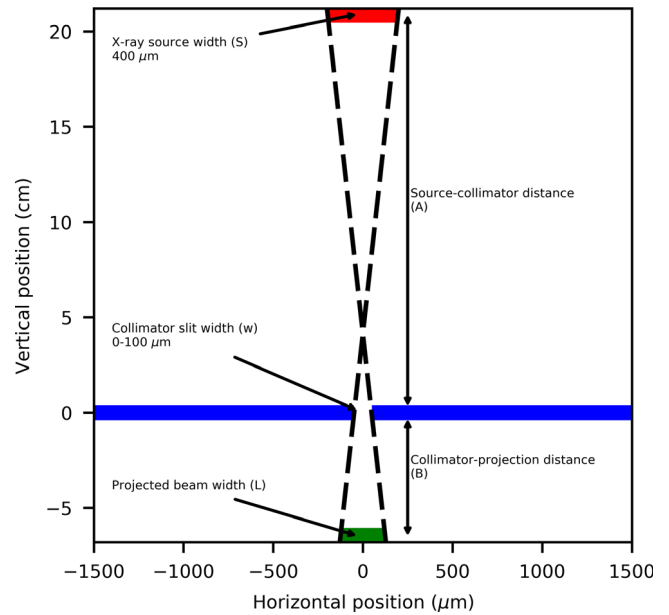


FIG. 14. Geometric setup of the microbeam collimator, resulting in the larger full width at half maximum (FWHM).

verification this would have been impossible to diagnose in real time with EBT3 films, due to the minimum 24 hr time required for film self-development. This highlights a potential application of the vM1212 detector for real time imaging of microbeams.

A comparison of microbeam nominal slit width to the measured FWHM can be seen in Fig. 13. As the vM1212 detector could take multiple readings with minimal dead time between them, a repeat set of measurements was performed to calculate the FWHM of the microbeams. Each time the slit

width was increased by 5 μm. Using this approach, it was possible to show that below 20 μm slit width, the value of the measured FWHM begins to increase (in relation to the expected nominal one). This effect is well documented for small fields in megavoltage x-ray beams<sup>38</sup> and is due to the finite size of the x-ray source being partially occluded by the collimator, causing an overlapping beam penumbra. If this geometrical penumbra is larger than the field size, then the FWHM of the resulting beam increases. Differences between

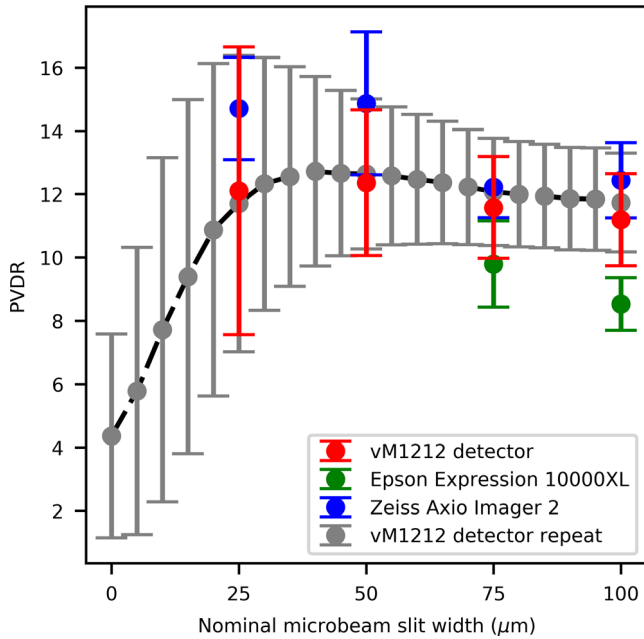


FIG. 15. Comparison of PVDR for different slit widths. The PVDR measurements for the 25 and 50 μm slit width Epson Expression 10000XL are omitted.

the two vM1212 detector measurements are attributed to subtle differences when repositioning the detector and uncertainties in the reproducibility of the collimator movements, however this effect appears to be minimal.

The larger FWHM for all measurements can be attributed to the finite size of the x-ray source. As shown in Fig. 14, for a finite source size (*S*), collimator slit width (*w*), source-collimator distance (*A*), and collimator-projection distance (*B*); the projected beam width can be approximated using Eq. (1).

$$L = \left[ \frac{B}{A} + 1 \right] w + \frac{BS}{A} \tag{1}$$

For this approximation and to simplify the scatter effects, we assumed that the collimator is infinitely thin and consists of only one layer instead of the three that comprise the actual and previously described design of the collimator. With the previous assumptions we are considering the calculated projected beam size as an approximation of the FWHM of the microbeam peak. Using the values described previously for *A*, *B* and *S*, the values for the theoretical resolvable slit size were plotted on Fig. 13 for comparison with measured results. With Eq. (1), the smallest microbeam peak FWHM created by the collimator that could be possible to resolve would be equal to  $128.3 \pm 13.0 \mu\text{m}$  (assuming 10% uncertainty of x-ray source size), whilst using the extrapolated results from the vM1212 detector the minimum is calculated to be  $126.0 \pm 0.7 \mu\text{m}$ . The differences in the slope between the derived (geometric approximation) and measured (vM1212 detector repeat linear fit) FWHMs are likely to be due to the numerous approximations and would need full Monte Carlo simulation with an accurate model of the geometry and scatter conditions.

### 3.C. Peak and Valley Measurements

By fitting Gaussians to each of the peaks in both the vM1212 detector and EBT3 film profiles, the Peak-to-Valley Dose Ratio (PVDR) can be estimated and compared to results reported in the literature (Fig. 15). The values calculated for the PVDR were comparable to what one might expect for this microbeam collimator when comparing to previous measurements in a similar collimator by Bartzsch *et al.* (where  $15.5 \pm 1.5$  was measured at 10 mm depth),<sup>39</sup> especially when considering the significantly larger SSD of this investigation.

The PVDRs obtained using the Epson Expression 10000XL for the 25 and 50 μm slit widths were found to be significantly larger than both predicted by literature and as reported by the vM1212 detector and the Zeiss Axio Imager 2 measurements. This can be attributed to a significant under response of the Epson Expression 10000XL to the microbeam valleys, as shown in Fig. 16. It is possible that the two film method used for optical microscopy could be applied to compensate for this and record a more accurate dose profile; however this was not within the scope of the investigation.

Using the vM1212 detector it was possible to rapidly calculate the PVDR for a large number of slit widths. As shown in Fig. 9, radiation leak is present through the collimator at slit width 0 μm from which a PVDR could be calculated. The decrease in PVDR below 20 μm is consistent with the increase in FWHM as observed in Fig. 13 which was attributed to an increased proportion of the radiation resulting from scatter with decreasing slit width.

### 3.D. Modulation transfer measurements

The results of modulation transfer measurements are shown in Fig. 17. It can be shown that while the spatial

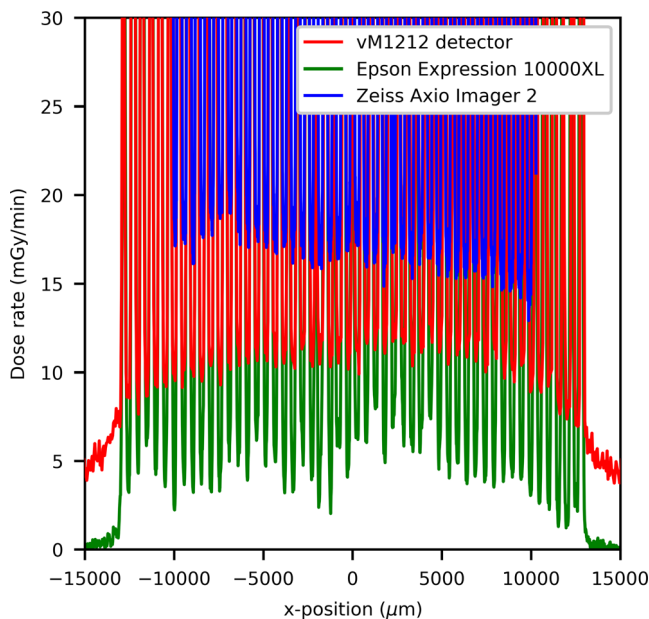


FIG. 16. 25 μm slit width valley profile comparison.

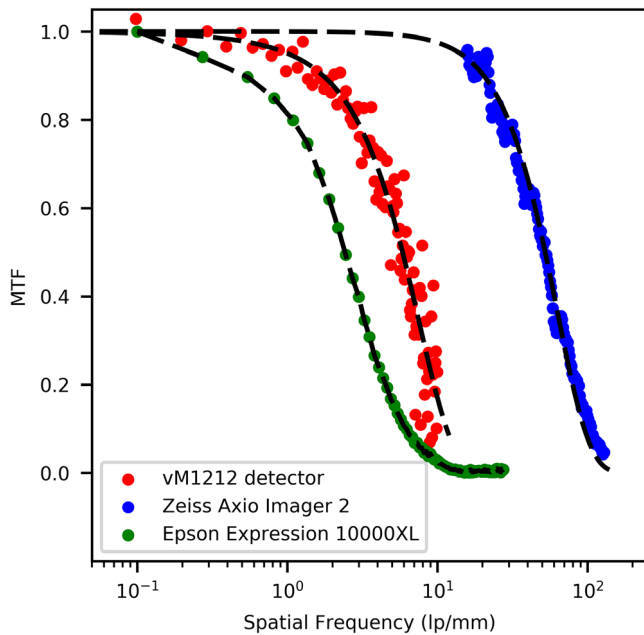


FIG. 17. Comparison of MTF for different measurement techniques.

resolution of the vM1212 detector is better than the Epson Expression 10000XL scanner, the Zeiss Axio Imager 2 microscope is superior to both.

#### 4. DISCUSSION

In comparison to dedicated facilities such as the European Synchrotron Radiation Facility (ESRF), the x-ray source used for this investigation was not optimized for microbeam radiotherapy with the dose rate measured after the collimator to be less than 0.05 Gy/s. This is substantially less than the dose rate used at synchrotrons for microbeam radiotherapy (often exceeding 100 Gy/s).<sup>40</sup> The microbeam FWHMs delivered in this investigation are significantly larger than the 25 μm wide beams capable at the ESRF and as such, further research of the vM1212 detector under such beam conditions is required. The mean energy of this investigation (approximately 95 keV

as calculated by the x-ray emission spectra calculation software SpekCalc<sup>41–43</sup>) was comparable to that of dedicated synchrotrons,<sup>44,45</sup> however undoubtedly the effect of the different spectra must be considered.

A comparison of the three microbeam detection methods evaluated in this work can be seen in Table II. Whilst the vM1212 detector has demonstrated the feasibility of a CMOS sensor for microbeams measurement in this investigation, significant deviations to established dosimetry methods were observed and further studies comparing to Monte Carlo simulations for relative dosimetry are still necessary. The Zeiss Axio Imager 2 remains a suitable readout method for commissioning and situations where maximum precision is required however, this method is relatively young and validated protocols and workflows need to be established to allow wider uptake for this method among microbeam community. The use of the Epson Expression 10000XL for microbeam measurements is not recommended due to the (relatively) poor spatial resolution.

The vM1212 detector does not possess the spatial resolution necessary for accurate microbeam dosimetry with its relatively large 50 μm pixels, compared to other quality assurance mechanisms discussed previously (such as the PTW microdiamond) with ~1 μm resolution. In addition, well established characteristics of other detection methods necessary for routine quality assurance such as dose rate and beam quality dependence have not been taken into account. The vM1212 detector operates using a "rolling shutter" frame acquisition method which does not present an issue for static or slow moving microbeam sources such as the type used in this investigation but may not be ideal for fast scanned microbeam spots. Additionally the maximum full field refresh rate of 34 fps may cause temporal blurring, however this effect could be minimized by binning pixels together or recording only a smaller region of interest. This refresh rate is still considerably lower than that of commercial radiotherapy electrometers (such as the Unidos webline with 1 kHz sampling rate<sup>46</sup>). Whilst the dose delivered to the films scanned by the Epson Expression 10000XL is relatively low (average peak dose of >1 Gy) for EBT3 film standards, it must be noted that the vM1212 detector is capable of

TABLE II. Comparison of the different microbeam detection methods evaluated in this work.

		Microbeam detection method		
		vM1212 detector	Zeiss Axio Imager 2 (+ EBT3 film)	Epson Expression 10000XL (+ EBT3 film)
Advantages	Real time measurement and analysis Short exposure is sufficient to obtain accurate profile information	Shortest exposure is sufficient to obtain accurate profile information	Highest spatial resolution No dose rate dependence <sup>49</sup>	Lower cost Established clinical workflow No dose rate dependence <sup>49</sup>
Disadvantages	Limited life expectancy due to cumulative radiation damage Spatial resolution limited by 50 μm pixel pitch Higher price	Limited life expectancy due to cumulative radiation damage Spatial resolution limited by 50 μm pixel pitch Higher price	24 hours self-development Complex and time consuming analysis process  Necessity to establish procedures and workflow for wider uptake of this method	24 hours self-development Poorest spatial resolution and hence limited suitability for microbeam applications  Software licensing costs

obtaining similar or better quality images in less than 2 mGy per frame, highlighting its potential for real-time microbeam verification.

Looking forward, CMOS sensors resistant to ionizing radiation have been developed for other harsh radiation environments (such as space), achieving pixel pitches of less than  $10\ \mu\text{m}$ <sup>47,48</sup> in size. The use of such sensors in the future could obtain real-time microbeam profile information surpassing even that of the Zeiss Axio Imager 2, however making these sensors large enough to cover the same field of view as the vM1212 detector could become prohibitively expensive due to the number of pixels required and sensor yield losses.

## 5. CONCLUSION

Microbeam radiotherapy is a rapidly developing method of cancer treatment with significant therapeutic improvements over conventional radiotherapy.<sup>50,51</sup> The dosimetric challenges associated with the high dose gradients in microbeam radiotherapy prevent the use of well-established dosimetry equipment used in radiotherapy and (to date), all novel techniques for monitoring microbeams have only obtained one dimensional profile information; limiting their clinical viability.

In this study, we have demonstrated the capacity of the two dimensional vM1212 pixelated detector to discriminate individual microbeams peaks with FWHM between 130 and 190  $\mu\text{m}$ . The high dynamic range of the vM1212 detector allows the signal detection of both the high dose peaks and the low dose valleys (of microbeams with less than 20 PVDR) to be measured in real-time, which provides a significant advantage over EBT3 films requiring at least 24 hr post-irradiation processing. Observed peak-to-valley dose ratios and peak to peak separations measured by the vM1212 detector were comparable those obtained using the optical microscopy method employing Zeiss Axio Imager 2 microscope. The use of pixelated sensors for in-vivo beam monitoring in conventional radiotherapy beams is already being researched by multiple groups<sup>52,53</sup> and as the technology behind the sensors matures, it is anticipated that future CMOS detectors will have all of the required characteristics for microbeam dosimetry.

## ACKNOWLEDGMENTS

The authors wish to thank Theresa Urban of the Technical University of Munich for measuring the modulation transfer function of the Zeiss Axio Imager 2 and generously providing the data for this publication. This work was supported by the Science and Technology Facilities Council (grant ST/P002552/1) and by the UK government's Department for Business, Energy and Industrial Strategy.

## CONFLICT OF INTEREST

Due to the prototype nature of the device, the manufacturer of the vM1212 detector, vivaMOS Ltd, has been

involved in data collection providing advice and technical support throughout the investigation.

<sup>a)</sup> Author to whom correspondence should be addressed. Electronic mail: sam.flynn@npl.co.uk.

## REFERENCE

1. Slatkin DN, Spanne P, Dilmanian FA, Sandborg M. Microbeam radiation therapy. *Med Phys*. 1992;19:1395–400.
2. Bouchet A, Serduc R, Laissue JA, Djonov V. Effects of microbeam radiation therapy on normal and tumoral blood vessels. *Phys Med*. 2015;31:634–41.
3. Serduc R, Christen T, Laissue J, et al. Brain tumor vessel response to synchrotron microbeam radiation therapy: a short-term *in vivo* study. *Phys Med Biol*. 2008;53:3609–22.
4. Crosbie JC, Anderson RL, Rothkamm K, et al. Tumor cell response to synchrotron microbeam radiation therapy differs markedly from cells in normal tissues. *Int J Radiat Oncol*. 2010;77:886–94.
5. Bouchet A, Serduc R, Laissue JA, Djonov V. Effects of microbeam radiation therapy on normal and tumoral blood vessels. *Phys Med*. 2015;31:634–41.
6. Prise KM, Schettino G, Folkard M, Held KD. New insights on cell death from radiation exposure. *Lancet Oncol*. 2005;6:520–8.
7. Fernandez-Palomo C, Bräuer-Krisch E, Laissue J, et al. Use of synchrotron medical microbeam irradiation to investigate radiation-induced bystander and abscopal effects *in vivo*. *Phys Med*. 2015;31:584–95.
8. Bagheri H, Soleimani A, Gharehaghaji N, et al. An overview on small-field dosimetry in photon beam radiotherapy: developments and challenges. *J Cancer Res Ther*. 2017;13:175.
9. Das JJ, Downes MB, Kassae A, Tochner Z. Choice of radiation detector in dosimetry of stereotactic radiosurgery-radiotherapy. *J Radiosurg*. 2000;3:177–86.
10. Bräuer-Krisch E, Serduc R, Siegbahn EA, et al. Effects of pulsed, spatially fractionated, microscopic synchrotron X-ray beams on normal and tumoral brain tissue. *Mutat Res – Rev Mutat Res*. 2010;704:160–6.
11. Regnard P, Le Duc G, Bräuer-Krisch E, et al. Irradiation of intracerebral 9L gliosarcoma by a single array of microplanar x-ray beams from a synchrotron: Balance between curing and sparing. *Phys Med Biol*. 2008;53:861–78.
12. Serduc R, Bouchet A, Bräuer-Krisch E, et al. Synchrotron microbeam radiation therapy for rat brain tumor palliation—influence of the microbeam width at constant valley dose. *Phys Med Biol*. 2009;54:6711–24.
13. Bräuer-Krisch E, Adam J-F, Alagoz E, et al. Medical physics aspects of the synchrotron radiation therapies: microbeam radiation therapy (MRT) and synchrotron stereotactic radiotherapy (SSRT). *Phys Med*. 2015;31:568–83.
14. Annabell N, Yagi N, Umetani K, Wong C, Geso M. Evaluating the peak-to-valley dose ratio of synchrotron microbeams using PRESAGE fluorescence. *J Synchrotron Radiat*; 2012;19(3):332–339.
15. Rosenfeld AB, Kaplan GI, Kron T, et al. MOSFET dosimetry of an X-ray microbeam. *IEEE Trans Nucl Sci*. 1999;46:1774–80.
16. Kaplan GI, Rosenfeld AB, Allen BJ, Booth JT, Carolan MG, Holmes-Siedle A. Improved spatial resolution by MOSFET dosimetry of an x-ray microbeam. *Med Phys*. 2000;27:239–44.
17. Livingstone J, Stevenson AW, Butler DJ, Häusermann D, Adam JF. Characterization of a synthetic single crystal diamond detector for dosimetry in spatially fractionated synchrotron x-ray fields. *Med Phys*. 2016;43:4283–93.
18. PTW Freiburg. 2013. IONIZING RADIATION DETECTORS: Including Codes of Practice 100.
19. Rosenfeld AB. Electronic dosimetry in radiation therapy. *Radiat Meas*. 2006;41:S134–53.
20. Archer J, Li E, Davis J, Cameron M, Rosenfeld A, Lerch M. High spatial resolution scintillator dosimetry of synchrotron microbeams. *Sci Rep*. 2019;9:6873.
21. Lerch MLF, Dipuglia A, Cameron M, et al. New 3D silicon detectors for dosimetry in microbeam radiation therapy. *J Phys Conf Ser*. 2017;777:012009.

22. Davis JA, Paino JR, Dipuglia A, et al. Characterisation and evaluation of a PNP strip detector for synchrotron microbeam radiation therapy *Biomed. Phys Eng Express*. 2018;4:044002.
23. Povolì M, Alagoz E, Bravin A, et al. Thin silicon strip detectors for beam monitoring in micro-beam radiation therapy. *J Instrum*. 2015;10:P11007.
24. Bartzsch S, Lott J, Welsch K, Bräuer-Krisch E, Oelfke U. Micrometer-resolved film dosimetry using a microscope in microbeam radiation therapy. *Med Phys*. 2015;42:4069–79.
25. Anon. GAFCHROMIC™ DOSIMETRY MEDIA, TYPE, EBT-3. [http://www.gafchromic.com/documents/EBT3\\_Specifications.pdf](http://www.gafchromic.com/documents/EBT3_Specifications.pdf)
26. Anon. Garchromic EBT Films - GAFchromic™. <http://www.gafchromic.com/gafchromic-film/radiotherapy-films/EBT/index.asp>
27. McLaughlin WL, Yun-Dong C, Soares CG, Miller A, Van Dyk G, Lewis DF. Sensitometry of the response of a new radiochromic film dosimeter to gamma radiation and electron beams. *Nucl Instruments Methods Phys Res Sect A: Accel Spectrometers Detect Assoc Equip*. 1991;302:165–76.
28. Li Y, Chen L, Zhu J, Liu X. The combination of the error correction methods of GAFCHROMIC EBT3 film. *PLoS ONE*. 2017;12:1–17.
29. Tagiling N, Ab Rashid R, Azhan SNA, Dollah N, Geso M, Rahman WN. Effect of scanning parameters on dose-response of radiochromic films irradiated with photon and electron beams. *Heliyon*. 2018;4:e00864.
30. Sedgwick I, Das D, Guerrini N, Marsh B, Turchetta R. LASSENA: a 6.7 megapixel, 3-sides buttable wafer-scale CMOS sensor using a novel grid-addressing architecture. *Proc Int Image Sens Work*. 2013;3–6.
31. Tryggestad E, Armour M, Iordachita I, Verhaegen F, Wong JW. A comprehensive system for dosimetric commissioning and Monte Carlo validation for the small animal radiation research platform. *Phys Med Biol*. 2009;54:5341–57.
32. Anon. ExaFlex™ - MacroMedics. <https://www.macromedics.com/files/upload/14/macromedics-productcatalogue.pdf>
33. Micke A, Lewis DF, Yu X. Multichannel film dosimetry with nonuniformity correction. *Med Phys*. 2011;38:2523–34.
34. Mayer RR, Ma F, Chen Y, et al. Enhanced dosimetry procedures and assessment for EBT2 radiochromic film. *Med Phys*. 2012;39:2147–55.
35. Anon. ZEISS Axio imager 2 for life science research.
36. Anon. 2015 BSI Standards Publication Medical electrical equipment — Characteristics of digital x-ray imaging devices Part 1–1: Determination of the detective quantum efficiency — Detectors used in.
37. Donini B, Rivetti S, Lanconelli N, Bertolini M. Free software for performing physical analysis of systems for digital radiography and mammography. *Med Phys*. 2014;41:051903.
38. Das IJ, Ding GX, Ahnesjö A. Small fields: nonequilibrium radiation dosimetry. *Med Phys*. 2007;35:206–15.
39. Bartzsch S, Cummings C, Eismann S, Oelfke U. A preclinical microbeam facility with a conventional x-ray tube. *Med Phys*. 2016;43:6301–8.
40. Eling L, Bouchet A, Nemoz C, et al. Ultra high dose rate synchrotron microbeam radiation therapy. preclinical evidence in view of a clinical transfer. *Radiother Oncol*. 2019;139:56–61.
41. Poludniowski GG, Evans PM. Calculation of x-ray spectra emerging from an x-ray tube. Part I. Electron penetration characteristics in x-ray targets. *Med Phys*. 2007;34:2164–74.
42. Poludniowski GG. Calculation of x-ray spectra emerging from an x-ray tube. Part II. X-ray production and filtration in x-ray targets. *Med Phys*. 2007;34:2175–86.
43. Poludniowski G, Landry G, DeBlois F, Evans PM, Verhaegen F. *SpekCalc* : a program to calculate photon spectra from tungsten anode x-ray tubes. *Phys Med Biol*. 2009;54:N433–8.
44. Martínez-Rovira I, Sempau J, Prezado Y. Development and commissioning of a Monte Carlo photon beam model for the forthcoming clinical trials in microbeam radiation therapy. *Med Phys*. 2012;39:119–31.
45. Livingstone J, Stevenson AW, Häusermann D, Adam J-F. Experimental optimisation of the X-ray energy in microbeam radiation therapy. *Phys Med*. 2018;45:156–61.
46. PTW. 2010 User Manual: UNIDOS webline Type 10021, Type 10022 and Type 10023.
47. Sellier C, Gambart D, Perrot N, Garcia-Sanchez E, Virmontois C, Mouallem W, Bardoux A. Development and qualification of a miniaturised CMOS camera for space applications (3DCM734/3DCM739) International Conference on Space Optics — ICSO 2018 vol 11180, ed Karafolas N, Sodnik Z, Cugny B. (SPIE). 2019;106.
48. Kim Woo-Tae, Park Cheonwi, Lee Hyunkeun, Lee Ilseop, Lee Byung-Geun. A high full well capacity CMOS image sensor for space applications. *Sensors*. 2019;19:1505.
49. Borca VC, Pasquino M, Russo G, et al. Dosimetric characterization and use of GAFCHROMIC EBT3 film for IMRT dose verification. *J Appl Clin Med Phys*. 2013;14:158.
50. Schültke E, Balosso J, Breslin T, et al. Microbeam radiation therapy — grid therapy and beyond: a clinical perspective. *Br J Radiol*. 2017;90:20170073
51. Prezado Y, Jouvion G, Patriarca A, et al. Proton minibeam radiation therapy widens the therapeutic index for high-grade gliomas. *Sci Rep*. 2018;8:16479.
52. Page RF, Abbott NL, Davies J, et al. Using a monolithic active pixel sensor for monitoring multileaf collimator positions in intensity modulated radiotherapy. *IEEE Trans Nucl Sci*. 2014;61:74–8.
53. Bartoli A, Scaringella M, Baldi A, et al. PO-0873: 2D pixelated diamond detector for patient QA in advanced radiotherapy treatments. *Radiother Oncol*. 2018;127:S459–60.



Contents lists available at ScienceDirect

## Nuclear Inst. and Methods in Physics Research, A

journal homepage: [www.elsevier.com/locate/nima](http://www.elsevier.com/locate/nima)

# First demonstration of real-time in-situ dosimetry of X-ray microbeams using a large format CMOS sensor



Samuel Flynn<sup>a,b,\*</sup>, Tony Price<sup>a,b</sup>, Philip P. Allport<sup>a</sup>, Ileana Silvestre Patallo<sup>b,c</sup>, Russell Thomas<sup>b</sup>, Anna Subiel<sup>b</sup>, Stefan Bartzsch<sup>d,e</sup>, Franziska Treibel<sup>e</sup>, Mabroor Ahmed<sup>e</sup>, Jon Jacobs-Headspith<sup>f</sup>, Tim Edwards<sup>f</sup>, Isaac Jones<sup>f</sup>, Dan Cathie<sup>f</sup>, Nicola Guerrini<sup>g</sup>, Iain Sedgwick<sup>g</sup>

<sup>a</sup> School of Physics and Astronomy, University of Birmingham, Birmingham, United Kingdom

<sup>b</sup> Medical Physics, National Physical Laboratory, Teddington, United Kingdom

<sup>c</sup> UCL Cancer Institute, University College London, London, United Kingdom

<sup>d</sup> Helmholtz Centre Munich, Institute for Radiation Medicine, Munich, Germany

<sup>e</sup> Technical University of Munich, School of Medicine, Klinikumrechtsder Isar, Department of Radiation Oncology, Munich, Germany

<sup>f</sup> vivaMOS Ltd, Southampton, United Kingdom

<sup>g</sup> Rutherford Appleton Laboratory, Oxford, United Kingdom

## ARTICLE INFO

MSC:  
00-01  
99-00

Keywords:  
CMOS  
Microbeam  
Radiotherapy  
Dosimetry

## ABSTRACT

Microbeam radiotherapy is a novel type of radiotherapy in which narrow beams of radiation (typically less than 500  $\mu\text{m}$ ) are spatially fractionated, delivering a non-uniform distribution to the target tumour volume. Due to the very high dose gradients and very small beams involved, new dosimetric techniques are required for translation into clinical practise. Current real-time beam monitoring is typically performed using 1 dimensional silicon strip detectors or wire chambers, with 2D beam information measured offline using radiochromic film (requiring a minimum of 24 h to self-develop).

Using an Xstrahl SARRP X-ray irradiation device with a bespoke microbeam collimator at the Technical University of Munich, Germany, the newly developed vM1212 detector was exposed to a variety of microbeams (220 kV, nominal slit widths 0–100  $\mu\text{m}$ ) for evaluation of in vivo real time verification.

The performance of the detector was assessed by changing the collimator slit width (and thus microbeam FWHM) mid-irradiation. Microbeam FWHMs of 130–190  $\mu\text{m}$  could be measured in this manner in addition to temporally monitoring other basic parameters such as the radiation intensity. More advanced parameters could be calculated as the tungsten slits within the microbeam collimator opened and closed such as the rate of change of FWHM; the peak–valley-dose-ratio (PVDR); and the sub-pixel movement of each microbeam peak.

This work demonstrates the potential of radiation hard CMOS sensors in radiotherapy for in vivo real-time monitoring of X-ray microbeams FWHM, intensity and position.

## 1. Introduction

Microbeam radiotherapy (MRT) is a novel type of external radiation treatment, in which the radiation field is spatially fractionated into narrow beams (typically less than 100  $\mu\text{m}$ ), delivering a non-uniform distribution to the target tumour volume [1]. Preclinical studies have indicated that despite the fact that not all the tumour cells receive a lethal dose, MRT produces greater efficacy for tumour control than traditional uniform radiation fields (with the same level of normal tissue sparing) [2], an effect attributed to preferential tumour vascular damage [3] and radiation-induced bystander and abscopal effects [4]. Together, these outcomes suggest that MRT could be used to treat radio-resistant tumours that are currently incurable [5]. Due to the

very high dose gradients and small beams involved, new dosimetric techniques are required for translation into clinical practise.

Currently, dosimetric measurements of MRT are typically performed using very small volume ionisation chambers, solid state detectors, or radiochromic film; however these are unsuitable for real-time in-situ dosimetry (with radiochromic films requiring a minimum of 24 h to self-develop). One dimensional silicon strip detectors have been used with success [6], however they cannot provide 2D profiles of the radiation field and will be sensitive to angular misalignment.

An annotated diagram of a few of the microbeam parameters is shown in Fig. 1, where the full width at half maximum (FWHM) and peak to peak separation are labelled. The commonly quoted parameter peak-to-valley-dose-ratio (PVDR) is calculated as a ratio of the peak

\* Corresponding author at: School of Physics and Astronomy, University of Birmingham, Birmingham, United Kingdom.  
E-mail address: [sam.flynn@npl.co.uk](mailto:sam.flynn@npl.co.uk) (S. Flynn).

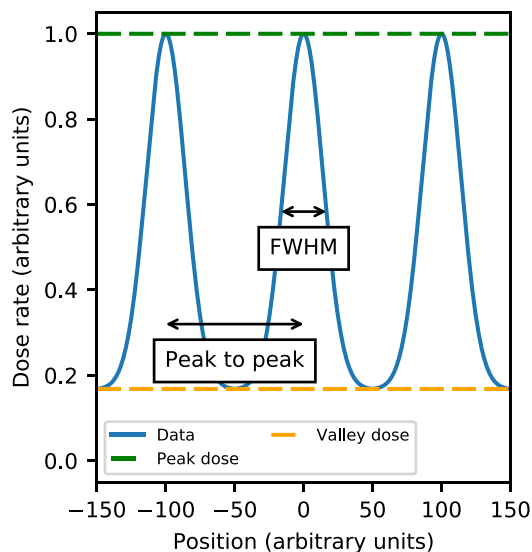


Fig. 1. Annotated diagram of microbeam profile features.

dose and the valley dose. It has been shown in preclinical studies that varying each of these parameters impacts the treatment outcome and a large amount of research is still ongoing to optimise these parameters [7–10].

The suitability of large format CMOS (complementary metal–oxide–semiconductor) sensors for microbeam dosimetry was first evaluated by Flynn et al. [11], where small field’s 2D dose distributions acquired with the vM1212 detector (based on the LASSENA pixel design [12]) were compared to EBT3 radiochromic film (scanned with two detection methods). Whilst agreement was found between the two methods, the investigation was limited in scope to microbeams of fixed width averaged over several minutes of exposure, due to the dose levels required with the radiochromic film.

In this investigation we evaluated and analysed individual frames acquired by the vM1212 detector for X-ray microbeams with static and changing FWHM to determine the potential suitability for in vivo or in-situ monitoring of microbeam deliveries with large format CMOS detectors.

## 2. Method

A vM1212 detector, a large format CMOS sensor with 50  $\mu\text{m}$  pixel pitch and approximately 6 x 6  $\text{cm}^2$  active area, was placed in a Small Animal Radiation Research Platform (SARRP) installed at the Technical University of Munich. A custom designed Tungsten X-ray microbeam collimator with fifty-one 100  $\mu\text{m}$  wide slits [13], based on the design by Bartzsch et al. [14], was installed within the X-ray cabinet and was used to shape the microbeams. The collimator consisted of three layers of tungsten, with the middle layer connected to two piezoelectric actuators, which were controlled via software. By aligning the middle layer, nominal slit widths of 0–100  $\mu\text{m}$  were achievable.

The detector was placed at a distance of 29 cm from the X-ray source, and 6.8 cm below the microbeam collimator. 1 cm of water equivalent bolus was placed on top of the vM1212 detector and used as build-up material to imitate build-up tissue conditions in animal preclinical irradiations.

The response of the vM1212 detector was calibrated within the SARRP (with an open field, chamber at SSD (Source Surface Distance) 33 cm, 2 cm depth in water and 5 cm backscatter material) against a PTW 30012 ionisation chamber, which was traceable to the National Physical Laboratory primary standard for medium energy X-rays. A consistent integration time of 28 ms was selected on the vM1212

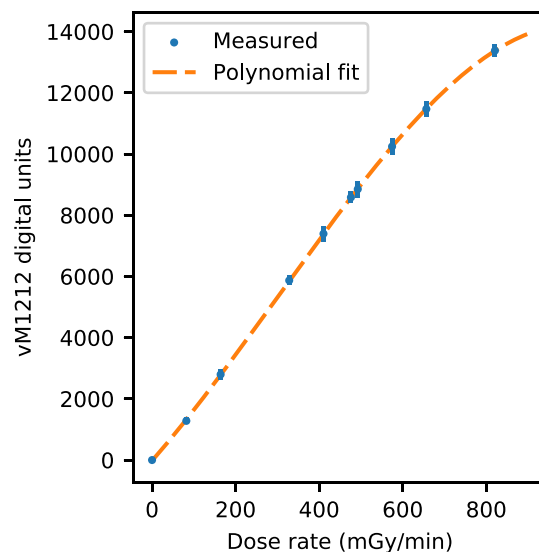


Fig. 2. Calibration curve of the vM1212 detector. Uncertainties shown are one standard deviation.

detector. For the investigation, the SARRP fine focus was selected, and the sensor was irradiated with 220 kV X-rays at the maximum beam current of 2.9 mA. The penetration quality of the beam defined by the half value layer (HVL) was measured to be 0.68 mm Cu. HVL represents the thickness of a material (in mm) that attenuates the intensity of the beam by 50%.

Temperature, pressure and relative humidity were recorded throughout the investigation to check for consistency but no additional corrections to the vM1212 detector were made. Due to the limitations of the low-performance laptop running the software to acquire the images from the detector, a maximum of 140 frames could be taken consecutively representing approximately 4 s of data.

Evaluation of the detector’s performance was achieved by changing the nominal width of the microbeam slits. Using the bespoke software to control the actuators, the nominal slit width was changed from 0 to 100  $\mu\text{m}$  as fast as it was able to. A measurement of the average dose rate for a variety of nominal slit widths was carried out (with 140 frames). Microbeam parameters for each of the peaks were fitted with a Python script using the SciPy module [15], assuming each peak was a perfect Gaussian with an offset. Associated uncertainties were calculated by comparing calculated parameters for the fitted microbeam peaks, with peaks rejected if the FWHM was determined to be greater than a non-physically possible 300  $\mu\text{m}$  width. In addition to stationary beams, the vM1212 detector was set to record while the nominal slit width dynamically changed.

## 3. Results

The calibration curve of the vM1212 detector is shown in Fig. 2, after subtraction of a dark current. Although the response of the vM1212 detector was found to be linear within the dose rate range used, a third order polynomial was applied to the signal from the vM1212 detector.

It was found that the vM1212 detector was able to obtain the full microbeam profile with an adequate level of discrimination between the low dose “valleys” and the high “peaks” regions for a single frame acquisition of static beams (Fig. 3). As reported by Flynn et al. [11], the produced microbeams were found to be larger than the nominal slit width, attributed to the finite size of the X-ray source (400  $\mu\text{m}$ ). The central three peaks for the different nominal slit widths are shown in Fig. 4, where the centre of each peak is observed to move in the positive x direction as the nominal slit width decreases.

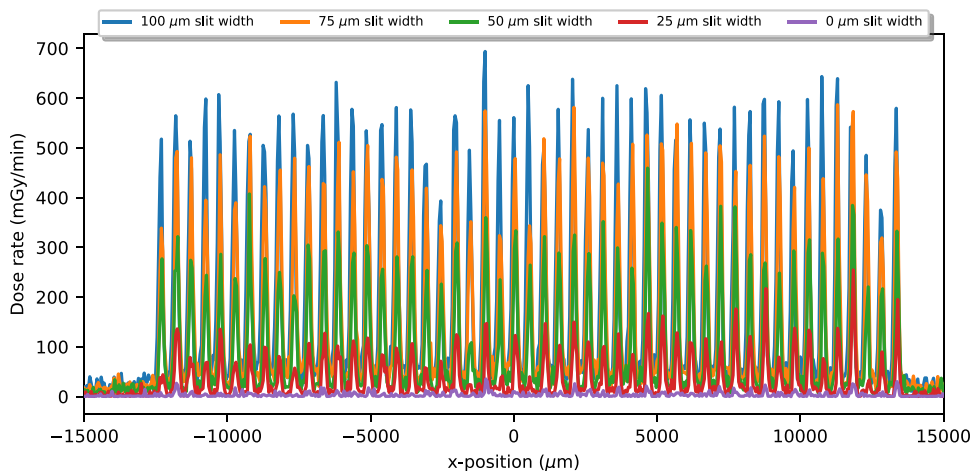


Fig. 3. Comparison of microbeam nominal slit widths acquired in single frames by the vM1212 detector.

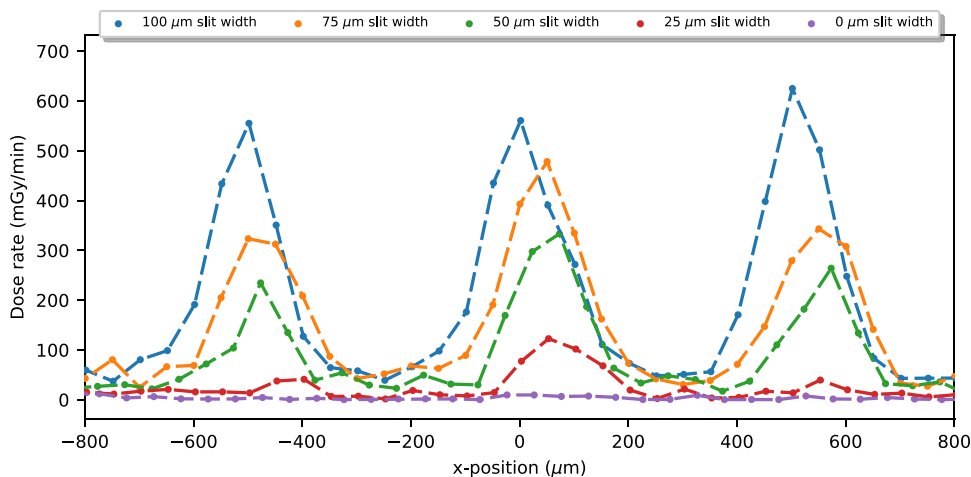


Fig. 4. Comparison of the central microbeam peaks acquired in single frames by the vM1212 detector.

As shown in Fig. 5, by using the calibrated response of the vM1212 detector, it was found that the mean dose rate (averaged within the  $\pm 15$  mm region shown on Fig. 3 for all of the 140 frames obtained at each nominal slit width) did not vary linearly with nominal slit width. This is likely due to complex scattering effects within the collimator. The coefficient of variation (defined as the standard deviation divided by the mean) rapidly increased for decreasing nominal slit width, indicating a larger variation between frames. As the X-ray source has not changed, this increase in variability in the intensity is likely due to photon shot noise.

Fig. 6 shows the variation of the investigated parameters during the recorded time while the nominal slit width was dynamically increased. The mean FWHM, as expected, was found to linearly increase, with a decrease in the FWHM standard deviation at larger nominal slit widths.

The PVDR remained approximately constant as the nominal slit width increased, with a smaller standard deviation for larger nominal slit widths. In Flynn et al. [11] it was observed that the PVDR measured by the vM1212 detector for static measurements remained approximately constant between 25 and 100  $\mu\text{m}$ , decreasing from approximately 14 at 25  $\mu\text{m}$  to 4 at 0  $\mu\text{m}$ . Due to the limited amount of data acquired for a moving slit, dynamic slit widths below 15  $\mu\text{m}$  were not able to be observed.

The peak to peak separation was observed to be approximately constant above 30  $\mu\text{m}$ , before which point the mean value and its standard deviation increased. As the physical separation of the microbeam slits did not change (only their widths), this increase in calculated peak to

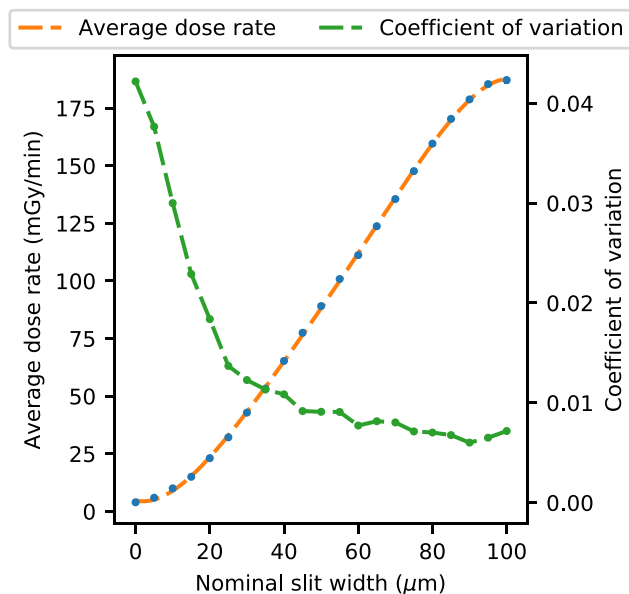


Fig. 5. Average dose rate and coefficient of variation (standard deviation/mean) of the microbeam field for various nominal slit widths.

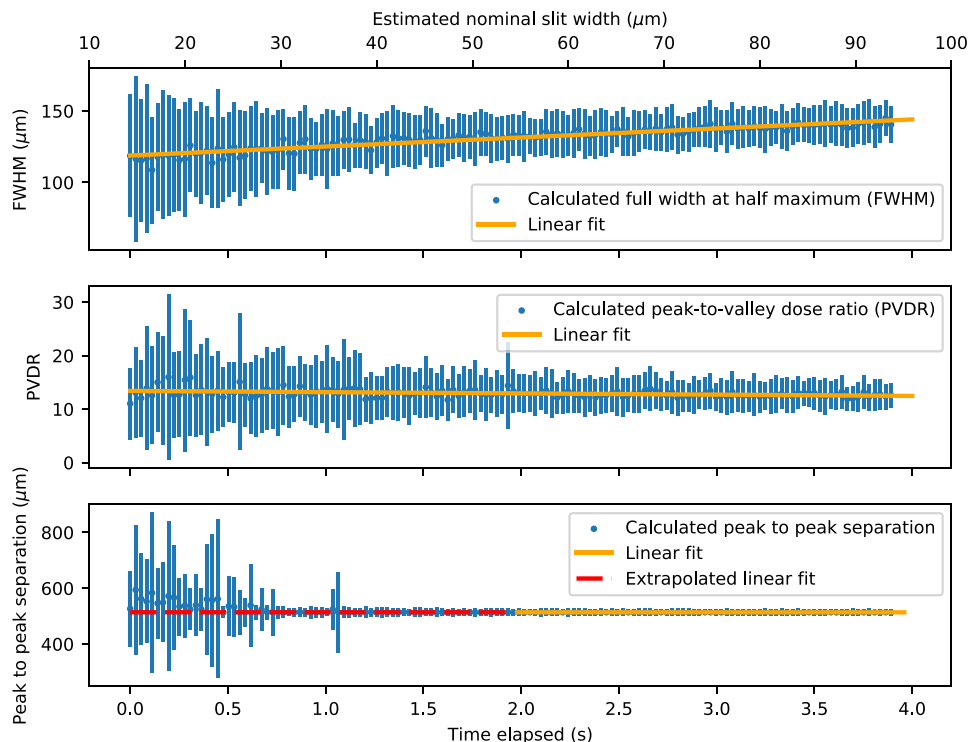


Fig. 6. Calculated parameters of the X-ray microbeam field as the nominal slit width increased (one standard deviation shown).

peak separation at low nominal slit widths is likely to be a consequence of the low intensity signal that was being recorded by the vM1212 detector.

#### 4. Discussion

As shown in Fig. 6 the uncertainty of all calculated parameters increases with decreasing nominal slit width, limiting potential pre-clinical impact of the vM1212 detector where slit widths of 25–50 μm are common. It is likely that photon shot noise contributes a significant source of uncertainty for low intensity signals. For *in vivo* monitoring this could be minimised by performing a moving average on several frames.

It is possible that the integration time of the detector could be automatically increased to compensate for poor signal, but this is beyond the scope of this investigation. In addition, it is possible that other methods for determining these parameters may be more suitable such as an auto-correlation function or fast-Fourier transform to determine the peak to peak separation, rather than relying heavily on fitted Gaussian profiles. The peak fitting function could also be improved, with more peaks that are not physically possible being rejected. This would likely have an effect of reducing the size of the standard deviations shown in Fig. 6.

Due to the limits of the electronic controller of the piezoelectric actuators that determine the nominal slit width, rapidly changing between several prescribed FWHMs for evaluation with the vM1212 detector was not possible. This is however, an area of interest for future research, as real-time verification of microbeam radiotherapy could be developed into a treatment control package.

#### 5. Conclusion

The results of this work demonstrate the feasibility of CMOS sensors for *in-situ* verification of microbeam X-ray irradiations. The vM1212 detector allowed for real time determination of beam position and shape which could be built into a future microbeam treatment planning

system. Further research is still required to develop future CMOS sensors with radiation tolerance in excess of 20 Mrad, higher frame rate for faster *in vivo* monitoring, smaller pixel pitch for greater spatial resolution, and with larger dynamic range to enable measurements of larger peak to valley dose ratio microbeams.

#### Declaration of competing interest

Due to the prototype nature of the device, the manufacturer of the vM1212 detector, vivaMOS Ltd, has been involved in data collection providing advice and technical support throughout the investigation.

#### Acknowledgements

This work was supported by the Science and Technology Facilities Council, United Kingdom (grant ST/P002552/1) and by the UK government's Department for Business, Energy and Industrial Strategy.

#### References

- [1] D.N. Slatkin, P. Spanne, F.A. Dilmanian, M. Sandborg, Microbeam radiation therapy, *Med. Phys.* 19 (6) (1992) 1395–1400, <http://dx.doi.org/10.1118/1.596771>.
- [2] A. Bouchet, R. Serduc, J.A. Laissue, V. Djonov, Effects of microbeam radiation therapy on normal and tumoral blood vessels, *Phys. Medica* 31 (6) (2015) 634–641, <http://dx.doi.org/10.1016/j.ejmp.2015.04.014>.
- [3] R. Serduc, et al., Brain tumor vessel response to synchrotron microbeam radiation therapy: a short-term *in vivo* study, *Phys. Med. Biol.* 53 (13) (2008) 3609–3622, <http://dx.doi.org/10.1088/0031-9155/53/13/015>.
- [4] E. Bräuer-Krisch, et al., Effects of pulsed, spatially fractionated, microscopic synchrotron X-ray beams on normal and tumoral brain tissue, *Mutat. Res. - Rev. Mutat. Res.* 704 (1–3) (2010) 160–166, <http://dx.doi.org/10.1016/j.mrrev.2009.12.003>.
- [5] F.A. Dilmanian, et al., Response of rat intracranial 9L gliosarcoma to microbeam radiation therapy, *Neuro Oncol.* 4 (1) (2002) 26–38, <http://dx.doi.org/10.1093/neuonc/4.1.26>.
- [6] M. Povoli, et al., Thin silicon strip detectors for beam monitoring in Micro-beam Radiation Therapy, *J. Instrum.* 10 (11) (2015) P11007, <http://dx.doi.org/10.1088/1748-0221/10/11/P11007>.

- [7] R. Serduc, et al., Synchrotron microbeam radiation therapy for rat brain tumor palliation—influence of the microbeam width at constant valley dose, *Phys. Med. Biol.* 54 (21) (2009) 6711–6724, <http://dx.doi.org/10.1088/0031-9155/54/21/017>.
- [8] E. Bräuer-Krisch, et al., Medical physics aspects of the synchrotron radiation therapies: Microbeam radiation therapy (MRT) and synchrotron stereotactic radiotherapy (SSRT), *Phys. Medica* 31 (6) (2015) 568–583, <http://dx.doi.org/10.1016/J.EJMP.2015.04.016>.
- [9] N. Annabell, N. Yagi, K. Umetani, C. Wong, M. Geso, Evaluating the peak-to-valley dose ratio of synchrotron microbeams using PRESAGE fluorescence, *J. Synchrotron Radiat.* (2012) <http://dx.doi.org/10.1107/S0909049512005237>.
- [10] P. Regnard, et al., Irradiation of intracerebral 9l gliosarcoma by a single array of microplanar x-ray beams from a synchrotron: Balance between curing and sparing, *Phys. Med. Biol.* 53 (4) (2008) 861–878, <http://dx.doi.org/10.1088/0031-9155/53/4/003>.
- [11] S. Flynn, et al., Evaluation of a pixelated large format CMOS sensor for x-ray microbeam radiotherapy, *Med. Phys.* 47 (3) (2020) 1305–1316, <http://dx.doi.org/10.1002/mp.13971>.
- [12] I. Sedgwick, D. Das, N. Guerrini, B. Marsh, R. Turchetta, LASSENA: A 6.7 Megapixel, 3-sides Buttable Wafer-Scale CMOS Sensor using a novel grid-addressing architecture, *Proc. Int. Image Sens. Work.* (2013) 3–6.
- [13] F. Treibel, J.J. Wilkens, S.E. Combs, S. Bartzsch, An optimized compact microbeam source for preclinical studies, <http://dx.doi.org/10.3252/psu.eu.ESTRO38.2019>.
- [14] S. Bartzsch, C. Cummings, S. Eismann, U. Oelfke, A preclinical microbeam facility with a conventional x-ray tube, *Med. Phys.* 43 (12) (2016) 6301–6308, <http://dx.doi.org/10.1118/1.4966032>.
- [15] P. Virtanen, et al., SciPy 1.0: Fundamental Algorithms for Scientific Computing in Python, *Nature Methods* 17 (2020) 261–272, <http://dx.doi.org/10.1038/s41592-019-0686-2>.